THE PROMOTION OF INSTABILITY OF A HIGHLY-DEFORMED PLATE UNDER FLUID LOADING AND ITS TRANSITION TO OSCILLATORY MOTION

A Dissertation

Presented to the Faculty of the Graduate School

of Cornell University

in Partial Fulfillment of the Requirements for the Degree of

Doctor of Philosophy

by

Diego Fernando Muriel Delgado

December 2018

ProQuest Number: 10982715

All rights reserved

INFORMATION TO ALL USERS
The quality of this reproduction is dependent upon the quality of the copy submitted.

In the unlikely event that the author did not send a complete manuscript
and there are missing pages, these will be noted. Also, if material had to be removed,
a note will indicate the deletion.

ProQuest 10982715

Published by ProQuest LLC (2019). Copyright of the Dissertation is held by the Author.

All rights reserved.
This work is protected against unauthorized copying under Title 17, United States Code
Microform Edition © ProQuest LLC.

ProQuest LLC.
789 East Eisenhower Parkway
P.O. Box 1346
Ann Arbor, MI 48106 – 1346

© 2018 Diego Fernando Muriel Delgado
ALL RIGHTS RESERVED

THE PROMOTION OF INSTABILITY OF A HIGHLY-DEFORMED PLATE UNDER FLUID LOADING AND ITS TRANSITION TO OSCILLATORY MOTION

Diego Fernando Muriel Delgado, Ph.D.

Cornell University 2018

Plates and membranes interacting with incoming fluids are canonical problems exhibiting rich physics concerning the onset of flutter instabilities. Such instabilities, once considered a failure state, are now exploited for new functionalities such as adaptive flow control, drag control, energy harvesting, and so forth. We present the dynamics of the fluid-structure interaction problem of a thin elastic plate buckled into a second mode-like deformation created by an external net compressive force. The deformed plate is immersed in an incompressible flow and is studied without the presence of oscillatory motions, and subsequently, in flow speeds where large oscillations are present. The presence of the deformation in the plate is intended to promote its oscillatory behavior at low flow velocities (i.e., early onset of flutter), increasing the potential for energy harvesting as well as the operational range of such devices.

Mathematically, we propose a description of the buckled plate considering that the amplitude of the deflection is greater than the thickness of the plate. First, we present the derivation of the equilibrium equations based on a heavy elastica model, and show the numerical solution of the nonlinear system of first-order equations for the static case. The results predict well the deformation (modes one and two) and point towards the existence of higher order deformation modes. Second, we show the derivation of dynamic terms and coupling

with a uniform incoming flow based on slender body theory. A linear stability analysis of the coupled mathematical model provides insights on the contribution towards a reduced critical flow velocity, U_c, from the combined destabilizing influence of the net compressive force and centrifugal forces, which allow for lower flow velocities to start the plate's large oscillatory movements. As we expect flow separation to occur due to adverse pressure gradients set up by the plate's deformation, there is a need for either a more elaborate coupling or an experimental approach to account for such flow separation, which is one of the main mechanisms involved on the onset of large oscillatory motions.

Experimentally, we subject the deformed plate to an incompressible flow to induce oscillations, and with the aid of image-based edge detection and acoustic Doppler velocimetry, find three states of motion: *a*) a buckled plate with weak perturbations below U_c, *b*) a plate with large oscillatory motions appearing as a superposition of traveling and standing waves above U_c, showing predictable dominant frequencies, and *c*) a plate with spatially-chaotic oscillatory motions above a transitional flow velocity (U_t), displaying a broad frequency spectrum. We find an early onset of flutter of the deformed plate compared to flag-type configurations (lower U_c). The main physical mechanisms contributing to the reduced U_c are the destabilizing action of the compressive force, a deformed locally-stable plate, and an unsteady flow field resulting in non-zero pressure drag and lift, all existent prior to structural oscillations.

Finally, based on particle image velocimetry, we present further experimental evidence of one mechanism contributing to the early onset of flutter: the occurrence of an unsteady flow field prior to oscillatory motions. We show a marginally dynamically stable plate progressively deforming as a function of flow regimes, with high production of vorticity and flow separation due to adverse pressure gradients, which renders the assumptions of irrotationality and those that lead to boundary layer equations inapplicable, as well as creating a non-zero pressure drag and lift. The unsteady flow field shows vorticity being diffused from boundary layers, advected out and downstream, creating unsteady "ejection" events. As critical flow velocity is approached, such events produce a suction high enough to compensate for the plate's restoring forces and weight, a reduction/increase in the magnitude of lift follows for the positive/negative phase, where the sign of the phase indicates to leading edge slope of the mode two deformation in the plate. These changes, by virtue of the non-linear boundary conditions (i.e., external forcing as a function of deformation), induce a change in deformation mode (dynamic mode branching or "snap-through"), and consequently, large oscillatory motions. Such behavior is also present on a dynamically unstable plate, albeit flow separation is present to a lesser degree (i.e., recirculation zones are smaller).

BIOGRAPHICAL SKETCH

The author was born in Cali, Colombia, in 1985. He graduated from Universidad Javeriana Cali, as a Civil Engineer in 2008. After spending three years in research on the hydrodynamics of Potable Water Storage Tanks and Chlorine Contact tanks, he moved in 2011 to Ithaca, NY, to pursue his graduate studies at Cornell University. During his MS in Civil and Environmental Engineering, he worked the first year with Professor Philip Liu studying the scaling factors of a device for wave energy extraction, and later joined a project of optimization of a novel self-powered water or fluid lifting device, which was the basis of his MS dissertation. In 2013 he continued onto his PhD, working with Professor Edwin (Todd) Cowen on the physical principles behind the oscillatory motions of fluid structure interaction of a buckled plate, a problem derived from his MS thesis and which is the basis of this document.

To my family.

ACKNOWLEDGEMENTS

First and foremost, I would like to express my sincere gratitude to Edwin (Todd) Cowen for his valuable advice and guidance during my time at Cornell, and for his endless source of ideas. Special thanks go to Pietro Filardo for allowing his idea to become the topic of study in this research. To Professor Rafael Tinoco for his support, guidance and encouragement during the early stages of the study. To Professor Phill L-F Liu for his guidance during my graduate studies and specially during my first year. I would also like to thank Professors Charles H. K. Williamson, Olivier Desjardins, and Rebecca Barthelmie for serving as members on my dissertation committee. Their valuable feedback has significantly informed the final version of this thesis

This work would not have been possible without the help of all the people that were at Cornell with me: thanks to Blair Johnson, Erika Johnson, Seth Schweitzer and Nimish Pujara for sharing their knowledge of techniques, facilities and equipment at the DeFrees Hydraulic Laboratory; to Mahmoud Sadek for entertaining the most little question I had and for having the patience to explain turbulence concepts to me; to Gustavo Rivera and Ignacio Sepulveda for the entraining discussions on any and all theoretical topics; to Paul Charles and Timothy Brock for their expertise at the machine shop; and to Jack Powers for his help and expertise in all related matters to the hydraulics lab. Special thanks to Jorge Escobar and Alexandra T. King to which I attribute my final decision of coming to Cornell in 2011.

Acknowledgment must go to the Colombian Science Foundation (Colombia), and the DeFrees Hydraulic Scholarship for partially funding the author's studies at Cornell University. Special thanks go to the Atkinson Center for Sustainable Future for their generous support. Any opinions and comments are those of the author and do not necessarily reflect the views of the sponsors.

TABLE OF CONTENTS

LIST OF TABLES

LIST OF FIGURES

CHAPTER 1

INTRODUCTION

1.1 Mechanics of motion of flexible plates immersed in free stream flows

Plates and membranes interacting with incoming flows are canonical problems exhibiting rich physics concerning the onset of structural and fluid instabilities. Such instabilities, once considered a failure state, are now exploited for novel applications such as adaptive flow control (Lucey, 1998; Jaiman et al., 2004), energy harvesting (Tang et al., 2009; Allen and Smits, 2001; Taylor et al., 2001; Techet et al., 2002; Akaydin et al., 2010; Li et al., 2011; Giacomello and Porfiri, 2011; Dunnmon et al., 2011), projectile stabilization (Fancett and Clayden, 1972; Auman and Wilks, 2005), and so forth. In the same way, progress understanding the physics has been useful to explain different phenomena such as biological flows (Huang, 1995; Balint and Lucey, 2005; Howell et al., 2009; Fenlon and David, 2001a,b; Smith et al., 2004), animal locomotion (Huber, 2000; Triantafyllou et al., 2000; Liao et al., 2003; Müller, 2003), induced vibrations on structures (Watanabe et al., 2002a,b; Chang and Moretti, 2002; Vandiver, 1993), to name just a few application areas. In general, the interaction of rigid or flexible plates with a flow is a problem that can be described by the interaction between the elastic, inertial, and damping forces of the structure, and the hydrodynamic forces of the fluid (Zhang et al., 2000; Shelley and Zhang, 2011).

Historically, Euler buckling is the very first example of elastic bifurcation and instability. It involves spontaneous symmetry breaking after a critical compressive load (Golubović et al., 1998). It is assumed elastic because the structure subject to buckling will immediately return to its straight configuration once external forces are removed. Euler and Bernoulli developed the theory of elastic lines (elastica curves), where large structural deformations are allowed under the elastic range. This theory was used to study the transition to buckling stability. In general, structural analysis is concerned with the transition of structures to deformations due to such instabilities and later collapse, and as a consequence, large deformations tend to be avoided.

On the fluid side, or more precisely the interaction of structures with fluids, contributions come from extensive studies in the areas of aeroelasticity (Dowell, 2015). Rayleigh (1879) presented the first available description of a flutter instability. Though incomplete, it constitutes the classical description of flapping flags, where the structure is represented by an always unstable infinite discontinuity surface, with zero mass, zero rigidity, and zero mean circulation. As in a Kelvin-Helmholtz instability, small perturbations amplify due to an unstable pressure distribution, causing the interface to evolve into a a greater number of vortices (Prandtl, 1952; Oertel, 2010). Since these descriptions by assumption neglect the presence of a plate, they ignore a plate's stabilizing forces, and are to date, corrected to include such effects (Zhang et al., 2000).

Flapping is therefore defined as a dynamical instability which can occur through flutter or divergence. The former is an oscillatory vibration of increasing amplitude, and the latter is an exponentially growing motion. On structures, buckling instabilities occur through divergence. Bigoni (2012) presents a detailed treatment of instabilities, and studies of rigid and flexible structures under fluid forcing, governing equations, and the nature of their instabilities are throughly explained in Dowell (1975, 2015), Dowell and Ilgamov (1988); Shelley and Zhang (2011), and Paidoussis (2016a,b). Here, elastic buckling instabilities are not to be confused with purely elastic instabilities occurring in viscoelastic fluids at Weissenberg numbers, Wi, of order unity, and vanishingly small Reynolds numbers, Re (Topea et al., 2007).

In addition to the literature mentioned above, the introductions by Tang and Paidoussis (2007); Eloy et al. (2007, 2008); Michelin et al. (2008); Alben and Shelley (2008); Doaré et al. (2011); Eloy et al. (2012); Schouveiler and Eloy (2012) summarize and group different theoretical and numerical efforts and identify the key aspects studied on the onset of the instability in a flag-type configuration, such as critical velocity for the onset of the instability, presence and wideness of the hysteresis loop where critical velocity will differ if it is found by increasing or decreasing flow velocity, confinement effects, aspect ratio, amongst others. In general, there are one-dimensional models using the Euler-Bernoulli beam equation, two-dimensional models, and realistic fluid flow solvers allowing simulations of moderate Re $O(10^2)$ such as the ones presented by Zhu and Peskin (2002); Connell and Yue (2007); Huang et al. (2007); Kim and Peskin (2007). It is well known that theoretical models underestimate the instability threshold, where experimental results tend to give larger critical velocities for the onset of flutter (Souilliez et al., 2006). Also, boundary layer separation as seen in the early experimental works by Taneda (1968); Taneda and Tomonari (1974) is not represented in such models.

Moreover, the use of the flutter instability as an energy harvester is a topic that has inspired multiple studies, each dealing with different problems from an experimental or mathematical standpoint. For such a device two options are possible: to couple it mechanically with an external generator (Tang et al., 2009), or to use piezoelectric materials (Sodano et al., 2004). Experimental studies have explored the fluid-structure coupling behavior when there is vortex shedding from an upstream structure (Allen and Smits, 2001; Techet et al., 2002; Akaydin et al., 2010), the efficiency of energy extraction (Taylor et al., 2001), alternative configurations to decrease the critical velocity, U_c, at which flutter first appears (Li et al., 2011; Ryu et al., 2015; Sader et al., 2016), and the influence of piezoelectric patches on the efficiency of the harvester (Giacomello and Porfiri, 2011; Dunnmon et al., 2011). Similarly, theoretical and mathematical studies have investigated the coupling between the fluid-solid-electric configuration (Doaré and Michelin, 2011; Akcabay and Young, 2012; Singh et al., 2012a,b; Michelin and Doaré, 2013; Xia et al., 2015).

In terms of energy harvesting efficiency for fluid-solid applications, a fundamental goal is to achieve stable structural oscillatory motions at low flow velocities (Kim et al., 2013; Xia et al., 2015). In other words, to induce the onset of flutter instabilities with as low a fluid forcing as possible. For example, piezoelectric flags (canonical configuration) are known to exhibit high U_c, requiring even higher flow velocities for consistent oscillations (Allen and Smits, 2001; Techet et al., 2002; Kim et al., 2013). Additionally, three-dimensional effects are known to delay the appearance of the instability in flag-type configurations (Souilliez et al., 2006; Eloy et al., 2012). Furthermore, alternative configurations such as the inverted flag, achieve oscillatory motions at low U_c (Kim et al., 2013), however, a direct consequence of this configuration is a limited operational range (OR, defined as the functional range of flow velocities measured upstream the device, U_o, for a given geometry, beginning once large oscillatory motions start and ending once stable oscillatory motions are not sustained). Interestingly, despite Dowell (1966, 1967, 1970, 1982) in the context of double-pinned plates, and Paidoussis (1966) for double-pinned cylinders showing that the action of compressive in-plane loads exacerbates the flutter instability; such a mechanism has not been implemented to enhance the transition to oscillatory motions for energy harvesters.

Herein, we test whether a plate's elastic instability and buckled configuration can be used to lower U_c at which large oscillatory motions start, and at the same time preserve or increase the range of regimes at which they occur when the plate is subjected to an incompressible flow. Specifically, we test whether a sinusoidally-buckled plate presents lower U_c and broader OR than those found under flag configurations (Fig. 2.1 and Fig. 2.2, Filardo (2013); Muriel et al. (2016)). First, a mathematical model based on the elastica approximation is presented and solved in the static case. As the vertical displacement of the induced deformation is greater than the thickness of the plate, the formulation contains geometric and boundary condition non-linearities. The results predict well the static deformation (modes one and two) and point towards the existence of higher order deformation modes. Fluid coupling is provided via slender body theory, and disregarding limitations about flow separation and high deformation, a linear stability analysis provides insights about the destabilizing action of external compressive and fluid centrifugal forces, and the stabilizing action of Coriolis and fluid induced tension. Second, the experimental results show that the deformation created by external compression induces the onset of structural oscillations at a low U_c compared to alternative flag-type configurations, with no need of vortex shedding from an upstream structure. The buckled configuration provides consistent oscillations at low U_o, allows the use of materials with higher damping, and gives rise to consistent oscillatory events at higher U_o, therefore achieving a broader OR. The hydrodynamics of the flow show high vorticity diffused from boundaries, advected out, and convected downstream, and flow separation behind the leading edge and first crest, rendering the irrotational assumption inapplicable. This unsteady flow is present before large oscillatory motions start, where the induced deformation creates a configuration of adverse and favorable pressure gradients. Despite being a dynamically stable plate (no large oscillatory motions), we find experimental evidence of small oscillatory motions, and “snap-through” events (dynamic jumps to a new displacement state at a fixed load level, Crisfield (1986)). With a compliant flexible structure, such small oscillations will transition into large motions following a change in sign of lift, cause by the activation of new boundary conditions restricting any further deformation to compensate for such change in sign.

1.2 Objectives

We want to characterize the fluid-structure interaction problem arising from a sinusoidally-deformed flexible plate immersed in an incompressible flow. To accomplish this, we propose the following objectives:

1. Objective 1: to characterize the oscillatory behavior as a function of the upstream flow velocity, defined above as U_o.
    - To determine the critical flow velocity, U_c, defined as the flow velocity to initiate large oscillatory behavior.
    - To investigate the presence of hysteresis in determining the critical velocity.

- To define the transitional Reynolds number Re_t defined as the flow velocity where transition to turbulent boundary layer occurs.
- To characterize the presence of spatial chaos and subharmonics in frequency spectra as precursors to chaos.
- To determine the evolution of oscillatory frequency as a function of U_o.
- To decompose the wave evolution of the plate's oscillatory motion into its traveling and standing components.

2. Objective 2: to describe the driving mechanics required to initiate the oscillatory behavior in different flow speeds.
   - To determine the phase-averaged flow field at five flow regimes prior to large oscillatory motions, for the two possible static equilibrium positions, and determine vorticity generation and flow separation.
   - To determine the phase-averaged flow field at three flow regimes after large oscillatory motions have occur (including critical flow velocity), and determine vorticity production and flow separation.
   - To calculate the mean pressure field, and lift and drag forces applied on the plate.
   - To model the deformation of the plate under static forces.
   - To study the contribution of forces towards stability based on a slender body theory coupling with the structural model of a flat plate.

1.3 Outline

Chap. §2 contains details of the methodology used in this study, with details on the design of the prototype, experimental facilities and techniques, as well as uncertainty an analysis. Chap. §3 presents the derivation and solutions of a mathematical model for the static deformation. Derivation of inertial and damping terms is also presented, and coupling with the fluid is provided via slender body theory. A linear stability analysis is also presented. Chap. §4 deals with the kinematics of the dynamically unstable plate, and presents a characterization of the oscillatory motions as a function of flow speed, while Chap. §5 takes care of the hydrodynamics of the fluid structure interaction, showing evidence of the mechanisms of transition to large oscillatory motions. Chap. §6 and Chap. §7 present conclusions and future work, respectively.

CHAPTER 2

METHODOLOGY

2.1 A second mode buckled plate

We induce the mode two like deformation presented in Fig. 2.1 and Fig. 2.2 with a series of tension lines that buckle a plate into a two-dimensional wave-like shape. The plate is made of a single translucent polycarbonate sheet with thickness $\delta = 0.400$ *mm*, length $L_p = 60$ *cm*, width $B = 30$ *cm*, density $\rho_p = 1.14$ g/cm^3, water absorption: 0.15% – 0.34%, and tensile modulus $E = 1.97$ *GPa* (see Sec. 2.6 for details on uncertainty analysis). The applied net compression is created using inner tension-lines mounted to parallel side-frame lines as seen in Fig. 2.1 and Fig. 2.2. The side-frame lines are made of micro-filament braided line (Spectra®), 0.4 *mm* diameter and rated to 471 *N*. Similarly, the tension-lines are composed of micro-filament with length $L_s = 7.62$ *cm*, separation along the plate of $\delta_p = 2.90$ *cm*, and separation on the side-frame of $\delta_f = 2.45$ *cm* (Fig. 2.2*a*). This difference between the two separations (δ_p and δ_f) provides the external compression force necessary to induce the plate's deformation, with maximum amplitude of 28.9 *mm* ($\sim 0.05\ L_p$, Fig. 3.3). The device is mounted on a frame made of extruded aluminum alloy, which sets the separation between side-frame lines to $B_r = 44.10$ *cm*, and positions the plate 15 *cm* above the bottom of a recirculating type open-channel flume.

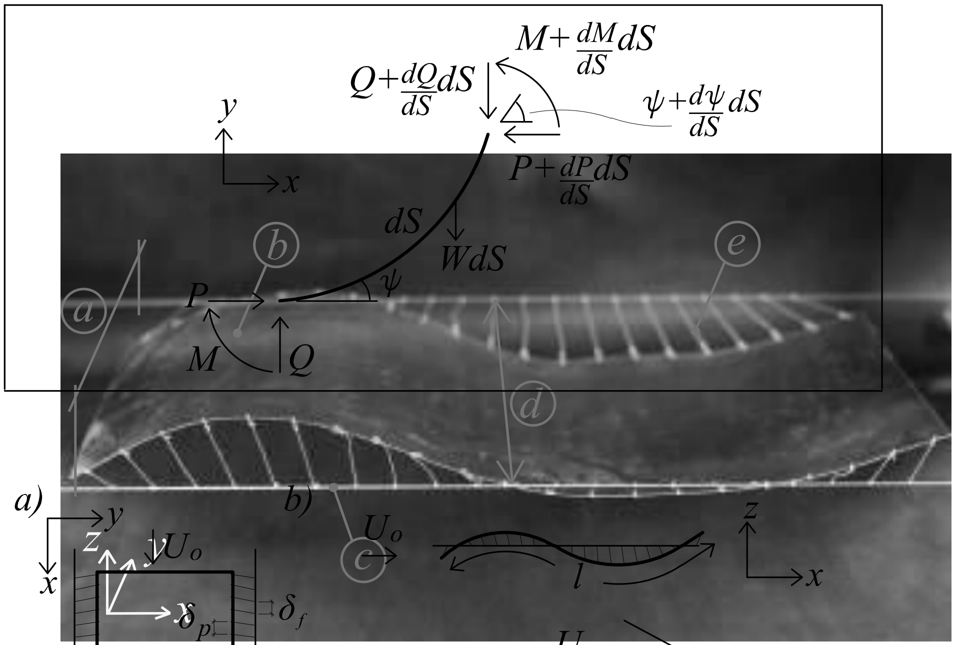

Figure 2.1: Experimental realization of a second mode-like deformation: *a*) Separation between side-frame lines (B), *b*) Translucent polycarbonate sheet, *c*) Side-frame lines (4 strand braids), *d*) Separation between side-frame lines at ½ (B_r), *e*) Compression lines.

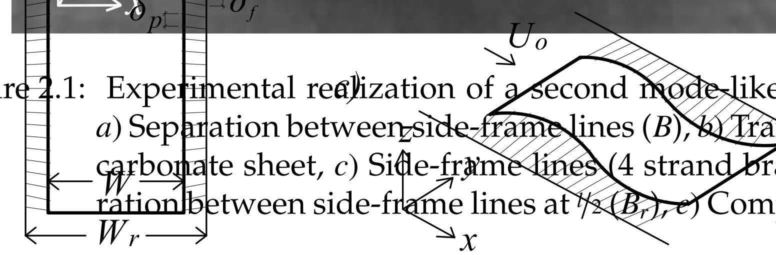

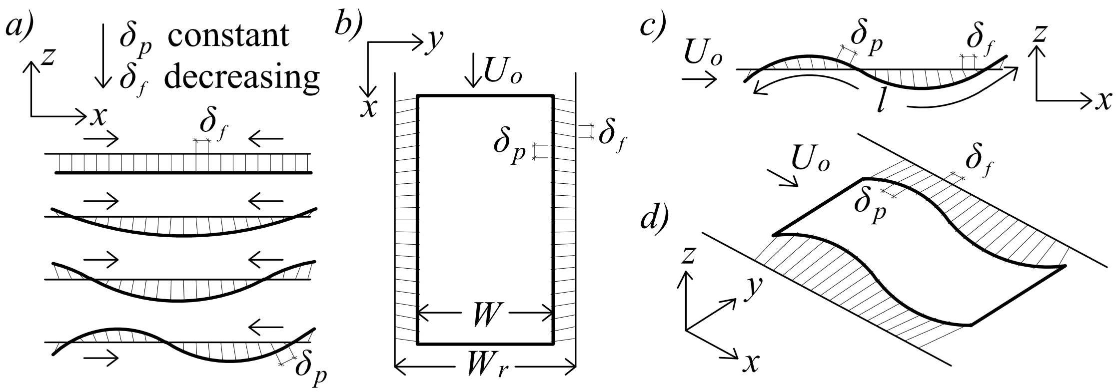

Figure 2.2: Isometric representation of the proposed deformed plate. a) Realization of wave-like deformation: separation between inner tension-lines in the device, δ_p, and in the frame, δ_f; b) Top view: flow velocity upstream the prototype, U_o, plate's width, B, separation between side-frame lines, B_r; c) Side view: plate's length, L; d) isometric projection.

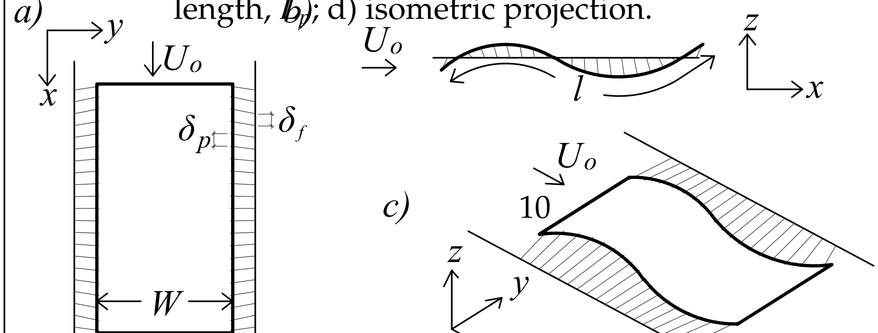

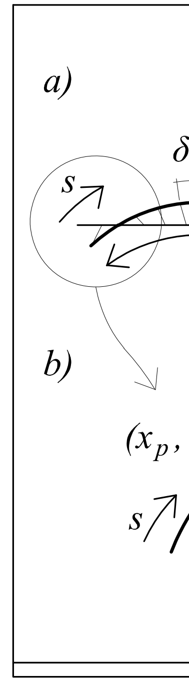

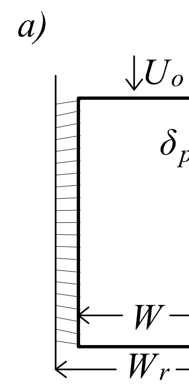

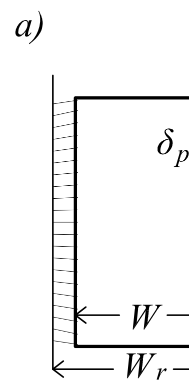

2.2 Facility

Experiments were conducted in an 8.0 m long, 0.60 m wide recirculating type open-channel flume with glass sidewalls and Super Abrasion Resistant (SAR) acrylic bed in the DeFrees Hydraulics Laboratory in the School of Civil and Environmental Engineering at Cornell University. Two variable frequency controlled centrifugal pumps drive the flow for a single water depth across experiments of $h = 37$ cm ($h = 35$ cm for particle image velocimetry tests), zero bed slope, and negligible stream-wise acceleration to experimental uncertainty ($\partial U_b^2/\partial x$, with the depth-averaged mean velocity at the centerline of the flume defined as $U_b \equiv (1/h)\int_0^h U dz$). A turbulent boundary layer is tripped by a 4 mm tall rectangular steel bar oriented in the cross-flow direction and located at the entrance of the flume test section downstream of inlet conditioning screens. A 15 μm felt is used to filter suspended particles of diameter greater than that of the felt. The coordinate system was defined with x in the streamwise direction, z as the vertical distance from the bed to the water surface, and y direction set by the right hand rule.

2.3 Experimental study cases

We investigate the interaction of the deformed plate with uniform incompressible incoming flows, and study its behavior in the presence of the plate's large oscillatory motions and lack thereof. To achieve this, three major data sets are collected. First, acoustic Doppler velocimetry (ADV) is used to determine the onset of large oscillatory motions, and to characterize the evolution of the plate's oscillatory frequency, f_o, as a function of flow velocity, U_o. Note that the specific

U_o where oscillatory motions first occur is defined as U_c. Second, special attention is given to the plate's oscillatory motion, and with the help of the ADV and image-based edge detection filtering (See Sec. §2.3.3), we characterize the plate's large oscillatory motions, including its wave composition and frequency, as a function of U_o. And third, we characterize the flow field based on particle image velocimetry (PIV), and present pressure fields and forces acting on the plate derived from these PIV measurements.

Tab. 2.1, Tab. 2.3, and Tab. 2.4 summarize the study cases using ADV, edge detection, and PIV, respectively.

2.3.1 Accoustic Doppler velocimetry

Velocity measurements (record lengths are 120 *min*) for all cases presented in Tab. 2.1 are performed with two Nortek Vectrino Acoustic Doppler Velocimeters (ADV) with + firmware at 200 *Hz*, where one ADV is deployed $5L_p$ upstream of the plate's leading edge for U_o analysis, and the other $3L_p/4$ downstream from the leading edge to determine f_o. Data is analyzed with one-dimensional spectra.

2.3.2 Image-based point detection

For all cases presented in Tab. 2.2, the plate's instantaneous location at a 9 equi-spaced points in space are extracted with an image-based edge detection filter using images collected from a 480×480 pixels $14-bit$ CMOS sensor (Phantom V9.1). Record lengths are 33 *min* for the lowest flow velocity, and 20 *min* for the

Table 2.1: Characterization of oscillatory frequency: experimental cases using acoustic Doppler velocimetry, ADV.

Test	U_o [cm/s]*	$Re/10^5 = U_o L_p/\nu$	$U_o L_p \sqrt{\frac{W}{Dg}}$
Increasing upstream flow velocity			
01	19.7	1.18	1.02
02	21.9	1.31	1.14
03	25.6	1.54	1.33
04	29.1	1.75	1.51
05	32.9	1.97	1.71
06	36.7	2.20	1.91
07	40.4	2.43	2.10
08	43.9	2.63	2.28
09	47.4	2.84	2.46
10	51.0	3.06	2.65
11	54.7	3.28	2.84
12	58.4	3.51	3.04
13	61.8	3.71	3.21
Decreasing upstream flow velocity			
14	62.2	3.73	3.23
15	59.2	3.55	3.08
16	55.9	3.36	2.91
17	52.3	3.14	2.72
18	48.9	2.93	2.54
19	45.3	2.72	2.36
20	41.8	2.51	2.17
21	37.0	2.22	1.92
22	33.2	1.99	1.73
23	29.6	1.78	1.54
24	26.2	1.57	1.36
25	22.9	1.37	1.19
26	20.6	1.24	1.07
27	18.9	1.13	0.98

* Maximum total error for upstream flow velocity, U_o, is $\pm 0.01 cm/s$ presented on Test 27.

Table 2.2: Characterization of plate's large oscillatory motion: experimental cases using image-based edge detection for single point location.

Test	U_o [cm/s]*	$Re/10^5 = U_oL_p/\nu$	$U_oL_p\sqrt{\frac{W}{Dg}}$	Equi-spaced points
01	19.8	1.19	1.02	9
02	22.0	1.32	1.14	9
03	25.6	1.54	1.33	9
04	29.1	1.75	1.51	9
05	32.8	1.97	1.70	9
06	36.8	2.21	1.91	9

* Maximum total error for upstream flow velocity, U_o, is $\pm 0.01 cm/s$ presented on Test 13.

Table 2.3: Characterization of plate's large oscillatory motion: experimental cases using image-based edge detection.

Test	U_o [cm/s]*	$Re/10^5 = U_oL_p/\nu$	$U_oL_p\sqrt{\frac{W}{Dg}}$
01	19.8	1.19	1.02
02	22.0	1.32	1.14
03	25.6	1.54	1.33
04	29.1	1.75	1.51
05	32.8	1.97	1.70
06	36.8	2.21	1.91
07	40.5	2.43	2.10
08	43.9	2.63	2.28
09	47.3	2.84	2.46
10	50.8	3.05	2.64
11	54.2	3.25	2.82
12	57.6	3.46	2.99
13	61.3	3.68	3.18

* Maximum total error for upstream flow velocity, U_o, is $\pm 0.01 cm/s$ presented on Test 13.

Table 2.4: Characterization of the flow field: experimental cases using particle image velocimetry, PIV.

Test	U_o [cm/s]*	$Re/10^5 = U_o L_p/\nu$	$\triangle t$ [s]	Length [min]	$U_o L_p \sqrt{\frac{W}{Dg}}$
01	6.9	0.41	0.0213	15	0.36
02**	6.9	0.41	0.0213	15	0.36
03	8.9	0.54	0.0165	15	0.46
04**	8.9	0.53	0.0165	15	0.46
05	10.8	0.65	0.0135	15	0.56
06**	10.9	0.65	0.0135	15	0.56
07	12.7	0.76	0.0114	15	0.66
08**	12.7	0.76	0.0114	15	0.66
09	14.6	0.89	0.0100	15	0.76
10***	16.7	1.00	0.0087	60	0.87
11	19.0	1.14	0.0076	60	0.99
12	28.8	1.73	0.0050	60	1.50
13	38.4	2.30	0.0038	60	1.99
14	48.0	2.88	0.0030	60	2.49
15	57.5	3.45	0.0025	60	2.98
16	61.2	3.67	0.0024	60	3.20

* Maximum total error for upstream flow velocity, U_o, is $\pm 0.01 cm/s$ presented on Test 3 and Test 16.

** Plate's deformation correspond to the mirror over the x-axis of the deformation of previous test.

*** Test corresponds to the critical velocity, U_c, which is the flow velocity at which large oscillatory motions start.

others, all at 18 Hz sampling frequency. Velocity measurements (record lengths of 30 min) are performed with two ADVs with + firmware at 200 Hz, where one ADV is deployed $5L_p$ upstream of the plate's leading edge for U_o analysis, and the other $3L_p/4$ downstream from the leading edge to determine f_o.

2.3.3 Image-based edge detection

For all cases presented in Tab. 2.3, the plate's instantaneous geometry is extracted with an image-based edge detection filter using images collected from a 1632×1200 pixels $14-bit$ CMOS sensor (Phantom V9.1). For the static deformation a single image per equilibrium position is used while for the large deformation cases 7000 images at 20 Hz are used per U_o. Velocity measurements (record lengths of 14 min) are performed with two ADVs with + firmware at 200 Hz, where one ADV is deployed $5L_p$ upstream of the plate's leading edge for U_o analysis, and the other $3L_p/4$ downstream from the leading edge to determine f_o. Data is analyzed with one or two-dimensional spectra ($2DFT$), and complex orthogonal decomposition (COD, Feeny (2008)).

The general idea behind the detection algorithm is to smooth and reduce noise, enhance edge detection and find the plate's position with sub-pixel accuracy in the vertical coordinate. The procedure is as follows:

1. Load image into a $16-bit$ unsigned integer format. This allows us to work in pixel coordinates and preserve the resolution of the original image.
2. Perform a median filtering in two dimensions (3-by-3 neighborhood with zero padding at the edges) over the loaded data. This step reduces background noise.

3. Implement a Laplacian Gaussian filter (5-by-5 kernel with standard deviation of 0.2). This filter enhances edges and provides a clear limit between background noise and edge data. Here, the filter increases the intensity count of what is expected to be a surface edge to the maximum possible value (2^{16}).

4. Apply a threshold filter. This step reduces the background noise that has been transformed into a white noise by the previous implementation of the Laplacian Gaussian filter, leaving at this point a mask that can be implemented over the original image.

5. Multiply the original image by the mask. This step drives the intensity count to zero on pixels where there is no presence of edges.

6. Apply a second round of the median filtering in two dimensions (3-by-3 neighborhood with zero padding at the edges). This filter is used to smooth and clean the residual noise.

7. Determine the maximum value of intensity count for every column (i.e. x-coordinate). This data provides the z-coordinate of the plate in pixel coordinates.

8. Apply a median filter in one dimension (15^{th} order). This filter is used to eliminate spurious points that could have entered during the detection of the pixel of maximum intensity.

9. Apply a Gaussian fit at each x-coordinate to seven pixels in the z-coordinate in double precision format, and determine the maximum value of the fit. These points include the pixel of maximum intensity, three above and three below in the z-coordinate, providing a sub-pixel approximation for the location of the plate. Since the Gaussian fit is over-prescribed, the fitting method is the non-linear least squares.

10. Apply a median filter in one dimension (15^{th} order). This filter is used to eliminate spurious points that could have entered during the Gaussian fit.

2.4 Particle image velocimetry

The flow velocity in the vicinity of the model is measured with particle image velocimetry for all cases presented in Tab. 2.4. Mean velocity, vorticity, and turbulent kinetic energy were measured by averaging the instantaneous flow fields for cases below U_c, and phase-averaging instantaneous velocity fields otherwise. Digital images were collected with two Andor Zyla 5.5 MP sCMOs (2160 $\times$ 2560 pixels, 16 $bits-per-pixel$, 20 $frames-per-second$ or 10 $Hz/image\ pair$) with a 50 mm Nikkor lens. Data is spooled to disc into two separate computers each equipped with 2TB SSD through a USB 3.0 interface. The image area was illuminated with a Spectra Physics PIV 200-10 Nd:YAG laser (200 $mJ/pulse$ at 532 nm, 10 Hz dual head). A laser light sheet was formed using a cylindrical lens ($f = -6.4$ mm) and the beam was focused with one spherical lens ($f = 1500$ mm) to provide a maximum light sheet thickness of 1 mm. This configuration provided a resolution of 144 $\mu m/pixel$ covering an area of 31.1 cm x 73.7 cm. Upstream velocity is measured with a single ADV located $5L_p$ upstream from the prototype leading edge, with $f_s = 200$ Hz and for the duration stated in Tab. 2.4.

A Berkeley Nucleonics Inc. (San Rafael, Calif.) BNC500A digital delay generator was used to trigger the flash lamps and Q-switches on the Nd:YAG laser system with temporal delay, Δt, presented in Tab. 2.4, chosen to limit the maximum particle motion to ~ 10 $pixels$, allowing a final PIV sub-window of 32×32 $pixels$ to be used to determine the displacement field. The tank was filled with water to the desired depth and seeded with Sphericel particles (hollow glass spheres, mean density 1.1 g/ml, median diameter 11.7 μm, manufactured by Potters Industries, Inc., Valley Forge, Pa.). Timing signals were generated in the Matlab data acquisition toolbox and sent simultaneously through a National Instrument AT AO-6 card to the digital cameras and the digital delay generator.

Prior to cross-correlation analysis, an intensity-count-based digital mask is found to reduce the influence of the highly illuminated plate. We do not conduct a correlation-tracking-based mask technique (Gui et al., 2003), instead, after the mean velocity field is subtracted from each image, pixels inside the digital mask are set to zero.

Image pairs in the $x-z$–plane are analyzed with the dynamic subwindow PIV scheme described by Cowen and Monismith (1997), and extended to second-order difference based on Wereley and Meinhart (2001). 4250 image pairs at 5 Hz are analyzed for cases below U_c, and the number of image pairs for cases above U_c is presented in Tab. 2.5 as they required phase averaging (see Sec. 2.4.2). The analysis comprises 5 passes for cases below U_c as follows (all with 50% overlapping): 64×64 *pixel* sub-window and an initial displacement estimate; 64×64 *pixel* sub window with mean velocity field from previous pass as displacement estimate; 32×32 *pixel* sub-window with mean velocity field from previous pass as displacement estimate; 32×32 *pixel* sub-window with mean velocity field from previous pass as displacement estimate; 32×32 *pixel* sub-window with filtered instantaneous velocity vectors from previous pass as displacement estimate. One additional pass with instantaneous results as the predictor is included for phase averaging cases above U_c. The final result is a 50% overlapping 32×32 *pixel* sub-window pass, with grid resolution

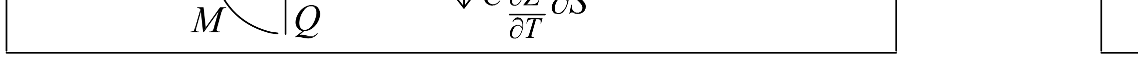

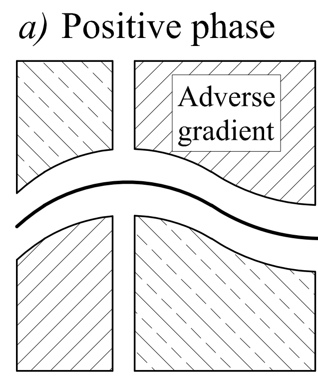

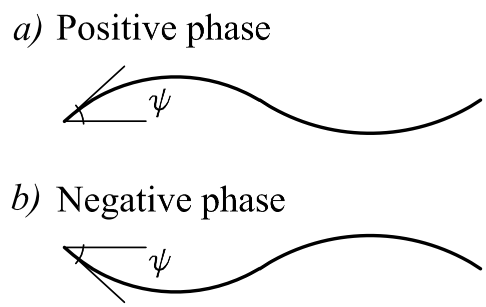

Figure 2.3: Phase definition based on initial curvature of the plate's deformation.

of ~ 2.3 *mm/sample* vertically and horizontally, resulting typically in 20724 analyzed subwindows per image pair. The full field of view is composed by two of this independent data fields (i.e., two cameras, each recording half of the field of view), forming a grid of 132 by 314 vectors in the vertical and horizontal axis, respectively.

2.4.1 Phase definition for dynamically stable cases

For flow velocities where there is no large oscillatory motion present, we test the plate twice for approximately the same flow velocity under two different equilibrium positions (See Tab. 2.4). For convenience, we provide a definition of such equilibrium positions based on the sign of the curvature (the angle between a horizontal line and a tangent to the plate) of the first section of the plate. If the deformation presents an initial positive curvature, ψ, it will be term "positive phase", or "negative phase" otherwise (see Fig. 2.3). The existence of such two equilibrium positions for the same load will be explained in Sec. 3.1.5.

Table 2.5: Number of image pairs used on particle image velocimetry analysis, PIV, when phase averaging is required.

Test	Phase	Image pairs	Tolerance*[pix]	Average Tolerance*[pix]
10**	a	144	10	10
	b	128	10	10
	c	94	10	10
	d	125	10	10
	e	31	10	15
	f	184	10	10
	g	111	10	10
	h	161	10	10
11	a	117	8	10
	b	112	8	15
	c	38	10	15
	d	80	8	15
	e	239	8	10
	f	82	8	15
	g	94	8	15
	h	89	8	15
12	a	73	10	10
	b	110	10	15
	c	137	11	15
	d	91	10	15
	e	40	11	15
	f	36	11	15
	g	34	11	15
	h	47	11	15

* This corresponds to allowed tolerance to determine image pairs, where the tolerance corresponds to the allowed tolerance from a target position, and averaged tolerance corresponds to the allowed tolerance from the 5 averaged previous positions of the target position.

** This test corresponds to critical flow velocity, U_c.

2.4.2 Phase-averaging procedure for dynamically unstable cases

PIV analysis for the unstable dynamic cases was performed using phase-averaged selected images. As the oscillatory motion is a nonlinear process, repeatability of deformations is expected to decrease as flow speed increases. We apply the edge detection algorithm described in Sec. 2.3.3 to the first image of the image pair, and extract the deformation of the plate in time (Fig. 2.4). To this image, we apply a median filter in time with a 15 point kernel, and subsequently a median filter in space with a 13 point kernel (See Fig. 2.5 for results). We can see in Fig. 2.6a that the result of filtering does not smooth out the real peaks of the deformation, and in turn allows us to eliminate noisy results of detecting tracer particles as potential plate locations. Notice from Fig. 2.4 and Fig. 2.5 that the leading and trailing edge have been truncated. These are locations particularly susceptible to errors in detection and therefore truncation was necessary to apply the filtering procedure. This does not mean that we are removing data for PIV analysis as this information is only needed for pre-selection of image pairs.

Once data is filtered out, we select a single point on the plate as our target position, and analyze the data in time looking for plate's positions close to the target position. We select those instances where the locations fulfill an established tolerance, and where the previous 5 time steps are within an average tolerance as well (See. Tab.2.5 and Fig. 2.7a for results of this step). The process is repeated for at least 5 additional locations (additional targets), leading to the final selected pairs within agreement of the established tolerances (See. Fig. 2.7b).

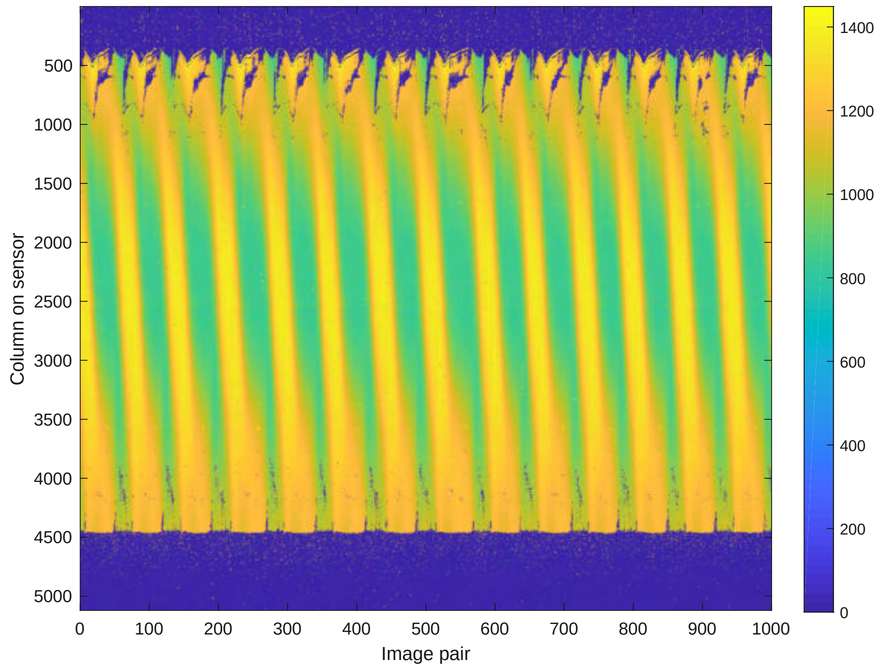

Figure 2.4: Example of plate's location as a function of time at critical flow velocity, U_c. The color-map indicates the position of the plate on a row of the sensor (i.e., the vertical coordinate of the plate for an specific time and an specific horizontal coordinate), the vertical axis indicates the column of the sensor (i.e., the horizontal coordinate), and the horizontal axis corresponds to the image pair or sequence in time. Data is unfiltered.

It remains to define the concept of phase of the selected cases. As linearity is not present, and considering the oscillatory period is described by a statistical distribution with positive skewness (see Fig. 2.8), we use the first oscillatory period of the first selected point as a guide to define phase. Within this period, eight phases where selected which describe the oscillation of said point, the first corresponding to $-\pi/2$, with $\pi/4$ increments. This phase angle is consistent with a sinusoidal wave, were zero is the Cartesian origin, and $-\pi/2$ and $\pi/2$ are the minimum and maximum, respectively. Nevertheless, this is not a mathematical definition of the phase of such experimental cases.

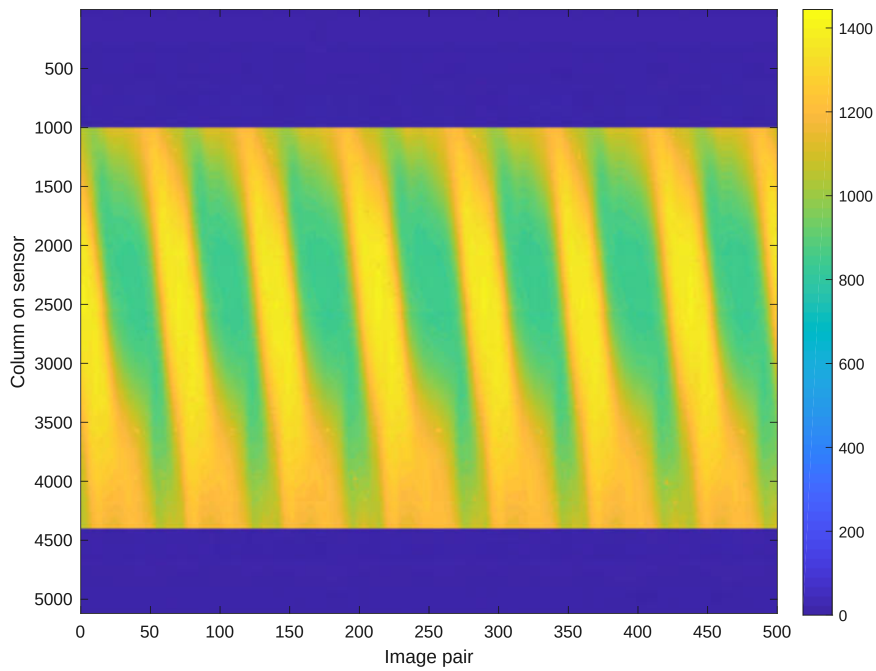

Figure 2.5: Filtered and truncated plate's locations as a function of time at critical flow velocity, U_c. The color-map indicates the position of the plate on a row of the sensor (i.e., the vertical coordinate of the plate for an specific time and an specific horizontal coordinate), the vertical axis indicates the column of the sensor (i.e., the horizontal coordinate), and the horizontal axis corresponds to the image pair or sequence in time.

2.5 Pressure and forces estimation

We assume the time-averaged flow field to be two dimensional and integrate the Reynolds averaged momentum equation (Eq. 2.1), to obtain time-averaged pressure fields for both dynamically stable and unstable cases. Following Einstein notation, the Reynolds average momentum equation is:

$$-\frac{\partial \bar{p}}{\partial x_i} = \rho \bar{u}_j \frac{\partial \bar{u}_i}{\partial x_j} + \rho \frac{\partial \overline{u_i' u_j'}}{\partial x_j} - \mu \frac{\partial^2 \overline{u_i'}}{\partial x_j x_j}, \tag{2.1}$$

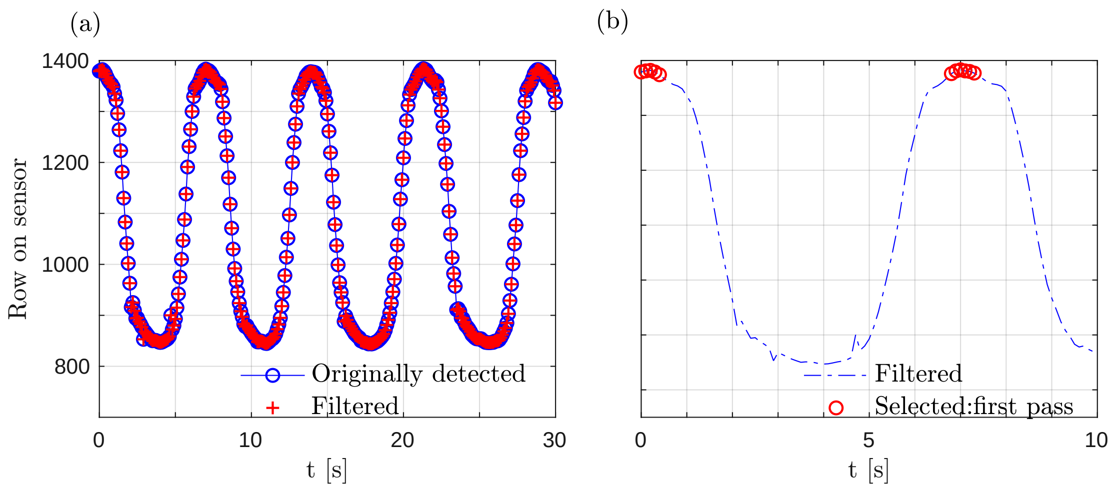

Figure 2.6: Displacement of a single point in the plate as a function of time at critical flow velocity, U_c. This example corresponds to column 2500 in the sensor array.

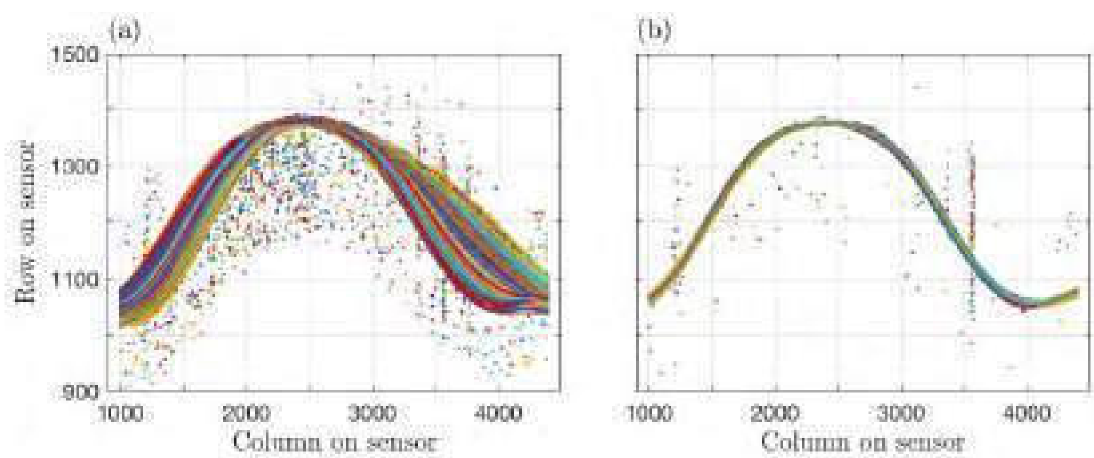

Figure 2.7: Selected plate's locations: a) Selected deformations fulfilling the allowable tolerance defined in Tab. 2.5 after analysis of column 2500 in sensor array; b) Final result after further analysis of columns and including the average error defined in Tab. 2.5.

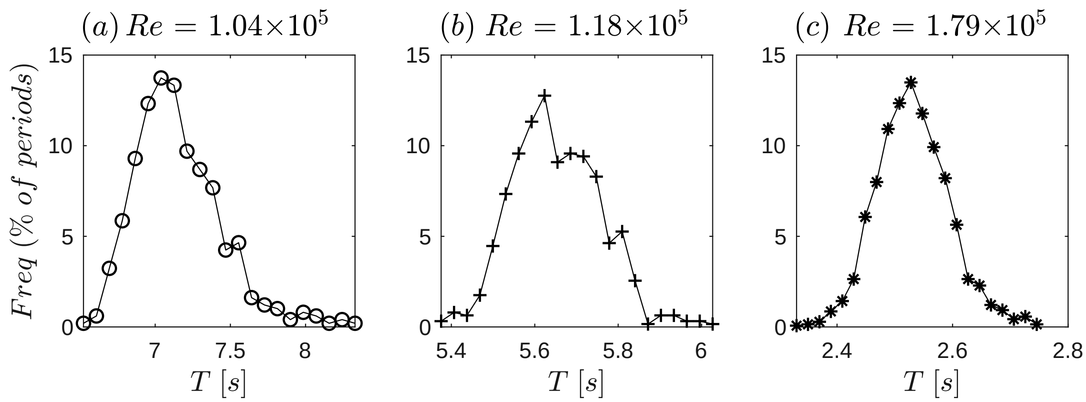

Figure 2.8: Distribution of periods for the three lowest flow speeds to which phase averaging was possible.

where the over-bar represents the time-mean, and the first, second, and third term on the right hand side represent the mean advection, fluctuating, and viscous stress terms.

Unlike methods where the pressure Poisson equation is solved (Koschatzky et al., 2011; Ghaemi et al., 2012; de Kat and van Oudheusden, 2012; Ghaemi and Scarano, 2013), the proposed scheme only involves the integration of the Navier-Stokes equations, with all possible shortest paths from boundary to each grid point (see for example Liu and Katz (2013); Zhang et al. (2017) for a more elaborated selection of paths to reduce computational cost). Comparison of the two methods (i.e., solving the Poisson equation or spatial integration of pressure gradients), is reviewed in (Charonko et al., 2010; van Oudheusden, 2013), showing that results are identical away from boundaries where Dirichlet boundary conditions are imposed. Pan et al. (2016) presents a study of the error propagation of the pressure derived from Poisson solvers, and showed that the error propagation for large domains is impacted by data errors inside the domain, while for small domains it is impacted by data errors on boundaries. Additionally, Pan et al. (2016) showed that the type of boundary conditions affects significantly the error propagation, where domains with pure Neumann boundary conditions need to satisfy the compatibility condition, which can prove difficult in PIV.

For the present fluid-structure interaction, solving the Poisson equation presents a number of challenges, and hence the calculation of the pressure takes the form of gradient integration. We leave the solution of the Poisson equation as a future work. First, being a pressure driven open channel flow, a non-zero pressure gradient is involved. Despite the slope of the water surface being negligible within experimental uncertainty, up- and downstream boundary pressure gradients are non-zero on the experimental domain (i.e., field of view). Second, the water surface is modulated by the immersed deformation (i.e., the plate), which again induces non-zero pressure gradients at the surface boundary. Moreover, the top boundary for the grid, does not match the surface exactly, partially due to the modulation and partially due to experimental design to reduce surface reflection errors. Additionally, the immersed boundary requires an appropriate handling of its boundary conditions, which requires a nontrivial handling of the plate curvature in relation to Newman boundary conditions applied onto a Cartesian grid.

The two dimensionality assumption is checked for each case trough the dimensionless divergence of the velocity field, $\left(\nabla \cdot \overrightarrow{u}\right) \triangle t$. This is presented in Fig. 2.9 for dynamically stable cases, and Fig. 2.10 to Fig. 2.12 for dynamically unstable cases. These fields show the fractional change in volume of an idealized infinitesimal fluid particle between adjacent velocity fields. In our case, since the diverge is computed on the average velocity field, the two adjacent velocity fields will correspond to the idealized field on the first and second image of a theoretical PIV image pair. Therefore, the divergence will show the degree of particles lost during the fractional time change Δt due to in-plane motions. From the figures we see that the two dimensionality assumption holds for the dynamically stable cases (Fig. 2.9), while for dynamically unstable cases, it shows good agreement for the two lowest flow velocities (Fig. 2.10 and Fig. 2.11) with some degree of in-plane motion accompanying vorticity being shed and advected out from the leading edge boundary layer. For the highest flow of the dynamically unstable cases (Fig. 2.12), the two dimensionality assumption is affected by the fact that the performance of the phase averaging is being affected by the reduced repeatability of the deformations (Sec. 2.4.2), phenomenon inherently related to the in-plane motions of the fluid and three-dimensional motions of the plate's deformations. Furthermore, as sugested by the simulations of an inclined vortex, a small to moderate degree of out-of-plane motion does not seriously affect the pressure field determination, provided the error is controlled with a multi-directional integration approach (Charonko et al., 2010; de Kat and van Oudheusden, 2012).

Given two-dimensionality of the average flow field, the momentum equation (Eq. 2.1) can be expanded to:

$$\begin{aligned}
-\frac{\partial \overline{p}}{\partial x} &= \rho\left(\overline{u}\frac{\partial \overline{u}}{\partial x} + \overline{w}\frac{\partial \overline{u}}{\partial z}\right) + \rho\left(\frac{\partial \overline{u'u'}}{\partial x} + \frac{\partial \overline{u'w'}}{\partial z}\right) - \mu\left(\frac{\partial^2 \overline{u}}{\partial x^2} + \frac{\partial^2 \overline{u}}{\partial w^2}\right),\\
-\frac{\partial \overline{p}}{\partial z} &= \rho\left(\overline{u}\frac{\partial \overline{w}}{\partial x} + \overline{w}\frac{\partial \overline{w}}{\partial z}\right) + \rho\left(\frac{\partial \overline{u'w'}}{\partial x} + \frac{\partial \overline{w'w'}}{\partial z}\right) - \mu\left(\frac{\partial^2 \overline{w}}{\partial x^2} + \frac{\partial^2 \overline{w}}{\partial w^2}\right),
\end{aligned} \tag{2.2}$$

where the apostrophe indicates the fluctuating terms. Moving the minus sign to the right hand side (R.H.S.), we can integrate Eq. 2.2 as follows ($\partial p/\partial x$ and $\partial p/\partial y$ represent the modified R.H.S. of Eq. 2.2):

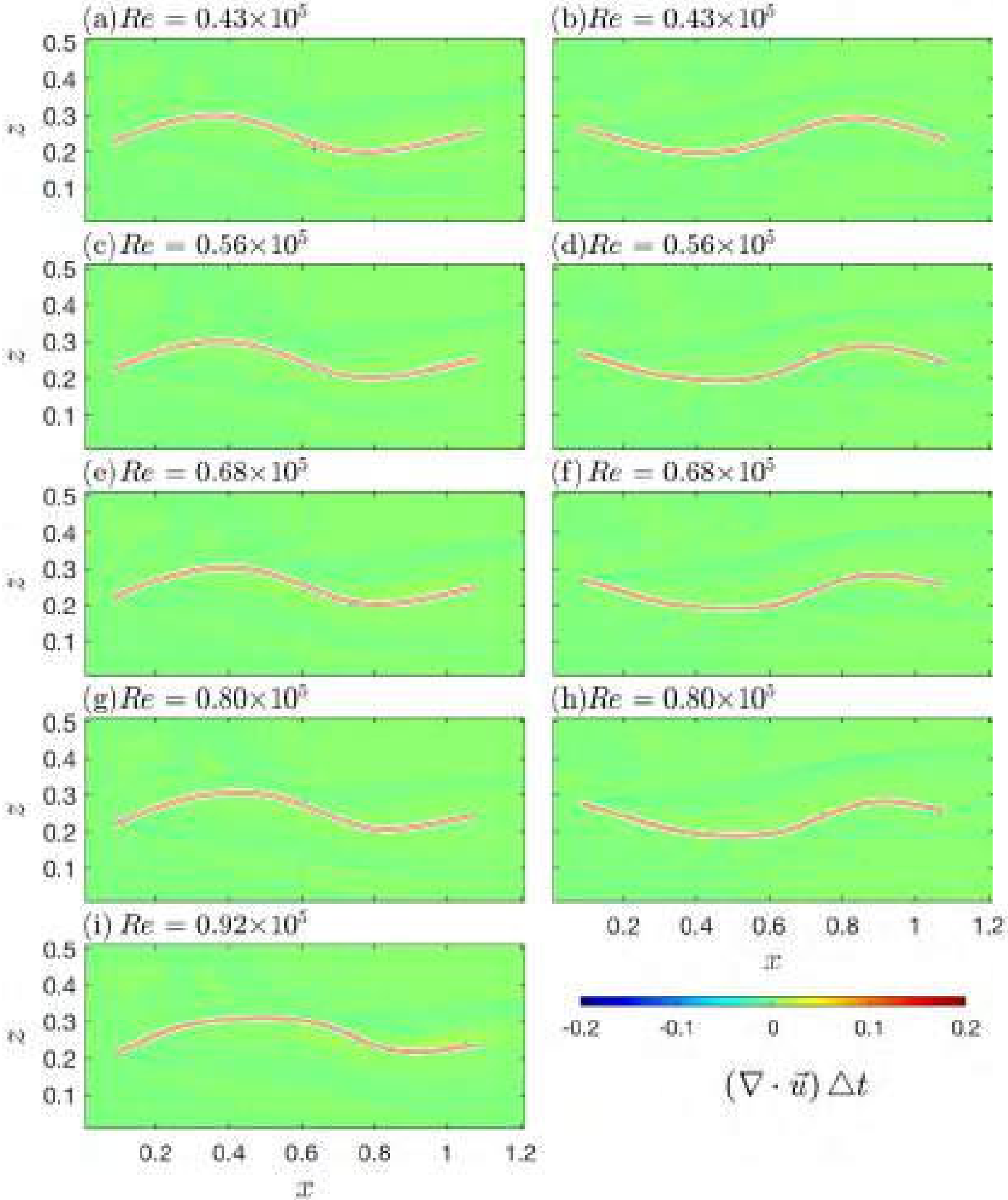

Figure 2.9: Two-dimensional divergence fields for dynamically stable cases. The fields are made non-dimensional by Δt (the temporal delay between two images of an image pair).

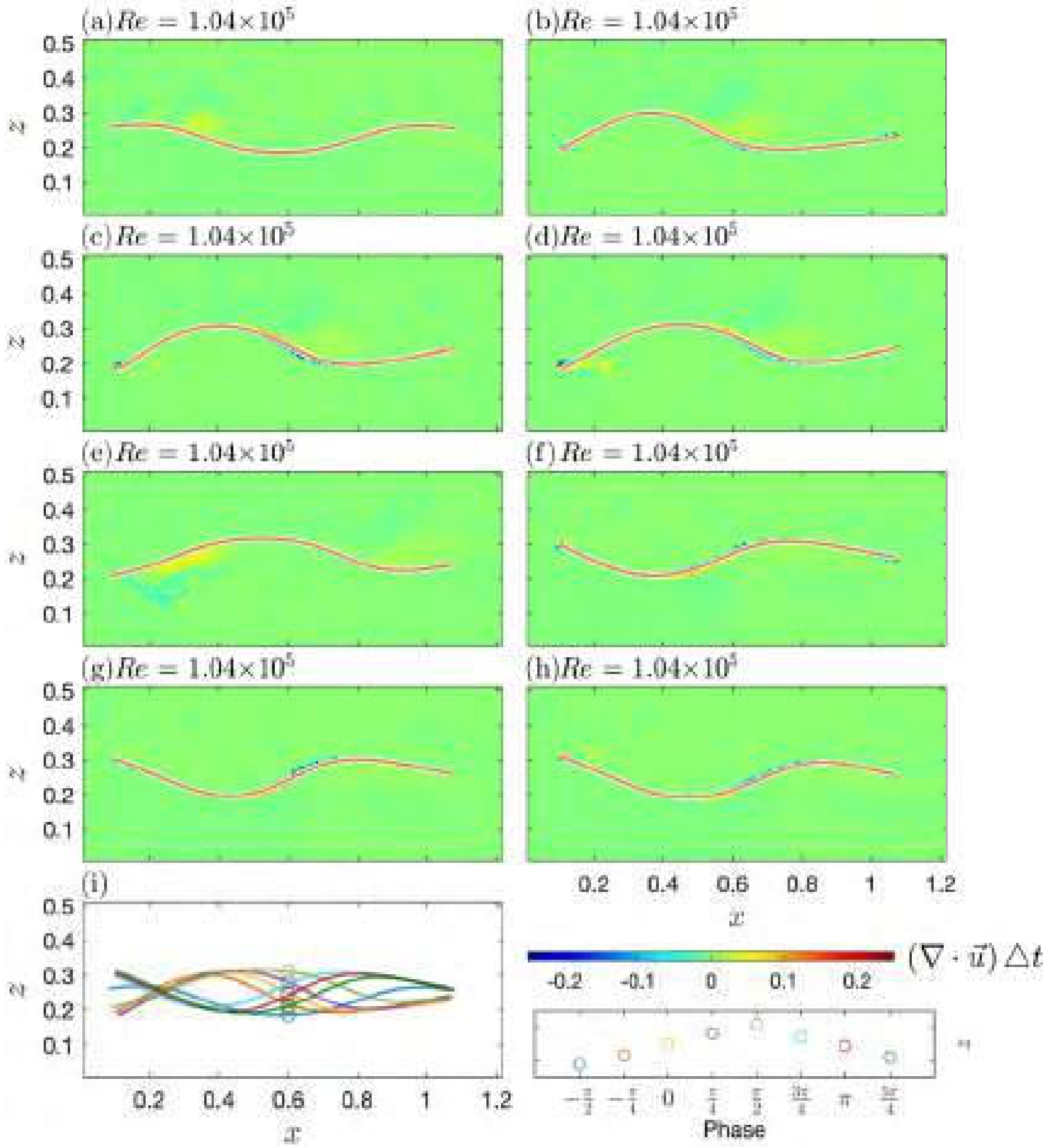

Figure 2.10: Two-dimensional divergence fields for dynamically unstable case at critical flow velocity ($Re = 1.04 \times 10^5$). The fields are made non-dimensional by Δt (the temporal delay between two images of an image pair).

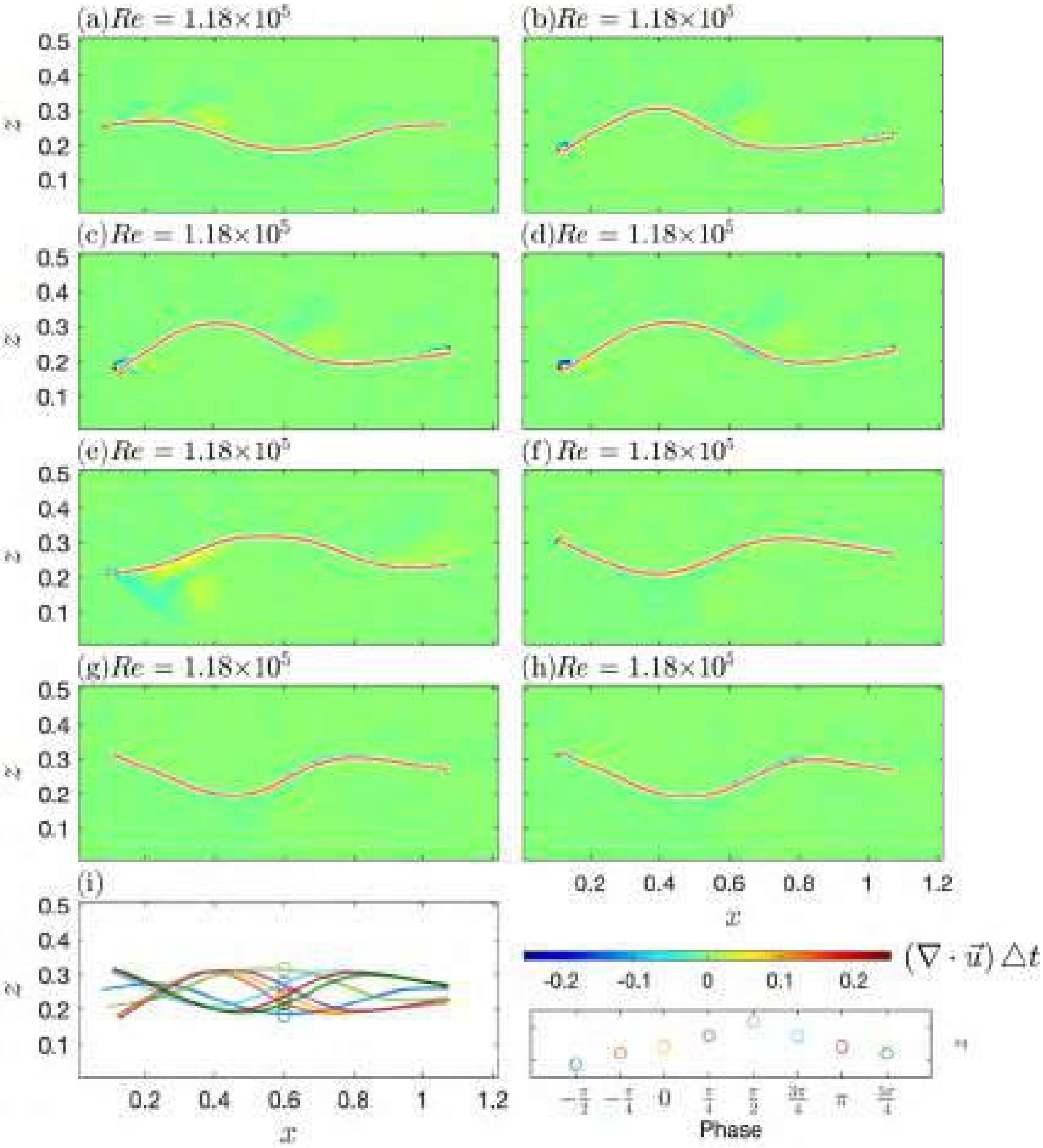

Figure 2.11: Two-dimensional divergence fields for dynamically unstable case at critical flow velocity ($Re = 1.18 \times 10^5$). The fields are made non-dimensional by Δt (the temporal delay between two images of an image pair).

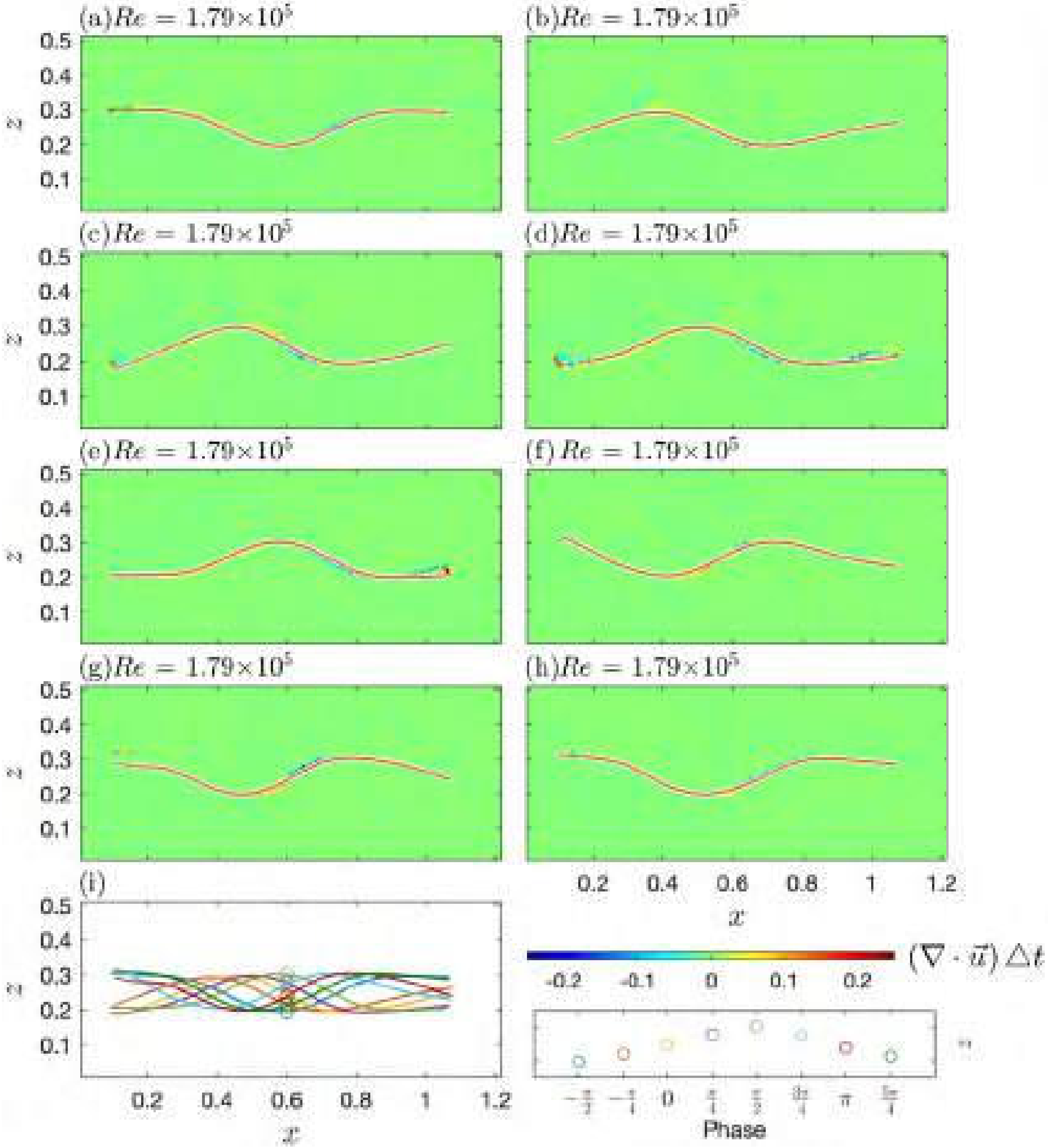

Figure 2.12: Two-dimensional divergence fields for dynamically unstable case at critical flow velocity ($Re = 1.79 \times 10^5$). The field has been normalized by Δt (the temporal delay between two images of an image pair).

$$p_2 - p_1 = \int_{x_1}^{x_2} \frac{\partial p(x,z)}{\partial x} dx + \int_{z_1}^{z_2} \frac{\partial p(x,z)}{\partial z} dz, \tag{2.3}$$

where p_1 is assumed to be equal to zero at the boundary for the first iteration, and the final result of the iteration is fed into the next iteration. The integration (trapezoidal rule) is carried out through all possible shortest paths from each boundary grid point to each other grid point, eliminating those paths that cross the immersed boundary (i.e., the plate), and averaging all results of valid paths. For an m by n grid, this involves $(2(m+n)-4) \times (mn-1)$ operations. A single grid value involves a maximum of $(2(m+n)-4)$ integration paths, minus those excluded due to immersed boundary crossing. Dabiri et al. (2014) used the median value of the integration paths (only 8 paths per grid point), while Liu and Katz (2006) used the mean value of the integration paths from their omni-directional algorithm (i.e., virtual boundary to avoid path clustering).

A straight line is used from (x_1, y_1) to (x_2, y_2) to identify the grid cells containing the grid points involved in the integration, but only horizontal and vertical movements are allowed (see Fig. 2.13).

We use seventy iterations to converge the assumption of p_1 on Eq. 2.3 and check the converge of all the points in the pressure field. All relative errors for dynamically stable and unstable cases are below 10^{-4}. Notably, we require more iterations than the 3 to 5 iterations suggested by Liu and Katz (2006) to achieve convergence. This can be explained first, by the fact that the length of our field of view is of the same order as the length of the plate, and second, by the fact that our algorithm does not implement the virtual boundary integration that reduces path clustering in Liu and Katz (2006).

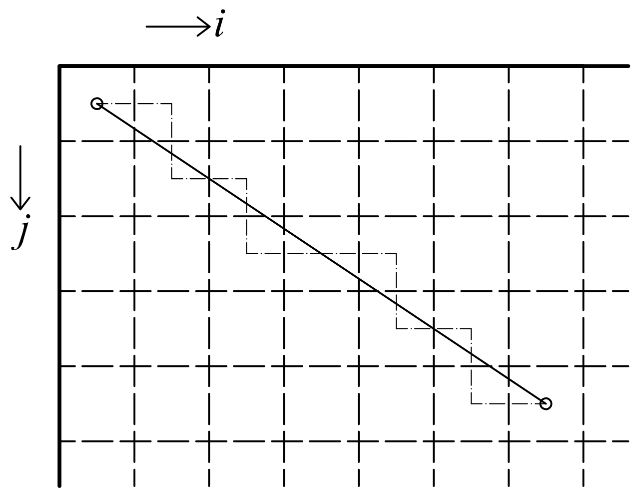

Figure 2.13: Example of shortest path between boundary grid point and interior grid point, and derived path based on allowed horizontal and vertical movements.

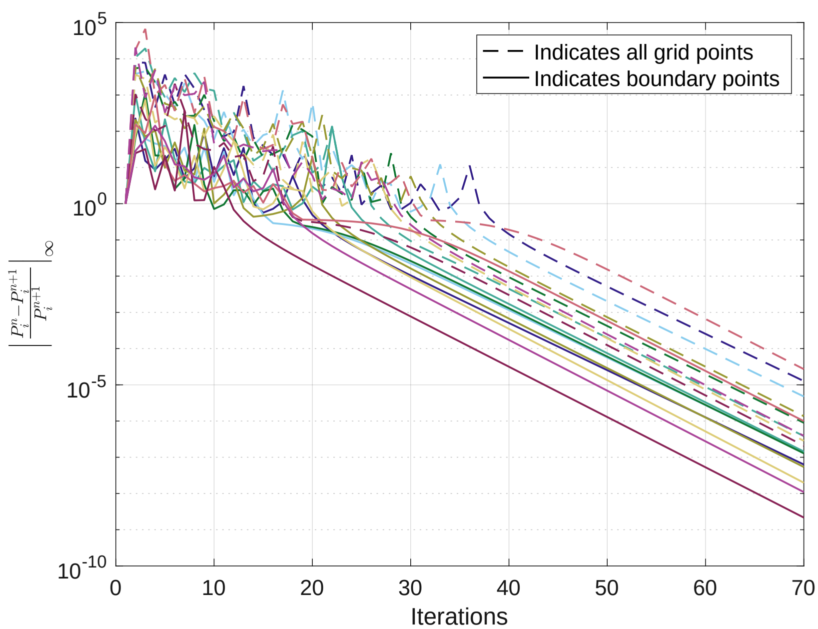

Figure 2.14: Infinity norm for the relative error including boundary grid points and all pressure field values for dynamically stable cases. Colors indicate different flow velocities.

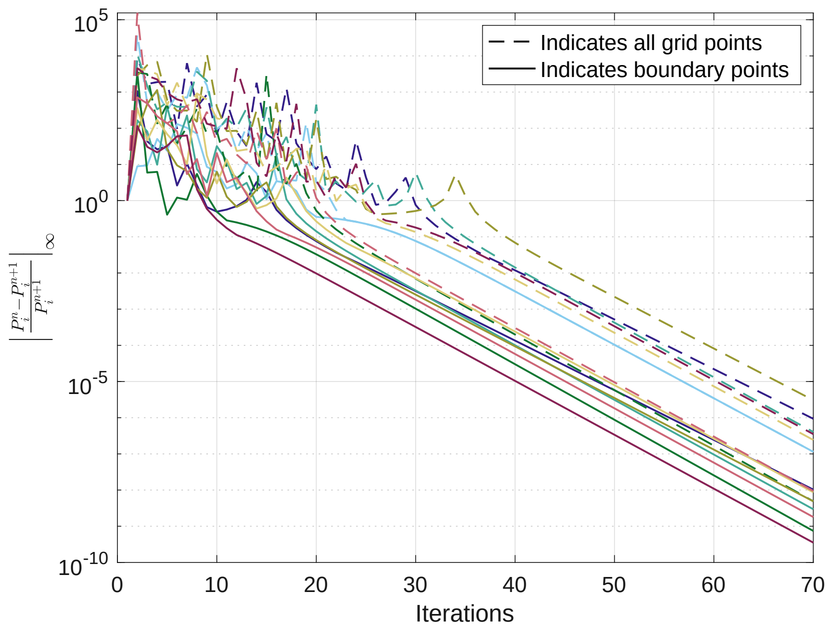

Figure 2.15: Infinity norm for the relative error including boundary grid points and all pressure field values for dynamically unstable case ($Re = 1.04 \times 10^5$). Colors indicate different deformation phases.

To determine the right hand side of Eq. 2.2 we use either centered finite differences for all interior points, or forward and backward finite differences for boundaries, all treated to second order. To determine the cells involved on a straight integration path, the Bresenham's line algorithm is implemented. This algorithm determines the points, in our case, coordinates, of an n-dimensional raster that should be selected in order to form a close approximation to the straight line between two points. The algorithm is cheap computationally as it only involves integer addition, subtraction, and bit-shifting. To determine the possibility of such a path intersecting the parametrized plate (i.e., plate's location represented by 2000 line segments) we evaluate the Bézier parameters as follows:

We define two lines L_1 and L_2 being the two lines the integration path and the

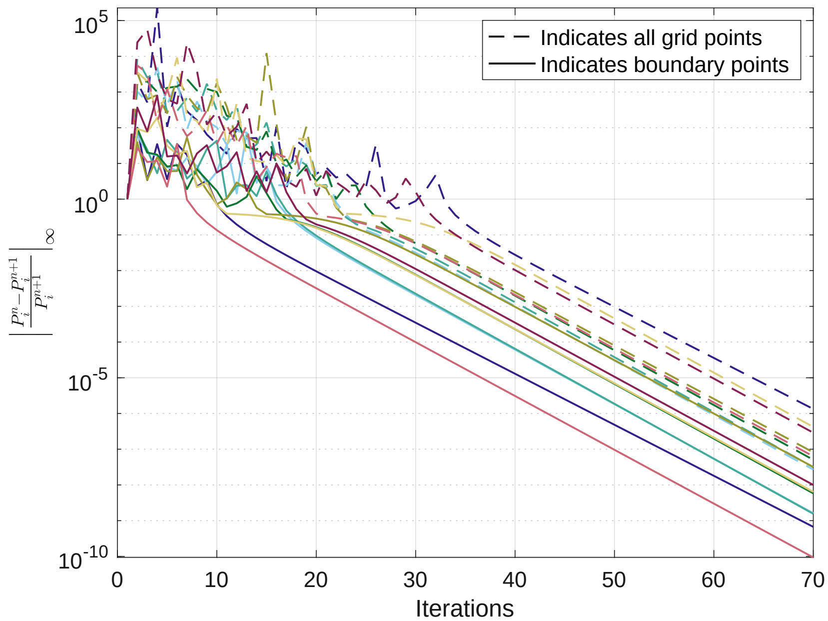

Figure 2.16: Infinity norm for the relative error including boundary grid points and all pressure field values for dynamically unstable cases ($Re = 1.18 \times 10^5$). Colors indicate different deformation phases.

segment of the plate being evaluated:

$$
\begin{aligned}
L_1 &= \begin{pmatrix} x_1 \\ y_1 \end{pmatrix} + tt \begin{pmatrix} x_2 - x_1 \\ y_2 - y_1 \end{pmatrix}, \\
L_2 &= \begin{pmatrix} x_3 \\ y_3 \end{pmatrix} + uu \begin{pmatrix} x_4 - x_3 \\ y_4 - y_3 \end{pmatrix},
\end{aligned}
\tag{2.4}
$$

where tt and uu are the first degree Bézier parameters to be evaluated, respectively defined as:

$$
tt = \frac{(x_1 - x_3)(y_3 - y_4) - (y_1 - y_3)(x_3 - x_4)}{(x_1 - x_2)(y_3 - y_4) - (y_1 - y_2)(x_3 - x_4)}, \tag{2.5}
$$

$$
uu = \frac{(x_1 - x_2)(y_1 - y_3) - (y_1 - y_2)(x_1 - x_3)}{(x_1 - x_2)(y_3 - y_4) - (y_1 - y_2)(x_3 - x_4)}. \tag{2.6}
$$

If $0 \leq tt \leq 1$ and $0 \leq uu \leq 1$, the two lines intersect and therefore the integration path is discarded.

A first calculation of the pressure field based on Dabiri et al. (2014) (i.e., integration of time dependent Navier-Stokes equation) showed that the methodology suffers from poor convergence under our experimental conditions. Such methodology is limited in the number of integration paths presenting directionality preference. Pressure results are further affected by not involving successive iterations to converge the boundary values used as an initial guess, assumed to be zero. Moreover, Dabiri et al. (2014) determined that the accuracy of their method is affected when the domain size is four times or less the length scale of the immersed object, which is directly related to the convergence of pressure boundary values.

Assuming the pressure field is sufficiently converged, we study the distribution of fluid forces acting on the plate, and their contribution towards transition to large oscillatory motions. The force of the fluid acting on the plate is given by:

$$\bar{F}_i = -\rho \iint_s \overline{u}_i \overline{u}_j n_j \mathrm{d}s - \rho \iint_s \overline{u'_i u'_j} n_j \mathrm{d}s - \iint_s \overline{p} n_i \mathrm{d}s + \mu \iint_s \left(\frac{\partial \overline{u}_i}{\partial x_j} + \frac{\partial \overline{u}_j}{\partial x_i} \right) n_j \mathrm{d}s \tag{2.7}$$

where the terms on the right hand side are the mean momentum transfer, the mean turbulent momentum transfer, the mean pressure contribution, and the mean viscous stress, respectively.

A dilation process was used to establish different control volumes over which forces where to be calculated 2.17. We define δ^{99}, the laminar boundary layer thickness of a flat plate, as a metric for dilation of the control surfaces

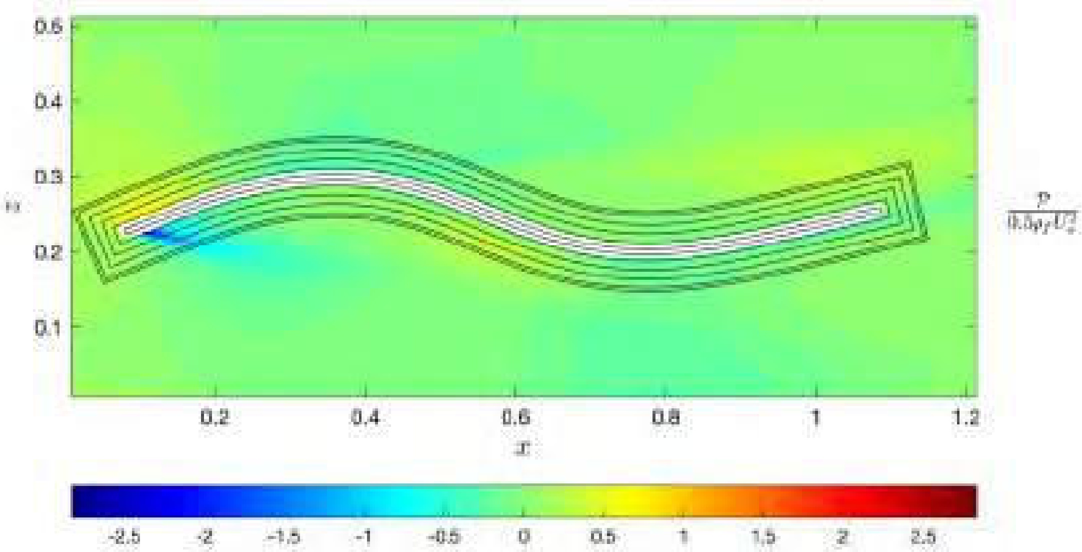

Figure 2.17: Examples of control volumes used at $Re = 0.43 \times 10^5$. The figure depicts the dilation at 0.5, 1.0, 1.5, 2.0, and 2.2 of δ^{99} from the plate's boundary.

away from the plate mean position:

$$\delta^{99} = \frac{5.0 L_p}{Re^{1/2}}, \tag{2.8}$$

where L_p is the plate's length. We explore using different fractions of δ^{99} (0.5 to 2.2) as the dilation length scale, and study the convergence of the total vertical and horizontal forces (lift and drag, respectively) as a function of such fraction.

The drag and lift coefficients are given by:

$$\begin{aligned} C_D &= \frac{F_D}{\frac{1}{2} L_p \rho_f U_o^2}, \\ C_L &= \frac{F_L}{\frac{1}{2} L_p \rho_f U_o^2}, \end{aligned} \tag{2.9}$$

where F_d and F_l are the drag and lift forces per unit width acting on the plate.

2.6 Uncertainty analysis

Unless otherwise stated, uncertainty associated with variables in text is as follows:

2.6.1 Bias errors

The accuracy of the ADV is reported by the manufacturer as ±0.5% of the measured value or ±1 mm/s, whichever is larger. To the former we add the error coming from misalignment on the experimental set-up or probes in the wrong position due to possible shocks during the usage. This additional error will be accounted for as roll, pitch and yaw movements, with an assumed maximum of 2° deviation angle, where only two out of the three rotations will be considered. If u_{real} is defined as $u_{real} = u_{bias}/\cos\theta$, the bias error due to roll movements is:

$$
\begin{aligned}
\varepsilon &= u_{real} - u_{bias}, \\
\varepsilon &= u_{real} - u_{real}\cos\theta, \\
\varepsilon &= \frac{u_{real} - u_{real}\cos\theta}{u_{real}} = 1 - \cos\theta,
\end{aligned}
\tag{2.10}
$$

where the total error now considering a second rotation due only to misalignment is:

$$
\begin{aligned}
\varepsilon &= \sqrt{(1 - \cos\theta)^2 + (1 - \cos\theta)^2}, \\
\varepsilon &= \sqrt{(1 - \cos(2^\circ))^2 + (1 - \cos(2^\circ))^2}, \\
\varepsilon &= 0.09\%,
\end{aligned}
\tag{2.11}
$$

and the total error considered as bias error for velocity components or magnitudes with the same units as the velocity (turbulent intensity) is $\varepsilon = \sqrt{0.09\%^2 + 0.5\%^2} = 0.51\%$. The error for the Reynolds stress will be considered as the square of this error. If the bias error calculated as the 0.51% of the measured value is less than 1 mm/s or $(1\ mm/s)^2$, the later is chosen as the bias error.

For quantitative image-based edge and single point detection, the root-sum-squares technique (Kline and McClintock, 1953) is considered for bias errors defined as $\delta R/R$:

$$\frac{\delta R}{R} = \left[\left(\frac{\partial L}{L} \right)_i^2 + \left(\frac{\partial T}{T} \right)_i^2 \right]^{1/2} \tag{2.12}$$

Taking into account the errors of spatial calibration (1 *pixel* per 1600 *pixels*), and camera trigger response time (1 μs per 0.005 s), for a maximum total bias error of $\varepsilon = 0.07\%$.

For particle image velocimetry, as with image-based detection, the root-sum-squares (Eq. 2.12) technique is considered for the bias calculations, with errors of sub-window displacement (0.5 *pixels* per 32 *pixels*, where 0.5 *pixels* is chosen as the sub-window displacement is sub-pixel accurate), spatial calibration (1 *pixel* per 2160 *pixels*), trigger response time (1 μs per 0.005 s), for a maximum total bias error of $\varepsilon = 1.56\%$.

2.6.2 Random error

The random error for both ADV and PIV is calculated based on the bootstrap analysis (Efron and Tibshirani, 1994) with 1000 re-samplings for the analysis of the *mean*, reporting the 95% confidence interval. The confidence interval band reported in all figures of spectral analysis has been done with this technique. The error reported in the edge detection results is the 95% confidence interval of the true error distribution (no bootstrap involved). We report for velocity and turbulent metrics the maximum random absolute error bounds, and the 10%, 50%, and 90% percentile values of the relative error distribution bounds (see App. D), values chosen as typical metrics of these distributions.

Special care is taken to report mean values of PIV for each variable of interest. We define absolute and relative errors as follows, taking the mean value of the horizontal velocity as an example ($\overline{u}$): the upper and lower error bounds are ε^+ and ε^-, respectively. These errors are the 95% confidence interval based on bootstrap analysis with 1000 re-samplings. The upper and lower absolute error bounds are $|\Delta\varepsilon^+| = |\,\varepsilon^+ - \overline{u}\,|$, and $|\Delta\varepsilon^-| = |\,\varepsilon^- - \overline{u}\,|$, respectively. These errors have the units of the variables of interest. Additionally, we report the dimensionless relative error, with upper and lower bounds define as $\left|\Delta\varepsilon_r^+\right| = |\,(\varepsilon^+ - \overline{u})\,/\overline{u}\,|$, and $|\Delta\varepsilon^-| = |\,(\varepsilon^- - \overline{u})\,/\overline{u}\,|$, respectively.

We present the maximum absolute error ($|\Delta\varepsilon|$), and the 10%, 50%, and 90% percentile value of the relative error distribution ($|\Delta\varepsilon_r|$) per case. For example, the maximum $|\Delta\varepsilon|$ is the maximum of an $m \times n$ PIV grid. In a similar way, the percentile value intervals for $|\Delta\varepsilon_r|$ are the respective percentiles of the $m \times n$ PIV grid. This is presented to avoid misleading the reader towards the erroneous interpretation of the existence of high errors in the current data set. Our experimental set-up involves developing boundary layers, flow separation, and recirculation zones that drive time-averaged velocities and fluctuations close to, if not exactly to, zero values. As expected, a relative error of such values grows inversely proportional to the mean value, and therefore, relative errors can be

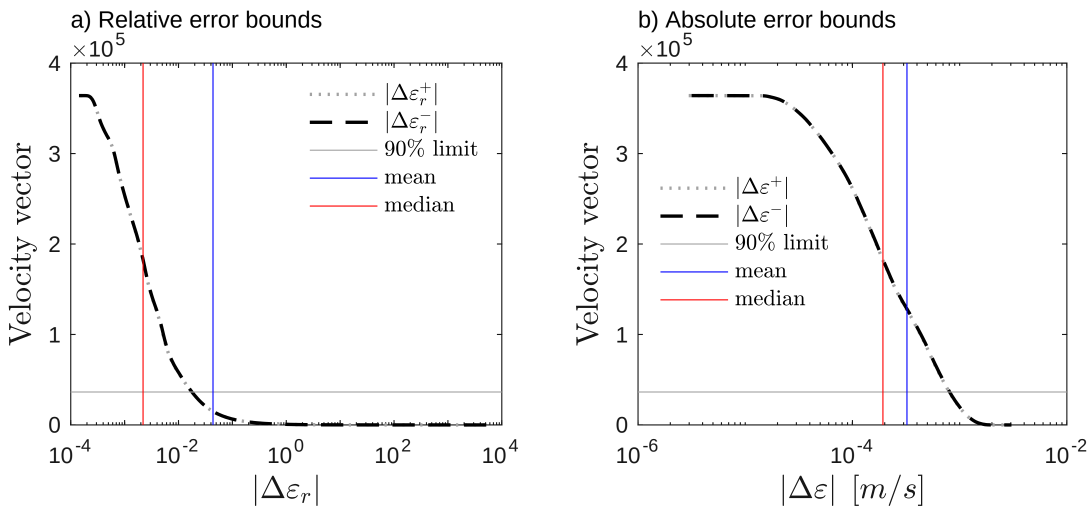

Figure 2.18: Sorted relative and absolute random uncertainty bounds for the mean horizontal velocity, $\overline{u}$, containing all dynamically stable cases. Sorting of absolute and relative errors is independent, and (+) and (-) signs indicate upper and lower bounds, respectively.

excessively large.

Notice, for example, how the value of the relative error grows to a considerably large value for $\overline{u}$ and $\overline{w}$, while the maximum absolute error remains low with respect to U_o (Fig. 2.18 and Fig. 2.19, respectively). These two distributions contain all velocity vectors for the static cases (i.e., all vectors contained in the $m \times n$ grids of the nine cases). An option here will be to simply normalize all values for U_o, but this option, as dividing by a small number, can be misleading as well.

Tab. 2.6, and Tab. 2.7, present the maximum absolute and relative error for dynamically stable cases, and dynamically unstable case, respectively.

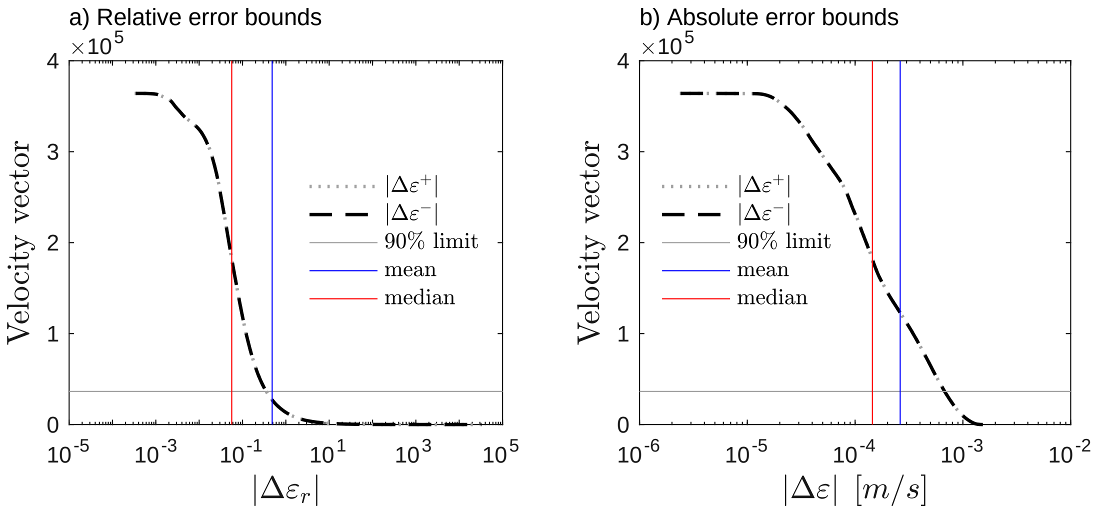

Figure 2.19: Sorted relative and absolute random uncertainty bounds for the mean vertical velocity, $\overline{w}$, containing all dynamically stable cases. Sorting of absolute and relative errors is independent, and (+) and (-) signs indicate upper and lower bounds, respectively.

Table 2.6: Absolute ($|\Delta\varepsilon|$) and relative ($|\Delta\varepsilon_r|$) error bounds for dynamically stable cases. Absolute error is the maximum error, and relative error is reported as a percentile of the distribution.

			Percentiles, reported as [%].					
			10^{th}		50^{th}		90^{th}	
	$\lvert\Delta\varepsilon^+\rvert\ [m/s]$	$\lvert\Delta\varepsilon^-\rvert\ [m/s]$	$\lvert\Delta\varepsilon_r^+\rvert$	$\lvert\Delta\varepsilon_r^-\rvert$	$\lvert\Delta\varepsilon_r^+\rvert$	$\lvert\Delta\varepsilon_r^-\rvert$	$\lvert\Delta\varepsilon_r^+\rvert$	$\lvert\Delta\varepsilon_r^-\rvert$
$\overline{u}$	0.0029	0.0031	0.05	0.05	0.22	0.23	1.78	1.78
$\overline{w}$	0.0017	0.0017	0.86	0.87	5.65	5.65	35.43	35.34
$\overline{u'}$	0.0019	0.0018	1.93	1.85	2.44	2.32	3.08	2.93
$\overline{w'}$	0.0012	0.0011	2.07	1.97	2.58	2.45	3.16	3.00
$\overline{u'w'}$	0.0001*	0.0001*	6.52	6.57	11.96	12.09	55.48	55.26

* Units are $[m^2/s^2]$.

Table 2.7: Absolute ($|\Delta\varepsilon|$) and relative ($|\Delta\varepsilon_r|$) error bounds for dynamically unstable cases. Absolute error is the maximum error, and relative error is reported as a percentile of the distribution.

			Percentile, reported as [%].					
			10^{th}		50^{th}		90^{th}	
	$\|\Delta\varepsilon^+\|$ $[m/s]$	$\|\Delta\varepsilon^-\|$ $[m/s]$	$\left\|\Delta\varepsilon_r^+\right\|$	$\left\|\Delta\varepsilon_r^-\right\|$	$\left\|\Delta\varepsilon_r^+\right\|$	$\left\|\Delta\varepsilon_r^-\right\|$	$\left\|\Delta\varepsilon_r^+\right\|$	$\left\|\Delta\varepsilon_r^-\right\|$
$\overline{u}$	0.1161	0.1332	0.22	0.22	0.81	0.82	3.63	3.78
$\overline{w}$	0.0752	0.1269	02.78	02.77	20.07	20.26	129.14	128.77
$\overline{u'}$	0.1194	0.1123	10.40	08.85	15.81	12.64	28.25	20.33
$\overline{w'}$	0.0854	0.0823	10.91	09.16	16.41	12.95	29.51	20.82
$\overline{u'w'}$	0.0131*	0.0346*	40.57	45.80	91.08	101.39	479.29	484.12

* Units are $[m^2/s^2]$.

2.6.3 Total error

With bias and random error defined, total error (ε_{tot}) can be determined by Eq. 2.13

$$\varepsilon_{tot} = \sqrt{\varepsilon_{bias}^2 + \varepsilon_{random}^2} \tag{2.13}$$

2.6.4 Other uncertainty

Additional uncertainty criteria is as follows:

1. Half of the maximum resolution for single-sample data (i.e. data associated with length scales, oscillatory frequencies (f_o) derived from one-dimensional spectral analysis, wave frequency (ω) and number (κ) derived from two-dimensional spectral analysis and complex orthogonal decom-

position).

2. Confidence interval for small samples size determined as $\overline{x} \pm t^*_{df} s/\sqrt{n}$ (Devore, 2016) where $\overline{x}$ is the mean value, t^*_{df} is the value of the Student's t-distribution with df degrees of freedom, s is the standard deviation, and n is the number of samples (i.e. plate's thickness, δ, plate's density, ρ_p, and tensile modulus, E).

3. Uncertainty for the critical Reynolds number, Re_c, corresponds to half of the step change of U_o in f_o vs U_o trend, when Re_c occurs.

4. Uncertainty for the reported hysteresis loop corresponds to maximum and minimum hysteresis loops considering the uncertainties associated to U_c.

2.6.5 Uncertainty associated with variables reported in text

1. Plate's thickness: $\delta = 0.400 \pm 0.007\ mm$.
2. Plate's length: $L_p = 60 \pm 0.05\ cm$.
3. Plate's width: $B = 30 \pm 0.05\ cm$.
4. Plate's density: $\rho_p = 1.14 \pm 0.03\ g/cm^3$.
5. Plate's tensile modulus: $E = 1.97 \pm 0.04\ GPa$.
6. Tension-line diamaeter: 0.4 mm.
7. Tension-lines' length: $L_s = 7.62 \pm 0.05\ cm$.
8. Separation of tension-lines along the plate: $\delta_p = 2.90 \pm 0.05\ cm$.
9. Separation of tension-lines on the side-frame: $\delta_f = 2.45 \pm 0.05\ cm$.
10. Separation between side-frame lines: $W_r = 44.10 \pm 0.05\ cm$.
11. Positions of plate above the bottom of recirculating flume: $15 \pm 0.05\ cm$.

12. Water depth: $h = 37 \pm 0.05$ cm.

CHAPTER 3

GOVERNING EQUATIONS

3.1 Numerical model of a periodically constrained heavy elastica

In this section (based on Muriel and Cowen (2018)), we limit our discussion to the study of static buckling of a periodically constrained heavy elastica in two dimensions (Fig. 3.1*a*). It will serve as a model for our plate by restricting the deflection to only cylindrical bending of the elemental strip, where the flexural rigidity, D, of the unit-width strip is $D = EI/(1-\nu^2)$, with E being the Young's modulus, I the area moment of inertia, and ν Poisson's ratio (Timoshenko and Woinowsky-Krieger, 1987).

We consider the elastica to be inextensible of length L_p (non-dimensional $l = 1$), of uniform cross-section, elasticity, density, and thin enough such that the Euler assumption holds (i.e., the total curvature is proportional only to the local moment Wang (1986)).

The basis of such a model follows from a straight plate of length L_p, with tension lines of length L_s, δ_p apart, and with connection coordinates $\left(x_p, z_p\right)$ (Fig. 3.1*b*). The other end of the tension lines are attached to an infinitely rigid frame, with connections spaced δ_f apart at coordinates (x_o, z_o). Originally, the plate hangs straight from the tension lines, which are being strained only by the action of the plate's weight. As we progressively decrease δ_f and keep δ_p constant, different tension lines activate or deactivate (Fig. 3.1*c*). On active lines, tension forces H appear, forces which induce a series of deformations as $\left(\delta_p - \delta_f\right)/\delta_p$

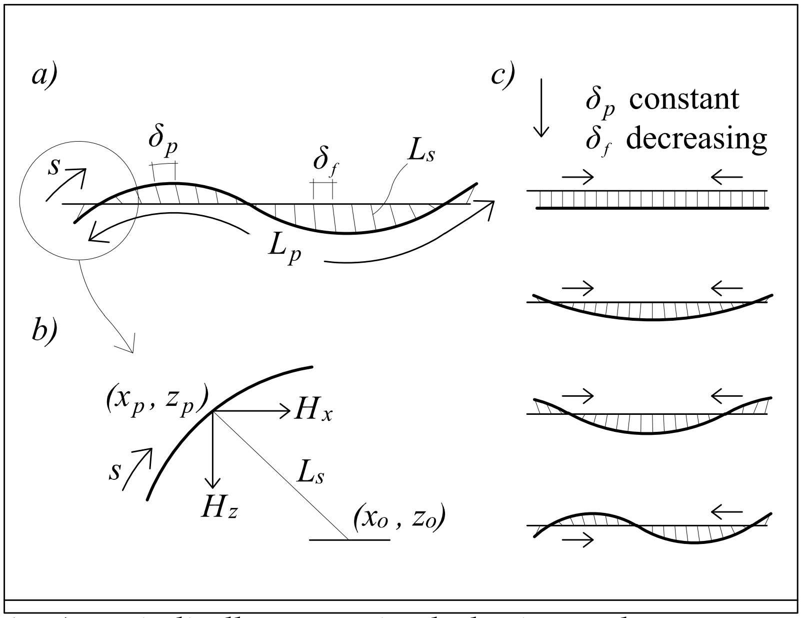

Figure 3.1: A periodically constrained elastica under a progressive increase of external forces.

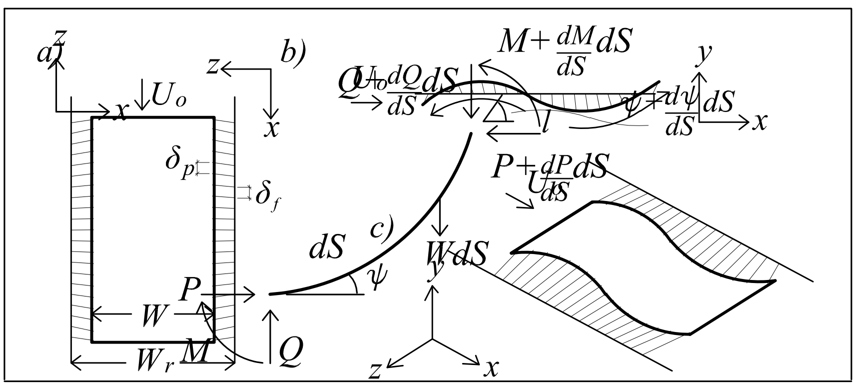

Figure 3.2: An elemental segment of the heavy elastica.

increases. The tension lines have a net compressive effect on the plate.

3.1.1 Equilibrium equations

From Fig. 3.2, the dimensional equilibrium equations are (Wang, 1986; Bickley, 1934; Lloyd et al., 1978; Wang, 1981; Watson and Wang, 1983; Wang, 1983, 1984a,b):

$$\begin{aligned} dX/dS &= \cos\psi, & dZ/dS &= \sin\psi, \\ d\psi/dS &= M/D, & dM/dS &= Q\cos\psi - P\sin\psi, \\ dP/dS &= 0, & dQ/dS &= -W, \end{aligned} \tag{3.1}$$

where P and Q are the internal forces parallel to the X and Z axis, M is the internal moment, S is the arc measured from a convenient origin, ψ the angle between the tangent and the horizontal, and W is the weight per unit length.

We define the following non-dimensional parameters:

$$\begin{aligned} x &= X/L_p, & z &= Z/L_p, \\ p &= PL_p^2/D, & q &= QL_p^2/D \\ s &= S/L_p, & m &= ML_p/D, \\ w &= WL_p^3/D, \end{aligned} \tag{3.2}$$

and we express Eq. 3.1 in non-dimensional form, with $'$ indicating $\partial/\partial s$:

$$\begin{aligned} x' - \cos\psi &= 0, & z' - \sin\psi &= 0, \\ \psi' - m &= 0, & m' - q\cos\psi + p\sin\psi &= 0, \\ p' &= 0, & q' + w &= 0. \end{aligned} \tag{3.3}$$

3.1.2 Contact modeling

The heavy elastica is periodically-constrained by a series of tension lines of unstrained length, L_s (Fig. 3.1a). The area of possible locations of the constrained support is defined by a circle of radius L_s. As not all the supports will be under tension at the same time, we define an active constraint as a support located at the circumference of such circle, and beyond. Active and inactive constraints will be determined as part of the equilibrium solutions of the nonlinear problem.

A tension force, H, appears at the location of active constraints. This force is transmitted to an infinitely rigid support by the tension lines connected to the elemental strip. This connection is considered as passive (i.e., contacts generate no friction, no moment, and no elastic singularity Roman and Pocheau (2002)). This implies continuity of angles and moments. We propose the following constitutive relation, mathematically consistent with Hooke's law, to model such forces:

$$H = -E_s A_s e, \tag{3.4}$$

where E_s is the tension lines' Young's modulus, A_s is the cross-sectional area of the unstrained tension line, and e is the engineering strain defined by $e = (l_e - L_s)/L_s$, where l_e is the deformed length of the tension lines. For any $e < 0$, the lines are considered slack, and therefore, no tension is transmitted. The signs give the directionality depicted in Fig 3.1*b*.

H can be decomposed into Cartesian components as follows:

$$H_x = -E_s A_s e \frac{\triangle x}{l_e}, \quad H_z = -E_s A_s e \frac{\triangle z}{l_e}, \tag{3.5}$$

and by knowing that $\triangle x = x_p - x_o$, $\triangle z = z_p - z_o$, and $l_e = \sqrt{\left(x_p - x_o\right)^2 + \left(z_p - z_o\right)^2}$, H can be expanded and presented in its nondimensional form as:

$$
\begin{aligned}
h_x &= -\left(\frac{E_s A_s L_p^2}{D}\right)\frac{\left(\sqrt{\left(x_p - x_o\right)^2 + \left(z_p - z_o\right)^2} - L_s\right)}{L_s} \\
&\quad \frac{\left(x_p - x_o\right)}{\sqrt{\left(x_p - x_o\right)^2 + \left(z_p - z_o\right)^2}}, \\
h_z &= -\left(\frac{E_s A_s L_p^2}{D}\right)\frac{\left(\sqrt{\left(x_p - x_o\right)^2 + \left(z_p - z_o\right)^2} - L_s\right)}{L_s} \\
&\quad \frac{\left(z_p - z_o\right)}{\sqrt{\left(x_p - x_o\right)^2 + \left(z_p - z_o\right)^2}}.
\end{aligned}
\tag{3.6}
$$

3.1.3 Boundary conditions

The proposed periodically-constrained heavy elastica is subject to the following boundary conditions:

$$
\begin{aligned}
m(0) &= 0, \quad m(1) = 0, \\
p(0) &= 0, \quad p(1) = 0, \\
q(0) &= 0, \quad q(1) = 0.
\end{aligned}
\tag{3.7}
$$

3.1.4 Solutions to the equilibrium equations

We approach the nonlinear problem posed by Eq. 3.3 and Eq. 3.6 as a minimization problem of the form:

$$
\min \boldsymbol{f}(\boldsymbol{a}) \tag{3.8}
$$

where the objective function $\boldsymbol{f}(\boldsymbol{a})$ is the error function (Eq. A.11, Eq. A.17, and Eq. A.22) formed by discretizing the strong form equations with a second order centered difference scheme (A). To solve the minimization problem in Eq. 3.8, we use the trust-region-dogleg (Powell, 1968) and Levenberg-Marquardt (Levenberg, 1944; Marquardt, 1963; Moré, 1978) algorithms from Matlab® Optimization Toolbox™. A convergence study is presented in App. B.

To obtain first mode deformations, the initial solution is the trivial plate state (i.e., straight). To obtain second mode deformations, the initial solution is a combination of the experimental deformation and theoretical moments, angles and shear forces of a double pinned elastica (App. B). To obtain additional deformations, δ_f is reduced progressively and the initial solution is the previous obtained deformation.

3.1.5 Results and discussion

Experimental results (Fig. 2.1 and Fig. 3.3*a*) show that the present configuration represents an elastic bifurcation and buckling instability (Bigoni, 2012). It is elastic because the plate immediately returns to the initially straight configuration when external forcing is removed. It is a bifurcation because the equilibrium path bifurcates when the solution loses its uniqueness, showing at least two equilibrium positions. It is an instability because the plate departs from its straight configuration at a critical load value and buckles, experiencing large deformations. Additionally, the two second mode equilibrium deformations defined by the black lines on Fig. 3.3*a*, represent a state of local stability, where small external forces (other than those induced by the tension lines) cause mode

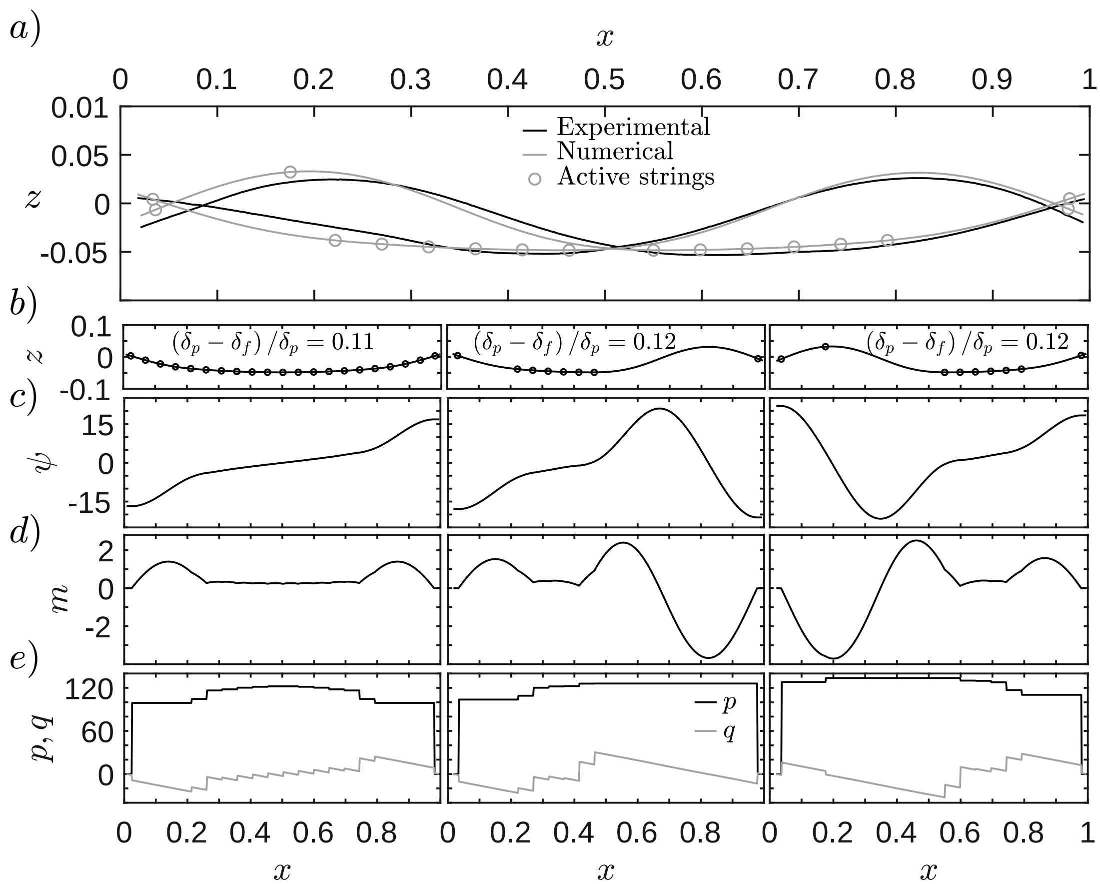

Figure 3.3: Results of equilibrium states: *a*) Experimental vs numerical second mode deformations. *b*) examples of deformations with their respective *c*) angles (ψ), *d*) moments (m), and *e*) internal forces (p and q). $\|\boldsymbol{f}(\boldsymbol{x})\|^2 = 0$ within machine precision for depicted modes ($\|\ \|$ represents the Euclidean norm).

branching (snap-through). The aforementioned is a similar behavior to that of a double well restoring force potential (Harne and Wang, 2013). Furthermore, first mode equilibrium positions also exist but are not shown, and deformations similar in shape to modes higher than one or two may exist but were not found experimentally.

The model equations show that compressive forces and the plate's weight always have a destabilizing effect (Eq. 3.3). This has important implications on fluid-structure interaction applications, as greater compressive forces will mean lower flow velocities required to initiate structural oscillatory motions. Furthermore, Eq. 3.3 and Eq. 3.6 show that the sources of nonlinearities are the geometry, as changes in shape are taken into account to set up the equilibrium equations, and force boundary conditions, as the applied forces by tension lines depend on the plate's deformation. Additionally, special care must be taken with force boundary conditions, as a small strain variation will cause large changes in tension forces (Eq. 3.4, where H grows rapidly with e). Taking this into consideration when analyzing solutions is important, as infinitesimal variations in displacement (within experimental uncertainty) will cause poor convergence.

The results show that the model predicts well the first and second mode deformations (Fig. 3.3), with $\|\boldsymbol{f}(\boldsymbol{x})\|^2 = 0$ within machine precision ($\| \; \|$ represents the Euclidean norm). A comparison of second mode deformations in Fig. 3.3*a*, reveals a close agreement between experimental and numerical results. The inflection points are correctly predicted, and active tension lines (gray circular markers on Fig. 3.3*a*) are the result of the numerical analysis. However, a discrepancy in the equilibrium shape is noted, specifically on the first lobe from left to right. This difference can be attributed to experimental uncertainty, where $\left(\delta_p - \delta_f\right)/\delta_p = 0.155 \pm 0.023$, and where the respective plotted deformations for comparison is the first and closest numerical result $\left(\delta_p - \delta_f\right)/\delta_p = 0.124$.

Moreover, Fig. 3.4 numerically confirms the bifurcation of the solution found experimentally. First mode deformations extend from the trivial equilibrium solution to $\left(\delta_p - \delta_f\right)/\delta_p = 0.1234$. The mode with opposite curvature to that of the first mode presented was not found numerically, which is attributed to conver-

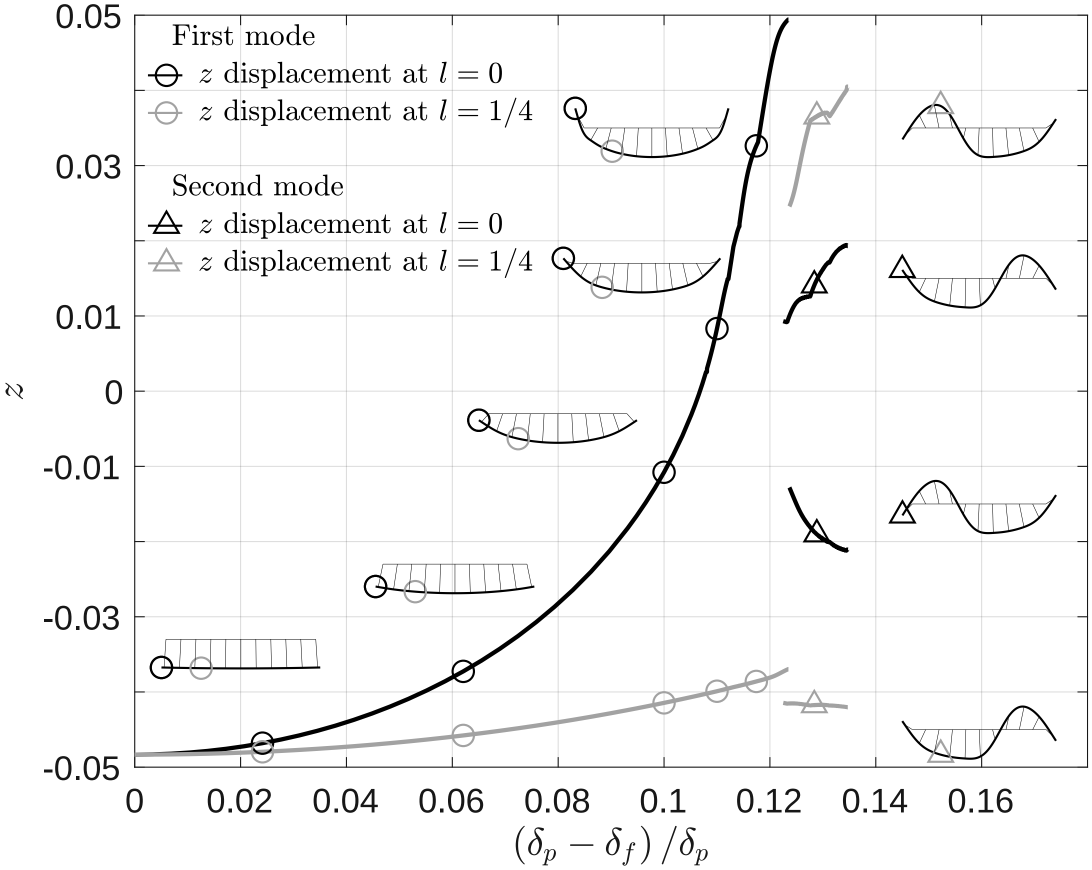

Figure 3.4: Bifurcation diagram. $\|\boldsymbol{f}(\boldsymbol{x})\|^2 = 9.7\mathrm{e}-07$ for first mode deformations, and $\|\boldsymbol{f}(\boldsymbol{x})\|^2 = 4.1\mathrm{e}-08$ for second mode deformations.

gence of the model rather than a statement of non-existence of such a deformation. Additionally, second mode deformations start from $\left(\delta_p - \delta_f\right)/\delta_p = 0.1224$ and extends to $\left(\delta_p - \delta_f\right)/\delta_p = 0.1348$. On one hand, this range shows an area where first and second mode deformations are possible, confirming the non-uniqueness of the solution. On the other hand, the range defines the bifurcation region found experimentally, where solutions for second mode deformations coexist. Here, small external forcing other than that provided by tension lines can cause mode branching.

Finally, discretization of the model as a strong form, in addition to the

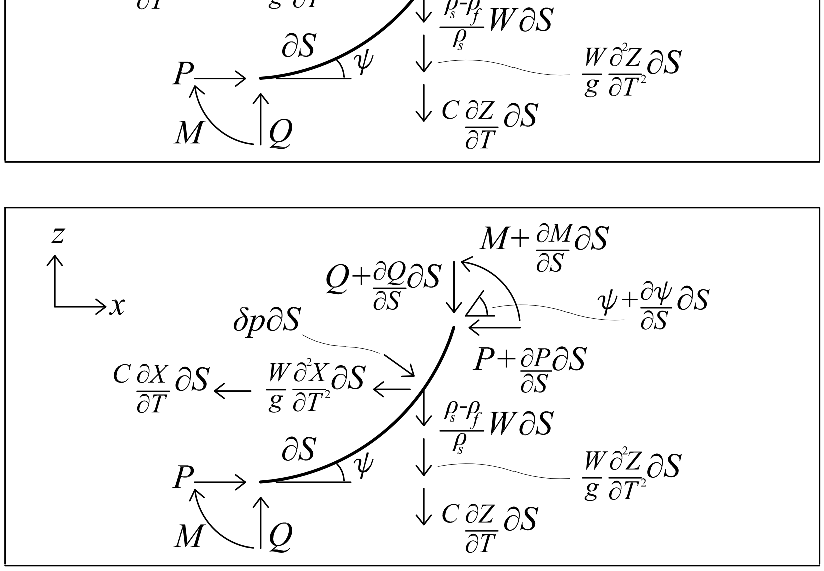

Figure 3.5: An elemental segment of the heavy elastica with inertial terms and fluid coupling.

algorithms implemented, may be affecting the convergence of other modes (e.g., see third deformation from top to bottom on Fig. 3.1*c*, or higher order modes), and the completeness of the equilibrium path shown in Fig. 3.4. While $\|\boldsymbol{f}(\boldsymbol{x} \setminus \boldsymbol{h})\|^2 = 0$ (with $\setminus$ indicating relative complement) within machine precision, $\|\boldsymbol{f}(\boldsymbol{h})\|^2$ presents unacceptable errors in terms of convergence. This is closely related to the rapid change of tension forces as a function of strain. For example, a discrepancy of 10 μm accounts for a changes in h of the same magnitude as that of internal forces presented in Fig. 3.3. While this error is unacceptable numerically, $10\mu m$ is far below experimental uncertainty.

3.2 Equilibrium equations with inertial and damping terms

By including structural inertial and damping terms (Santillan et al., 2006), the effect of buoyancy and fluid coupling, Eq. 3.1 becomes (Fig. 3.5):

$$
\begin{aligned}
\partial X/\partial S &= \cos\psi, \\
\partial Z/\partial S &= \sin\psi, \\
\partial \psi/\partial S &= M/D, \\
\partial M/\partial S &= Q\cos\psi - P\sin\psi, \\
\partial P/\partial S &= -(W/g)\,\partial^2 X/\partial T^2 - C\partial X/\partial T + \delta p\sin\psi, \\
\partial Q/\partial S &= -\left[\left(\rho_p - \rho_f\right)/\rho_p\right] W - (W/g)\,\partial^2 Z/\partial T^2 - C\partial Z/\partial T - \delta p\cos\psi,
\end{aligned}
\tag{3.9}
$$

where T is the dimensional time, C is the structural damping coefficient, and δp the pressure jump per unit width. Here, the term accounting for buoyancy will be active only if the pressure jump term is not active, otherwise it should be zero.

3.3 Fluid coupling based on slender body theory

Here we consider coupling based on slender body theory (Munk, 1924; Lighthill, 1960a,b; Coene, 1992). We assume slenderness, where the plate's dimensions and movements at right angles to the direction of motion are taken to be small compared to its length (i.e., lateral dimensions/movements must not exceed εl, and lateral velocities εU). Therefore, relative velocity between the body and the fluid flow past it can be defined as:

$$
w(S,T) = \frac{\partial Z}{\partial T} + U_o \frac{\partial Z}{\partial S}, \tag{3.10}
$$

the momentum per unit length as:

$$M_a w, \tag{3.11}$$

the rate of change of momentum creating a force equal and opposite on the plate:

$$\left(\frac{\partial}{\partial T} + U_o \frac{\partial}{\partial S}\right) M_a w, \tag{3.12}$$

where M_a is the added mass per unit width of the plate. Eq. 3.9 can now be expressed as follows, where only vertical (z-direction) displacements are considered, and deformations due to shear are neglected:

$$\begin{aligned}
\partial X/\partial S &= \cos\psi, \\
\partial Z/\partial S &= \sin\psi, \\
\partial \psi/\partial S &= M/D, \\
\partial M/\partial S &= Q\cos\psi - P\sin\psi, \\
\partial P/\partial S &= -\left(W/g\right)\partial^2 X/\partial T^2 - C\partial X/\partial T, \\
\partial Q/\partial S &= -\left[\left(\rho_p - \rho_f\right)/\rho_p\right] W - \left(W/g\right)\partial^2 Z/\partial T^2 - C\partial Z/\partial T \\
&\quad - M_a \left(\frac{\partial}{\partial T} + U_o \frac{\partial}{\partial S}\right)^2 Z.
\end{aligned} \tag{3.13}$$

We define the additional non-dimensional parameters:

$$\begin{aligned}
t &= T/L_p^2\sqrt{(Dg/W)}, \quad & c &= CL_p^2\sqrt{(g/WD)}, \\
\mu &= M_a g/W, & u &= U_o L_p\sqrt{W/Dg}, \\
b &= \left(\rho_p - \rho_f\right)/\rho_p.
\end{aligned} \tag{3.14}$$

where μ, u, and b are the non-dimensional added mass, the reduced velocity, and the buoyancy contribution, respectively.

We express Eq. 3.13 in non-dimensional form:

$$\begin{aligned}
&\partial x/\partial s = \cos\psi, \\
&\partial z/\partial s = \sin\psi, \\
&\partial\psi/\partial s = m, \\
&\partial m/\partial s = q\cos\psi - p\sin\psi, \\
&\partial p/\partial s = -\partial^2 x/\partial t^2 - c\partial x/\partial t, \\
&\partial q/\partial s = -bw - \partial^2 y/\partial t^2 - c\partial y/\partial t - \mu\left(\partial^2 z/\partial t^2 + 2u\partial^2 z/\partial t\partial s + u^2\partial^2 z/\partial s^2\right),
\end{aligned} \tag{3.15}$$

where buoyancy has been kept for completeness, and where the terms associated to $\partial^2 z/\partial t^2$, to $\partial^2 z/\partial t\partial s$, and to $\partial^2 z/\partial s^2$ are the inertial force, Coriolis force ($\partial^2 z/\partial t\partial s = \partial\theta/\partial t = \Omega$), and centrifugal force ($\partial^2 z/\partial s^2 \sim 1/R$), respectively, where R is the radius of curvature and Ω the local angular velocity (Paidoussis, 2016a).

3.4 Linear stability analysis

Let us know consider the limit where Eq. 3.13 is linear (i.e., no buckling has occurred). Under this assumption:

$$\frac{\partial X}{\partial S} = 1, \quad \frac{\partial Z}{\partial S} = \sin\psi, \quad \frac{\partial Z}{\partial X} \approx \psi, \tag{3.16}$$

and Eq. 3.13 can be simplified to by ignoring damping terms:

$$
\begin{aligned}
&\partial\psi/\partial X = M/D, \quad \Rightarrow \quad D\partial^2\psi/\partial X^2 = \partial M/\partial X, \\
&\partial M/\partial X = Q - P\sin\psi, \quad \Rightarrow \quad \partial M/\partial X = Q - P\partial Y/\partial X, \\
&\partial P/\partial X = -(W/g)\,\partial^2 X/\partial T^2, \\
&\partial Q/\partial X = -\left[\left(\rho_p - \rho_f\right)/\rho_p\right] W - (W/g)\,\partial^2 Z/\partial T^2 \\
&\qquad - M_a\left(\frac{\partial}{\partial T} + U_o\frac{\partial}{\partial X}\right)^2 Z,
\end{aligned}
\tag{3.17}
$$

from which it follows:

$$
\begin{aligned}
D\frac{\partial^2\psi}{\partial X^2} &= Q - P\frac{\partial Z}{\partial X}, \\
D\frac{\partial^3\psi}{\partial X^3} &= \frac{\partial}{\partial X}Q - \frac{\partial}{\partial X}\left(P\frac{\partial Z}{\partial X}\right), \\
D\frac{\partial^4 Y}{\partial X^4} &= \frac{\partial}{\partial X}Q - \frac{\partial}{\partial X}\left(P\frac{\partial Z}{\partial X}\right).
\end{aligned}
\tag{3.18}
$$

If we neglect the effect of gravity, i.e., no weight or buoyancy (weight provides always a destabilizing effect), we obtain from Eq. 3.17 and Eq. 3.18 by additionally ignoring the inertial term in the x-direction:

$$
\left(\frac{W}{g}\right)\frac{\partial^2 Z}{\partial T^2} + \frac{\partial}{\partial X}\left(P\frac{\partial Z}{\partial X}\right) + D\frac{\partial^4 Z}{\partial X^4} + M_a\left(\frac{\partial}{\partial T} + U_o\frac{\partial}{\partial X}\right)^2 Z = 0. \tag{3.19}
$$

Now considering the compressive force constant, and adding the effects of fluid induced tension, F, we finally obtain:

$$
\left(\frac{W}{g} + M_a\right)\frac{\partial^2 Z}{\partial T^2} + \left(P - F + M_a U_o^2\right)\frac{\partial^2 Z}{\partial X^2} + D\frac{\partial^4 Z}{\partial X^4} + 2M_a U_o\frac{\partial^2 Z}{\partial X\partial T} = 0. \tag{3.20}
$$

a similar expression of that of Connell and Yue (2007), but considering the effects of an external constant compression.

Now (following Connell and Yue (2007)), using a constant value for fluid induced tension based on Blasius laminar boundary layer written as:

$$F = 1.3\rho_f L_p U^2 Re^{-1/2}, \tag{3.21}$$

with ρ_f as the mass per unit length of fluid. Redefining $W/g = \rho_p \delta$ as the mass per length of the plate, and nondimensional time t as:

$$t = \frac{TU_o}{L_p}, \tag{3.22}$$

we obtained the nondimentional form of Eq. 3.20 as:

$$(r + m_a)\frac{\partial^2 z}{\partial t^2} + \left(p^* - 1.3Re^{-1/2} + m_a\right)\frac{\partial^2 z}{\partial x^2} + \beta\frac{\partial^4 z}{\partial x^4} + 2m_a\frac{\partial^2 z}{\partial x \partial t} = 0. \tag{3.23}$$

where $r = \rho_p\delta/\rho_f L_p$, $m_a = M_a/\rho_f L_p$, $\beta = D/\rho_f U_o^2 L_P^3$, and $p^* = \rho_f U_o^2 L_P$ are the non-dimensional mass ratio, added mass, bending stiffness, and compression force.

Assuming a traveling-wave mode, $z = Ae^{i(kx-\omega t)}$, where k and ω are the nondimensional wavenumber and frequency. The equation of motion yields the dispersion relation:

$$(r + m_a)\,\omega^2 + \left(p^* - 1.3Re^{-1/2} + m_a\right)k^2 - \beta k^4 - 2m_a\omega k = 0. \tag{3.24}$$

Solving for ω, we obtain:

$$\begin{aligned}\omega &= \frac{m_a k}{r + m_a} \pm \frac{1}{r + m_a}\sqrt{(m_a k)^2 - (r + m_a)\left(p^* k^2 + m_a k^2 - 1.3Re^{-1/2}k^2 - \beta k^4\right)} \\ &= \frac{m_a k}{r + m_a} \pm \frac{k}{r + m_a}\sqrt{-rm_a + (r + m_a)\left(-p^* + 1.3Re^{-1/2} + \beta k^2\right)}.\end{aligned} \tag{3.25}$$

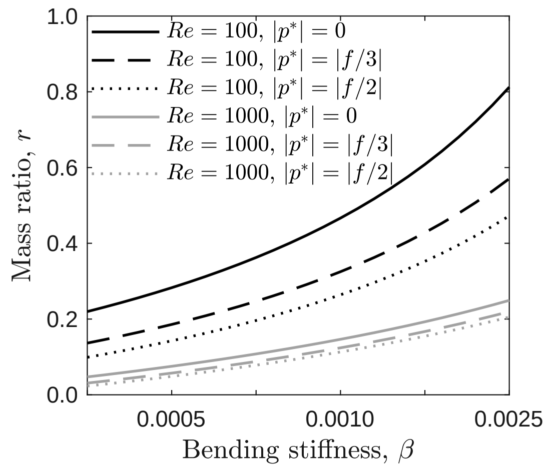

Figure 3.6: The influence of compression on the critical mass ratio, r, as a function of bending stiffness, β, for flutter using Eq. 3.17 for $k = 2\pi$ mode.

From this we see that bending rigidity, fluid induced tension, and Coriolis are stabilizing, while external compression and centrifugal forces are destabilizing. Eq. 3.25 becomes unstable when the argument of the radical becomes negative:

$$\frac{rm_a}{(r + m_a)} > \left(-p^* + 1.3Re^{-1/2} + \beta k^2\right). \tag{3.26}$$

From potential flow theory, the added mass coefficient can be approximated as that of the infinite waving plate Coene (1992) as $m_a = 2/k$. With this, the instability criteria follows the form:

$$\frac{r}{\frac{1}{2}rk + 1} > \left(-p^* + 1.3Re^{-1/2} + \beta k^2\right). \tag{3.27}$$

Fig. 3.6 shows the stability citeria based on Eq. 3.17. When the compressive force is zero, we recover the stability criteria of Connell and Yue (2007), and as compressive force increases, the limit at which the instability occurs decreases.

3.5 A note on fluid coupling

The major obstacle solving the fully non-linear plate equation coupled with potential flow theory (i.e., Eq. 3.15) is the convergence of the contact points of the plate with the tension lines and their induced tension force (Eq. 3.6). As occurs with the static solution presented in Muriel and Cowen (2018) and in the preceding sections, with E_s being one order of magnitude greater than E, any small change in e compared to any deformation on the plate will produce a large H. This means that while e is within margins of acceptable error, H will already be considerably larger. One possible solution is to consider the tension lines as a column, and use the elastica formulation presented herein for each line. In this solution, care must be taken under slack conditions as the buckled columns will transmit forces, again, linked to E_s. Additionally, and not trivially solved as the slack condition, is the fact that if such a formulation is considered, a critical load is supported by the line when totally straight. This means that the tension line will be able to support a compressive load equivalent to the critical load of a column of elastic modulus E_s, and inertia I_s. Therefore, at the contact point with the plate an equivalent compressive force will be transmitted. The remaining question is what is the magnitude of the force to be considered, which could be between zero and the critical buckling load. As a consequence, if this formulation is considered, the magnitude of the force jump on contact points can not be predicted but only prescribed, therefore resembling an empirical model.

Additionally, we consider the appropriateness of Slender Body theory. Lighthill (1960a) presents a thoughtful description of its accuracy, and mentions that it depends not only on the body being slender (e.g., maximum angle of inclination, ε being a measure of slenderness), but also being smooth. On the specifics of our problem, this means that the plate must not make any abrupt changes in direction. Provided that this conditions are satisfied, then the errors in the disturbed quantities are of order $\varepsilon^2 \log\varepsilon$. That is, errors in lateral velocities are of order $U\varepsilon^2 \log\varepsilon$, and errors in pressure are of order $\rho U^2 \varepsilon^4 \left(\log\varepsilon\right)^2$.

Furthermore, if deducing pressure from the Bernoulli's equation, it is necessary to use not the small-perturbation form (linear):

$$p = -\rho U \frac{\partial \phi}{\partial x} \tag{3.28}$$

but a more accurate form, including the squares of lateral velocities (nonlinear):

$$p = -\rho U \frac{\partial \phi}{\partial x} - \frac{1}{2}\rho \left[\left(\frac{\partial \phi}{\partial y}\right)^2 + \left(\frac{\partial \phi}{\partial z}\right)^2\right] \tag{3.29}$$

Physically, this can be interpreted as a dominant two-dimensional flow locally near the surface, with is pressure given by the last term in Eq. 3.29, and with velocities greater than the perturbation velocities associated with the large-scale flow (Lighthill, 1960a). Additionally, changes in the local flow as fluid passes the body give rise to transient pressures, represented by the first term in Eq. 3.29.

In terms of limitations, we can first consider the separation of boundary layers (Lighthill, 1960a). When the slenderness condition is not achieved, and curvature or angle of incidence increase, boundary layer separation can occur. The basic difference from the unseparated flow is that the lateral momentum does not depend on the local relative velocity, v. As the boundary layer sheds more vorticity into the flow, the cross-flow momentum rises above the unseparated value. As the boundary layer progresses, the vorticity shed builds up and can

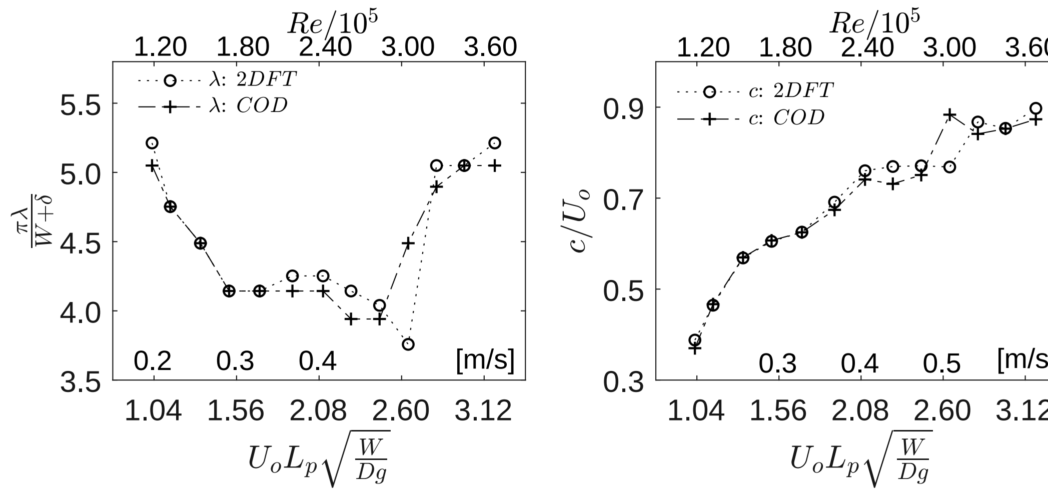

Figure 3.7: Criteria for virtual mass approximation: results for plate's wave length, λ, based on two-dimensional Fourier transform, $2DFT$, and complex orthogonal decomposition, COD), extracted on dynamically unstable cases.

form a vortex pair.

Another consideration is the fact that the flexibility of the plate allows for different cross-sections to push the water at different velocities, proving the approximation of the virtual mass per unit length of our plate as that of a cylinder with the same cross-section. Lighthill (1970) suggested that the corrections are not large provided that significant harmonic components of the cross-section shape or velocity along the body wavelengths, λ, of at least 5 times the depth of the theoretical cylinder cross-section. For our problem, this means that:

$$\frac{\pi\lambda}{W+\delta} \geq 10. \tag{3.30}$$

Fig. 3.7 shows that the requirement is not met, partially compensated by considering our flattened shape, where lateral water motions should reflect more closely that of the local body cross-section. Additional to this, the sudden accel-

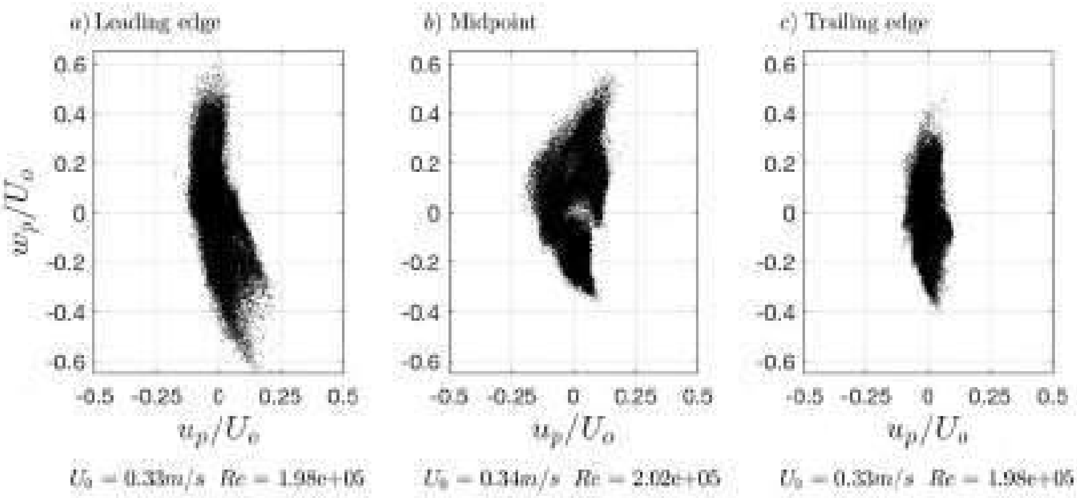

Figure 3.8: Example of phase plots at the leading, midpoint, and trailing edge, showing that velocities in the horizontal and vertical plains are of the same order.

eration caused by the constraints as well as the magnitude of vertical velocity should be considered (Fig. 3.8), which could violate the restrictions of vertical velocities of order εU. One essential property of elongated body theory is that the virtual mass per unit length of vertical motions is large, while for horizontal is negligible.

Furthermore, the above coupling neglects the effect of the vortex wake on the pressure distribution around the body. Lighthill (1970) provided a discussion on the limitation, and Cheng et al. (1991) provided a model designed to incorporate such effects on the pressure distribution. In the same way, the limitations of small oscillatory motions has been relaxed on Lighthill's extended theory for large amplitude motions (Lighthill, 1971). Regardless of its applicability to our problem, the slow convergence of the solution mentioned above remains, which leaves no special point in pursuing further the discussion of more elaborated models, motivating as a consequence the use of an experimental approach to determine critical flow velocities, and to describe kinematics of the plate and the hydrodynamics of the fluid structure interaction problem, reinforced by the hypothesis of non-zero pressure drag prior to oscillatory motions of the deformed plate.

CHAPTER 4

KINEMATICS OF THE EARLY ONSET OF LARGE OSCILLATORY MOTIONS

4.1 Characterization of oscillatory frequency and plate's deformation as a function of flow velocity

Our results show that large structural oscillations are initiated at $U_c = 0.197 \pm 0.001$ m/s with a $4.1 \pm 1.0\%$ hysteresis loop Fig. (4.1). No vortex shedding from upstream structures is implemented to initiate or enhance oscillatory movements, as is done for some flag-type configurations (Allen and Smits, 2001; Taylor et al., 2001; Techet et al., 2002; Jia and Yin, 2008; Akaydin et al., 2010). The same plate (i.e., material, thickness, and aspect ratio), was tested in a flag-type configuration, that is with a tethered leading edge and presents weak perturbations above $U_o = 0.211 \pm 0.001$ m/s (of order less than a percent of plate's length), small amplitude and intermittent oscillatory motions above $U_o = 0.460 \pm 0.002$ m/s (hovering), and shows no evidence of a developed flutter instability up to $U_o = 0.710 \pm 0.004$ m/s, where our facility reaches maximum U_o. Such perturbations are attributed to surface and three-dimensional effects. Other flag type configurations show oscillatory motions experimentally at $U_o > 0.90$ m/s (Shelley et al., 2005), and $U_o = 0.57$ m/s (Giacomello and Porfiri, 2011) and $U_o = 0.81$ m/s (Shelley et al., 2005) if using added lateral stiffness to prevent three-dimensional effects. Care must be taken when exploring such differences in U_c for different configurations. For example, in the presence of a buckled plate (i.e., this study), a non-zero pressure drag (see below) is exerted on the plate before oscillations start. On the contrary, on a flat plate, the evolution of oscillatory motions is coupled with the evolution of the unsteady hydrodynamic forces. Other considerations include added mass and bending rigidity.

Three primary reasons explain the onset of oscillatory motions at low U_c. First, the destabilizing action of the compressive force, which creates an early onset of oscillatory motions. As occurs on double-pinned plates presented by Dowell (1966, 1967, 1970, 1982), or double-pinned cylinders studied by Paidoussis (1966), the action of compressive in-plane loads exacerbates the instability. Second, by inducing an elastic instability through external compression, we force the device into a state of permanent deformation and local equilibrium, similar to a double-well restoring force potential of a bistable oscillator (Harne and Wang, 2013). Therefore, the plate is driven out of this state with the action of a small external force, and as a consequence a new locally-stable deformed position is established. This is equivalent to the low-energy intra-well vibration exhibited by bistable devices (Harne and Wang, 2013). As we see in Fig. 3.3, the plate presents at least two physically realizable static deformations. Similar to a beam buckled by end-loads, the geometric non-linear stiffness is one of the causes of more than one equilibrium position (Moon, 2004), force boundary conditions being the other source of nonlinearities for the proposed device (Muriel and Cowen, 2018). Third, in the presence of a flow but before the plate oscillates, the sinusoid-like deformation causes non-negligible pressure drag as occurs on blunt bodies (e.g., cylinders (Williamson, 1996)). Analogous to the sinusoidally bent rigid body presented by Shelley and Zhang (2011, see Figure 2e), the difference between the high pressure at the frontal stagnation point and the low pressure in the rear separated region, in this case, that of the immobile flexible buckled plate, a large form drag contribution is generated. The combined effects of a compressive force, a locally-stable plate, and the non-zero pressure drag leads to the low U_c found in our experiments.

By further studying the plate under various flow conditions ($U_o > 0$), we can define three states of motion based on the relationship between f_o, its harmonics, and U_o (Fig. 4.1*a*). Firstly, below U_c, the induced buckled state is represented by a sinusoid-like deformation with weak perturbations localized on the crests and troughs, and no oscillatory motions. This indicates the predominance of the plate's stabilizing forces over external fluid forces. Secondly, above U_c, a flutter instability appears and subsequent oscillations are a superposition of traveling and standing waves, whose decomposition can be obtained through $2DFT$ or COD. This state presents a predictable dominant frequency, f_o, accompanied by higher-order harmonics, and evidence of bi-stability. At this state, hydrodynamic pressure and viscous drag drive the locally-stable plate out of equilibrium and into oscillatory motions. Lastly, above a transitional flow velocity, $U_t = 0.517 \pm 0.005\ m/s$ (with associated Reynolds number, $Re_t = U_t l/\nu = 3.10 \pm 0.04 \times 10^5$, ν being the kinematic viscosity), oscillations evolve into chaos, characterized by a drop in the trend of f_o. In this regime, the plate shows an increasingly broad subharmonic energy range under the spectrum (i.e., precursor to chaos, Fig. 4.3 and Moon (2004)), loss of detectable higher-harmonics, and an unstable limit-cycle (Fig. 4.4*e* and Fig. 4.4*f*).

The plate under study also evinces an improved OR with respect to flag or inverted flag configurations. Experimental results show that once U_c is exceeded, the plate will oscillate with frequency f_o directly proportional to U_o, a tendency that will drop slightly at U_t, and then it will keep increasing beyond U_t (Fig. 4.1*a* and Fig. 4.1*b*, where higher U_o were not tested to preserve the physical integrity of the device). In contrast, the OR is limited for a device such

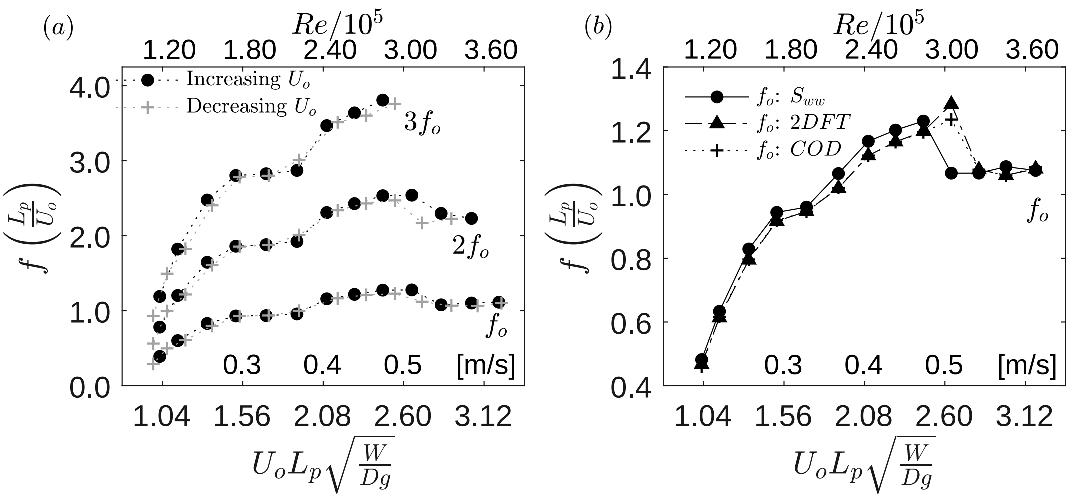

Figure 4.1: a) Evolution of oscillatory frequency, f_o, and higher order harmonics as a function of flow velocity, U_o. b) Results for f_o (spectral analysis of a fluid parcel, S_{ww}, two-dimensional Fourier transform, $2DFT$, and complex orthogonal decomposition, COD), and wave celerity, c ($2DFT$ and COD).

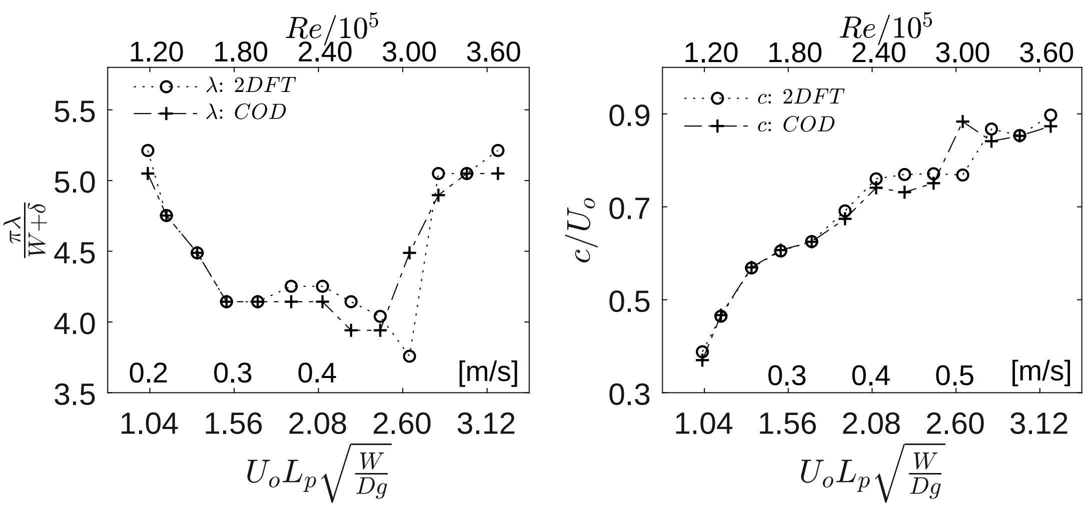

Figure 4.2: Results for wave celerity, c, based on two-dimensional Fourier transform, $2DFT$, and complex orthogonal decomposition, COD).

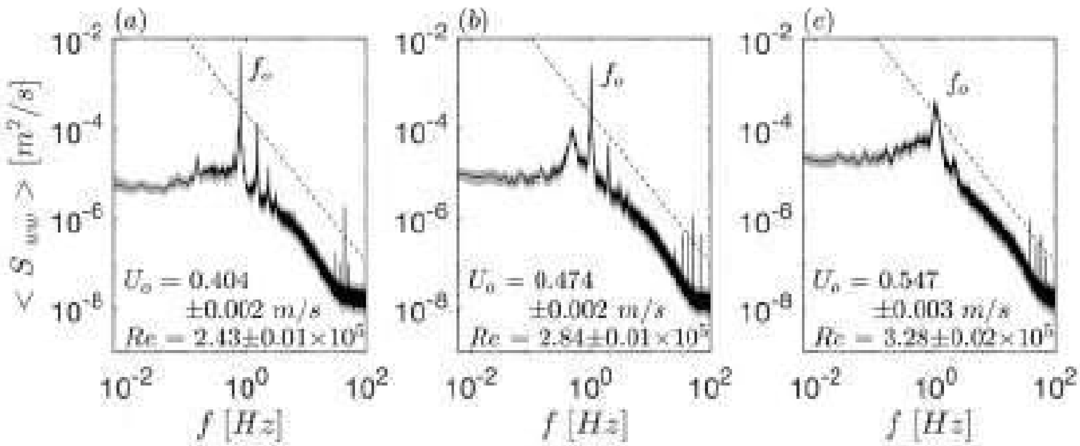

Figure 4.3: Spectral analysis for the vertical velocity component of a fluid parcel located $3l/4$ downstream of the plate's leading edge: ■ 95% uncertainty, — S_{ww}, --- Kolmogorov's $-5/3$ law.

as the inverted flag (Kim et al., 2013). This drop in frequency indicates the transition from a laminar to turbulent boundary layer on the plate, reinforcing the importance of flow separation in the dynamics of the present fluid-structure interaction problem.

The reductions in U_c and the improvements in OR can be further analyzed with the evolution of the oscillatory motions as as a function of U_o (Fig. 4.4). First, the onset of oscillatory motions are partially explained by the destabilization process of the sinusoid-like deformation at U_c. Fig. 4.4*a* at U_c presents a locally-stable position set by compression, inertia, and elastic rigidity, represented by the denser black region in the image (i.e., more space filling). These locally-stable positions are progressively destabilized by fluid forces until a first cycle of motion is initiated. Then, once this cycle is completed the plate returns to a similar state of equilibrium, triggering the phenomenon again. Second, we consider that the OR begins once U_c is exceeded and ends once stable oscillatory motions are no longer present. The OR presents first, stable oscillatory

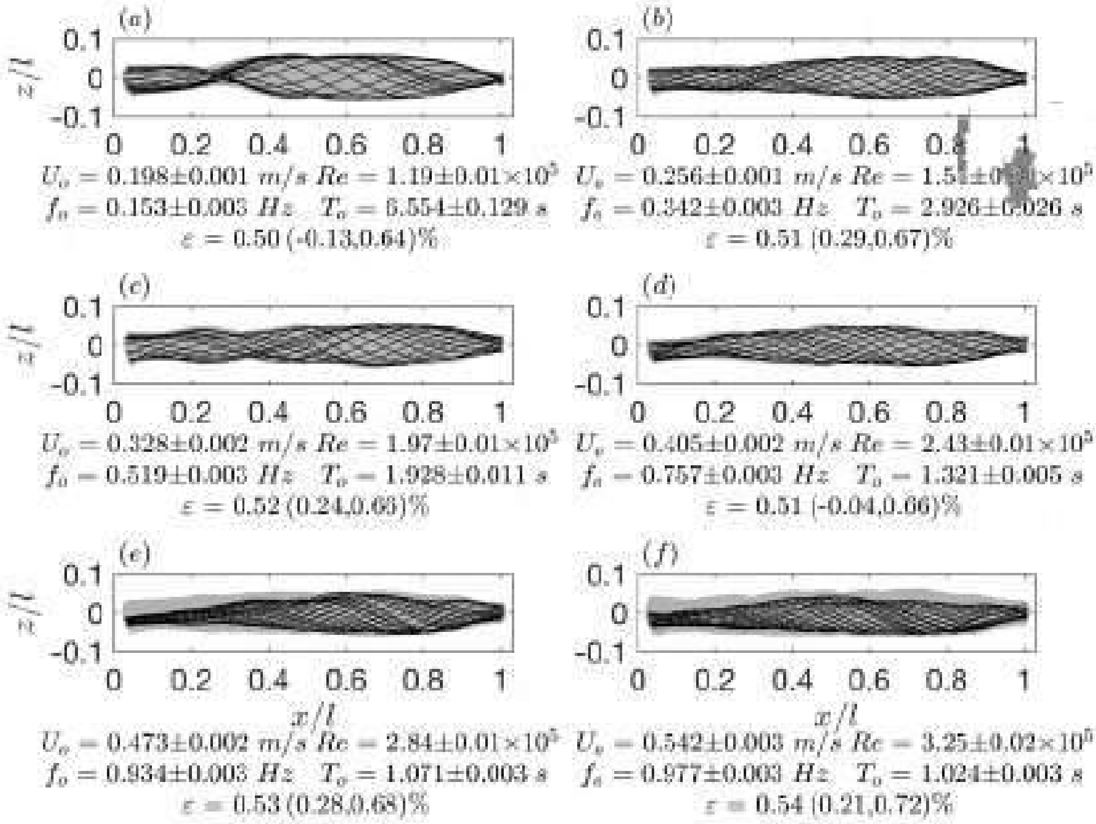

Figure 4.4: Evolution of oscillatory motions over one period (T_o): — 15 plate locations equally spaced in time ($T_o/15$) over one oscillation period ($T_o = 1/f_o$), ■ envelope of maximum vertical excursions achieved in the test (350 s sampled at 20 Hz). Flow direction is from left to right.

limit-cycles (Fig. 4.4*b* to Fig. 4.4*d*), and second, unstable limit-cycles close and above to the transition to chaos (Fig. 4.4*e* and Fig. 4.4*f* respectively). Despite unstable limit cycles above the chaotic transition, the plate still exhibits stable motions during part of an oscillation cycle. In this regime of motion, the oscillations are accompanied by more frequent and longer bursts of three-dimensional effects, which can be seen in Fig. 4.5.

Our results show that the fluid flow transitions to a chaotic state before the plate does (Fig. 4.1*b*). Physically, this can be interpreted as the boundary layer

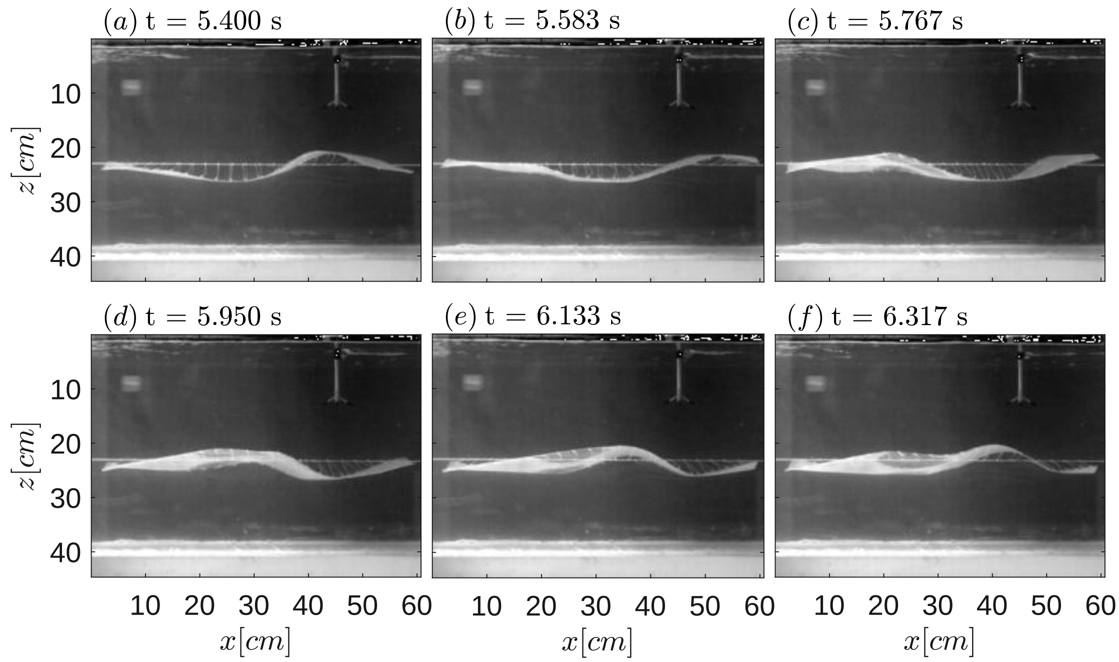

Figure 4.5: Oscillatory motions at flow velocity $U_o = 0.540\ m/s$ ($Re = 3.24 \times 10^5$), with dominant oscillatory frequency $f_o = 1.080\ Hz$ ($T_o = 0.926\ s$). Flow direction is from left to right, and images are equally spaced in time covering a full oscillation cycle.

on the plate transitioning to a turbulent regime earlier than the plate shows chaotic oscillatory motions. This is seen in the transition region to chaos where both the plate and the fluid show a drop in the respective f_o trends at different U_o. To obtain this result, we performed $2DFT$ and COD analysis of the data presented in Fig. 4.4. These two methodologies extract wave frequency, ω, and wave number, κ. Fig. 4.1b presents consistent f_o trends between the spectral analysis of the fluid (1DFT of the vertical velocity component of a fluid parcel, S_{ww}), and the $2DFT$ (f_o obtained from $\omega = 2\pi f_o$) and COD analysis of the plate (f_o obtained from the complex modal coordinates of the first mode of the COD). As stated above, the exception is the transition region, indicating that the fluid develops first a turbulent boundary layer, followed by the plate's transition to chaos. Additionally, the plate's wave celerity, $c = \omega/\kappa$ shows no thrust force

(Lighthill, 1969; Shelley et al., 2005; Jia and Yin, 2009) with consistency between the trends obtained with $2DFT$ and the first mode of COD. For COD, the first mode contains most of the energy, with a decrease from 94.9% to 67.8% from lowest to highest U_o, respectively. To the contrary, mode two (three) shows an increase from 3.2% to 19.5% (1.3% to 8.3%) from lowest to highest U_o, respectively.

Finally, the plate's oscillations contain traveling and standing wave components (Fig. 4.6). This is particularly important if simplified mathematical models are implemented. First, using $2DFT$, a traveling wave ratio, TWR, is defined as the fraction of the amplitude of the traveling wave to the total amplitude of the composition (Feldman, 2011). Second, using COD, a traveling index, TI, is defined as the reciprocal of the condition number of the matrix whose two columns are the real and imaginary components of the complex mode (Feeny, 2008). Both ratios will have a value of zero for a standing wave and one for a purely traveling wave. The TWR indicates that as we increase U_o the standing component decreases and it partially recovers after the chaotic transition. Similarly, the TI shows mode one with a strong traveling component and a considerable standing component in the lower U_o range.

4.2 An interpretation of large oscillatory motions based on strain energy for different flow velocities

To better understand the fluid coupling we explore the evolution of the strain energy as a function of U_o. Here we define dimensionless strain energy, Es, dimensionless kinetic energy, Ek, and conversion factor, R, as follows:

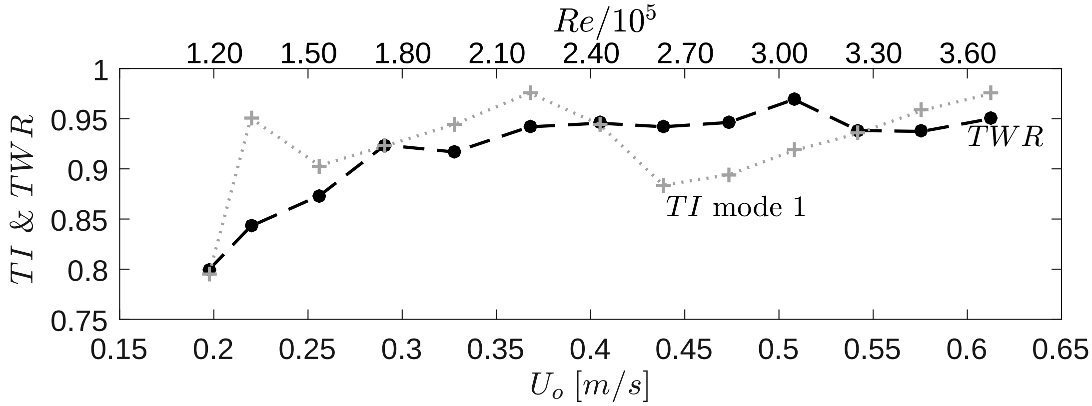

Figure 4.6: Traveling wave ratio, TWR, based on two-dimensional fast Fourier transform ($2DFT$), and traveling index, TI for mode one, based on complex orthogonal decomposition (COD).

$$Es = \frac{\frac{1}{2}D\int_0^{L_p} K^2 dX}{\rho U_o^2 L_p^3}, \tag{4.1}$$

$$Ek = \frac{\frac{1}{2}\rho_f U_o^3 B A_{avg} T_o}{\rho_f U_o^2 L_p^3}, \tag{4.2}$$

$$R = Es/Ek, \tag{4.3}$$

where curvature is defined as

$$K = \frac{\partial^2 Z/\partial X^2}{\left(1 + (\partial Z/\partial X)^2\right)^{3/2}}, \tag{4.4}$$

and A_{avg} is the average amplitude during the period $T_o = 1/f_o$. In order to calculate the derivatives required for K, we fit a 20-th degree polynomial with centering and scaling to avoid an ill-conditioned Vandermonde matrix in the fit calculation and the amplification of noise through numerical differentiation. The maximum error in length introduced by these polynomials is $\varepsilon = 0.27(-0.05, 0.38)\%$ based on the true distribution error from each data set. On the one hand, we see from Fig. 4.7*a* that Es remains almost constant over the U_o tested. This is a result of the external forcing, i.e., the tension lines, guaranteeing the presence of the elastic instability even if oscillatory motions are achieved. This figure also shows that Ek decreases as as a result of the decrease in T_o while U_o increases. Furthermore, Ek shows a slight increase in the transition to turbulent boundary layer ($Re_t = 2.94 \pm 0.10 \times 10^5$). On the other hand, R confirms that the OR covers the U_o tested since a significant R is present for each data set. Additionally, no significant decrease in R is found in the transition to chaos. Lastly, it is important to notice that we are working with a non-dimensional bending stiffness, $\beta = D/\rho_f U_o^2 L_p^3$ (with flexural rigidity, $D = E\delta^3/12(1-\nu)$) two orders of magnitude lower than those reported by Kim et al. (2013), and in the same way as in their inverted-flag configuration, the Es reported herein is conservative. The consideration of energy transfer to dissipative energy forms is beyond the scope of this effort (i.e., damping of specific materials and damping from mechanical or piezoelectric coupling).

The associated analysis of the dominant geometry and its strain energy shows higher R when there is more than one wavelength, λ, and greater energy content in higher order modes (Fig. 4.8). On the one hand, if the geometry is close to the initial induced deformation, the R is in the 2.5th percentile ($R\,(\eta(0.025))$, Fig. 4.8*a*). Within this percentile the instantaneous geometry exhibits a mild curvature containing approximately one λ, and as we increase U_o, there is a reduction in λ and an increase in energy content of higher order modes, but not enough to create a steeper curvature. Once the plate transitions to chaos

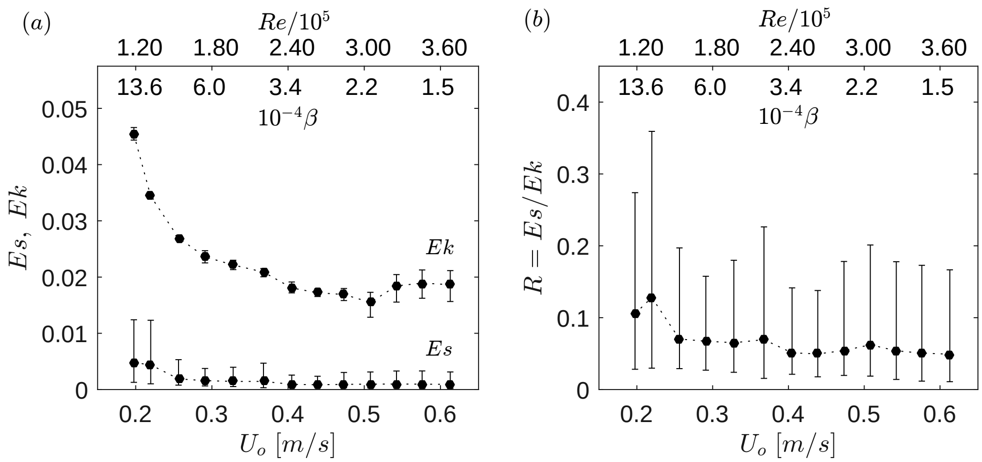

Figure 4.7: a) Evolution of strain energy, Es, and kinetic energy, Ek, as a function of flow velocity, U_o. b) Evolution of conversion factor, $R = Es/Ek$ as a function of U_o. For both figures, mass ratio, M, is fixed but non-dimensional bending stiffness, β, varies as a function of U_o. Reported uncertainty corresponds to the mean value and 95% confidence interval of the true error distribution obtained for each data set. $\delta U_o = \pm 0.003\ m/s$ at highest U_o.

(highest *Re* in Fig. 4.8*a*), one of the dominant geometries shows an almost flat curvature at the plate's crest, creating further reductions in R as seen in Fig. 4.7*b*. On the other hand, for R greater than $R\,(\eta(0.975))$ shown in Fig. 4.8*b*, instantaneous geometries are characterized by the presence of more than one λ and greater energy content in higher order modes, creating steeper curvatures. Finally, once the plate transitions to chaos (highest *Re* in Fig. 4.8*b*) the energy content of higher order modes creates new geometry events, but contrary to $R\,(\eta(0.025))$, with steeper curvatures that produce higher R.

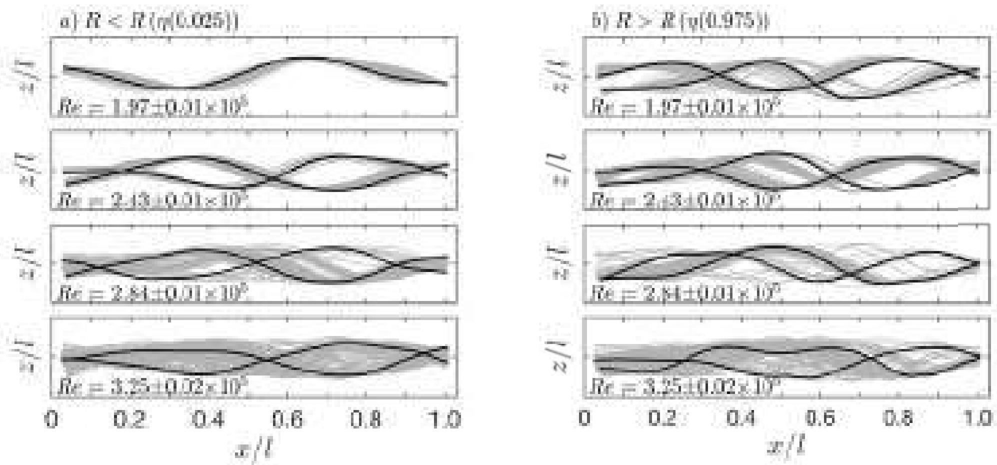

Figure 4.8: a) Dominant plate's instantaneous geometry with conversion factor, $R = Es/Ek$, above 97.5th percentile ($R > R\,(\eta(0.975))$), and b) plate's geometry with R in the 2.5th percentile ($R < R\,(\eta(0.025))$).

CHAPTER 5

DYNAMICS OF THE ONSET OF OSCILLATORY MOTIONS: SMALL PERTURBATIONS AND LARGE OSCILLATORY MOTIONS

5.1 A dynamically-stable buckled plate under a steady incompressible flow

5.1.1 The influence of the presence of a buckled plate on the dynamics of the flow

Cases of the dynamically-stable plate under uniform flow show a process of adaptability of the flexible plate to the incoming flow. This is evidence of divergence due to the external dynamic load provided by the unsteady flow field. Without transitioning to large oscillatory motions, the deformation resembling a second-mode deformation is preserved, while the maximum and minimum curvature points (i.e., $\max(\psi)$ and $\min(\psi)$, respectively), as well as the zero curvature (i.e., $\psi = 0$) are moved downstream (see Fig. 5.1 and Fig. 5.2). This is a direct response of the forces of the fluid applied onto the plate, where at higher flow speeds, a new equilibrium position must be achieved by the flexible plate.

Such deformable behavior is only possible by the fact that the configuration is marginally stable, and that the boundary conditions induced by the tension lines are restricting the range of motion of certain locations to an area rather than a fixed point in space. For example, while tension lines are active at the leading and trailing edge, they are slack in the midspan, allowing for further

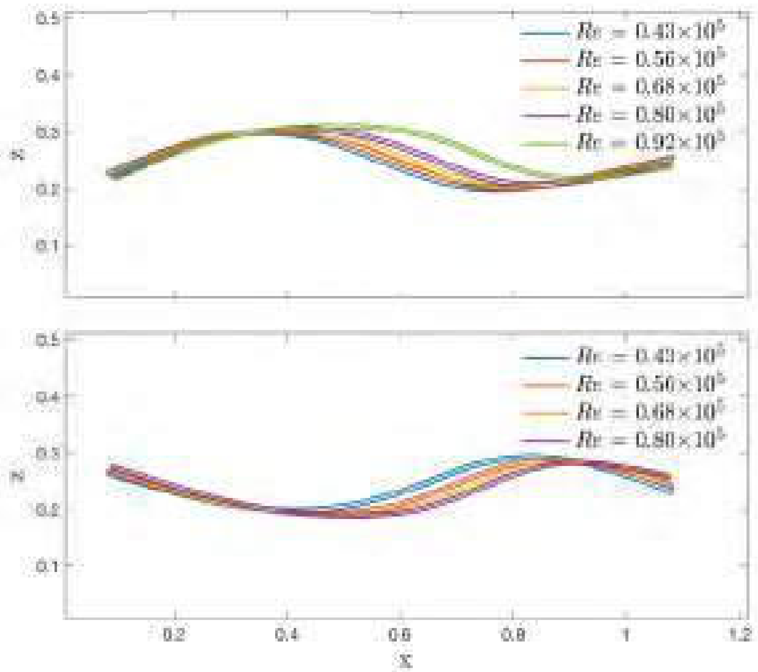

Figure 5.1: Shape adaptability as a function of flow speed. Plate's deformations are extracted from the first image of the PIV pair, and represent the average location of the plate during the test under study.

equilibrium positions. As fluid forces overcome the stabilizing effect of bending rigidity, snap-through events are expected to occur as the deformation is marginally stable.

It should be noticed that we present four cases for the negative phase, while there are five cases for the positive phase (one additional close to the transitional flow velocity to large oscillatory motions). This is due to the fact that at $Re = 0.92 \times 10^5$ (i.e., the fifth flow speed presented for the positive phase), with the deformation started with a negative phase, the plate will snap-through into the positive phase, and acquire an equilibrium position without transitioning to large oscillatory motions. Such behavior is expected as the deformation is an elastic instability (not to be confused with the fluid elastic instability).

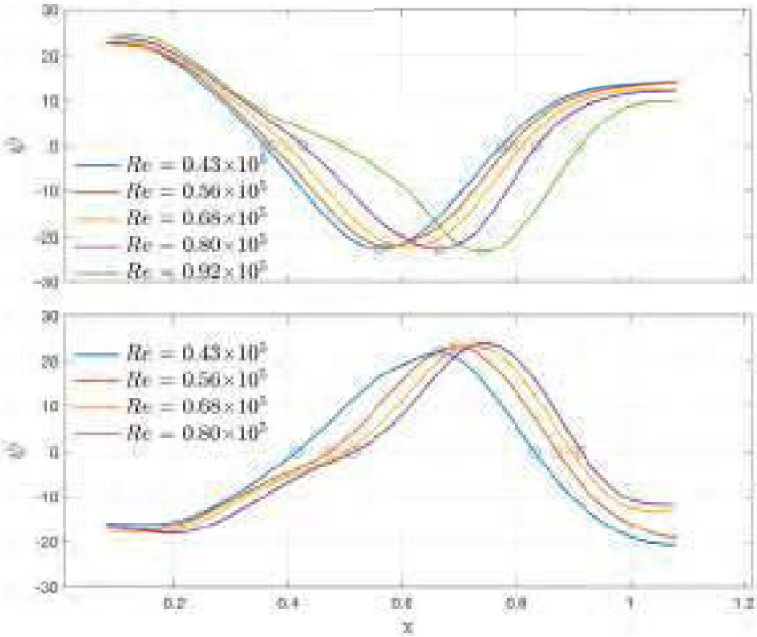

Figure 5.2: Variation of curvature as a function of flow speed. First and last circular markers (the left-most and right-most markers on each curvature plot) represent zero curvature locations, and the marker in the middle of each curvature represents the inflection point.

Turning our attention to the characteristics of the flow, we can see how an irrotational description of the problem is not appropriate (Fig. 5.3). The two-dimensional mean vorticity slices show vorticity diffused from the boundary layer into the concave face behind the leading edge, as well as in the concave face on and after the first location of zero curvature, $\psi = 0$. In the linear sense, this position will mark one quarter of a wave length of the deformation if our problem allowed a linear description. High vorticity events are present, particularly behind the leading edge, on the first location of zero curvature, as well as in the boundary layer around the plate, where the no-slip boundary condition must hold.

The deformation created has an additional effect on the characteristics of the

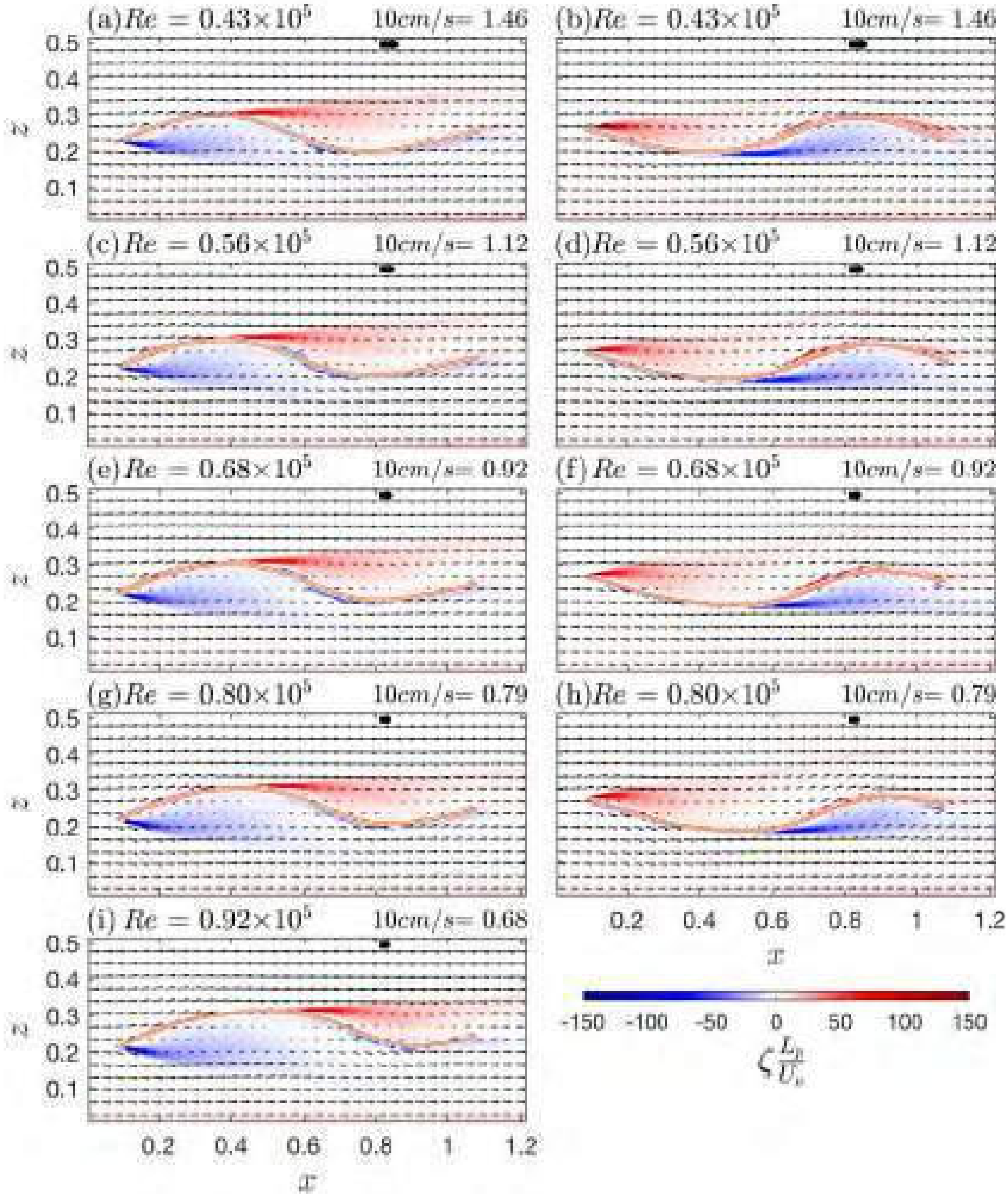

Figure 5.3: Two-dimensional vorticity fields for dynamically stable cases. The vectors represent the velocity fields.

flow, which is influenced by the creation of unfavorable and favorable pressure gradients. The former forces the viscous boundary layer to separate, and the latter makes a boundary layer more robust to separation. The effect of the pressure gradients can be seen in the recirculation zones depicted by the streamlines in Fig. 5.4. If we assume the boundary layer profile is defined by $u(x, z)$, the boundary layer equation is (Kundu and Cohen, 2008):

$$u\frac{\partial u}{\partial x} + w\frac{\partial w}{\partial x} = -\frac{1}{\rho}\frac{\partial p}{\partial x} + \nu\frac{\partial^2 u}{\partial z^2}, \tag{5.1}$$

where the pressure gradient is found from the external velocity field as $dp/dx = -\rho U\,(dU/dx)$, with x along the surface of the body. At the wall, the boundary layer equation becomes:

$$\mu\left(\frac{\partial^2 u}{\partial z^2}\right)_{wall} = \frac{\partial p}{\partial x}. \tag{5.2}$$

In an accelerating flow $dp/dx < 0$, and therefore:

$$\left(\frac{\partial^2 u}{\partial z^2}\right)_{wall} < 0. \tag{5.3}$$

In contrast, for a decelerating flow, the curvature of the velocity profile at the wall is:

$$\left(\frac{\partial^2 u}{\partial z^2}\right)_{wall} > 0, \tag{5.4}$$

meaning that for an accelerating flow the curvature of the velocity profile must change signs to merge smoothly with the external flow.

Additionally, from continuity we can see that the boundary layer thickness tends to increase for a decelerating pressure gradient:

$$w(z) = -\int_0^z \frac{\partial u}{\partial x} dz, \tag{5.5}$$

and relative to a flat plate, a decelerating external flow causes larger $-\partial u/\partial x$ within the boundary layer as the decelerating outer flow adds to the effects of viscous deceleration. Therefore, from Eq. 5.5 it follows that for an adversed pressure gradient, the amplitude of the $w(z)$ field, directed away from the surface, is larger, thickening the boundary layer not only by viscous diffusion, but also through advection away form the surface.

If the adverse pressure gradient is sufficiently strong, as a consequence of the inflection point of the curvature of the velocity field, reversed flow can occur (see Fig. 5.4). We say the flow "separates" from the flow and define the point of separation as the limit of forward and backward flow of the fluid near the wall, where the stress vanishes:

$$\left(\frac{\partial u}{\partial z}\right)_{wall} = 0. \tag{5.6}$$

A common characteristic (See Sec. 5.1.3), is that the flow downstream of the separation points is often unsteady and chaotic, and results in non-negligible pressure drag (form drag). Also, as long as the boundary layer remains laminar, the location of separation points remains independent of *Re* as can be seen in Fig. 5.5. Also in in Fig. 5.5, a slight change in the location of separation points can be seen. This change is explained by the fact that the plate adapts its shape to the flow velocity and effectively reconfigures itself, moving the location of

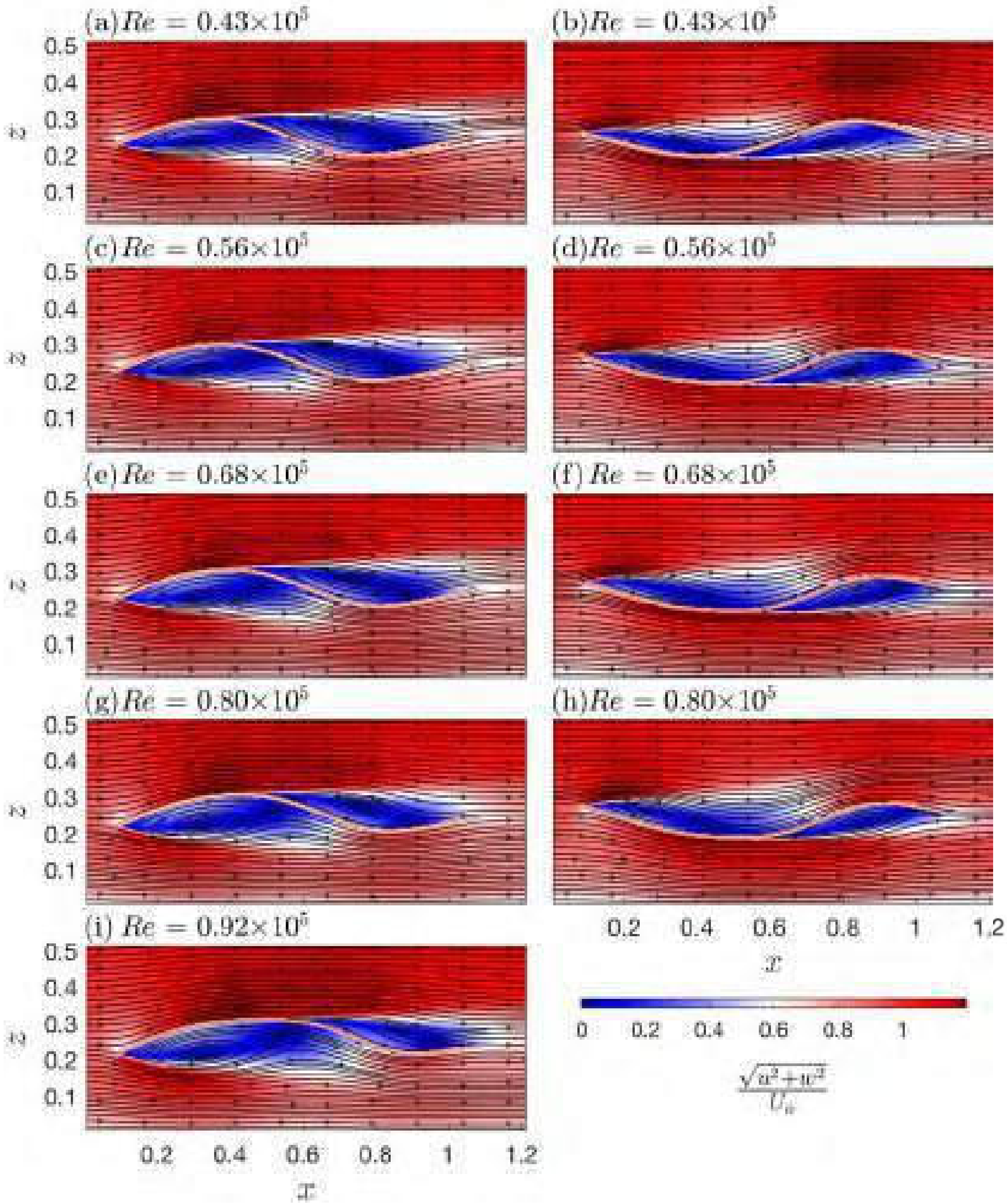

Figure 5.4: Two-dimensional velocity magnitude fields and streamlines for dynamically stable cases.

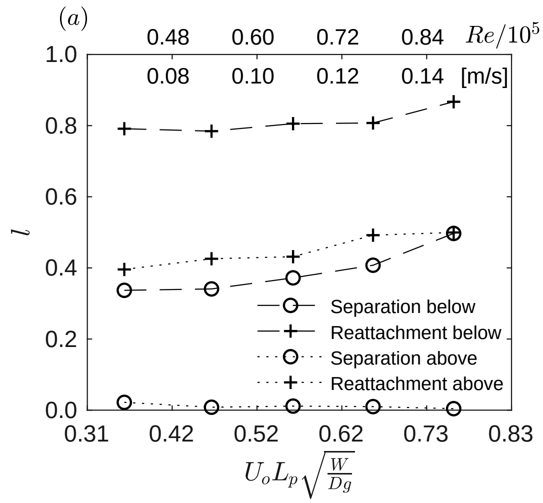

Figure 5.5: Location of separation and reattachment points along the plate: a) separation and reattachment for positive phase; b) separation and reattachment for negative phase.

the separation points. Notice that at *Re* close to U_c, this is the highest flow speed which is the closest to causing large oscillatory motions, the reattachment points of the lower face are located in the same place on the plate as the separation point of the opposite face, achieving symmetry.

Within this discussion we can expand on the nature of the boundary layer of our problem. First, the plate is immersed in a zero-pressure gradient (within experimental uncertainty) turbulent boundary layer, created by tripping it with a cross-flow bar at the entrance to the test section and downstream of the entrance section conditioning screens. Once the flow encounters the plate, a laminar boundary layer is initiated on the plate, transitioning to turbulent at U_t, depicted in Fig. 4.1b, where we hypothesize the drop in oscillatory frequency is a direct consequence of a transition to turbulence delaying the separation, as a turbulent boundary layer is more robust to separation, and therefore reducing pressure drag and lift. Finally, beyond the points of separation, the boundary layer equation becomes invalid as the boundary layer becomes so thick as to violate the underlying assumptions. Moreover, the parabolic nature of the boundary layer equation requires that a numerical integration is only valid in the direction of advection (along which information is propagated). A forward (downstream) integration of the boundary layer equation therefore breaks down after the separation point. Last, we can no longer apply potential flow theory to find the pressure in the separated region, as the effective boundary of the irrotational flow is no longer the solid surface but some unknown shape encompassing part of the boundary plus the separated region (Kundu and Cohen, 2008).

A closer look into locations of zero curvature and inflection points on the plate shows that $u/U_o\,(z)$ and $w/U_o\,(z)$ are weakly dependent on Re, while $\zeta\,(z)$ is not detectable to experimental uncertainty. Changes of the selected locations in $u/U_o\,(x)$ can all be explained by the reconfiguration of the plate, the subsequent change of the locations of interest downstream, and conservation of mass. For example, consider the second point of zero curvature for the positive phase (Fig. 5.6e). As Re increases, the location of the point of interest moves downstream and slightly up, creating a greater space between the flume's bottom and the plate. This causes a slight increase in $u/U_o\,(x)$ on the upper side of the plate, while slowing down the flow on the lower side.

Furthermore, closer to transition, there is an increase of vertical advection ($w/U_o\,(z)$), except for the upper face (Fig. 5.6a). The increase can be associated with ejection events and small amplitude vibrations increasing gradually as the plate reaches new equilibrium conditions with the new imposed flow velocities.

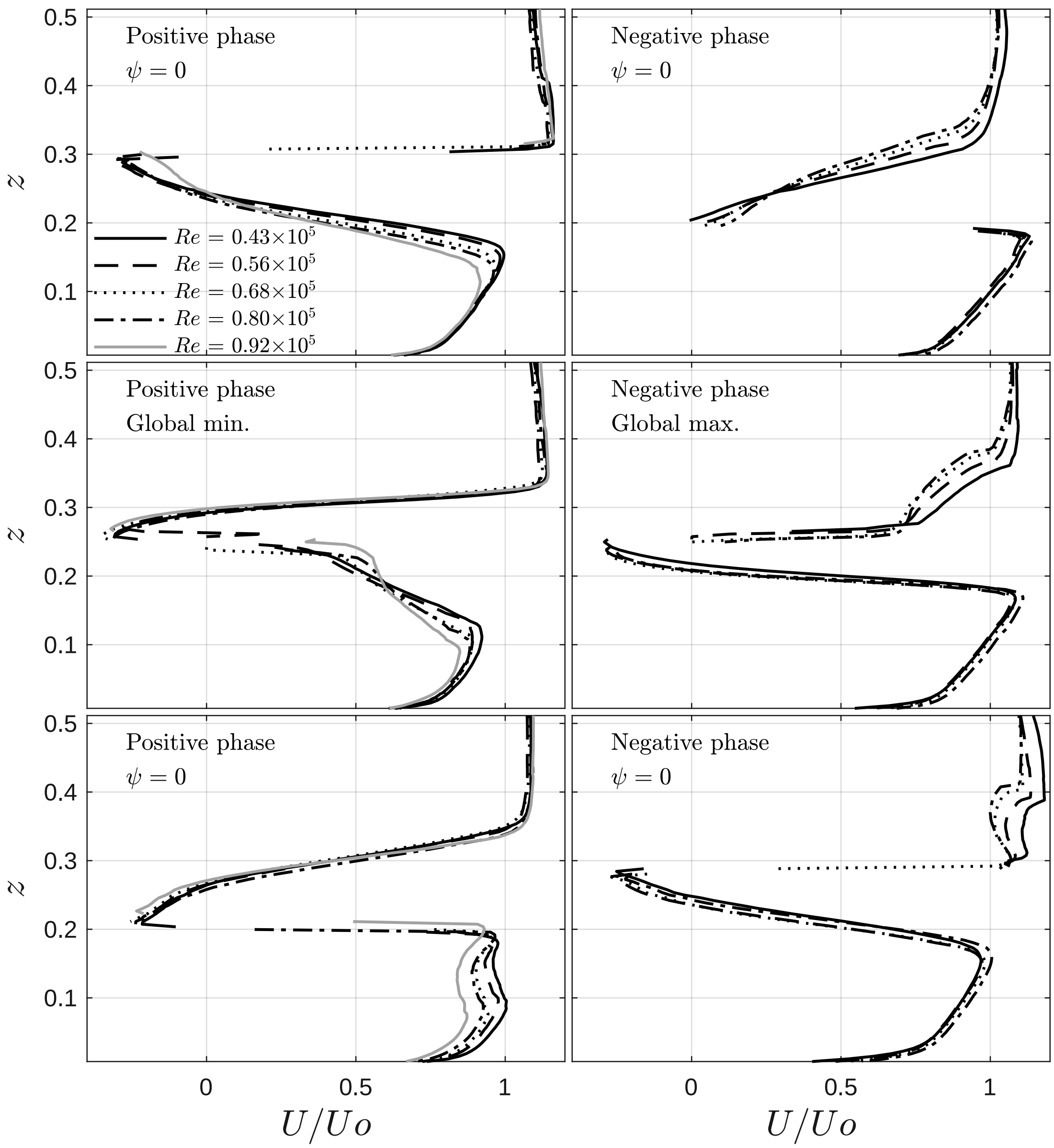

Figure 5.6: Self-similarity of horizontal velocity fields for positive and negative phases, and for the three locations in the horizontal axis identified in Fig. 5.1.

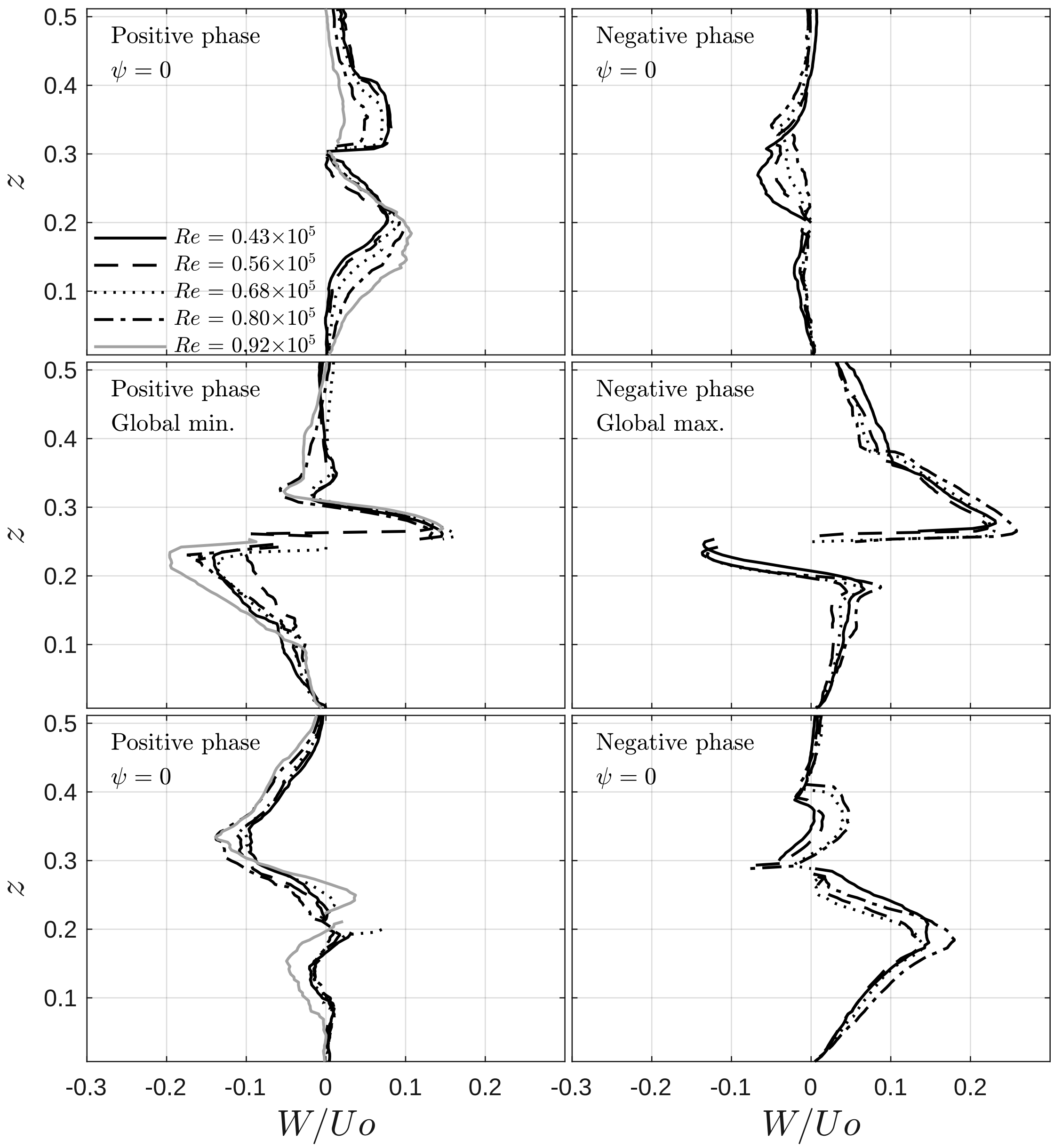

Figure 5.7: Self-similarity of vertical velocity fields for positive and negative phases, and for the three locations in the horizontal axis identified in Fig. 5.1.

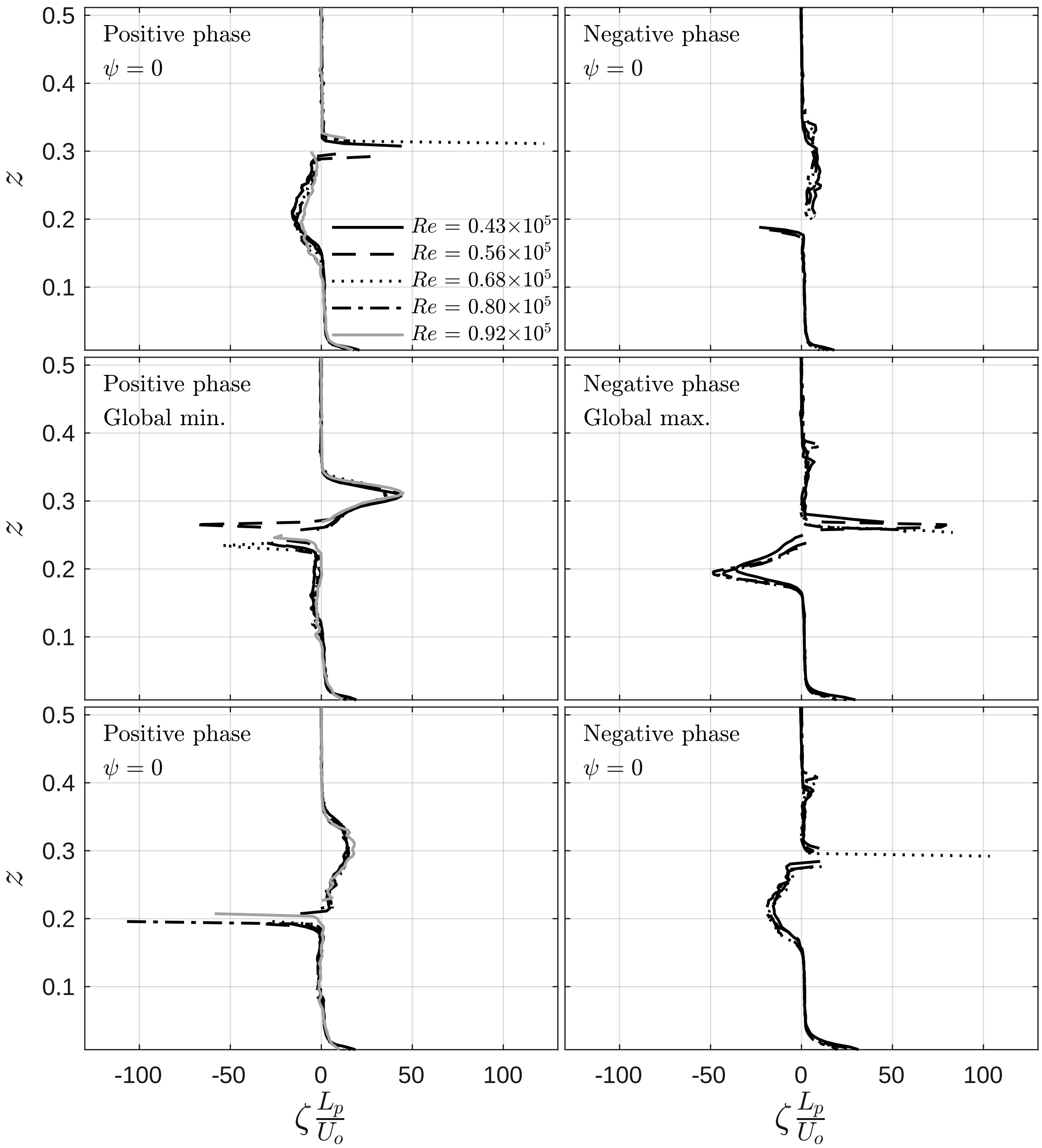

Figure 5.8: Self-similarity of vorticity fields for positive and negative phases, and for the three locations in the horizontal axis identified in Fig. 5.1.

5.1.2 Mean pressure field and forces and their influence on plate deformation and transition to large oscillatory motions

Mean pressure fields corroborate the presence of favorable and unfavorable pressure gradients, which contribute to the existence of flow separation, recirculation zones, and reattachment (Fig. 5.9). In the same way, such fields allow the identification of zones where suction can occur ($\frac{P}{0.5\rho_f U_o^2} < 0$), where their contribution towards increasing/decreasing lift/drag depends on the curvature and the face of the plate being analyzed.

Fig. 5.10 and Fig. 5.11 show the cumulative and convergence of vertical and horizontal forces (i.e., lift and drag, respectively) throughout the plate, for upper and lower faces, and for positive and negative phases. Fig. 5.10 (the control surface of the examples presented in (a) and (c) is $1.9\delta^{99}$) shows the role of high/low pressure zones where, depending on the curvature and face, the contribution could be positive or negative. Fig. 5.10*b* and Fig. 5.10*d* present the convergence of the total lift and drag forces over the plate. Notice that lift forces tend to vary depending on control surface, especially in the presence of flow recirculation, responding to the effects of flow separation. On the other hand, drag presents better convergence throughout the plate at the lowest flow speed, but shows weaker convergence as flow increases (Fig. 5.11).

Fig. 5.12 presents the convergence of the total force per control surface as a function of *Re*, where drag increases with flow velocity and lift exhibits decreases/increases in its magnitude for the positive/negative phase as it approaches flow velocities where transition is seen to occur. We can see that, for

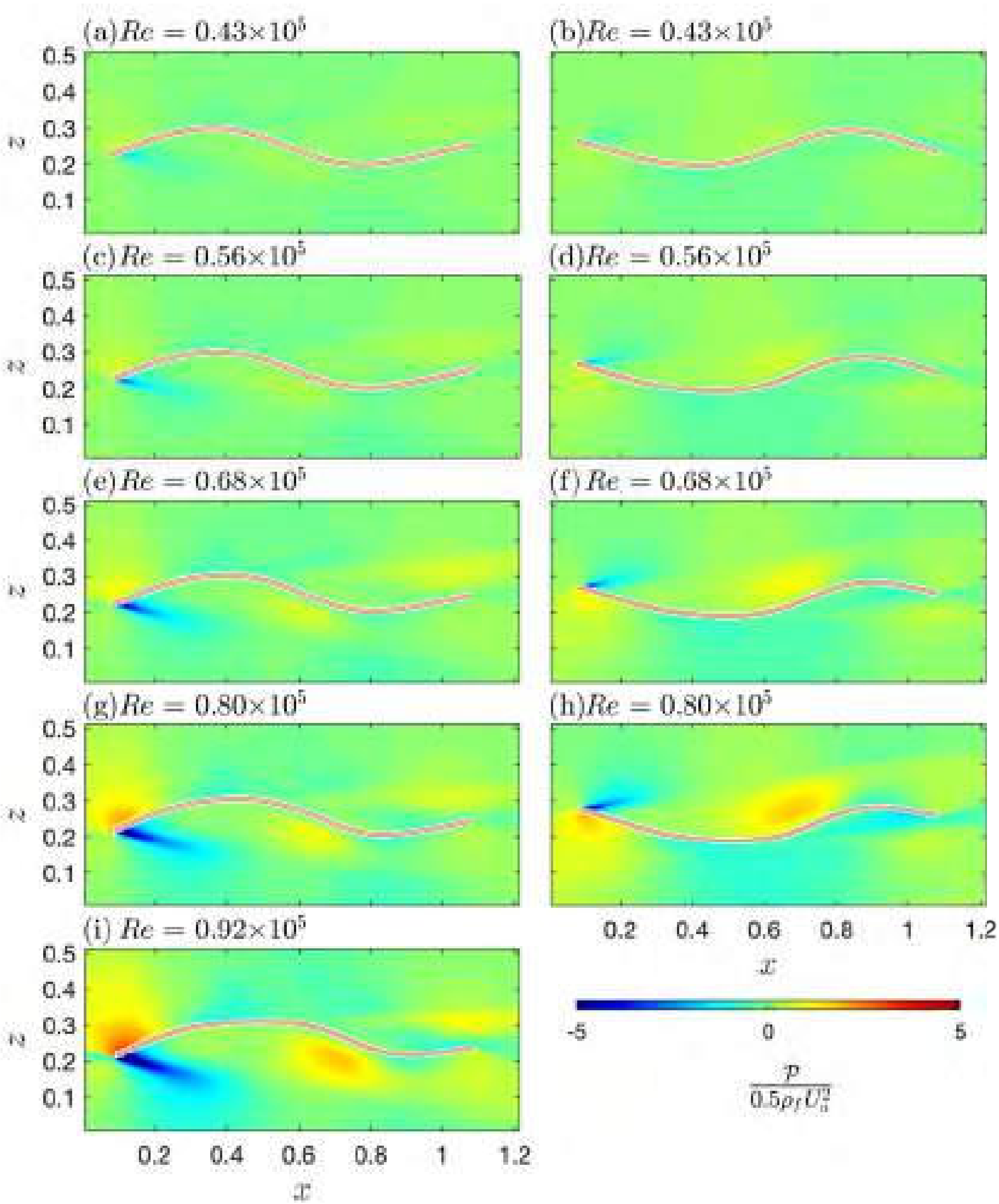

Figure 5.9: Dimensionless pressure fields for dynamically stable cases.

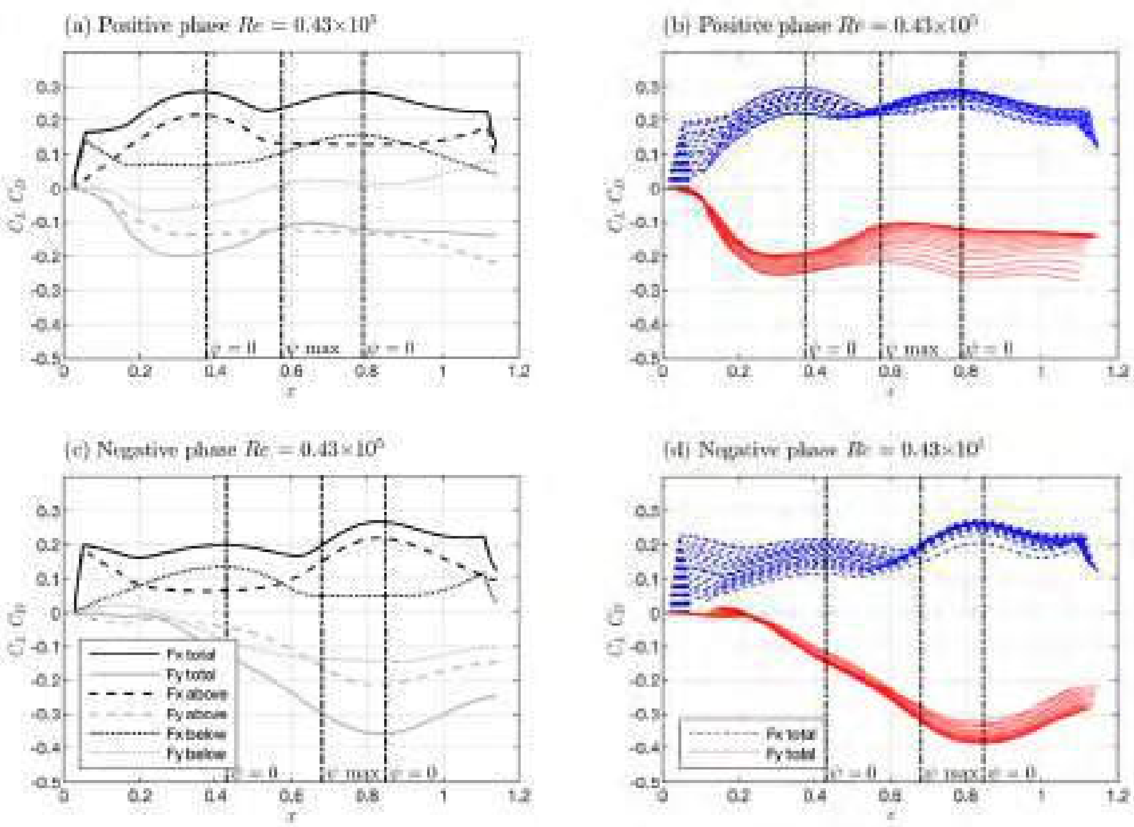

Figure 5.10: Cumulative and convergence of lift and drag forces over the plate for positive and negative phases at $Re = 0.43 \times 10^5$.

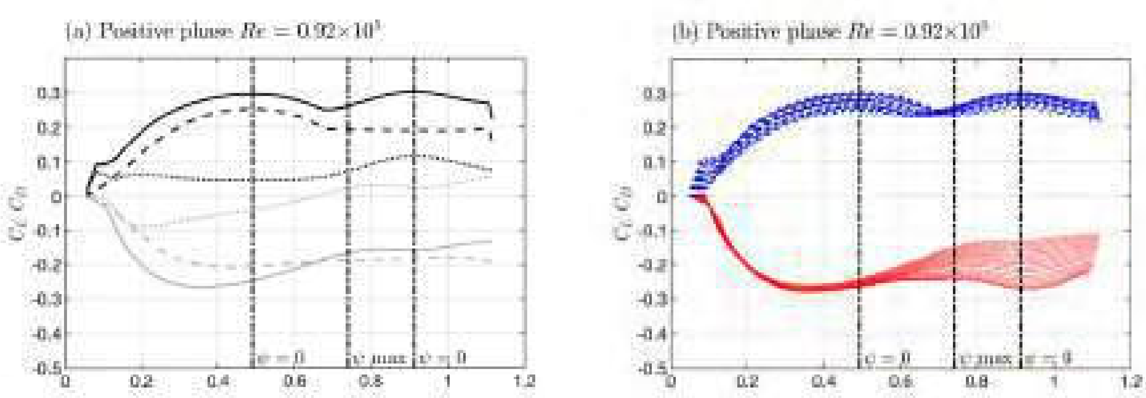

Figure 5.11: Cumulative and convergence of lift and drag forces over the plate for positive phase at $Re = 0.92 \times 10^5$.

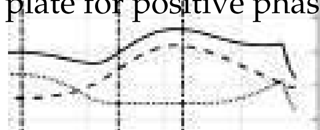

a specific plate configuration, first, there is always a positive mean drag, which can be considered constant (except at the lowest flow velocity for the positive and negative phases), and such drag is of the same order for both phases. Second, each phase has a predominantly negative lift. More importantly, as flow velocity increases, the lift on the positive phase decreases in magnitude (Fig. 5.12*b*), while for the negative phase it increases in magnitude (Fig. 5.12*d*). As the deformation is marginally stable, this change indicates the limits where a reconfiguration will be necessary to maintain equilibrium. Since further deformation of the plate are not possible (i.e., the crest of the positive phase or the valley of the negative cannot be deformed indefinitely), the increasing change in lift cannot be sustained under the same phase deformation. Physically, the increase in flow speed progressively deforms the plate, and as boundary conditions restrict the deformation (i.e., tension lines), there is a regime where equilibrium will not be achieved due to such restrictions, inducing either the phase change (snap-through) or large oscillatory motions. Finally, the change in the average lift can be explained by the increasingly positive component of lift provided by suction on the upper face of the positive phase, or similarly, the increasingly negative component of lift provided by suction on the lower face of the negative phase.

5.1.3 The unsteady flow field and the presence of small perturbations prior to onset of large oscillatory motions

Our experiments reveal small amplitude displacements prior to large oscillatory motions (see Fig. 5.13). The unsteady fluid forces induce the plate to a constant

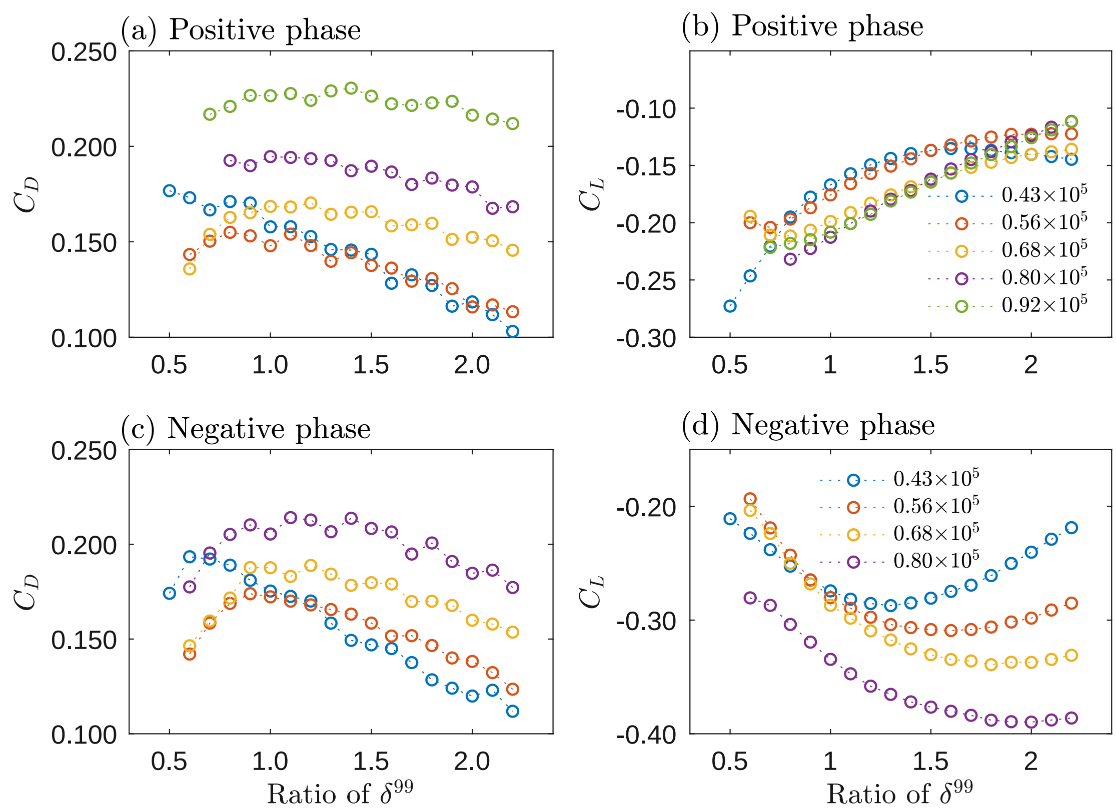

Figure 5.12: Convergence of forces at trailing edge as a function of control surface dilation and *Re*.

state of reconfiguration to achieve equilibrium, without transitioning into the plate's large oscillatory motions. Such behavior is possible not only by the action of the unsteady fluid forces, but also by the fact that the deformation of the plate is marginally stable. Large ejection events can be seen in Fig. 5.14, where the location provided in each subfigure is the mean average position, and the instantaneous plate location can be identified from the high vorticity streak close to mean plate's position. Additionally, it can be seen how vorticity is formed in the concave face behind the leading edge, diffused by action of the boundary layer, advected out by virtue of flow separation, and convected down by the mean stream flow.

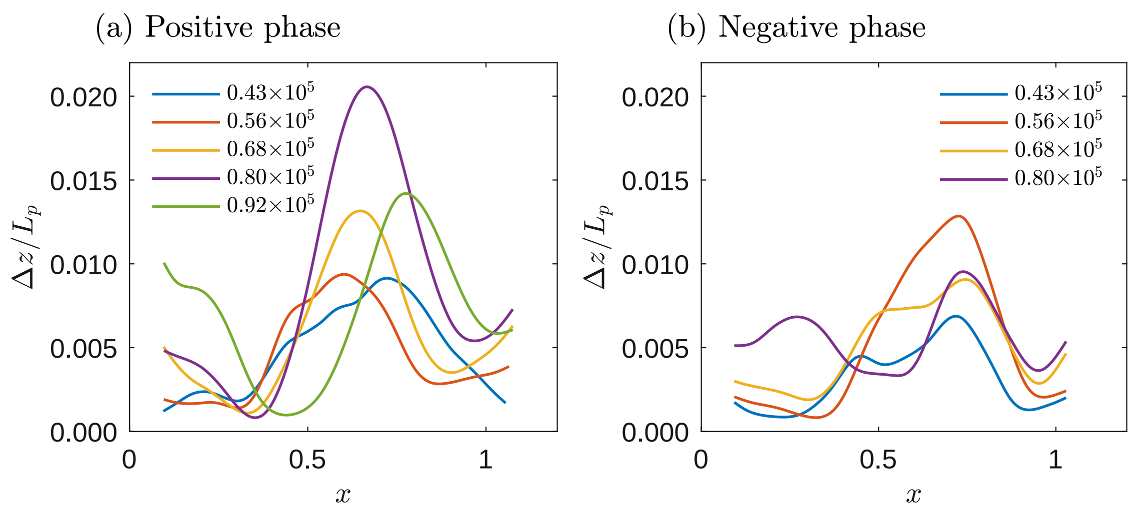

Figure 5.13: Small amplitude vibrations below critical flow velocity, U_c.

As flow speed increases, the frequency of convected vorticity events increases. Negative pressure creates suction events (particularly on ψ_{max} and ψ_{min}), causing the small amplitude oscillations. Such small amplitude oscillatory motions will grow progressively, aided by the progressive change in lift, which in turn will induce large oscillatory motions as flow speed increases.

5.1.4 Mean turbulent transport

We study the characteristics of turbulence and its ability to transport and mix fluid when interacting with a steady plate. Fig. E.1 and Fig. E.2 show the mean field and 1D-slices of horizontal turbulent intensities. Production is high behind separation points, noticeable in the peaks of 1D slices on Fig. E.2, where a weak dependence on *Re* can be identified, with horizontal turbulent intensities increasing as *Re* increases (i.e., for curvature extremes).

Fig. E.3 and Fig. E.4 show the mean field and 1D-slices of vertical turbu-

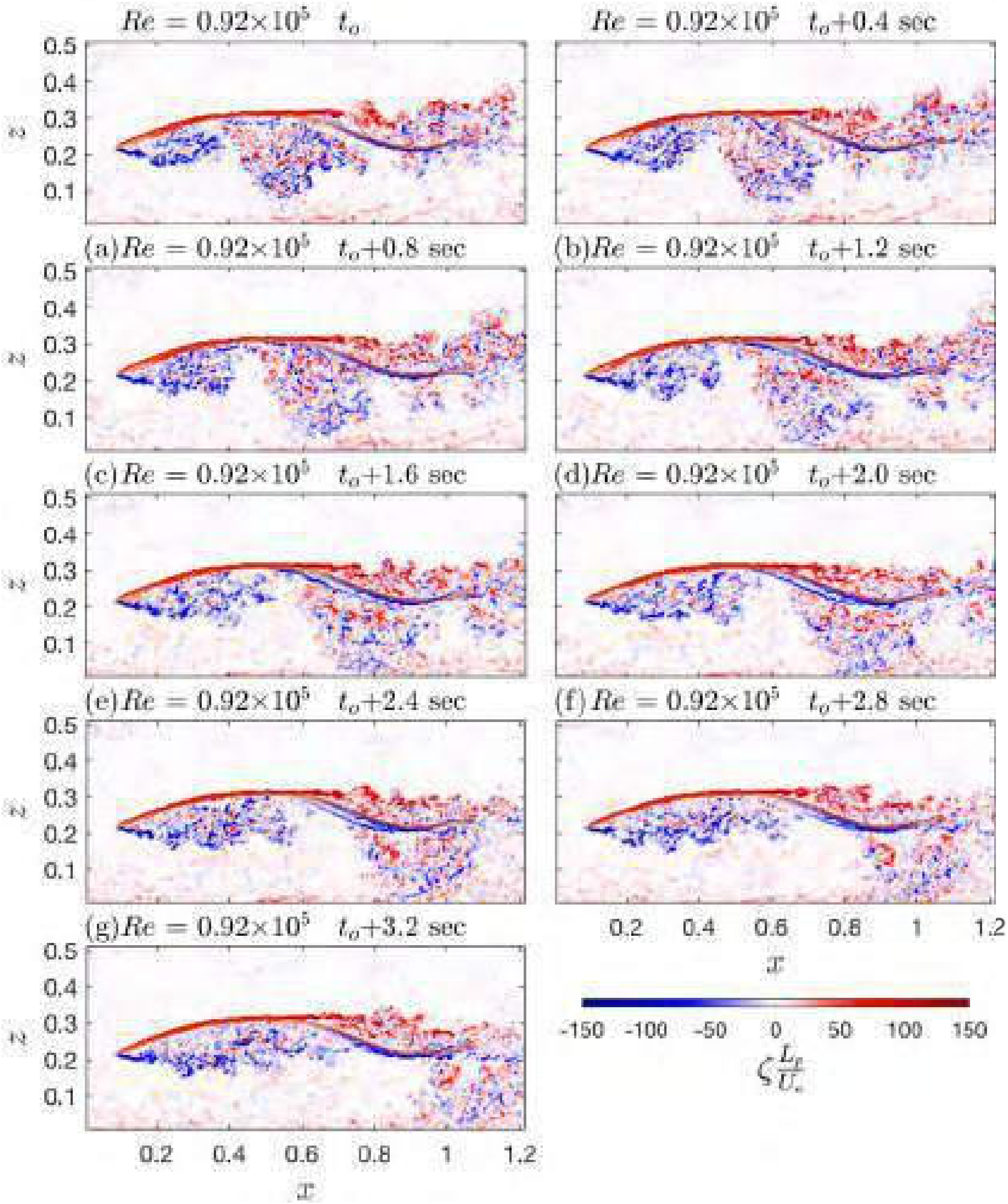

Figure 5.14: Unsteady flow field close to critical flow velocity, U_c. The dimensionless vorticity fields are depicted for $Re = 0.92 \times 10^5$, which is the highest flow velocity tested for dynamically stable cases before the transition to large oscillatory motions.

lent intensities. As with horizontal intensities, production is high behind the locations where flow separation is exhibited.

Fig. E.5 and Fig. E.6 show the vertical turbulent advection of streamwise turbulent momentum. Again, high momentum transport is seen behind locations of flow separation. On Fig. E.5 we can identify small patches of Reynolds stress that seem to challenge the directionality of turbulent momentum transport. For example, behind the leading edge, either for the positive or negative phase, there is a small area with $u'w'/U_o^2$ of opposite sign of that following it. This can be explained by the fact that immediately behind the leading edge, flow is accelerated, leaving this layer of fluid with higher momentum than that of the layer beneath/above it (i.e., towards/away from zero in the z-direction for positive/negative phase), therefore fulfilling the directionality of momentum transport. The same occurs in zones of favorable pressure gradients, where again the flow is accelerated in comparison to the layer away from the boundary, therefore leaving patches where momentum transport is in the opposite direction to the plate, again, without challenging the expected directionality of momentum transport.

Fig. E.7 presents a 2-D estimate of turbulent kinetic energy by using $\overline{u'^2 + w'^2}/U_o^2$, which follows the main story of momentum transport and turbulent intensities, where maximums are behind flow separation points.

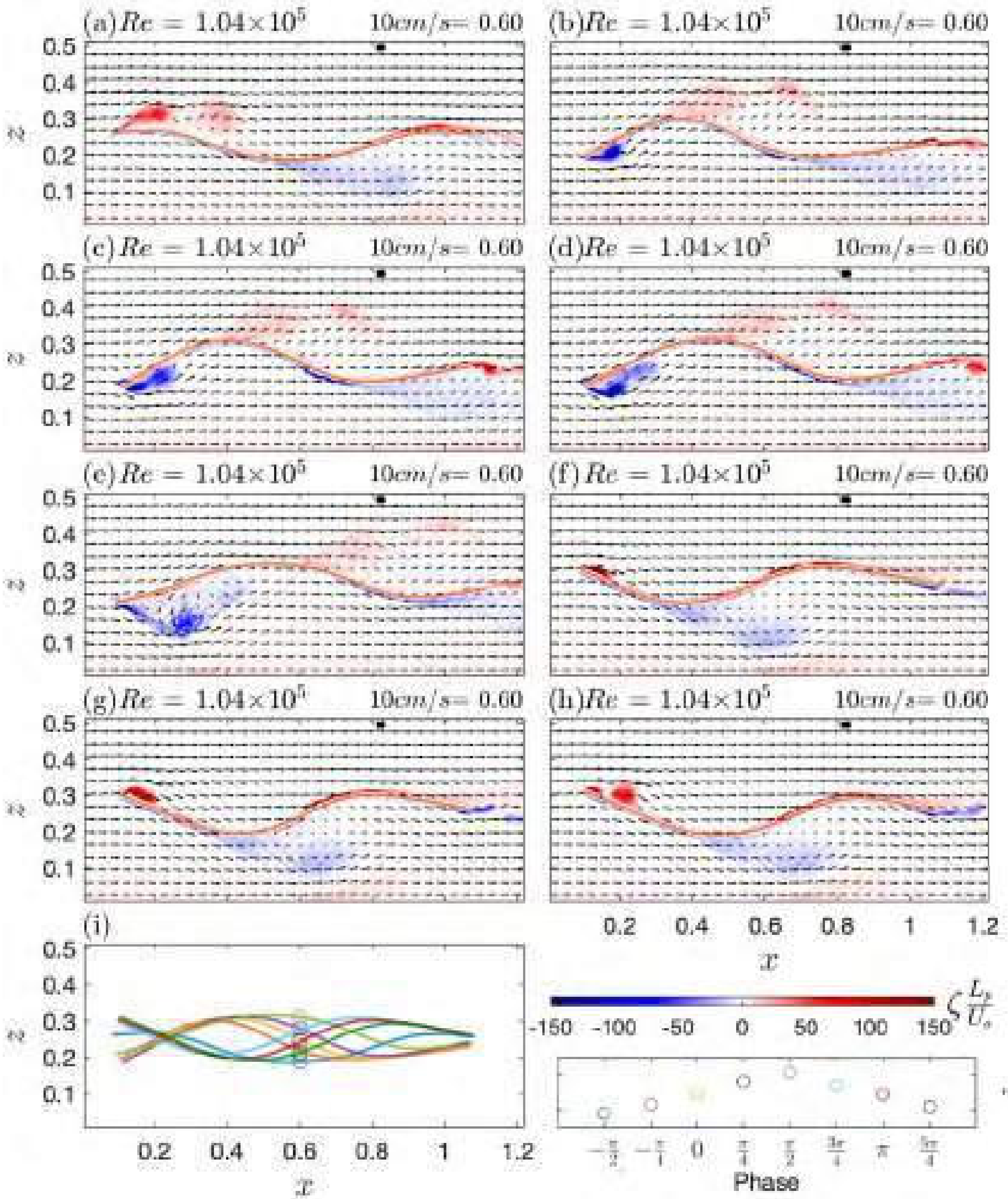

Figure 5.15: Phase-averaged two dimensional vorticity fields for $Re = 1.04 \times 10^5$.

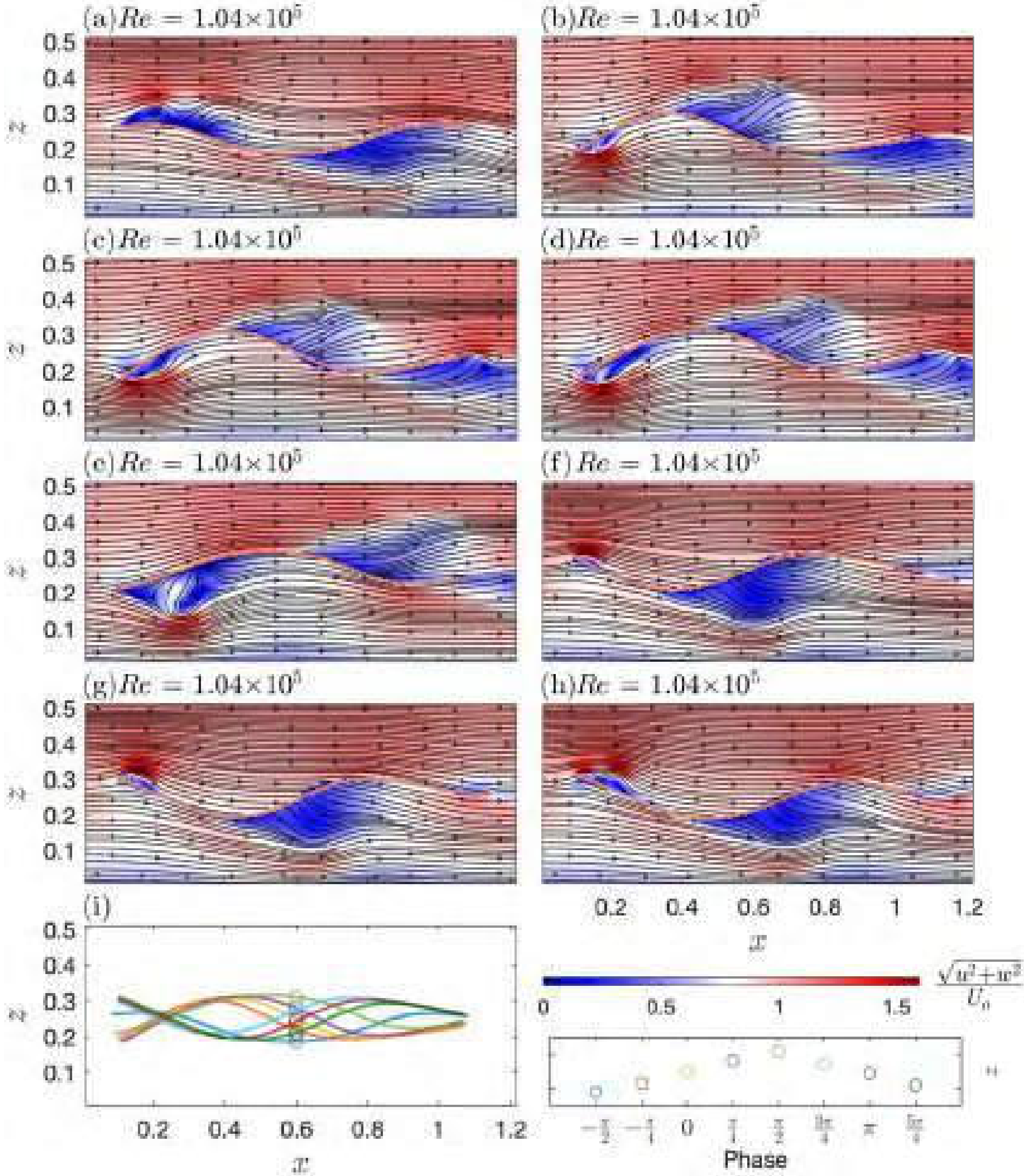

Figure 5.16: Phase-averaged two dimensional velocity magnitude fields for $Re = 1.04 \times 10^5$.

5.2 Phase-average large oscillatory motions of a dynamically-unstable buckled plate under a steady incompressible flow

Phase-averaged vorticity fields show the generation and advection of vorticity, carrying down areas of low pressure, that induce suction, and that are accompanied by high pressure zones acting on the opposite face, and reveal that they drive the oscillatory motions of the plate. Fig. 5.15 shows the vorticity field for U_c. Here, flow separation can be seen behind the leading edge. Generated vorticity is seen throughout the plate's boundaries. The characteristics of the flow show that, if we start on a phase resembling the steady plate positive phase ($-\pi/4$), a clockwise rotating vortex is formed behind the leading edge. This vortex is advected away by the action of the increased vertical advection (adversed pressure gradient) and the plate's acceleration. Then, the plate deforms further following advection of vorticity. The generation of the counterclockwise rotating vortex follows the same mechanics. Such events can be further appreciated in the 2D velocity magnitude fields (Fig. 5.16), where it can be notice that a full separation bubble (as seen on the steady plate) has insufficient time to form.

2D pressure fields corroborate the above story (Fig. 5.17), where the center of the flow separated vortices have low pressure. These events are paired with high pressure areas on the side facing the flow. Not surprisingly, zones of low pressure are advected downstream. Notice also that despite the convergence of the pressure algorithm, some fields present artifacts due to the in-plane motions (e.g., Fig. 5.17*e*)

By increasing *Re* we notice that the characteristics of the flow remain the same (Fig. 5.18 to Fig. 5.20). High vorticity generation is present on flow sepa-

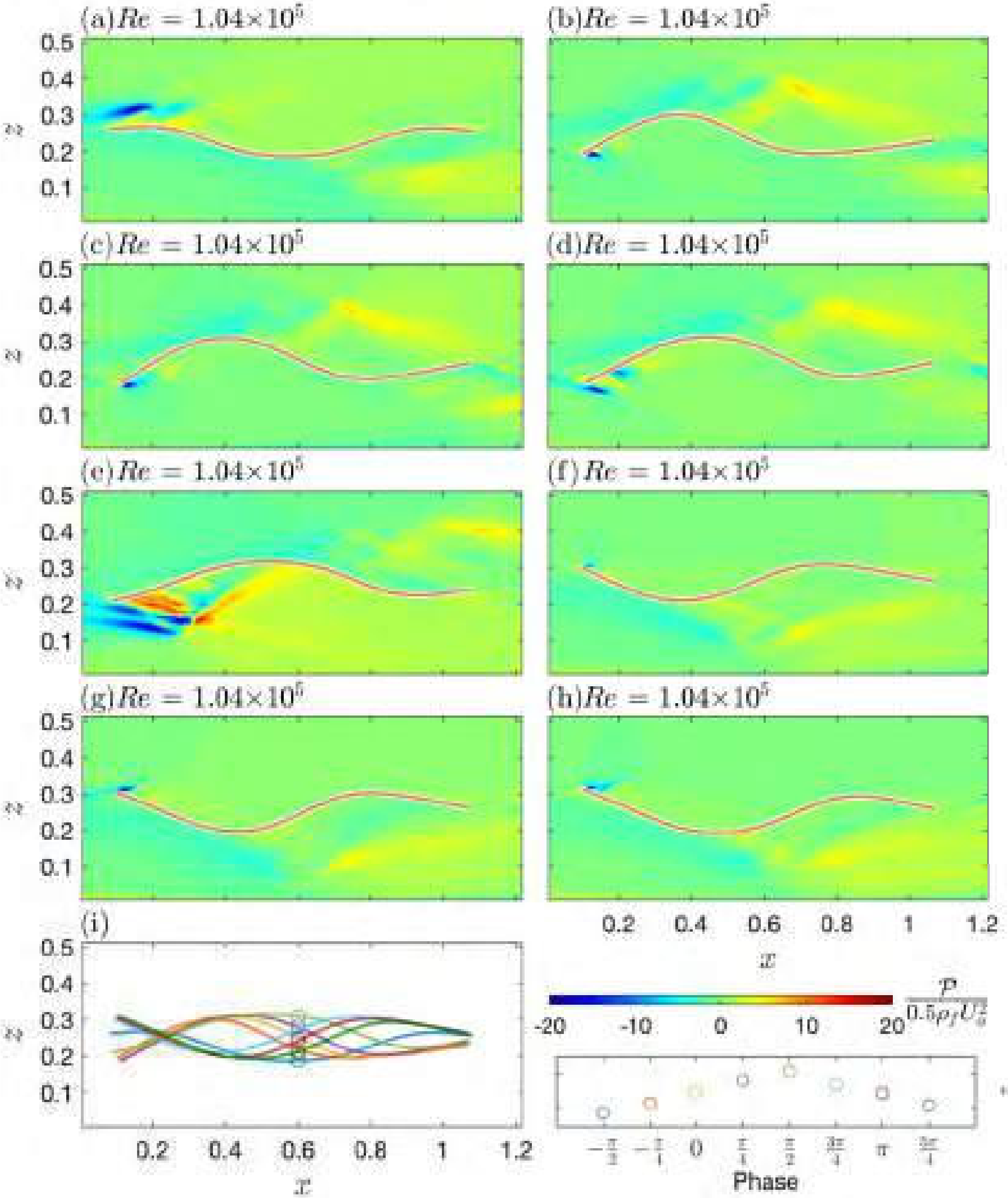

Figure 5.17: Phase-averaged two dimensional pressure fields for $Re = 1.04 \times 10^5$.

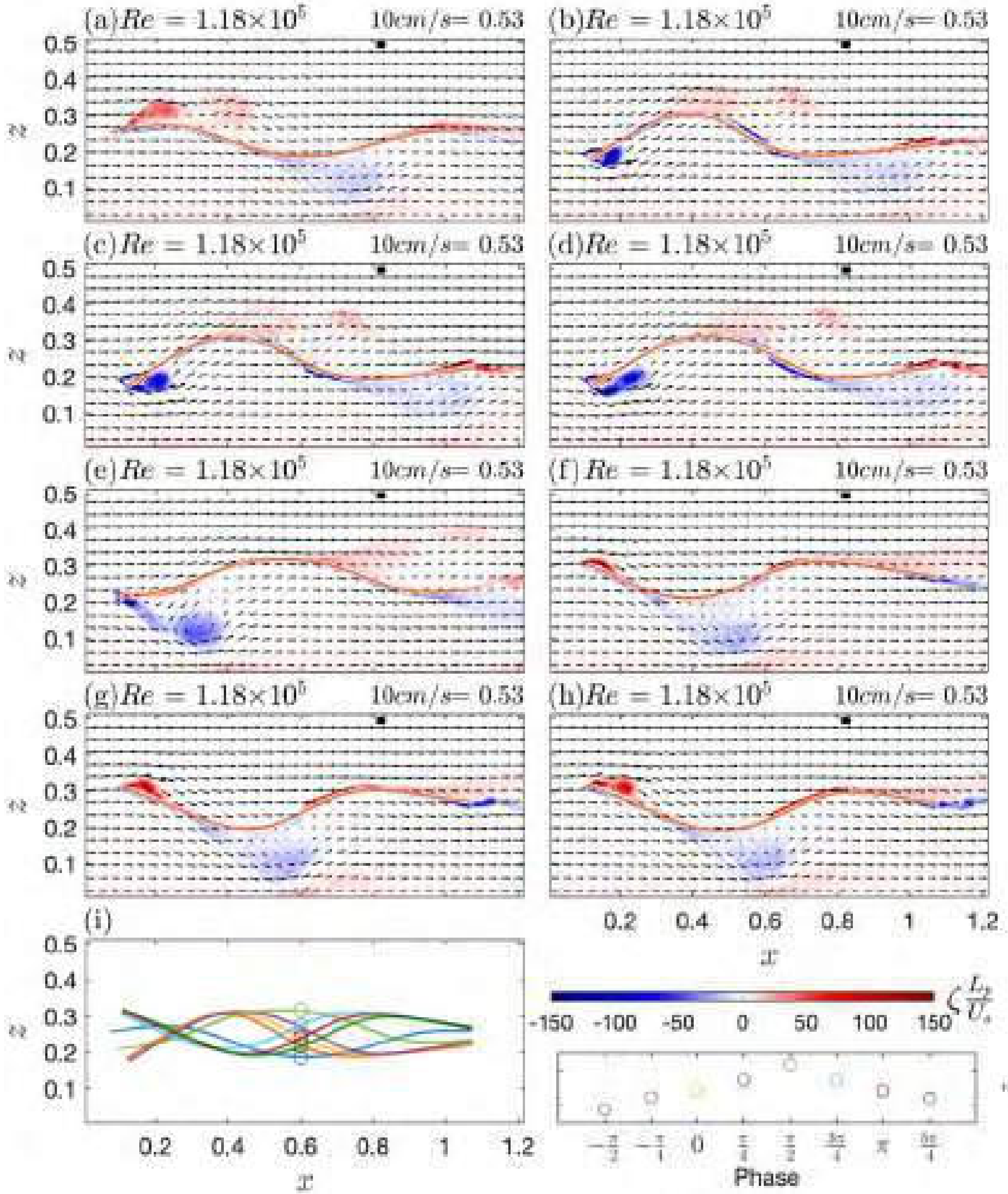

Figure 5.18: Phase-averaged two dimensional vorticity and velocity fields for $Re = 1.18 \times 10^5$.

ration locations behind the leading edge, and close to the boundaries where the no-slip condition must hold. It can be noticed though, that despite the selection criteria provided for phases, there are dissimilarities between plate deformation, particularly at the leading and trailing edges. Despite these dissimilarities, mechanisms responsible for generation and transport of vorticity hold. At this *Re*, velocity magnitude shows the separation zones behind the leading edge, and pressure fields reveal the advection of the low pressure areas paired with high pressure zones on opposite faces of the plate.

We choose to show an additional vorticity field at higher *Re* than the first two previously presented. As can be seen, phase averaging turns more problematic as excursions of the plate are less repeatable the higher the flow rate it is. This is a direct consequence of the nonlinearity of the oscillatory motions, which we have established the main sources to be geometric and boundary condition nonlinearities.

5.2.1 Phase averaged forces and their influence on plate deformation during large oscillatory motions

We can see from Fig. 5.21 that the convergence of lift forces is better for dynamically unstable cases than that presented on dynamically stable cases. This means that the control surfaces used capture better the overall influence of the flow field, particularly due to the fact that separation zones do not extend further back from the initial point of flow reversal.

Furthermore, Fig. 5.22*a* shows that the case at U_c (i.e., $Re = 1.05 \times 10^5$)

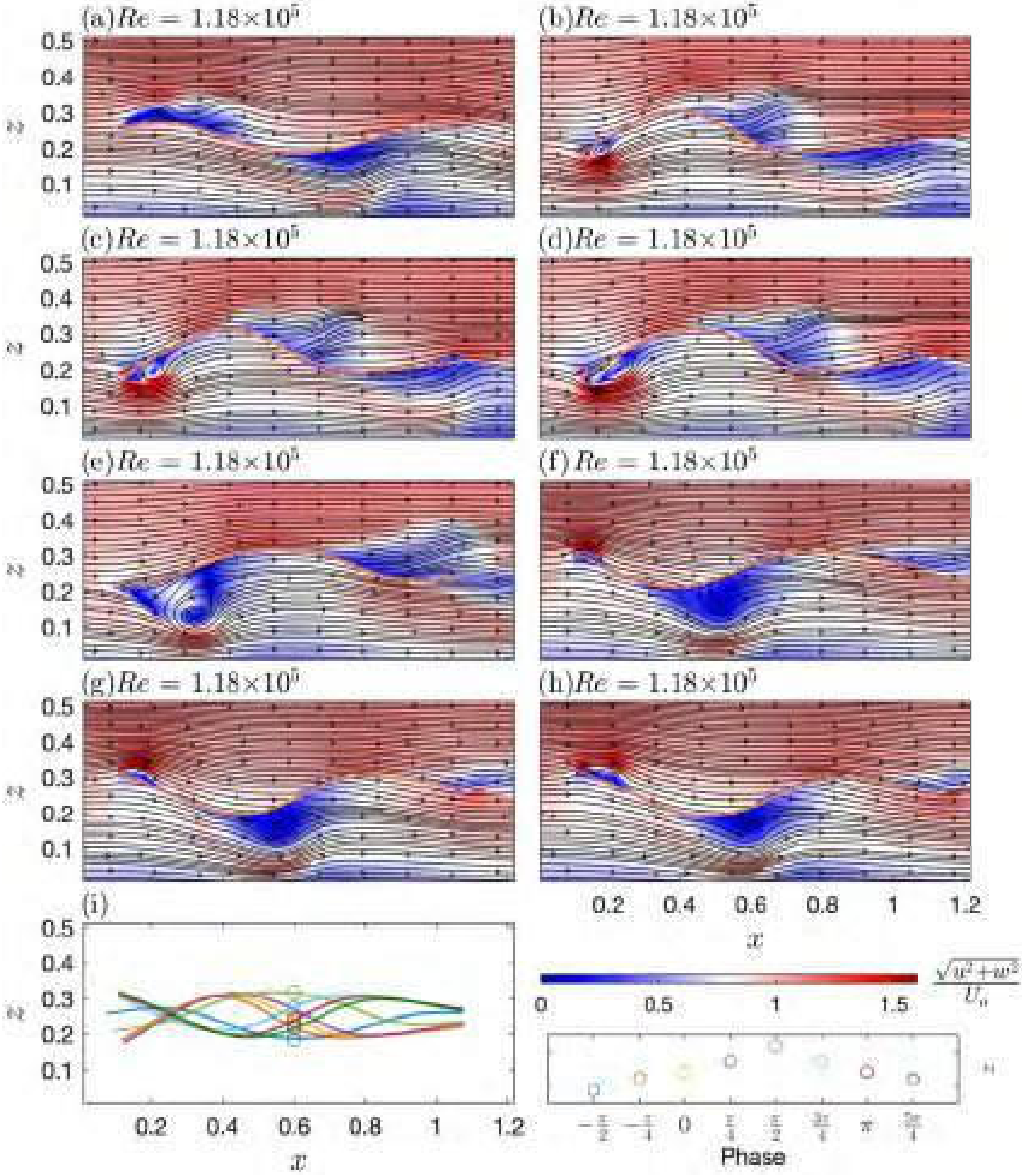

Figure 5.19: Phase-averaged two dimensional velocity magnitude fields for $Re = 1.18 \times 10^5$.

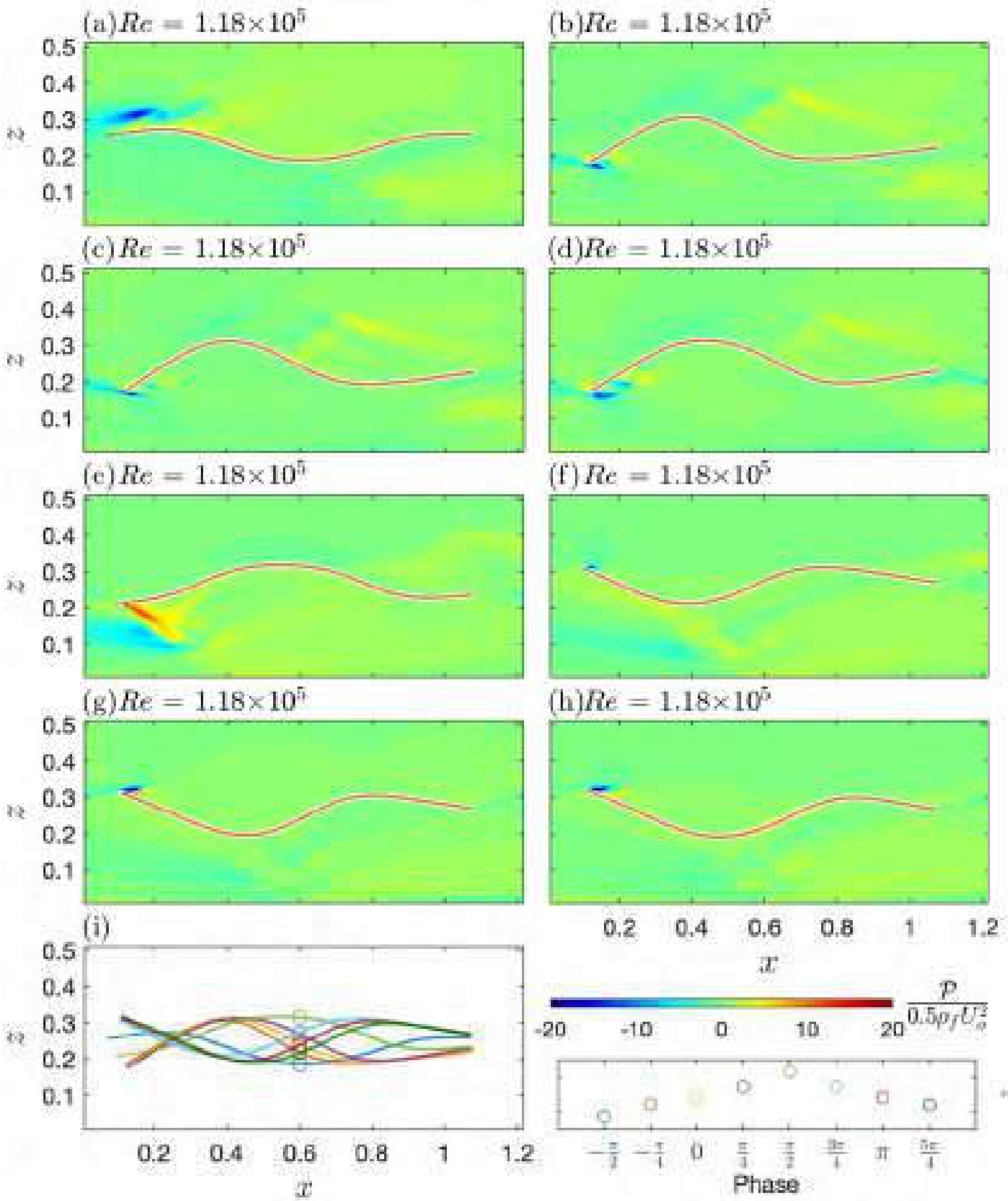

Figure 5.20: Phase-averaged two dimensional pressure fields for $Re = 1.18 \times 10^5$.

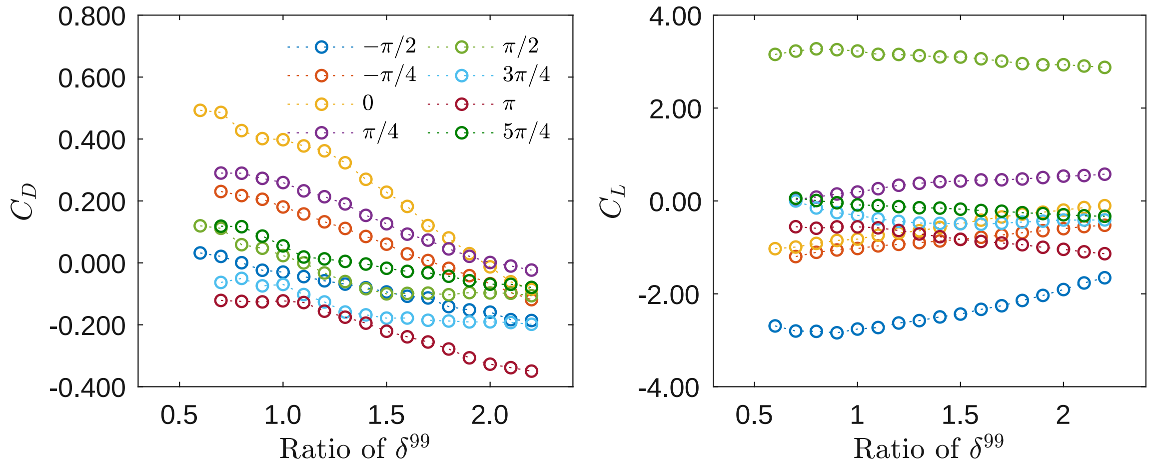

Figure 5.21: Phase-averaged force convergence over control surfaces at $Re = 1.05 \times 10^5$.

(a) Drag coefficient at 1.9 δ^{99}

(b) Lift coefficient at 1.9 δ^{99}

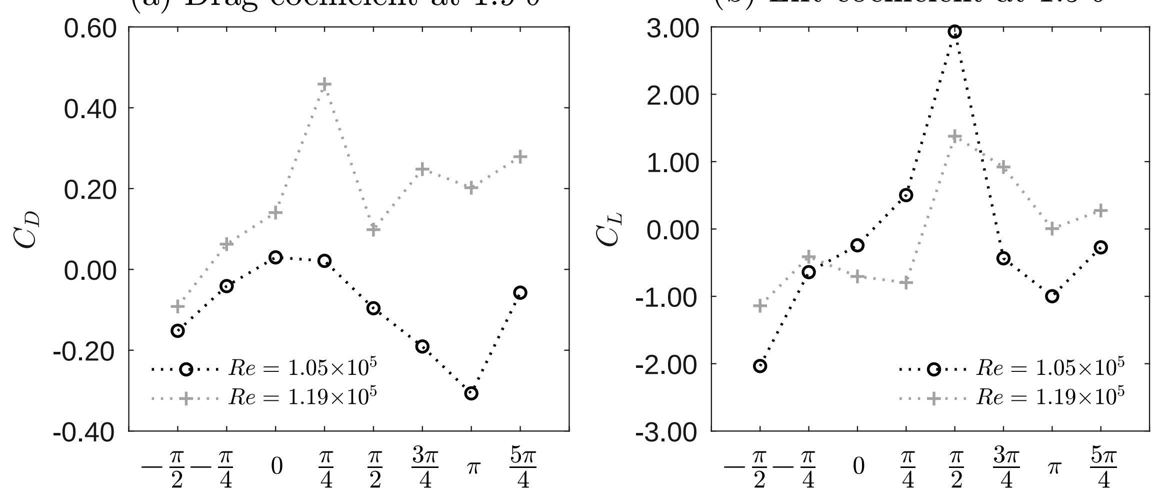

Figure 5.22: Phase-averaged drag and lift for $Re = 1.05 \times 10^5$ and $Re = 1.19 \times 10^5$.

presents thrust at every phase for the control volume presented. Despite the thrust at phases 0 and $\pi/4$ being close to zero, they are still negative and therefore produce thrust. On the contrary, for $Re = 1.19 \times 10^5$ only $-\pi/4$ shows evidence of thrust. On the other hand, Fig. 5.22*b* shows lift changing as a function of curvature deformation. As the fluid forces change, the plate responds by deforming in an attempt to acquire an equilibrium position. As the flow rapidly responds (for an incompressible fluid the speed at which information travels can be considered infinite) new conditions are set, and the plate is kept in motion as it tries to find an equilibrium between fluid forces and its inertial and rigidity response.

5.2.2 Phase-averaged turbulent transport

For the dynamically unsteady plate, high horizontal and vertical turbulent intensities are linked to flow separation and advection of vorticity. Fig G.1 to Fig G.4 show $\sqrt{u'^2}/U_o$ and $\sqrt{w'^2}/U_o$ for the two lowest Re tested. Horizontal turbulent intensity is particularly strong behind the leading edge and crest, where flow separation can ocurr, while vertical intensities are strong behind the leading edge and at the core of vortex events.

Finally, Fig. G.5 and Fig. G.6 shows the turbulent vertical advection of the streamwise turbulent momentum. Transport is high behind the leading edge and crests, linked again to vorticity events. The wakes show a predominant downward advection on top of a layer of predominant upward advection, independent of phase, as seen for steady plate results.

CHAPTER 6
CONCLUSIONS

We presented the study of a periodically constrained plate, induced into a second mode deformation, and explore the underlying mechanics of its transition to large oscillatory motions. Experimentally, and without the presence of a liquid or flow, the buckling instability and elastic bifurcation of second mode deformations with snap-through are self-evident. The results of a numerical model of the static deformation, based on a two-dimensional periodically constrained heavy elastica, corroborate experimental findings, and point towards the possibility of multiple equilibrium solutions (bifurcation), where first and second mode deformations are solutions of a single control parameter $\left(\delta_p - \delta_f\right)/\delta_p$. Results show good convergence, but sensitivity to tension force components, h_x and h_z, represents difficulties in finding the full equilibrium path and other possible equilibrium positions with shapes resembling higher order modes.

The static mathematical model shows that the nonlinear nature of the problem arises from geometry and boundary conditions. Both are intrinsic physical characteristics of the problem, where for the former, the vertical deformation of the plate is much greater than its thickness, and for the latter, the external tensioning that restricts the plate's position to an area rather than a fixed point will become active as a function of the plate's deformation. Furthermore, this model shows that weight and compression are always destabilizing forces. For our case, divergence (buckling) occurs as a combination of the destabilizing effects of both forces, working against the stabilizing effect of the bending rigidity of the plate. The activation of tension forces as the plate deforms is an essential design aspect, as a second mode would not be physically realizable without it.

A linear stability analysis based on the mathematical model coupled with slender body theory, and with geometric and boundary condition non-linearities simplified, shows the positive effect of compression in the early onset of large oscillatory motions. Apart from ignoring the intrinsic nonlinearities of the problem, this analysis disregards the limitations of a coupling based on slender body theory, where flow separation is not expected to occur. Experimental findings also show that the horizontal and vertical displacements and velocities of the plate are of the same order of magnitude, while slender body theory considers only the vertical displacements and velocities as the relevant quantities. Despite this, the linear analysis allows us to see the stabilizing effect of fluid induced tension and Coriolis forces, and the destabilizing effect of the centrifugal and compression forces.

Experimentally, and in the presence of an incompressible flow, the highly buckled plate reveals the critical velocity, U_c, at which large oscillatory motions start, to be much lower than that of a flag type configuration (plate held by its leading edge). The experimental study of the kinematics shows that the sinusoidally-deformed plate exhibits three states of motion: (1) a prescribed elastic instability followed by second mode buckling, showing weak perturbations below U_c, (2) a flutter instability at U_c followed by stable periodic oscillatory motions above U_c, and (3) oscillatory motions and burst events of three-dimensional effects after a transition regime (U_t). As a result of the external compression and despite entering into spatial chaos, an oscillatory trend beyond U_t is predictable (Fig. 4.1*a* and Fig. 4.1*b*). The transitional regime is also an indication of the delay of flow separation and transition to a turbulent boundary layer on the plate. Additionally, the frequency spectra show an increasing sub-harmonic energy range, a signature indicative of a precursor to chaos.

The hydrodynamic study shows that the presence of the plate causes an unsteady velocity field prior to the onset of large oscillatory motions, showing flow separation behind the leading edge and crest due to adverse pressure gradients. This flow configuration in turn causes a significant form-drag, and therefore non-zero drag in addition to lift forces. Moreover, the so-called dynamically stable plate exhibits small perturbations prior large oscillatory motions. These vibrations, of the order of one percent of the plate's length (L_p), are cause by the ejection events of vorticity exhibited in this unsteady flow field, where vorticity is diffused from boundaries, advected out, and convected downstream. Rojratsirikul et al. (2011) suggested that small vibrations of flexible membranes are only negligible when the flow remains attached, consistent with our findings and reinforcing the importance of flow separation in the onset of small perturbations and later transition to large oscillatory motions.

Prior to the onset of large oscillatory motions, lift decreases/increases in magnitude for the positive/negative phase. As a consequence of this, and by virtue of the plate's flexibility and marginal stability, the mean deformation changes as a function of flow velocity. This is evidence of divergence, in this case caused by a dynamic external load (i.e., unsteady flow field). Curvature extremes are seen to move downstream. Such adaptability is limited by the boundary conditions, where in the vicinity to critical flow velocity, U_c, the activation of new tension lines will restrict any further deformation, and therefore cause snap-through events. These events occur at a different follow regimes for each of the phases studied. While the snap-through event causes the negative phase to transition into a positive phase, it will cause, at a higher flow velocity, the positive phase to transition into large oscillatory motions.

For the dynamically unstable plate, flow separation is evident but recirculation zones do not grow as they did under dynamically stable conditions. Low pressure zones accompanying vorticity events are transported away from boundaries by virtue of the additional vertical advection (a result of adversed pressure gradients) and the plate's inertia, and convected downstream, followed by propagation of the plate's deformation.

For both dynamically stable and unstable plates, the turbulent intensities as well as turbulent transport are strong behind leading edge and crests of the deformations. For small amplitude oscillations, the plate excites the shear layer and causes the roll-up of large vortices, which are one of the main mechanisms for large oscillatory motions. This flow separation and advection of vorticity has been studied previously, albeit, for cambered membrane airfoils at different angles of attack Rojratsirikul et al. (2011). Our dynamically unstable plate, despite showing smaller flow separation events, still presents high turbulent kinetic energy downstream of the leading edge and crests. Independent of the dynamical stability of the plate, the wake shows a predominant downward advection on top of a layer of predominant upward advection.

Finally, the findings presented herein can be use to improve the design of the original design from which this study was inspired on: the self-powered pump Muriel et al. (2016). Based on the above conclusions, we hypothesize that the lateral reinforcement of the plate (a series of wood dowels used to prevent warping in the later direction) is essential and provides a destabilizing effect by an additional flow separation, helping the transition to oscillatory motions. Once large oscillatory motions are established, the presence of this same reinforcement tends to reduce the oscillatory frequency. As occurs for a golf ball and its dimples, the transverse reinforcement induces an early transition to a turbulent boundary later, which in turn reduces the oscillatory frequency as seen in this study. How much effect, if any, this reinforcement has in the transition to turbulence of the plate's boundary layer is an open question, as the reinforcements are not fully attached to the plate. In general, this configuration opens new possibilities for energy harvesting with a reduction of the critical flow velocity, U_c, and improved operational range, OR. Moreover, as occurs with flapping filaments or flags (Müller, 2003; Jia and Yin, 2008; Ristroph and Zhang, 2008), the striking resemblance of the induced oscillatory movements presented herein with animal locomotions poses the question of applicability of the proposed deformation as a propulsion design opportunity in this area, or as a model to study locomotion itself.

CHAPTER 7

FUTURE WORK

Mathematically, work remains on nonlinear stability analysis, large and small vibrations, and full coupling with fluids as part of the larger scope of the problem, for which the deformation was originally conceived. For these topics, extensive studies have been conducted on plates (see Dowell (1975); Dowell and Ilgamov (1988); Paidoussis (2016b); Dowell (2015) and references therein). The use of external forcing, first to induce a departure from trivial stability into a buckling instability, and at the same time to locally stabilize second mode deformations, has larger implications for fluid-structure interaction problems: the applications of such deformations can prove useful in reducing critical flow velocities to start structural oscillations, and increasing operational range of such applications (Dowell and Ilgamov, 1988; Dowell, 1982). Stability analysis could also be studied with a nonlinear structural formulation coupled with slender body theory, with the plate's Youngs' modulus artificially reduced to improve convergence. Both experimental and numerical results (static formulation) could aid in determining such artificial reduction.

Experimentally, work remains to be carried out to understand the transition regime and higher Reynolds number flows. The reduction of repeatability (same plate's deformation in time) as flow speed increases also calls for a more powerful tool to detect edges. Neural networks could be implemented to aid in the detection of moving surfaces in the presence of particles (Mathis et al., 2018). The derivation of pressure can be further investigated to reduce the errors caused by some integration paths. The methodology implemented herein should take care of such errors through the large number of paths used, but the determination of such erroneous paths may improve the pressure estimates presented herein. Other aspects that remain are the study of the wake, the change in boundary conditions to produce other deformations, the possibility of tunable lift and drag through deformable adaptations to flow, among others. Progress on the study of the wake of membrane airfoils has been made by Rojratsirikul et al. (2010), works that suggests that the amplitude and mode of vibration depends on the location and magnitude of the unsteadiness of the shear layer.

APPENDIX A

PLATE DISCRETIZATION

We used a center difference scheme of order $O(2)$ to solve the boundary value problem posed by Eq. 3.3, which we reproduce here for convenience:

$$\begin{aligned} x' - \cos\psi &= 0, & z' - \sin\psi &= 0, \\ \psi' - m &= 0, & m' - q\cos\psi + p\sin\psi &= 0, \\ p' &= 0, & q' + w &= 0, \end{aligned} \tag{A.1}$$

The values $x(s)$, $z(s)$, $\psi(s)$, $m(s)$, $p(s)$, and $q(s)$ may be discretized along the arc-length, s, so that:

$$x_k(s_k), z_k(s_k), m_k(s_k), \psi_k(s_k), p_k(s_k), q_k(s_k), \tag{A.2}$$

with

$$s_k = (k)\triangle s, \quad k = 1, 2, \ldots n \tag{A.3}$$

where $n = 1/\Delta s$, and $n + 1$ is the number of nodes along s. A vector $\boldsymbol{a}$ of node values is created so that:

$$\boldsymbol{a} = \begin{pmatrix} a_1 \\ a_2 \\ a_3 \\ a_4 \\ a_5 \\ a_6 \\ \vdots \\ a_{6n+1} \\ a_{6n+2} \\ a_{6n+3} \\ a_{6n+4} \\ a_{6n+5} \\ a_{6n+6} \end{pmatrix} = \begin{pmatrix} x_1 \\ z_1 \\ m_1 \\ \psi_1 \\ p_1 \\ q_1 \\ \vdots \\ x_{n+1} \\ y_{n+1} \\ m_{n+1} \\ \psi_{n+1} \\ p_{n+1} \\ q_{n+1} \end{pmatrix} \tag{A.4}$$

A.1 Indexing of contact points and force vector

We identify the indexing of contact points along s. The coordinates of the tension line at the infinitely-rigid frame and at the plate are:

$$\begin{aligned} (x_o, z_o) &= \left((k_s - 1)\,\frac{\delta_f}{L_p}, 0\right), \\ \left(x_p, z_p\right) &= (a_{6k_c-5}, a_{6k_c-4}) \end{aligned} \tag{A.5}$$

where $k_s = 1, 2, \ldots n_s$, n_s is the number of contact points, $k_c = k_i, k_i + k_p, k_i + 2k_p ... k_f$ is the vector containing the nodes of each contact point, $k_i = n/60 + 1$ and $k_f = \left(\delta_p n/L_p\right)(n_s - 1) + k_i$ are the nodes of the first and last contact points, respectively, and $k_p = \delta_p n/L_p + 1$ is the number of nodes between contact points.

Now we can define the force vector associated with these contact points, and appended to Eq. A.4 as:

$$\boldsymbol{a} = \begin{pmatrix} \vdots \\ a_{6n+6} \\ a_{6n+7} \\ a_{6n+8} \\ \vdots \\ a_{6n+6+2n_s-1} \\ a_{6n+6+2n_s} \end{pmatrix} = \begin{pmatrix} \vdots \\ q_{n+1} \\ h_{x_1} \\ h_{y_1} \\ \vdots \\ h_{x_{k_s}} \\ h_{y_{k_s}} \end{pmatrix} \tag{A.6}$$

A.2 Discretization by finite difference for static case - nodes with no influence of contact points

The vector k is redifined once the location of the contact points are known. k is now the relative complement of k_c in k: $k = k \setminus k_c$, representing those nodes with no influence of an external load.

Using the centered difference scheme given by Eq. A.7 and $2h = \Delta s$, the derivatives between each node can be estimated.

$$f'(x_o) = \frac{f(x_o + h) - f(x_o - h)}{2h} \tag{A.7}$$

The approximation error for Eq. A.1 is given by:

$$
\begin{aligned}
&\frac{x_{k+1}-x_k}{\Delta s} - \cos\left(\frac{\psi_{k+1}+\psi_k}{2}\right),\\
&\frac{z_{k+1}-z_k}{\Delta s} - \sin\left(\frac{\psi_{k+1}+\psi_k}{2}\right),\\
&\frac{\psi_{k+1}-\psi_k}{\Delta s} - \left(\frac{m_{k+1}+m_k}{2}\right),\\
&\frac{m_{k+1}-m_k}{\Delta s} - \left(\frac{q_{k+1}+q_k}{2}\right)\cos\left(\frac{\psi_{k+1}+\psi_k}{2}\right)\\
&\qquad\qquad + \left(\frac{p_{k+1}+p_k}{2}\right)\sin\left(\frac{\psi_{k+1}+\psi_k}{2}\right),\\
&\frac{p_{k+1}-p_k}{\Delta s},\\
&\frac{q_{k+1}-q_k}{\Delta s} + w,
\end{aligned}
\tag{A.8}
$$

where k and k_c (i.e., discretization of nodes affected by external forces), generate $6n$ equations for $6\,(n+1)$ unknowns. The necessary remaining equations are given by the boundary conditions:

$$
\begin{aligned}
m\,(0) &= a_3 = 0, \quad & m\,(1) &= a_{6n+3} = 0,\\
p\,(0) &= a_5 = 0, \quad & p\,(1) &= a_{6n+5} = 0,\\
q\,(0) &= a_6 = 0, \quad & q\,(1) &= a_{6n+6} = 0.
\end{aligned}
\tag{A.9}
$$

By knowing that:

$$
\begin{aligned}
x_k &= a_{6k-5}, \quad & x_{k+1} &= a_{6k+1},\\
z_k &= a_{6k-4}, \quad & z_{k+1} &= a_{6k+2},\\
m_k &= a_{6k-3}, \quad & m_{k+1} &= a_{6k+3},\\
\psi_k &= a_{6k-2}, \quad & \psi_{k+1} &= a_{6k+4},\\
p_k &= a_{6k-1}, \quad & p_{k+1} &= a_{6k+5},\\
q_k &= a_{6k}, \quad & q_{k+1} &= a_{6k+6},
\end{aligned}
\tag{A.10}
$$

and after enforcing boundary conditions with Eq. A.9, we rewrite Eq. A.8 and Eq. A.9 as an objective vector function, $\boldsymbol{f}\,(\boldsymbol{a})$, where:

$$
\begin{aligned}
f_1 &= a_3, \qquad f_2 = a_5, \qquad f_3 = a_6, \\
f_{6k-2} &= \frac{a_{6k+1} - a_{6k-5}}{\Delta s} - \cos\left(\frac{a_{6k+4} + a_{6k-2}}{2}\right), \\
f_{6k-1} &= \frac{a_{6k+2} - a_{6k-4}}{\Delta s} - \sin\left(\frac{a_{6k+4} + a_{6k-2}}{2}\right), \\
f_{6k} &= \frac{a_{6k+3} - a_{6k-3}}{\Delta s} \\
&\quad - \left(\frac{a_{6k+6} + a_{6k}}{2}\right)\cos\left(\frac{a_{6k+4} + a_{6k-2}}{2}\right) \\
&\quad + \left(\frac{a_{6k+5} + a_{6k-1}}{2}\right)\sin\left(\frac{a_{6k+4} + a_{6k-2}}{2}\right), \\
f_{6k+1} &= \frac{a_{6k+4} - a_{6k-2}}{\Delta s} - \left(\frac{a_{6k+3} + a_{6k-3}}{2}\right), \\
f_{6k+2} &= \frac{a_{6k+5} - a_{6k-1}}{\Delta s}, \\
f_{6k+3} &= \frac{a_{6k+6} - a_{6k}}{\Delta s} + w, \\
f_{6n+4} &= a_{6n+3}, \\
f_{6n+5} &= a_{6n+5}, \\
f_{6n+6} &= a_{6n+6}.
\end{aligned} \tag{A.11}
$$

To compute these error vector values, initial values $\boldsymbol{a}_o$ are necessary for all $n+1$ nodes along the length.

Because the error function, $\boldsymbol{f}(\boldsymbol{a})$, is a vector, the Jacobian matrix must be computed, with the non-zero elements being:

$$
\begin{aligned}
\frac{\partial f_1}{\partial a_3} = \frac{\partial f_2}{\partial a_5} = \frac{\partial f_3}{\partial a_6} \\
&= \frac{\partial f_{6n+4}}{\partial a_{6n+3}} = \frac{\partial f_{6n+5}}{\partial a_{6n+5}} = \frac{\partial f_{6n+6}}{\partial a_{6n+6}} = 1 \\
&= J_{1,3} = J_{2,5} = J_{3,6} \\
&= J_{6n+4,\,6n+3} = J_{6n+5,\,6n+5} = J_{6n+6,\,6n+6} \\
\frac{\partial f_{6k-2}}{\partial a_{6k-5}} = \frac{\partial f_{6k-1}}{\partial a_{6k-4}} = \frac{\partial f_{6k+1}}{\partial a_{6k-2}} \\
&= \frac{\partial f_{6k}}{\partial a_{6k-3}} = \frac{\partial f_{6k+2}}{\partial a_{6k-1}} = \frac{\partial f_{6k+3}}{\partial a_{6k}} = -\frac{1}{\Delta s} \\
&= J_{6k-2,\,6k-5} = J_{6k-1,\,6k-4} = J_{6k+1,\,6k-2} \\
&= J_{6k,\,6k-3} = J_{6k+2,\,6k-1} = J_{6k+3,\,6k} \\
\frac{\partial f_{6k-2}}{\partial a_{6k+1}} = \frac{\partial f_{6k-1}}{\partial a_{6k+2}} = \frac{\partial f_{6k+1}}{\partial a_{6k+4}} \\
&= \frac{\partial f_{6k}}{\partial a_{6k+3}} = \frac{\partial f_{6k+2}}{\partial a_{6k+5}} = \frac{\partial f_{6k+3}}{\partial a_{6k+6}} = \frac{1}{\Delta s} \\
&= J_{6k-2,\,6k+1} = J_{6k-1,\,6k+2} = J_{6k+1,\,6k+4} \\
&= J_{6k,\,6k+3} = J_{6k+2,\,6k+5} = J_{6k+3,\,6k+6} \\
\frac{\partial f_{6k+1}}{\partial a_{6k-3}} = \frac{\partial f_{6k+1}}{\partial a_{6k+3}} = -\frac{1}{2} \\
&= J_{6k+1,\,6k-3} = J_{6k+1,\,6k+3}
\end{aligned}
\tag{A.12a}
$$

$$
\begin{aligned}
\frac{\partial f_{6k-2}}{\partial a_{6k-2}} &= \frac{\partial f_{6k-2}}{\partial a_{6k+4}} = \frac{\partial f_{6k}}{\partial a_{6k-1}} = \frac{\partial f_{6k}}{\partial a_{6k+5}} \\
&= \frac{1}{2}\sin\left(\frac{a_{6k+4} + a_{6k-2}}{2}\right) = J_{6k-2,\,6k-2} \\
&= J_{6k-2,\,6k+4} = J_{6k,\,6k-1} = J_{6k,\,6k+5} \\
\frac{\partial f_{6k-1}}{\partial a_{6k-2}} &= \frac{\partial f_{6k-1}}{\partial a_{6k+4}} = \frac{\partial f_{6k}}{\partial a_{6k}} = \frac{\partial f_{6k}}{\partial a_{6k+6}} \\
&= -\frac{1}{2}\cos\left(\frac{a_{6k+4} + a_{6k-2}}{2}\right) = J_{6k-1,\,6k-2} \\
&= J_{6k-1,\,6k+4} = J_{6k,\,6k} = J_{6k,\,6k+6} \\
\frac{\partial f_{6k}}{\partial a_{6k-2}} &= \frac{\partial f_{6k}}{\partial a_{6k+4}} \\
&= \frac{1}{2}\left(\frac{a_{6k+6} + a_{6k}}{2}\right)\sin\left(\frac{a_{6k+4} + a_{6k-2}}{2}\right) \\
&+ \frac{1}{2}\left(\frac{a_{6k+5} + a_{6k-1}}{2}\right)\cos\left(\frac{a_{6k+4} + a_{6k-2}}{2}\right) \\
&= J_{6k,\,6k-2} = J_{6k,\,6k+4}.
\end{aligned}
\tag{A.12b}
$$

A.3 Discretization of nodes in contact with tension lines

We treat the external tension forces produced by the deformation of the tension lines as point forces affecting the nodes of contact between the plate and the lines. These forces crate a jump in shear and axial forces (i.e., q and p respectively). The discontinuity of a given function can be expressed as:

$$[f(\xi)] = f(\xi^{+}) - f(\xi^{-}) \tag{A.13}$$

where $f(\xi^{+})$ indicates the value of the function approching from the right, and $f(\xi^{-})$ the value approching from the left. Therefore, the discontinuities of internal forces on active nodes can be defined as:

$$
\begin{aligned}
[h_x] &= p(\xi^+) - p(\xi^-) \\
[h_z] &= q(\xi^+) - q(\xi^-)
\end{aligned}
\tag{A.14}
$$

Therefore, the approximation error for Eq. A.1 for nodes with influence of an external load is given by:

$$
\begin{aligned}
&\frac{x_{k_c+1} - x_{k_c}}{\Delta s} - \cos\left(\frac{\psi_{k_c+1} + \psi_{k_c}}{2}\right), \\
&\frac{z_{k_c+1} - z_{k_c}}{\Delta s} - \sin\left(\frac{\psi_{k_c+1} + \psi_{k_c}}{2}\right), \\
&\frac{\psi_{k_c+1} - \psi_{k_c}}{\Delta s} - \left(\frac{m_{k_c+1} + m_{k_c}}{2}\right), \\
&\frac{m_{k_c+1} - m_{k_c}}{\Delta s} - \left(\frac{q_{k_c+1} + q_{k_c} + t_{y_{k_s}}}{2}\right)\cos\left(\frac{\psi_{k_c+1} + \psi_{k_c}}{2}\right) \\
&\qquad + \left(\frac{p_{k_c+1} + p_{k_c} + t_{x_{k_s}}}{2}\right)\sin\left(\frac{\psi_{k_c+1} + \psi_{k_c}}{2}\right), \\
&\frac{p_{k_c+1} - p_{k_c} - t_{x_{k_s}}}{\Delta s}, \\
&\frac{q_{k_c+1} - q_{k_c} - t_{y_{k_s}}}{\Delta s} + w,
\end{aligned}
\tag{A.15}
$$

By knowing Eq. A.10 and:

$$
h_{x_{k_s}} = a_{6n+6+2k_s-1}, \quad h_{z_{k_s}} = a_{6n+6+2k_s},
\tag{A.16}
$$

we rewrite Eq. A.15 as the remaining objective vector function, $\boldsymbol{f}(\boldsymbol{a})$, where:

$$
\begin{aligned}
f_{6k_c-2} &= \frac{a_{6k_c+1} - a_{6k_c-5}}{\Delta s} - \cos\left(\frac{a_{6k_c+4} + a_{6k_c-2}}{2}\right), \\
f_{6k_c-1} &= \frac{a_{6k_c+2} - a_{6k_c-4}}{\Delta s} - \sin\left(\frac{a_{6k_c+4} + a_{6k_c-2}}{2}\right), \\
f_{6k_c} &= \frac{a_{6k_c+3} - a_{6k_c-3}}{\Delta s} \\
&\quad - \left(\frac{a_{6k_c+6} + a_{6k_c} + a_{6n+6+2k_s}}{2}\right)\cos\left(\frac{a_{6k_c+4} + a_{6k_c-2}}{2}\right) \\
&\quad + \left(\frac{a_{6k_c+5} + a_{6k_c-1} + a_{6n+6+2k_s-1}}{2}\right)\sin\left(\frac{a_{6k_c+4} + a_{6k_c-2}}{2}\right), \\
f_{6k_c+1} &= \frac{a_{6k_c+4} - a_{6k_c-2}}{\Delta s} - \left(\frac{a_{6k_c+3} + a_{6k_c-3}}{2}\right), \\
f_{6k_c+2} &= \frac{a_{6k_c+5} - a_{6k_c-1} - a_{6n+6+2k_s-1}}{\Delta s}, \\
f_{6k_c+3} &= \frac{a_{6k_c+6} - a_{6k_c} - a_{6n+6+2k_s}}{\Delta s} + w,
\end{aligned}
\tag{A.17}
$$

and the non-zero elements of its Jacobian matrix being:

$$
\begin{aligned}
\frac{\partial f_{6k_c-2}}{\partial a_{6k_c-5}} &= \frac{\partial f_{6k_c-1}}{\partial a_{6k_c-4}} = \frac{\partial f_{6k_c+1}}{\partial a_{6k_c-2}} \\
&= \frac{\partial f_{6k_c}}{\partial a_{6k_c-3}} = \frac{\partial f_{6k_c+2}}{\partial a_{6k_c-1}} = \frac{\partial f_{6k_c+3}}{\partial a_{6k_c}} \\
&= \frac{\partial f_{6k_c+2}}{\partial a_{6n+6+2k_s-1}} = \frac{\partial f_{6k_c+3}}{\partial a_{6n+6+2k_s}} = -\frac{1}{\Delta s} \\
&= J_{6k_c-2,\,6k_c-5} = J_{6k_c-1,\,6k_c-4} = J_{6k_c+1,\,6k_c-2} \\
&= J_{6k_c,\,6k_c-3} = J_{6k_c+2,\,6k_c-1} = J_{6k_c+3,\,6k_c} \\
&= J_{6k_c+2,\,6n+6+2k_s-1} = J_{6k_c+3,\,6n+6+2k_s} \\
\frac{\partial f_{6k_c-2}}{\partial a_{6k_c+1}} &= \frac{\partial f_{6k_c-1}}{\partial a_{6k_c+2}} = \frac{\partial f_{6k_c+1}}{\partial a_{6k_c+4}} \\
&= \frac{\partial f_{6k_c}}{\partial a_{6k_c+3}} = \frac{\partial f_{6k_c+2}}{\partial a_{6k_c+5}} = \frac{\partial f_{6k_c+3}}{\partial a_{6k_c+6}} = \frac{1}{\Delta s} \\
&= J_{6k_c-2,\,6k_c+1} = J_{6k_c-1,\,6k_c+2} = J_{6k_c+1,\,6k_c+4} \\
&= J_{6k_c,\,6k_c+3} = J_{6k_c+2,\,6k_c+5} = J_{6k_c+3,\,6k_c+6} \\
\frac{\partial f_{6k_c+1}}{\partial a_{6k_c-3}} &= \frac{\partial f_{6k_c+1}}{\partial a_{6k_c+3}} = -\frac{1}{2} \\
&= J_{6k_c+1,\,6k_c-3} = J_{6k_c+1,\,6k_c+3} \\
\frac{\partial f_{6k_c-2}}{\partial a_{6k_c-2}} &= \frac{\partial f_{6k_c-2}}{\partial a_{6k_c+4}} = \frac{\partial f_{6k_c}}{\partial a_{6k_c-1}} = \frac{\partial f_{6k_c}}{\partial a_{6k_c+5}} = \frac{\partial f_{6k_c}}{\partial a_{6n+6+2k_s-1}} \\
&= \frac{1}{2}\sin\left(\frac{a_{6k_c+4} + a_{6k_c-2}}{2}\right) = J_{6k_c-2,\,6k_c-2} \\
&= J_{6k_c-2,\,6k_c+4} = J_{6k_c,\,6k_c-1} = J_{6k_c,\,6k_c+5} \\
&= J_{6k_c,\,6n+6+2k_s-1}
\end{aligned}
\tag{A.18a}
$$

$$
\begin{aligned}
\frac{\partial f_{6k_c-1}}{\partial a_{6k_c-2}} &= \frac{\partial f_{6k_c-1}}{\partial a_{6k_c+4}} = \frac{\partial f_{6k_c}}{\partial a_{6k_c}} = \frac{\partial f_{6k_c}}{\partial a_{6k_c+6}} = \frac{\partial f_{6k_c}}{\partial a_{6n+6+2k_s}} \\
&= -\frac{1}{2}\cos\left(\frac{a_{6k_c+4} + a_{6k_c-2}}{2}\right) = J_{6k_c-1,\,6k_c-2} \\
&= J_{6k_c-1,\,6k_c+4} = J_{6k_c,\,6k_c} = J_{6k_c,\,6k_c+6} \\
&= J_{6k_c,\,6n+6+2k_s} \\
\frac{\partial f_{6k_c}}{\partial a_{6k_c-2}} &= \frac{\partial f_{6k_c}}{\partial a_{6k_c+4}} \\
&= \frac{1}{2}\left(\frac{a_{6k_c+6} + a_{6k_c} + a_{6n+6+2k_s}}{2}\right) \\
&\quad \sin\left(\frac{a_{6k_c+4} + a_{6k_c-2}}{2}\right) \\
&+ \frac{1}{2}\left(\frac{a_{6k_c+5} + a_{6k_c-1} + a_{6n+6+2k_s-1}}{2}\right) \\
&\quad \cos\left(\frac{a_{6k_c+4} + a_{6k_c-2}}{2}\right) \\
&= J_{6k_c,\,6k_c-2} = J_{6k_c,\,6k_c+4}.
\end{aligned}
\tag{A.18b}
$$

A.4 External forces: the remaining objective functions and Jacobian elements

The slack condition $e < 0$ is equally expressed as $l_e < L_s$, for which we define the following sets:

$$
k_{s_i} = \{k_s : l_e < L_s\}, \qquad k_{c_i} = \{k_c : l_e < L_s\}, \tag{A.19}
$$

which can be expanded to:

$$
\begin{aligned}
k_{s_i} &= \left\{k_s : \sqrt{\left(a_{6k_c-5} - (k_s - 1)\frac{\delta_f}{L_p}\right)^2 + \left(a_{6k_c-4}\right)^2} < L_s\right\}, \\
k_{c_i} &= \left\{k_c : \sqrt{\left(a_{6k_c-5} - (k_s - 1)\frac{\delta_f}{L_p}\right)^2 + \left(a_{6k_c-4}\right)^2} < L_s\right\},
\end{aligned}
\tag{A.20}
$$

and their relative complements expressed as:

$$k_{s_a} = k_s \setminus k_{s_i}, \qquad k_{c_a} = k_c \setminus k_{c_i}. \tag{A.21}$$

Now, the remaining set of objective functions are:

$$\begin{aligned}
f_{6n+6+2k_{s_i}-1} &= a_{6n+6+2k_{s_i}-1}, \\
f_{6n+6+2k_{s_i}} &= a_{6n+6+2k_{s_i}}, \\
f_{6n+6+2k_{s_a}-1} &= a_{6n+6+2k_{s_a}-1} + \left(E_s A_s L_p^2 / D\right) \\
&\quad \frac{\left(\sqrt{\left(a_{6k_{c_a}-5} - (k_{s_a}-1)\frac{\delta_f}{L_p}\right)^2 + \left(a_{6k_{c_a}-4}\right)^2} - L_s\right)}{L_s} \\
&\quad \frac{\left(a_{6k_{c_a}-5} - (k_{s_a}-1)\frac{\delta_f}{L_p}\right)}{\sqrt{\left(a_{6k_{c_a}-5} - (k_{s_a}-1)\frac{\delta_f}{L_p}\right)^2 + \left(a_{6k_{c_a}-4}\right)^2}},
\end{aligned} \tag{A.22a}$$

$$\begin{aligned}
f_{6n+6+2k_{s_a}} &= a_{6n+6+2k_{s_a}} + \left(E_s A_s L_p^2 / D\right) \\
&\quad \frac{\left(\sqrt{\left(a_{6k_{c_a}-5} - (k_{s_a}-1)\frac{\delta_f}{L_p}\right)^2 + \left(a_{6k_{c_a}-4}\right)^2} - L_s\right)}{L_s} \\
&\quad \frac{\left(a_{6k_{c_a}-4}\right)}{\sqrt{\left(a_{6k_{c_a}-5} - (k_{s_a}-1)\frac{\delta_f}{L_p}\right)^2 + \left(a_{6k_{c_a}-4}\right)^2}}.
\end{aligned} \tag{A.22b}$$

The non-zero elements of the Jacobian corresponding to Eq. A.22 are:

$$\begin{aligned}
&\frac{\partial f_{6n+6+2k_s-1}}{\partial a_{6n+6+2k_s-1}} = \frac{\partial f_{6n+6+2k_s}}{\partial a_{6n+6+2k_s}} = 1 \\
&\quad = J_{6n+6+2k_s-1,\, 6n+6+2k_s-1} = J_{6n+6+2k_s,\, 6n+6+2k_s}.
\end{aligned} \tag{A.23a}$$

$$
\begin{aligned}
&\frac{\partial f_{6n+6+2k_{s_a}-1}}{\partial a_{6k_{c_a}-5}} = \left(E_s A_s L_p^2 / D\right) \Bigg\{ \\
&\left[-\left(a_{6k_{c_a}-5} - (k_{s_a}-1)\frac{\delta_f}{L_p}\right)^2 \right. \\
&\left(\sqrt{\left(a_{6k_{c_a}-5} - (k_{s_a}-1)\frac{\delta_f}{L_p}\right)^2 + \left(a_{6k_{c_a}-4}\right)^2} - L_s \right) / \\
&\left. L_s \left(\left(a_{6k_{c_a}-5} - (k_{s_a}-1)\frac{\delta_f}{L_p}\right)^2 + \left(a_{6k_{c_a}-4}\right)^2\right)^{3/2} \right] + \\
&\left[\left(a_{6k_{c_a}-5} - (k_{s_a}-1)\frac{\delta_f}{L_p}\right)^2 / \right. \\
&\left. L_s \left(\left(a_{6k_{c_a}-5} - (k_{s_a}-1)\frac{\delta_f}{L_p}\right)^2 + \left(a_{6k_{c_a}-4}\right)^2\right) \right] + \\
&\left[\left(\sqrt{\left(a_{6k_{c_a}-5} - (k_{s_a}-1)\frac{\delta_f}{L_p}\right)^2 + \left(a_{6k_{c_a}-4}\right)^2} - L_s \right) / \right. \\
&\left. L_s \sqrt{\left(a_{6k_{c_a}-5} - (k_{s_a}-1)\frac{\delta_f}{L_p}\right)^2 + \left(a_{6k_{c_a}-4}\right)^2} \right] \Bigg\} \\
&\quad = J_{6n+6+2k_{s_a}-1,\,6k_{c_a}-5}
\end{aligned}
\tag{A.23b}
$$

$$
\begin{aligned}
&\frac{\partial f_{6n+6+2k_{s_a}-1}}{\partial a_{6k_{c_a}-4}} = \frac{\partial f_{6n+6+2k_{s_a}}}{\partial a_{6k_{c_a}-5}} = \left(E_s A_s L_p^2 / D\right) \Bigg\{ \\
&\left[-\left(a_{6k_{c_a}-5} - (k_{s_a}-1)\frac{\delta_f}{L_p}\right)\left(a_{6k_{c_a}-4}\right) \right. \\
&\left(\sqrt{\left(a_{6k_{c_a}-5} - (k_{s_a}-1)\frac{\delta_f}{L_p}\right)^2 + \left(a_{6k_{c_a}-4}\right)^2} - L_s \right) / \\
&\left. L_s \left(\left(a_{6k_{c_a}-5} - (k_{s_a}-1)\frac{\delta_f}{L_p}\right)^2 + \left(a_{6k_{c_a}-4}\right)^2\right)^{3/2} \right] + \\
&\left[\left(a_{6k_{c_a}-5} - (k_{s_a}-1)\frac{\delta_f}{L_p}\right)\left(a_{6k_{c_a}-4}\right) / \right. \\
&\left. L_s \left(\left(a_{6k_{c_a}-5} - (k_{s_a}-1)\frac{\delta_f}{L_p}\right)^2 + \left(a_{6k_{c_a}-4}\right)^2\right) \right] \Bigg\} \\
&\quad = J_{6n+6+2k_{s_a}-1,\,6k_{c_a}-5} = J_{6n+6+2k_{s_a},\,6k_{c_a}-5}
\end{aligned}
\tag{A.23c}
$$

$$
\begin{aligned}
&\frac{\partial f_{6n+6+2k_{s_a}}}{\partial a_{6k_{c_a}-4}} = \left(E_s A_s L_p^2/D\right)\Bigg\{ \\
&\Bigg[-\left(a_{6k_{c_a}-4}\right)^2 \\
&\left(\sqrt{\left(a_{6k_{c_a}-5}-(k_{s_a}-1)\frac{\delta_f}{L_p}\right)^2+\left(a_{6k_{c_a}-4}\right)^2}-L_s\right)/ \\
&L_s\left(\left(a_{6k_{c_a}-5}-(k_{s_a}-1)\frac{\delta_f}{L_p}\right)^2+\left(a_{6k_{c_a}-4}\right)^2\right)^{3/2}\Bigg]+ \\
&\Bigg[\left(a_{6k_{c_a}-4}\right)^2/ \\
&L_s\left(\left(a_{6k_{c_a}-5}-(k_{s_a}-1)\frac{\delta_f}{L_p}\right)^2+\left(a_{6k_{c_a}-4}\right)^2\right)\Bigg]+ \\
&\Bigg[\left(\sqrt{\left(a_{6k_{c_a}-5}-(k_{s_a}-1)\frac{\delta_f}{L_p}\right)^2+\left(a_{6k_{c_a}-4}\right)^2}-L_s\right)/ \\
&L_s\sqrt{\left(a_{6k_{c_a}-5}-(k_{s_a}-1)\frac{\delta_f}{L_p}\right)^2+\left(a_{6k_{c_a}-4}\right)^2}\Bigg]\Bigg\} \\
&\quad = J_{6n+6+2k_{s_a},\,6k_{c_a}-4}
\end{aligned}
\tag{A.23d}
$$

APPENDIX B

GRID CONVERGENCE BASED ON COMPARISON TO THE THEORETICAL SOLUTION OF THE DOUBLE-PINNED ELASTICA SUBJECT TO COMPRESSIVE LOAD

We use the closed form equilibrium solutions of the double-pinned elastica subject to end thrust to determine the validity of the optimization methods applied to our nonlinear problem. This problem is a simple example of elastic bifurcation and instability Bigoni (2012), and provides a closed form solution for all possible equilibrium configurations. As an axial external force is applied to one end, that end moves creating an elastic buckling instability. Further details can be found in Love (1927); Reiss (1969); Bigoni (2012).

The differential equation of the elastica is:

$$\frac{\partial^2 \psi}{\partial s^2} + \frac{F}{EI} \sin\psi = 0, \tag{B.1}$$

where ψ is the angle of inclination of the tangent to the elastica. By defining $\lambda^2 = F/EI$, $\alpha = \psi(0)$, and $k_m = \sin\frac{\alpha}{2}$, the equations describing the deformation of the elastica are:

$$\begin{aligned} x &= -s + \frac{2}{\lambda}\{\mathrm{E}\left[\mathrm{am}\left(s\lambda + K\left(k_m\right), k_m\right), k_m\right] \\ &\quad - \mathrm{E}\left[\mathrm{am}\left(K\left(k_m\right), k_m\right), k_m\right]\} \\ z &= -\frac{2k_m}{\lambda}\mathrm{cn}\left(s\lambda + K\left(k_m\right), k_m\right) \end{aligned} \tag{B.2}$$

where s is the curvilinear coordinate, $l\lambda = 2mK\left(k_m\right)$, m is the bifurcation mode, am is the Jacobi amplitude function, cn is the Jacobi cosine amplitude, $K(k_m)$ is the complete elliptic integral of the first kind defined as:

$$K\left(k_m\right) = \int_0^{\frac{\pi}{2}} \frac{d\phi}{\sqrt{1 - k_m^2 \sin^2\phi}}, \tag{B.3}$$

and $\mathrm{E}\left(x, k_m\right)$ is the incomplete elliptic integral of the second kind of modulus k_m, defined as:

$$\mathrm{E}\left(x, k_m\right) = \int_0^{x} \sqrt{1 - k_m \sin^2 t dt}. \tag{B.4}$$

Additionally, the applied force is:

$$F = \frac{EI}{l^2} 4m^2 \left[K\left(k_m\right)\right]^2. \tag{B.5}$$

Solutions to the displacement equations (Eq. B.2) are accompanied by solutions to shear forces, moments, and angles of inclination.

The error of the numerical solution is :

$$f_{exact} - f\left(h\right), \tag{B.6}$$

where f_{exact} is the exact solution presented above, $f\left(h\right)$ is the numerical solution, and $h = 1/\left(2n\right)$.

Both trust region and Levenberg-Marquardt algorithms show second order convergence rates (Fig. B.1). The methods were implemented for different grid spacings (n equal to 200, 400, 600, ,1000, 1500, 2500, and 4000), a single end-support displacement (0.05 l), and the first two deformation modes. We provided a deformed theoretical solution as an initial solution (e.g., 0.02 l displacement). For both methods, how close the initial solution is to the theoretical one,

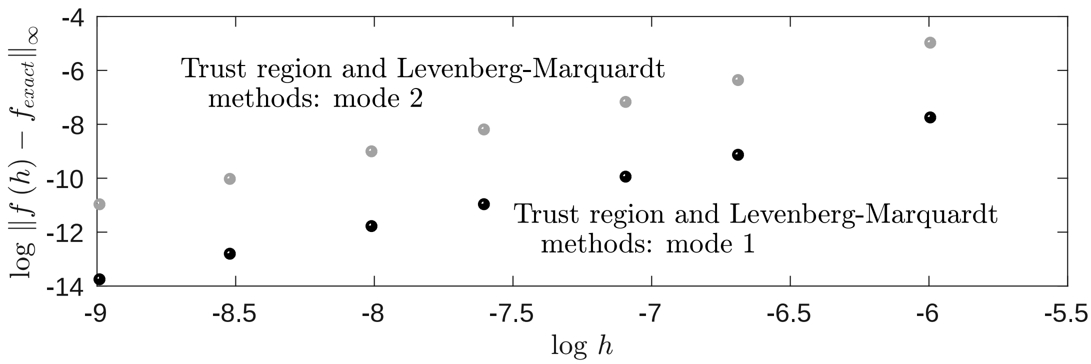

Figure B.1: Grid convergence study of Newton's and interior point methods for various end-support displacements and deflection modes ($\| \|_\infty$ represents the infinity norm).

will determine the number of iterations required to satisfy to the convergence criteria.

We chose 601 nodes as the grid resolution for the periodically-constrained elastica. This resolution presents a convergence error of $\|f(h) - f_{exact}\|_\infty = 4.6 \times 10^{-5}$ and allows a proper discretization of the constraints.

APPENDIX C

ELASTIC MODULUS FOR POLYCARBONATE AND MICROFILAMENT BRAIDED LINE

Fig. C.1 reports the tensile modulus for the polycarbonate plate and Spectra® fiber (polyethylene) used for the experimental model presented in Fig. 2.1. The experimental procedure for polycarbonate and fibers followed AST (2012) and AST (2015) respectively. Modulus for the plate and the fiber are $E = 1.97 \pm 0.04\, GPa$ and $E_s = 88.9 \pm\ 2.43 GPa$, respectively.

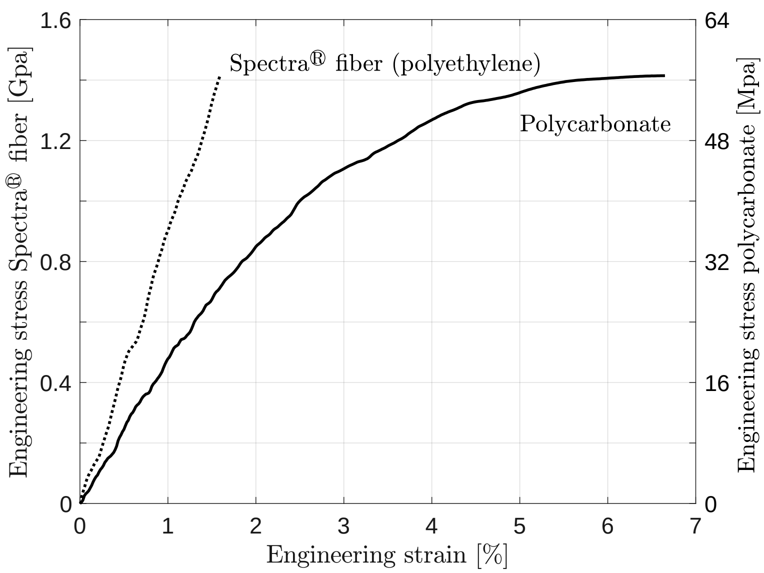

Figure C.1: Polycarbonate and Spectra® fiber tensile modulus

APPENDIX D

MAXIMUM ABSOLUTE AND RELATIVE RANDOM ERROR FOR PIV DERIVED QUANTITIES

Table D.1: Maximum absolute random uncertainty bounds.

Test		$\overline{u}$	$\overline{w}$	$\overline{u'}$	$\overline{w}$	$\overline{u'w'}*$
01	$\lvert\Delta\varepsilon^{+}\rvert$ [m/s]	0.0012	0.0008	0.0009	0.0005	0.0001
	X/L_p	0.1235	0.2851	0.1042	0.2389	0.6739
	Y/L_p	0.2228	0.2190	0.2267	0.2305	0.2959
	$\lvert\Delta\varepsilon^{-}\rvert$ [m/s]	0.0012	0.0009	0.0008	0.0005	0.0001
	X/L_p	0.1081	0.2351	0.1042	0.2081	0.2158
	Y/L_p	0.2267	0.2190	0.2267	0.2190	0.2190
02	$\lvert\Delta\varepsilon^{+}\rvert$ [m/s]	0.0016	0.0008	0.0009	0.0006	0.0001
	X/L_p	0.6931	0.1658	0.1620	0.1774	0.1889
	Y/L_p	0.2767	0.2690	0.2729	0.2613	0.2652
	$\lvert\Delta\varepsilon^{-}\rvert$ [m/s]	0.0016	0.0008	0.0009	0.0006	0.0001
	X/L_p	0.7393	0.1812	0.1235	0.1658	0.1927
	Y/L_p	0.2882	0.2652	0.2690	0.2613	0.2690
03	$\lvert\Delta\varepsilon^{+}\rvert$ [m/s]	0.0017	0.0010	0.0011	0.0007	0.0001
	X/L_p	0.1119	0.6046	0.1081	0.2158	0.2967
	Y/L_p	0.2228	0.3036	0.2228	0.2074	0.2074
	$\lvert\Delta\varepsilon^{-}\rvert$ [m/s]	0.0016	0.0010	0.0010	0.0007	0.0001
	X/L_p	0.1119	0.6085	0.1081	0.1927	0.2428
	Y/L_p	0.2228	0.3036	0.2228	0.2190	0.2074
	$\lvert\Delta\varepsilon^{+}\rvert$ [m/s]	0.0019	0.0011	0.0012	0.0008	0.0001
	X/L_p	0.1235	0.2120	0.1081	0.1812	0.2081
	Y/L_p	0.2729	0.2767	0.2690	0.2729	0.2767
	$\lvert\Delta\varepsilon^{-}\rvert$ [m/s]	0.0018	0.0011	0.0012	0.0007	0.0001
	X/L_p	0.1273	0.1927	0.1081	0.1735	0.1927
	Y/L_p	0.2729	0.2690	0.2690	0.2690	0.2690
05	$\lvert\Delta\varepsilon^{+}\rvert$ [m/s]	0.0021	0.0012	0.0014	0.0009	0.0001
	X/L_p	0.1273	0.1735	0.1158	0.2235	0.2351
	Y/L_p	0.2151	0.2074	0.2190	0.2190	0.2074

Table D.1 – continued from previous page

Test		$\overline{u}$	$\overline{w}$	$\overline{u'}$	$\overline{w}$	$\overline{u'w'}*$
	$\lvert\Delta\varepsilon^{-}\rvert$ [m/s]	0.0020	0.0012	0.0014	0.0008	0.0001
	X/L_p	0.1119	0.6008	0.1158	0.1774	0.3737
	Y/L_p	0.2190	0.3075	0.2190	0.2151	0.2074
06	$\lvert\Delta\varepsilon^{+}\rvert$ [m/s]	0.0023	0.0013	0.0014	0.0009	0.0001
	X/L_p	0.1042	0.2274	0.1081	0.1504	0.2928
	Y/L_p	0.2729	0.2767	0.2729	0.2767	0.2729
	$\lvert\Delta\varepsilon^{-}\rvert$ [m/s]	0.0023	0.0012	0.0014	0.0008	0.0001
	X/L_p	0.1042	0.1850	0.1196	0.1774	0.1504
	Y/L_p	0.2729	0.2806	0.2767	0.2767	0.2767
07	$\lvert\Delta\varepsilon^{+}\rvert$ [m/s]	0.0024	0.0014	0.0014	0.0010	0.0001
	X/L_p	0.1235	0.3660	0.1196	0.2043	0.3660
	Y/L_p	0.2113	0.2074	0.2113	0.2036	0.2151
	$\lvert\Delta\varepsilon^{-}\rvert$ [m/s]	0.0025	0.0014	0.0013	0.0010	0.0001
	X/L_p	0.1235	0.4083	0.1273	0.2389	0.4121
	Y/L_p	0.2113	0.2113	0.2113	0.2036	0.1959
08	$\lvert\Delta\varepsilon^{+}\rvert$ [m/s]	0.0029	0.0015	0.0019	0.0011	0.0001
	X/L_p	0.1158	0.2967	0.1235	0.1658	0.2120
	Y/L_p	0.2806	0.2806	0.2806	0.2844	0.2806
	$\lvert\Delta\varepsilon^{-}\rvert$ [m/s]	0.0028	0.0016	0.0018	0.0010	0.0001
	X/L_p	0.1119	0.2428	0.1081	0.1812	0.2351
	Y/L_p	0.2806	0.2767	0.2806	0.2806	0.2882
09	$\lvert\Delta\varepsilon^{+}\rvert$ [m/s]	0.0028	0.0017	0.0017	0.0012	0.0001
	X/L_p	0.1235	0.3852	0.1312	0.3236	0.3621
	Y/L_p	0.2074	0.2190	0.2074	0.2113	0.1997
	$\lvert\Delta\varepsilon^{-}\rvert$ [m/s]	0.0031	0.0017	0.0017	0.0011	0.0001
	X/L_p	0.1081	0.3467	0.1273	0.2851	0.3121
	Y/L_p	0.2113	0.2113	0.2074	0.2151	0.2036
10a	$\lvert\Delta\varepsilon^{+}\rvert$ [m/s]	0.0153	0.0104	0.0113	0.0087	0.0008
	X/L_p	0.1434	0.2050	0.1434	0.2319	0.1588
	Y/L_p	0.2918	0.3265	0.3072	0.2918	0.2918
	$\lvert\Delta\varepsilon^{-}\rvert$ [m/s]	0.0173	0.0097	0.0089	0.0073	0.0008
	X/L_p	0.1511	0.2011	0.1588	0.2358	0.2281

Table D.1 – continued from previous page

Test		$\overline{u}$	$\overline{w}$	$\overline{u'}$	$\overline{w}$	$\overline{u'w'}*$
	Y/L_p	0.3034	0.3265	0.2918	0.2918	0.3188
10b	$\lvert\Delta\varepsilon^{+}\rvert$ [m/s]	0.0190	0.0096	0.0131	0.0073	0.0005
	X/L_p	0.1126	0.1703	1.0672	0.6746	0.4783
	Y/L_p	0.1918	0.1841	0.2456	0.3842	0.3534
	$\lvert\Delta\varepsilon^{-}\rvert$ [m/s]	0.0208	0.0097	0.0144	0.0062	0.0006
	X/L_p	0.1126	0.1703	1.0672	0.6784	0.4513
	Y/L_p	0.1918	0.1841	0.2456	0.3804	0.3534
10c	$\lvert\Delta\varepsilon^{+}\rvert$ [m/s]	0.0453	0.0321	0.0312	0.0316	0.0040
	X/L_p	0.1241	0.1626	0.1357	0.1626	0.1549
	Y/L_p	0.1802	0.1841	0.1764	0.1841	0.1841
	$\lvert\Delta\varepsilon^{-}\rvert$ [m/s]	0.0395	0.0288	0.0263	0.0210	0.0034
	X/L_p	0.1357	0.1472	0.1318	0.1626	0.1626
	Y/L_p	0.1764	0.1802	0.1764	0.1841	0.1879
10d	$\lvert\Delta\varepsilon^{+}\rvert$ [m/s]	0.0148	0.0107	0.0106	0.0086	0.0007
	X/L_p	0.7439	1.1788	0.7477	0.2204	0.1703
	Y/L_p	0.2071	0.2533	0.2071	0.1879	0.2110
	$\lvert\Delta\varepsilon^{-}\rvert$ [m/s]	0.0126	0.0125	0.0115	0.0070	0.0005
	X/L_p	0.7862	1.1788	0.7477	0.2204	1.1596
	Y/L_p	0.1994	0.2225	0.2071	0.1879	0.2418
10e	$\lvert\Delta\varepsilon^{+}\rvert$ [m/s]	0.0516	0.0556	0.0449	0.0536	0.0070
	X/L_p	0.2589	0.2897	0.2974	0.2781	0.2935
	Y/L_p	0.1456	0.2418	0.1609	0.1918	0.1379
	$\lvert\Delta\varepsilon^{-}\rvert$ [m/s]	0.0500	0.0619	0.0281	0.0329	0.0069
	X/L_p	0.2935	0.3089	0.1126	0.3012	0.2165
	Y/L_p	0.1533	0.1687	0.2033	0.1494	0.1956
10f	$\lvert\Delta\varepsilon^{+}\rvert$ [m/s]	0.0199	0.0112	0.0105	0.0097	0.0006
	X/L_p	0.1049	0.1395	0.6130	0.1395	0.1395
	Y/L_p	0.3034	0.3034	0.2918	0.3034	0.3034
	$\lvert\Delta\varepsilon^{-}\rvert$ [m/s]	0.0230	0.0121	0.0090	0.0079	0.0008
	X/L_p	0.1049	0.1395	1.0711	0.1395	0.1395
	Y/L_p	0.3034	0.3034	0.2495	0.3034	0.3034
10g	$\lvert\Delta\varepsilon^{+}\rvert$ [m/s]	0.0174	0.0125	0.0162	0.0096	0.0006

Table D.1 – continued from previous page

Test		$\overline{u}$	$\overline{w}$	$\overline{u'}$	$\overline{w}$	$\overline{u'w'}*$
	X/L_p	0.6861	0.6400	0.6130	0.6091	0.7015
	Y/L_p	0.2957	0.1148	0.2687	0.1263	0.1263
	$\|\Delta\varepsilon^-\|$ [m/s]	0.0146	0.0123	0.0148	0.0071	0.0006
	X/L_p	0.7323	0.6707	0.7362	0.6861	0.6515
	Y/L_p	0.3034	0.1148	0.3034	0.0994	0.1533
10h	$\|\Delta\varepsilon^+\|$ [m/s]	0.0134	0.0116	0.0112	0.0098	0.0006
	X/L_p	0.7477	0.2204	0.6553	0.1742	0.1934
	Y/L_p	0.2841	0.2957	0.2456	0.3034	0.3072
	$\|\Delta\varepsilon^-\|$ [m/s]	0.0128	0.0109	0.0105	0.0077	0.0007
	X/L_p	0.6553	0.2127	0.6553	0.1742	0.1819
	Y/L_p	0.2456	0.2918	0.2456	0.3034	0.3034
11a	$\|\Delta\varepsilon^+\|$ [m/s]	0.0133	0.0104	0.0117	0.0086	0.0006
	X/L_p	0.2473	0.2589	0.2473	0.3551	0.2473
	Y/L_p	0.3226	0.2957	0.3226	0.3342	0.3226
	$\|\Delta\varepsilon^-\|$ [m/s]	0.0147	0.0108	0.0098	0.0066	0.0008
	X/L_p	0.2473	0.3859	0.2473	0.7670	0.2473
	Y/L_p	0.3226	0.3226	0.3226	0.1263	0.3226
11b	$\|\Delta\varepsilon^+\|$ [m/s]	0.0123	0.0088	0.0150	0.0093	0.0005
	X/L_p	0.6784	0.6707	0.6130	0.6130	0.6823
	Y/L_p	0.1879	0.3650	0.2033	0.1994	0.3496
	$\|\Delta\varepsilon^-\|$ [m/s]	0.0143	0.0089	0.0097	0.0059	0.0006
	X/L_p	1.0595	1.0403	1.0595	0.6784	0.6669
	Y/L_p	0.2379	0.1571	0.2379	0.3573	0.3688
11c	$\|\Delta\varepsilon^+\|$ [m/s]	0.0670	0.0751	0.0775	0.0620	0.0127
	X/L_p	0.1626	0.1434	0.1472	0.1472	0.1472
	Y/L_p	0.1725	0.1687	0.1687	0.1687	0.1725
	$\|\Delta\varepsilon^-\|$ [m/s]	0.0820	0.0653	0.0698	0.0441	0.0056
	X/L_p	0.1434	0.1472	0.1395	0.1472	0.1472
	Y/L_p	0.1687	0.1725	0.1687	0.1687	0.1687
11d	$\|\Delta\varepsilon^+\|$ [m/s]	0.0496	0.0364	0.0570	0.0332	0.0040
	X/L_p	0.1703	0.1780	0.1703	0.1780	0.1665
	Y/L_p	0.1609	0.1687	0.1609	0.1687	0.1609

Table D.1 – continued from previous page

Test		$\overline{u}$	$\overline{w}$	$\overline{u'}$	$\overline{w}$	$\overline{u'w'}*$
	$\lvert\Delta\varepsilon^{-}\rvert$ [m/s]	0.0488	0.0376	0.0284	0.0224	0.0053
	X/L_p	0.1703	0.1742	0.1703	0.1665	0.1703
	Y/L_p	0.1609	0.1609	0.1609	0.1609	0.1609
11e	$\lvert\Delta\varepsilon^{+}\rvert$ [m/s]	0.0205	0.0141	0.0145	0.0105	0.0013
	X/L_p	0.1164	0.1241	0.1203	0.1241	0.1203
	Y/L_p	0.2033	0.2033	0.2033	0.2033	0.2033
	$\lvert\Delta\varepsilon^{-}\rvert$ [m/s]	0.0214	0.0133	0.0120	0.0085	0.0015
	X/L_p	0.1087	0.1280	0.1203	0.1164	0.1241
	Y/L_p	0.2033	0.2033	0.2033	0.2033	0.2033
11f	$\lvert\Delta\varepsilon^{+}\rvert$ [m/s]	0.0546	0.0419	0.0447	0.0420	0.0036
	X/L_p	0.1164	0.1434	0.1203	0.1318	0.1395
	Y/L_p	0.3111	0.3034	0.3111	0.3072	0.3034
	$\lvert\Delta\varepsilon^{-}\rvert$ [m/s]	0.0537	0.0441	0.0307	0.0256	0.0047
	X/L_p	0.1164	0.1357	0.1588	0.1434	0.1434
	Y/L_p	0.3111	0.3034	0.2918	0.3034	0.3072
11g	$\lvert\Delta\varepsilon^{+}\rvert$ [m/s]	0.0405	0.0351	0.0398	0.0318	0.0056
	X/L_p	0.1703	0.1665	0.1703	0.1703	0.1703
	Y/L_p	0.3149	0.3188	0.3149	0.3149	0.3149
	$\lvert\Delta\varepsilon^{-}\rvert$ [m/s]	0.0348	0.0408	0.0225	0.0249	0.0040
	X/L_p	0.1280	0.1703	0.1703	0.1703	0.1819
	Y/L_p	0.3149	0.3149	0.3149	0.3149	0.3072
11h	$\lvert\Delta\varepsilon^{+}\rvert$ [m/s]	0.0488	0.0295	0.0309	0.0310	0.0038
	X/L_p	0.1280	0.1395	0.1318	0.1357	0.1280
	Y/L_p	0.3188	0.3188	0.3226	0.3226	0.3226
	$\lvert\Delta\varepsilon^{-}\rvert$ [m/s]	0.0455	0.0315	0.0292	0.0203	0.0047
	X/L_p	0.1357	0.1395	0.1280	0.1357	0.1357
	Y/L_p	0.3226	0.3188	0.3188	0.3226	0.3188
12a	$\lvert\Delta\varepsilon^{+}\rvert$ [m/s]	0.0475	0.0341	0.0414	0.0317	0.0074
	X/L_p	0.0933	0.1703	0.1703	0.1742	0.1665
	Y/L_p	0.2995	0.3149	0.3149	0.3188	0.3188
	$\lvert\Delta\varepsilon^{-}\rvert$ [m/s]	0.0480	0.0341	0.0348	0.0195	0.0037
	X/L_p	0.1703	0.1665	0.0972	0.1742	0.1703

Table D.1 – continued from previous page

Test		$\overline{u}$	$\overline{w}$	$\overline{u'}$	$\overline{w}$	$\overline{u'w'}*$
	Y/L_p	0.3149	0.3188	0.3034	0.3188	0.3149
12b	$\lvert\Delta\varepsilon^{+}\rvert$ [m/s]	0.0234	0.0113	0.0218	0.0101	0.0007
	X/L_p	0.6400	0.3782	0.6130	0.3744	0.3474
	Y/L_p	0.1956	0.3380	0.2033	0.3342	0.3226
	$\lvert\Delta\varepsilon^{-}\rvert$ [m/s]	0.0180	0.0117	0.0215	0.0074	0.0009
	X/L_p	0.6400	1.2135	0.6400	0.3898	0.3859
	Y/L_p	0.1956	0.2841	0.1956	0.3457	0.3457
12c	$\lvert\Delta\varepsilon^{+}\rvert$ [m/s]	0.0204	0.0102	0.0270	0.0081	0.0024
	X/L_p	0.6938	0.1126	0.1126	0.1126	0.1126
	Y/L_p	0.1918	0.1918	0.1918	0.1918	0.1918
	$\lvert\Delta\varepsilon^{-}\rvert$ [m/s]	0.0259	0.0102	0.0233	0.0080	0.0020
	X/L_p	0.1126	0.1126	0.1126	0.1126	0.1126
	Y/L_p	0.1918	0.1918	0.1918	0.1918	0.1918
12d	$\lvert\Delta\varepsilon^{+}\rvert$ [m/s]	0.0638	0.0463	0.0429	0.0495	0.0118
	X/L_p	0.1472	0.1395	0.1126	0.1434	0.1434
	Y/L_p	0.1994	0.1879	0.1956	0.1879	0.1879
	$\lvert\Delta\varepsilon^{-}\rvert$ [m/s]	0.0654	0.0395	0.0457	0.0314	0.0099
	X/L_p	0.1126	0.1434	0.1126	0.1395	0.1395
	Y/L_p	0.1956	0.1879	0.1956	0.1879	0.1879
12e	$\lvert\Delta\varepsilon^{+}\rvert$ [m/s]	0.0631	0.0348	0.0435	0.0334	0.0058
	X/L_p	0.1703	0.1703	1.0018	0.2127	0.1703
	Y/L_p	0.1956	0.1918	0.2187	0.1918	0.1879
	$\lvert\Delta\varepsilon^{-}\rvert$ [m/s]	0.0646	0.0361	0.0440	0.0234	0.0059
	X/L_p	0.9941	0.1703	0.9941	0.1857	0.2127
	Y/L_p	0.2187	0.1879	0.2187	0.1879	0.1918
12f	$\lvert\Delta\varepsilon^{+}\rvert$ [m/s]	0.0694	0.0196	0.0332	0.0185	0.0018
	X/L_p	0.6900	0.5668	0.6823	0.4590	0.1241
	Y/L_p	0.3072	0.2418	0.3072	0.1494	0.3149
	$\lvert\Delta\varepsilon^{-}\rvert$ [m/s]	0.0566	0.0197	0.0474	0.0126	0.0038
	X/L_p	0.6823	0.5553	0.6823	0.4552	0.1241
	Y/L_p	0.3072	0.2302	0.3072	0.1379	0.3149
12g	$\lvert\Delta\varepsilon^{+}\rvert$ [m/s]	0.1083	0.0627	0.0858	0.0853	0.0131

Table D.1 – continued from previous page

Test		$\overline{u}$	$\overline{w}$	$\overline{u'}$	$\overline{w}$	$\overline{u'w'}*$
	X/L_p	0.1472	0.1472	0.1472	0.1472	0.1472
	Y/L_p	0.3149	0.3149	0.3226	0.3149	0.3149
	$\lvert\Delta\varepsilon^-\rvert$ [m/s]	0.1152	0.1269	0.0946	0.0823	0.0345
	X/L_p	0.1472	0.1472	0.1511	0.1472	0.1472
	Y/L_p	0.3188	0.3149	0.3188	0.3149	0.3149
12h	$\lvert\Delta\varepsilon^+\rvert$ [m/s]	0.1160	0.0617	0.1193	0.0681	0.0096
	X/L_p	0.1241	0.1241	0.1280	0.1164	0.1203
	Y/L_p	0.3188	0.3188	0.3188	0.3188	0.3188
	$\lvert\Delta\varepsilon^-\rvert$ [m/s]	0.1331	0.0842	0.1122	0.0576	0.0149
	X/L_p	0.1241	0.1164	0.1357	0.1164	0.1357
	Y/L_p	0.3188	0.3188	0.3188	0.3188	0.3149

* Units of $\overline{u'v'}$ are $[m/s]^2$.

Table D.2: Maximum relative random uncertainty bounds. 10^{th} percentile value.

Test		$\overline{u}$	$\overline{w}$	$\overline{u'}$	$\overline{w}$	$\overline{u'w'}$
01	$\lvert\Delta\varepsilon_r^+\rvert$	0.0004	0.0068	0.0190	0.0210	0.0647
	X/L_p	0.2543	0.0657	0.8432	0.7778	1.0357
	Y/L_p	0.3537	0.3075	0.3113	0.2767	0.2998
	$\lvert\Delta\varepsilon_r^-\rvert$	0.0004	0.0069	0.0183	0.0199	0.0652
	X/L_p	0.3775	0.2235	0.4160	0.4160	0.9395
	Y/L_p	0.4653	0.4769	0.2074	0.2228	0.2690
02	$\lvert\Delta\varepsilon_r^+\rvert$	0.0004	0.0122	0.0191	0.0206	0.0659
	X/L_p	0.8663	1.2012	0.5738	1.1666	0.8163
	Y/L_p	0.4268	0.4307	0.2575	0.5000	0.2382
	$\lvert\Delta\varepsilon_r^-\rvert$	0.0004	0.0121	0.0182	0.0194	0.0668
	X/L_p	0.8317	1.0049	0.9241	0.6046	0.4352
	Y/L_p	0.4538	0.3999	0.0150	0.4114	0.5038
03	$\lvert\Delta\varepsilon_r^+\rvert$	0.0004	0.0059	0.0200	0.0211	0.0649
	X/L_p	0.2197	0.1273	1.0434	0.4699	1.0742
	Y/L_p	0.4461	0.1497	0.2767	0.2190	0.2305

Table D.2 – continued from previous page

Test		$\overline{u}$	$\overline{w}$	$\overline{u'}$	$\overline{w}$	$\overline{u'w'}$
	$\lvert\Delta\varepsilon_r^-\rvert$	0.0004	0.0059	0.0191	0.0201	0.0656
	X/L_p	0.8663	0.3005	1.1281	0.4660	1.1242
	Y/L_p	0.5115	0.4653	0.2459	0.2421	0.3229
	$\lvert\Delta\varepsilon_r^+\rvert$	0.0005	0.0154	0.0195	0.0209	0.0659
	X/L_p	0.1850	0.1620	0.0272	0.4583	0.3159
	Y/L_p	0.3652	0.4076	0.0650	0.5115	0.0381
	$\lvert\Delta\varepsilon_r^-\rvert$	0.0005	0.0153	0.0186	0.0198	0.0673
	X/L_p	0.0657	0.0927	0.0157	0.1850	0.4352
	Y/L_p	0.3267	0.1343	0.1073	0.0727	0.4846
05	$\lvert\Delta\varepsilon_r^+\rvert$	0.0004	0.0053	0.0197	0.0209	0.0641
	X/L_p	0.3198	0.3236	0.9356	0.8279	0.1466
	Y/L_p	0.4153	0.4538	0.3152	0.2421	0.4692
	$\lvert\Delta\varepsilon_r^-\rvert$	0.0004	0.0054	0.0189	0.0199	0.0645
	X/L_p	0.1504	0.1235	0.0619	0.8779	0.9318
	Y/L_p	0.4076	0.1651	0.3537	0.2575	0.3190
06	$\lvert\Delta\varepsilon_r^+\rvert$	0.0006	0.0141	0.0194	0.0208	0.0656
	X/L_p	0.2389	0.1273	0.1504	0.1696	0.5392
	Y/L_p	0.5115	0.1150	0.1150	0.0419	0.3075
	$\lvert\Delta\varepsilon_r^-\rvert$	0.0006	0.0139	0.0185	0.0196	0.0664
	X/L_p	0.1850	0.4583	0.4776	0.4545	0.8086
	Y/L_p	0.2305	0.1651	0.2382	0.2806	0.3614
07	$\lvert\Delta\varepsilon_r^+\rvert$	0.0004	0.0050	0.0197	0.0209	0.0694
	X/L_p	0.3082	0.1427	0.5815	0.1427	0.6161
	Y/L_p	0.3999	0.3383	0.3652	0.0689	0.2151
	$\lvert\Delta\varepsilon_r^-\rvert$	0.0004	0.0050	0.0189	0.0200	0.0697
	X/L_p	0.6816	0.0619	0.8894	0.6085	0.4006
	Y/L_p	0.4538	0.1920	0.2882	0.5115	0.2382
08	$\lvert\Delta\varepsilon_r^+\rvert$	0.0007	0.0122	0.0197	0.0205	0.0658
	X/L_p	0.4198	0.8240	0.5623	0.4853	0.9934
	Y/L_p	0.1843	0.1343	0.1189	0.1266	0.0689
	$\lvert\Delta\varepsilon_r^-\rvert$	0.0007	0.0121	0.0187	0.0194	0.0669
	X/L_p	0.3429	0.9818	0.2466	0.0080	0.9010

Table D.2 – continued from previous page

Test		$\overline{u}$	$\overline{w}$	$\overline{u'}$	$\overline{w}$	$\overline{u'w'}$
	Y/L_p	0.4730	0.1304	0.1343	0.3691	0.0650
09	$\left\|\Delta\varepsilon_r^+\right\|$	0.0005	0.0043	0.0160	0.0202	0.0603
	X/L_p	0.0157	0.1504	0.1119	1.0011	1.2012
	Y/L_p	0.2536	0.3383	0.3421	0.2690	0.3267
	$\left\|\Delta\varepsilon_r^-\right\|$	0.0005	0.0043	0.0156	0.0192	0.0600
	X/L_p	0.0195	0.1927	0.8048	0.6547	0.7547
	Y/L_p	0.2767	0.3922	0.4191	0.5115	0.3960
10a	$\left\|\Delta\varepsilon_r^+\right\|$	0.0016	0.0185	0.0960	0.1024	0.3432
	X/L_p	0.5553	0.3936	0.8940	0.3859	0.6669
	Y/L_p	0.4265	0.4112	0.0339	0.4766	0.2456
	$\left\|\Delta\varepsilon_r^-\right\|$	0.0016	0.0183	0.0830	0.0863	0.3787
	X/L_p	1.1788	1.1981	0.9671	0.4629	0.6246
	Y/L_p	0.4150	0.3765	0.0493	0.2418	0.4381
10b	$\left\|\Delta\varepsilon_r^+\right\|$	0.0018	0.0206	0.1010	0.1101	0.3637
	X/L_p	0.8940	0.9748	0.1203	0.8709	0.4090
	Y/L_p	0.4304	0.2687	0.3881	0.2610	0.1687
	$\left\|\Delta\varepsilon_r^-\right\|$	0.0018	0.0207	0.0853	0.0919	0.4030
	X/L_p	0.9710	0.2820	0.3744	0.5822	1.1635
	Y/L_p	0.3380	0.4804	0.1571	0.1764	0.2302
10c	$\left\|\Delta\varepsilon_r^+\right\|$	0.0022	0.0224	0.1160	0.1265	0.4165
	X/L_p	0.0395	0.3898	0.9364	0.7593	0.0510
	Y/L_p	0.4150	0.2495	0.1494	0.3303	0.4573
	$\left\|\Delta\varepsilon_r^-\right\|$	0.0022	0.0224	0.0965	0.1042	0.4408
	X/L_p	0.7362	0.3205	0.5360	0.7015	0.8093
	Y/L_p	0.4920	0.1918	0.1417	0.1841	0.3226
10d	$\left\|\Delta\varepsilon_r^+\right\|$	0.0019	0.0186	0.1041	0.1098	0.3652
	X/L_p	0.1280	0.3474	0.9017	0.0856	1.1750
	Y/L_p	0.4920	0.2572	0.1032	0.4997	0.1841
	$\left\|\Delta\varepsilon_r^-\right\|$	0.0019	0.0187	0.0877	0.0916	0.4029
	X/L_p	0.7939	0.4090	0.0933	0.0779	0.1819
	Y/L_p	0.4997	0.4420	0.0724	0.1994	0.0570
10e	$\left\|\Delta\varepsilon_r^+\right\|$	0.0040	0.0409	0.2022	0.2051	0.5721

Table D.2 – continued from previous page

Test		$\overline{u}$	$\overline{w}$	$\overline{u'}$	$\overline{w}$	$\overline{u'w'}$
	X/L_p	1.2097	0.2050	0.4975	0.1588	0.7054
	Y/L_p	0.4920	0.4535	0.5112	0.4958	0.4112
	$\lvert\Delta\varepsilon_r^-\rvert$	0.0040	0.0413	0.1585	0.1609	0.6767
	X/L_p	0.5206	0.1318	1.0287	0.7554	0.6823
	Y/L_p	0.4035	0.3496	0.2649	0.0724	0.3149
	$\lvert\Delta\varepsilon_r^+\rvert$	0.0015	0.0184	0.0837	0.0930	0.3320
	X/L_p	0.4590	0.1819	1.2135	1.0557	0.5861
	Y/L_p	0.4381	0.1725	0.3149	0.4265	0.4843
10f	$\lvert\Delta\varepsilon_r^-\rvert$	0.0015	0.0181	0.0736	0.0787	0.3578
	X/L_p	0.2435	0.8440	1.1635	0.0087	0.5861
	Y/L_p	0.4458	0.4150	0.4227	0.2379	0.4612
	$\lvert\Delta\varepsilon_r^+\rvert$	0.0019	0.0190	0.1020	0.1177	0.4019
	X/L_p	0.6938	0.0664	0.9902	0.3898	0.6900
	Y/L_p	0.4651	0.3342	0.4458	0.0378	0.4804
10g	$\lvert\Delta\varepsilon_r^-\rvert$	0.0020	0.0189	0.0893	0.0965	0.4517
	X/L_p	0.5091	0.2050	0.8901	1.1365	0.3898
	Y/L_p	0.3611	0.3496	0.3034	0.1533	0.1648
	$\lvert\Delta\varepsilon_r^+\rvert$	0.0016	0.0151	0.0860	0.0967	0.3433
	X/L_p	0.2204	0.3282	0.8440	0.2011	0.2204
	Y/L_p	0.4073	0.4420	0.3765	0.4227	0.0647
10h	$\lvert\Delta\varepsilon_r^-\rvert$	0.0016	0.0151	0.0759	0.0824	0.3736
	X/L_p	0.1472	0.3744	0.6091	1.0595	0.0779
	Y/L_p	0.3650	0.3111	0.2841	0.0609	0.1648
	$\lvert\Delta\varepsilon_r^+\rvert$	0.0019	0.0278	0.1019	0.1013	0.3941
	X/L_p	0.1665	0.4898	0.4667	0.5784	0.4744
	Y/L_p	0.3957	0.4420	0.4997	0.5035	0.2302
11a	$\lvert\Delta\varepsilon_r^-\rvert$	0.0019	0.0271	0.0892	0.0881	0.4541
	X/L_p	0.3666	0.4436	0.8863	0.1934	0.9055
	Y/L_p	0.4343	0.3996	0.3496	0.1302	0.2610
	$\lvert\Delta\varepsilon_r^+\rvert$	0.0020	0.0258	0.1116	0.1051	0.3916
	X/L_p	0.9364	0.2242	0.8478	0.2743	1.0903
	Y/L_p	0.4458	0.1302	0.1494	0.4766	0.4073
11b						

Table D.2 – continued from previous page

Test		$\overline{u}$	$\overline{w}$	$\overline{u'}$	$\overline{w}$	$\overline{u'w'}$
	$\lvert\Delta\varepsilon_r^-\rvert$	0.0020	0.0259	0.0934	0.0899	0.4572
	X/L_p	0.4783	0.6091	0.2781	0.4013	0.9941
	Y/L_p	0.4804	0.1802	0.1841	0.2918	0.2726
11c	$\lvert\Delta\varepsilon_r^+\rvert$	0.0034	0.0398	0.1817	0.1805	0.5627
	X/L_p	0.9941	0.1973	0.7824	0.3282	0.3590
	Y/L_p	0.3957	0.4189	0.2726	0.4073	0.0493
	$\lvert\Delta\varepsilon_r^-\rvert$	0.0035	0.0399	0.1466	0.1454	0.6998
	X/L_p	1.0595	0.3012	0.7785	0.1318	0.9133
	Y/L_p	0.4112	0.1186	0.0224	0.4689	0.1918
11d	$\lvert\Delta\varepsilon_r^+\rvert$	0.0024	0.0277	0.1315	0.1254	0.4651
	X/L_p	0.5245	1.0249	0.8247	0.0933	0.6900
	Y/L_p	0.5074	0.3072	0.0570	0.3996	0.3265
	$\lvert\Delta\varepsilon_r^-\rvert$	0.0024	0.0278	0.1095	0.1047	0.5257
	X/L_p	1.0557	0.1896	0.9517	1.1057	0.6553
	Y/L_p	0.3072	0.3881	0.0301	0.2764	0.3111
11e	$\lvert\Delta\varepsilon_r^+\rvert$	0.0014	0.0197	0.0788	0.0720	0.2906
	X/L_p	0.2319	0.4128	0.9248	1.0595	0.9748
	Y/L_p	0.4689	0.1533	0.4189	0.3881	0.0686
	$\lvert\Delta\varepsilon_r^-\rvert$	0.0014	0.0197	0.0684	0.0627	0.2930
	X/L_p	0.8670	0.4205	0.9594	0.9133	1.1211
	Y/L_p	0.4843	0.1032	0.3265	0.0878	0.2495
11f	$\lvert\Delta\varepsilon_r^+\rvert$	0.0026	0.0354	0.1198	0.1255	0.4725
	X/L_p	0.7824	0.0510	0.8594	0.9710	0.0395
	Y/L_p	0.3380	0.3688	0.2957	0.0917	0.0185
	$\lvert\Delta\varepsilon_r^-\rvert$	0.0026	0.0349	0.1033	0.1052	0.5190
	X/L_p	0.2781	0.3282	0.9325	0.5514	0.1087
	Y/L_p	0.3996	0.2995	0.2803	0.1494	0.1148
11g	$\lvert\Delta\varepsilon_r^+\rvert$	0.0023	0.0283	0.1138	0.1147	0.4595
	X/L_p	0.5707	0.4475	0.2011	1.1712	0.5437
	Y/L_p	0.3842	0.3611	0.4189	0.0840	0.4112
	$\lvert\Delta\varepsilon_r^-\rvert$	0.0024	0.0276	0.0965	0.0974	0.5096
	X/L_p	0.6053	0.1896	1.1481	1.0634	0.2589

Table D.2 – continued from previous page

Test		$\overline{u}$	$\overline{w}$	$\overline{u'}$	$\overline{w}$	$\overline{u'w'}$
	Y/L_p	0.4073	0.2033	0.0185	0.0724	0.0224
11h	$\lvert\Delta\varepsilon_r^+\rvert$	0.0024	0.0276	0.1147	0.1162	0.4748
	X/L_p	0.3666	0.4436	1.1750	0.9517	0.0972
	Y/L_p	0.4189	0.3765	0.3265	0.0493	0.1071
	$\lvert\Delta\varepsilon_r^-\rvert$	0.0024	0.0272	0.0985	0.0987	0.5367
	X/L_p	0.1511	0.3628	0.9710	0.5014	0.4398
	Y/L_p	0.4881	0.4035	0.1225	0.2572	0.1109
12a	$\lvert\Delta\varepsilon_r^+\rvert$	0.0028	0.0368	0.1191	0.1447	0.4398
	X/L_p	0.5707	0.3551	0.8940	0.8670	1.0595
	Y/L_p	0.4727	0.2957	0.4381	0.2225	0.0416
	$\lvert\Delta\varepsilon_r^-\rvert$	0.0028	0.0366	0.1021	0.1175	0.5373
	X/L_p	0.7862	0.3821	0.9787	0.6246	1.0018
	Y/L_p	0.3996	0.4265	0.4881	0.3380	0.4535
12b	$\lvert\Delta\varepsilon_r^+\rvert$	0.0023	0.0583	0.1041	0.1261	0.3899
	X/L_p	0.8979	0.6784	0.5553	0.2473	0.1357
	Y/L_p	0.3265	0.3804	0.4458	0.2033	0.0532
	$\lvert\Delta\varepsilon_r^-\rvert$	0.0022	0.0549	0.0903	0.1038	0.4533
	X/L_p	0.8132	0.5091	0.1010	0.6284	1.1981
	Y/L_p	0.4420	0.2533	0.1571	0.4073	0.2726
12c	$\lvert\Delta\varepsilon_r^+\rvert$	0.0019	0.0241	0.0955	0.1067	0.3554
	X/L_p	0.8286	0.6823	0.6592	1.0980	0.2974
	Y/L_p	0.4073	0.2379	0.4573	0.4881	0.0724
	$\lvert\Delta\varepsilon_r^-\rvert$	0.0019	0.0238	0.0830	0.0908	0.4112
	X/L_p	0.7246	0.5553	0.3397	0.8247	0.1203
	Y/L_p	0.3534	0.3380	0.4766	0.1725	0.4458
12d	$\lvert\Delta\varepsilon_r^+\rvert$	0.0023	0.0326	0.1075	0.1333	0.4049
	X/L_p	0.2627	0.3474	0.0202	1.0942	0.1395
	Y/L_p	0.3380	0.3650	0.1879	0.3688	0.0378
	$\lvert\Delta\varepsilon_r^-\rvert$	0.0023	0.0328	0.0926	0.1096	0.4814
	X/L_p	0.2088	0.6246	0.9517	1.0056	0.5976
	Y/L_p	0.4343	0.2379	0.1494	0.2687	0.0994
12e	$\lvert\Delta\varepsilon_r^+\rvert$	0.0034	0.0528	0.1547	0.1917	0.5139

Table D.2 – continued from previous page

Test		$\overline{u}$	$\overline{w}$	$\overline{u'}$	$\overline{w}$	$\overline{u'w'}$
	X/L_p	0.2512	0.4051	0.8786	0.1357	1.2058
	Y/L_p	0.4496	0.3034	0.3072	0.3842	0.0416
	$\lvert\Delta\varepsilon_r^-\rvert$	0.0035	0.0520	0.1292	0.1504	0.6504
	X/L_p	0.3089	1.1519	0.0433	0.5091	0.7323
	Y/L_p	0.4689	0.2341	0.3534	0.1764	0.0147
12f	$\lvert\Delta\varepsilon_r^+\rvert$	0.0036	0.0595	0.1800	0.1984	0.5177
	X/L_p	0.1203	0.6861	0.4167	0.1973	0.7362
	Y/L_p	0.2687	0.4035	0.3688	0.1841	0.4343
	$\lvert\Delta\varepsilon_r^-\rvert$	0.0037	0.0586	0.1459	0.1546	0.7008
	X/L_p	0.2204	0.5553	0.7246	0.2319	0.7169
	Y/L_p	0.3265	0.3534	0.0147	0.1994	0.4496
12g	$\lvert\Delta\varepsilon_r^+\rvert$	0.0035	0.0562	0.1850	0.1962	0.5360
	X/L_p	1.1327	0.4128	1.1635	0.6669	0.4513
	Y/L_p	0.4035	0.2687	0.1225	0.3457	0.3996
	$\lvert\Delta\varepsilon_r^-\rvert$	0.0035	0.0571	0.1496	0.1552	0.7195
	X/L_p	0.2589	0.6400	1.1712	0.2550	0.5014
	Y/L_p	0.3881	0.2225	0.2418	0.4920	0.4535
12h	$\lvert\Delta\varepsilon_r^+\rvert$	0.0034	0.0439	0.1563	0.1792	0.4985
	X/L_p	0.5591	1.1019	0.8363	1.1327	0.0472
	Y/L_p	0.4958	0.2610	0.1379	0.2418	0.2572
	$\lvert\Delta\varepsilon_r^-\rvert$	0.0034	0.0434	0.1301	0.1418	0.6441
	X/L_p	0.4436	0.3397	0.7246	0.7593	0.6323
	Y/L_p	0.5035	0.1417	0.2610	0.5112	0.0609

Table D.3: Maximum relative random uncertainty bounds. 50^{th} percentile value.

Test		$\overline{u}$	$\overline{w}$	$\overline{u'}$	$\overline{w}$	$\overline{u'w'}$
01	$\lvert\Delta\varepsilon_r^+\rvert$	0.0026	0.0579	0.0243	0.0256	0.1225
	X/L_p	0.8818	1.1358	0.7740	0.7432	0.3544
	Y/L_p	0.0573	0.4961	0.0111	0.2190	0.1728
	$\lvert\Delta\varepsilon_r^-\rvert$	0.0026	0.0581	0.0230	0.0243	0.1237
	X/L_p	0.2158	0.5623	0.3814	0.6046	0.5122

Table D.3 – continued from previous page

Test		$\overline{u}$	$\overline{w}$	$\overline{u'}$	$\overline{w}$	$\overline{u'w'}$
	Y/L_p	0.0188	0.0458	0.1420	0.2729	0.2882
02	$\lvert\Delta\varepsilon_r^+\rvert$	0.0020	0.0436	0.0238	0.0255	0.1044
	X/L_p	0.0080	0.6238	1.0088	1.1858	0.1273
	Y/L_p	0.1227	0.1112	0.0535	0.0111	0.1458
	$\lvert\Delta\varepsilon_r^-\rvert$	0.0020	0.0433	0.0226	0.0242	0.1066
	X/L_p	0.3352	0.2928	0.2736	1.0742	0.6393
	Y/L_p	0.0573	0.4384	0.0227	0.2074	0.1150
03	$\lvert\Delta\varepsilon_r^+\rvert$	0.0026	0.0601	0.0247	0.0259	0.1271
	X/L_p	0.8740	0.6931	1.1358	0.5276	0.9587
	Y/L_p	0.0573	0.0958	0.0188	0.1805	0.1959
	$\lvert\Delta\varepsilon_r^-\rvert$	0.0026	0.0604	0.0234	0.0246	0.1269
	X/L_p	0.9241	0.6547	0.2197	0.1235	0.9934
	Y/L_p	0.0766	0.3806	0.0111	0.4037	0.2536
	$\lvert\Delta\varepsilon_r^+\rvert$	0.0020	0.0502	0.0239	0.0259	0.1044
	X/L_p	0.8548	0.4314	0.3390	0.6431	0.8509
	Y/L_p	0.1343	0.3614	0.2190	0.4230	0.3229
	$\lvert\Delta\varepsilon_r^-\rvert$	0.0020	0.0499	0.0228	0.0245	0.1073
	X/L_p	0.5161	1.1242	0.5507	1.0088	0.5315
	Y/L_p	0.0535	0.3383	0.0265	0.0766	0.1073
05	$\lvert\Delta\varepsilon_r^+\rvert$	0.0028	0.0771	0.0247	0.0259	0.1334
	X/L_p	0.7586	0.7047	0.5546	0.6777	0.4737
	Y/L_p	0.0650	0.0342	0.3229	0.2921	0.1458
	$\lvert\Delta\varepsilon_r^-\rvert$	0.0028	0.0778	0.0235	0.0246	0.1344
	X/L_p	0.5854	0.5815	0.1312	0.1158	0.5007
	Y/L_p	0.0612	0.2729	0.3768	0.1843	0.3883
06	$\lvert\Delta\varepsilon_r^+\rvert$	0.0021	0.0538	0.0241	0.0259	0.1047
	X/L_p	0.2120	0.8509	0.8202	0.2158	0.7778
	Y/L_p	0.0727	0.1882	0.2575	0.4692	0.2382
	$\lvert\Delta\varepsilon_r^-\rvert$	0.0021	0.0535	0.0230	0.0246	0.1082
	X/L_p	0.8818	0.1042	0.5931	0.2428	1.0627
	Y/L_p	0.1381	0.0342	0.4538	0.2113	0.3267
07	$\lvert\Delta\varepsilon_r^+\rvert$	0.0026	0.0690	0.0250	0.0263	0.1473

Table D.3 – continued from previous page

Test		$\overline{u}$	$\overline{w}$	$\overline{u'}$	$\overline{w}$	$\overline{u'w'}$
	X/L_p	1.0280	0.6469	0.0696	0.3313	0.8356
	Y/L_p	0.3575	0.2882	0.4153	0.1728	0.3383
	$\left\|\Delta\varepsilon_r^-\right\|$	0.0026	0.0696	0.0238	0.0249	0.1464
	X/L_p	0.0503	0.7355	0.4237	0.5661	0.2043
	Y/L_p	0.0381	0.3190	0.0881	0.4769	0.4730
08	$\left\|\Delta\varepsilon_r^+\right\|$	0.0020	0.0491	0.0244	0.0261	0.1066
	X/L_p	0.2274	0.3544	0.0734	1.1204	0.7740
	Y/L_p	0.0612	0.3152	0.3036	0.3768	0.2959
	$\left\|\Delta\varepsilon_r^-\right\|$	0.0021	0.0489	0.0231	0.0248	0.1102
	X/L_p	0.5353	0.8779	0.9934	0.6662	0.1466
	Y/L_p	0.0342	0.3267	0.3383	0.0419	0.1343
09	$\left\|\Delta\varepsilon_r^+\right\|$	0.0026	0.0612	0.0243	0.0255	0.1286
	X/L_p	0.4121	0.5045	0.7509	0.1889	0.2851
	Y/L_p	0.0881	0.1535	0.0265	0.4576	0.1535
	$\left\|\Delta\varepsilon_r^-\right\|$	0.0026	0.0617	0.0231	0.0242	0.1292
	X/L_p	0.0349	0.7162	0.7470	1.0742	0.5892
	Y/L_p	0.0304	0.1882	0.2652	0.1458	0.4153
10a	$\left\|\Delta\varepsilon_r^+\right\|$	0.0055	0.1262	0.1312	0.1319	0.7383
	X/L_p	0.4706	0.3243	1.0403	1.2020	0.1588
	Y/L_p	0.1494	0.4073	0.2456	0.1994	0.1533
	$\left\|\Delta\varepsilon_r^-\right\|$	0.0056	0.1291	0.1066	0.1066	0.7718
	X/L_p	0.0279	0.3282	0.1318	0.1665	0.1780
	Y/L_p	0.2649	0.4920	0.3188	0.2071	0.3957
10b	$\left\|\Delta\varepsilon_r^+\right\|$	0.0077	0.1869	0.1376	0.1430	0.7194
	X/L_p	1.1635	0.9325	0.0241	0.9402	0.4359
	Y/L_p	0.2572	0.4381	0.4343	0.2687	0.1494
	$\left\|\Delta\varepsilon_r^-\right\|$	0.0079	0.1862	0.1111	0.1140	0.7808
	X/L_p	0.5591	0.8209	0.1395	1.0595	1.0133
	Y/L_p	0.1109	0.1148	0.0840	0.1456	0.4535
10c	$\left\|\Delta\varepsilon_r^+\right\|$	0.0090	0.1993	0.1624	0.1689	0.8518
	X/L_p	0.3782	1.2173	0.6130	0.2473	0.1626
	Y/L_p	0.3496	0.3149	0.3496	0.4458	0.0724

Table D.3 – continued from previous page

Test		$\overline{u}$	$\overline{w}$	$\overline{u'}$	$\overline{w}$	$\overline{u'w'}$
	$\left\|\Delta\varepsilon_r^-\right\|$	0.0094	0.1995	0.1272	0.1309	0.9182
	X/L_p	0.3513	1.1134	0.1357	0.5668	0.8709
	Y/L_p	0.3149	0.2995	0.4458	0.3996	0.3265
10d	$\left\|\Delta\varepsilon_r^+\right\|$	0.0081	0.1529	0.1397	0.1455	0.7693
	X/L_p	0.7939	0.4706	0.9864	0.2858	0.9748
	Y/L_p	0.0609	0.1609	0.4689	0.2649	0.1379
	$\left\|\Delta\varepsilon_r^-\right\|$	0.0084	0.1501	0.1124	0.1166	0.8228
	X/L_p	0.0587	0.4783	0.5245	1.1249	0.5514
	Y/L_p	0.0955	0.2418	0.4035	0.1263	0.1571
10e	$\left\|\Delta\varepsilon_r^+\right\|$	0.0187	0.3332	0.2938	0.3021	1.4165
	X/L_p	0.7670	0.6246	0.5861	0.9864	0.6130
	Y/L_p	0.1609	0.4189	0.5074	0.1109	0.1494
	$\left\|\Delta\varepsilon_r^-\right\|$	0.0196	0.3195	0.2092	0.2141	1.5372
	X/L_p	0.9710	0.9748	1.0480	1.1712	1.0865
	Y/L_p	0.0878	0.3457	0.3111	0.1533	0.5112
10f	$\left\|\Delta\varepsilon_r^+\right\|$	0.0066	0.1312	0.1134	0.1163	0.7407
	X/L_p	0.1511	0.6477	0.1010	0.6861	0.6900
	Y/L_p	0.1417	0.3957	0.2918	0.0455	0.2264
	$\left\|\Delta\varepsilon_r^-\right\|$	0.0068	0.1343	0.0947	0.0959	0.7531
	X/L_p	1.0364	0.3859	0.6053	0.6438	0.8401
	Y/L_p	0.3303	0.4997	0.4189	0.4920	0.4958
10g	$\left\|\Delta\varepsilon_r^+\right\|$	0.0076	0.1440	0.1478	0.1516	0.8693
	X/L_p	0.0087	0.8132	1.2173	0.5014	0.9787
	Y/L_p	0.2726	0.2649	0.2456	0.0917	0.1609
	$\left\|\Delta\varepsilon_r^-\right\|$	0.0079	0.1490	0.1180	0.1191	0.9011
	X/L_p	0.3358	0.6630	0.8940	1.2020	0.6938
	Y/L_p	0.1302	0.3380	0.2841	0.2764	0.1879
10h	$\left\|\Delta\varepsilon_r^+\right\|$	0.0059	0.1061	0.1222	0.1241	0.7280
	X/L_p	0.1896	1.1943	0.0818	1.1403	0.2897
	Y/L_p	0.3611	0.4073	0.0686	0.0378	0.1533
	$\left\|\Delta\varepsilon_r^-\right\|$	0.0059	0.1085	0.1006	0.1012	0.7494
	X/L_p	0.1434	1.0249	0.4975	0.6015	0.8940

Table D.3 – continued from previous page

Test		$\overline{u}$	$\overline{w}$	$\overline{u'}$	$\overline{w}$	$\overline{u'w'}$
	Y/L_p	0.1802	0.1687	0.4535	0.0070	0.2033
11a	$\lvert\Delta\varepsilon_r^+\rvert$	0.0062	0.1601	0.1455	0.1453	0.8779
	X/L_p	0.0279	0.2897	0.5745	0.0356	0.3936
	Y/L_p	0.5035	0.4150	0.0532	0.2071	0.4458
	$\lvert\Delta\varepsilon_r^-\rvert$	0.0061	0.1646	0.1167	0.1159	0.9190
	X/L_p	0.5091	1.0364	0.5168	0.6707	1.0980
	Y/L_p	0.4804	0.1956	0.1609	0.1841	0.1956
11b	$\lvert\Delta\varepsilon_r^+\rvert$	0.0070	0.1902	0.1504	0.1490	0.7559
	X/L_p	0.3590	1.2058	1.1712	0.8979	0.7785
	Y/L_p	0.2726	0.1802	0.1609	0.0917	0.1340
	$\lvert\Delta\varepsilon_r^-\rvert$	0.0072	0.1925	0.1193	0.1179	0.8223
	X/L_p	0.1511	1.0749	0.3358	0.0356	1.1673
	Y/L_p	0.0994	0.2649	0.2148	0.2110	0.2572
11c	$\lvert\Delta\varepsilon_r^+\rvert$	0.0121	0.3036	0.2663	0.2671	1.2560
	X/L_p	0.3436	1.2097	1.0326	0.5283	0.6784
	Y/L_p	0.3265	0.1879	0.3573	0.4573	0.0801
	$\lvert\Delta\varepsilon_r^-\rvert$	0.0129	0.3045	0.1914	0.1907	1.4480
	X/L_p	0.0587	0.1241	0.7169	0.7169	0.2935
	Y/L_p	0.1802	0.4612	0.0455	0.2533	0.4573
11d	$\lvert\Delta\varepsilon_r^+\rvert$	0.0088	0.1916	0.1803	0.1811	1.0001
	X/L_p	0.7477	1.1442	0.3898	0.1434	0.9825
	Y/L_p	0.0994	0.2533	0.2918	0.3765	0.3842
	$\lvert\Delta\varepsilon_r^-\rvert$	0.0091	0.1922	0.1388	0.1387	1.0952
	X/L_p	0.4282	0.5861	0.9787	0.4706	0.0664
	Y/L_p	0.3034	0.1417	0.1109	0.1032	0.4843
11e	$\lvert\Delta\varepsilon_r^+\rvert$	0.0066	0.1300	0.0996	0.1005	0.6202
	X/L_p	0.5707	0.2358	0.6130	1.0518	0.9055
	Y/L_p	0.2764	0.5074	0.4035	0.5074	0.0994
	$\lvert\Delta\varepsilon_r^-\rvert$	0.0067	0.1307	0.0845	0.0851	0.6351
	X/L_p	0.0972	1.0287	1.0903	0.4783	0.8286
	Y/L_p	0.1148	0.0763	0.2456	0.3265	0.1148
11f	$\lvert\Delta\varepsilon_r^+\rvert$	0.0094	0.2350	0.1730	0.1780	1.1142

Table D.3 – continued from previous page

Test		$\overline{u}$	$\overline{w}$	$\overline{u'}$	$\overline{w}$	$\overline{u'w'}$
	X/L_p	0.0587	0.0664	0.0241	1.0056	1.0980
	Y/L_p	0.1764	0.1417	0.0378	0.2418	0.1994
	$\lvert\Delta\varepsilon_r^-\rvert$	0.0093	0.2451	0.1353	0.1367	1.1407
	X/L_p	0.0587	1.0557	0.9671	1.2058	0.2281
	Y/L_p	0.2033	0.0763	0.3188	0.4381	0.3380
11g	$\lvert\Delta\varepsilon_r^+\rvert$	0.0083	0.1791	0.1619	0.1631	1.0369
	X/L_p	1.2058	0.5861	1.0210	0.6630	0.5591
	Y/L_p	0.3919	0.0609	0.1032	0.3842	0.0224
	$\lvert\Delta\varepsilon_r^-\rvert$	0.0083	0.1854	0.1271	0.1275	1.0616
	X/L_p	0.0818	0.5553	0.8401	0.9210	0.9902
	Y/L_p	0.2418	0.4112	0.5035	0.2071	0.0609
11h	$\lvert\Delta\varepsilon_r^+\rvert$	0.0083	0.1618	0.1664	0.1674	1.0611
	X/L_p	0.2974	0.4860	0.3513	0.8555	0.7785
	Y/L_p	0.1879	0.0262	0.0647	0.3226	0.3149
	$\lvert\Delta\varepsilon_r^-\rvert$	0.0083	0.1654	0.1299	0.1302	1.1079
	X/L_p	0.7747	0.7246	1.0480	0.9286	0.4359
	Y/L_p	0.3034	0.1071	0.0955	0.2764	0.3611
12a	$\lvert\Delta\varepsilon_r^+\rvert$	0.0070	0.2474	0.1833	0.1968	0.9371
	X/L_p	0.0779	0.3089	0.0703	1.2020	0.4321
	Y/L_p	0.2341	0.4997	0.1148	0.3188	0.1379
	$\lvert\Delta\varepsilon_r^-\rvert$	0.0069	0.2463	0.1412	0.1489	1.0574
	X/L_p	1.1365	1.1712	0.8901	0.1318	0.9133
	Y/L_p	0.2726	0.3804	0.4150	0.2957	0.4035
12b	$\lvert\Delta\varepsilon_r^+\rvert$	0.0057	0.2757	0.1467	0.1605	0.7251
	X/L_p	0.2011	0.3859	0.6861	0.6400	0.8594
	Y/L_p	0.4881	0.0994	0.4651	0.3727	0.2880
	$\lvert\Delta\varepsilon_r^-\rvert$	0.0057	0.2805	0.1182	0.1262	0.8120
	X/L_p	0.4860	0.0587	0.7362	0.3590	0.8555
	Y/L_p	0.1879	0.4804	0.0532	0.4227	0.2803
12c	$\lvert\Delta\varepsilon_r^+\rvert$	0.0051	0.1583	0.1312	0.1397	0.6794
	X/L_p	0.9248	0.0087	0.7939	0.8247	0.1742
	Y/L_p	0.5112	0.2071	0.5035	0.0763	0.3534

Table D.3 – continued from previous page

Test		$\overline{u}$	$\overline{w}$	$\overline{u'}$	$\overline{w}$	$\overline{u'w'}$
	$\lvert\Delta\varepsilon_r^-\rvert$	0.0050	0.1609	0.1078	0.1128	0.7547
	X/L_p	0.9440	0.5168	0.5476	0.2627	0.1164
	Y/L_p	0.2456	0.1263	0.0686	0.3380	0.2110
12d	$\lvert\Delta\varepsilon_r^+\rvert$	0.0062	0.1910	0.1609	0.1753	0.7602
	X/L_p	0.1280	1.1442	0.6861	0.9210	1.0018
	Y/L_p	0.2264	0.4265	0.2379	0.4804	0.3919
	$\lvert\Delta\varepsilon_r^-\rvert$	0.0061	0.1940	0.1276	0.1355	0.8787
	X/L_p	0.7593	1.0403	0.2435	0.5168	0.9325
	Y/L_p	0.4920	0.2341	0.2687	0.4227	0.1494
12e	$\lvert\Delta\varepsilon_r^+\rvert$	0.0092	0.3045	0.2443	0.2702	1.0626
	X/L_p	1.0749	0.1357	0.1588	0.0587	0.7400
	Y/L_p	0.1417	0.3342	0.4881	0.0147	0.4804
	$\lvert\Delta\varepsilon_r^-\rvert$	0.0093	0.3040	0.1803	0.1929	1.2899
	X/L_p	0.0972	0.0472	0.3282	0.5129	0.5822
	Y/L_p	0.3188	0.2379	0.0532	0.2803	0.0378
12f	$\lvert\Delta\varepsilon_r^+\rvert$	0.0095	0.3582	0.2673	0.2864	1.1928
	X/L_p	0.4821	1.1904	0.9633	0.7285	0.9787
	Y/L_p	0.2649	0.1379	0.3919	0.2341	0.3804
	$\lvert\Delta\varepsilon_r^-\rvert$	0.0094	0.3631	0.1957	0.2014	1.4283
	X/L_p	1.1981	1.0287	0.2512	0.0549	0.1318
	Y/L_p	0.4573	0.2302	0.2379	0.3072	0.4573
12g	$\lvert\Delta\varepsilon_r^+\rvert$	0.0099	0.2997	0.2774	0.2887	1.1489
	X/L_p	0.3859	0.3282	0.0356	0.6091	0.9248
	Y/L_p	0.3457	0.0686	0.3919	0.1994	0.1225
	$\lvert\Delta\varepsilon_r^-\rvert$	0.0098	0.2943	0.1992	0.2049	1.4487
	X/L_p	0.1549	0.3782	0.6515	0.5938	0.4590
	Y/L_p	0.2726	0.4689	0.4535	0.2572	0.4573
12h	$\lvert\Delta\varepsilon_r^+\rvert$	0.0086	0.2998	0.2353	0.2510	1.1167
	X/L_p	1.0249	0.6169	0.3089	0.5091	0.2512
	Y/L_p	0.2495	0.4535	0.0647	0.1609	0.1802
	$\lvert\Delta\varepsilon_r^-\rvert$	0.0086	0.2994	0.1737	0.1806	1.3104
	X/L_p	0.1318	1.1904	0.5899	0.3358	0.4090

Table D.3 – continued from previous page

Test		$\overline{u}$	$\overline{w}$	$\overline{u'}$	$\overline{w}$	$\overline{u'w'}$
	Y/L_p	0.2841	0.1918	0.1571	0.5112	0.2610

Table D.4: Maximum relative random uncertainty bounds. 90^{th} percentile value.

Test		$\overline{u}$	$\overline{w}$	$\overline{u'}$	$\overline{w}$	$\overline{u'w'}$
01	$\lvert\Delta\varepsilon_r^+\rvert$	0.0187	0.3821	0.0301	0.0313	0.5610
	X/L_p	0.4506	0.5353	0.0696	0.5738	0.2697
	Y/L_p	0.1997	0.4114	0.3460	0.1381	0.4422
	$\lvert\Delta\varepsilon_r^-\rvert$	0.0187	0.3848	0.0286	0.0297	0.5550
	X/L_p	0.9125	0.7932	0.2466	1.1897	0.1889
	Y/L_p	0.3036	0.0573	0.1959	0.3806	0.3883
02	$\lvert\Delta\varepsilon_r^+\rvert$	0.0120	0.2097	0.0308	0.0315	0.5045
	X/L_p	0.4468	0.9472	0.0426	1.1127	1.1704
	Y/L_p	0.2844	0.0342	0.1766	0.3845	0.4538
	$\lvert\Delta\varepsilon_r^-\rvert$	0.0122	0.2100	0.0294	0.0300	0.5067
	X/L_p	0.5815	0.7971	0.2197	0.7740	0.8432
	Y/L_p	0.2844	0.2806	0.1843	0.3691	0.4615
03	$\lvert\Delta\varepsilon_r^+\rvert$	0.0192	0.3734	0.0301	0.0312	0.5525
	X/L_p	0.8856	0.7085	1.0242	1.2051	0.9010
	Y/L_p	0.3075	0.2882	0.3499	0.3691	0.0458
	$\lvert\Delta\varepsilon_r^-\rvert$	0.0192	0.3728	0.0286	0.0296	0.5451
	X/L_p	0.9164	0.3621	0.7624	0.1466	0.8702
	Y/L_p	0.2998	0.0150	0.4307	0.4653	0.0727
	$\lvert\Delta\varepsilon_r^+\rvert$	0.0141	0.3595	0.0310	0.0318	0.6639
	X/L_p	0.5392	0.5161	0.0234	0.8548	1.0434
	Y/L_p	0.2921	0.2613	0.4076	0.4153	0.5038
	$\lvert\Delta\varepsilon_r^-\rvert$	0.0142	0.3580	0.0296	0.0302	0.6708
	X/L_p	0.5661	0.5084	0.6700	0.5161	1.0627
	Y/L_p	0.2921	0.4538	0.3499	0.3922	0.4923
05	$\lvert\Delta\varepsilon_r^+\rvert$	0.0213	0.3849	0.0304	0.0312	0.5729
	X/L_p	0.2004	0.9241	0.9895	0.5700	0.3621
	Y/L_p	0.2382	0.2344	0.4884	0.1266	0.5077

Table D.4 – continued from previous page

Test		$\overline{u}$	$\overline{w}$	$\overline{u'}$	$\overline{w}$	$\overline{u'w'}$
	$\lvert\Delta\varepsilon_r^-\rvert$	0.0214	0.3839	0.0289	0.0297	0.5664
	X/L_p	0.7162	0.0118	0.7432	0.0773	0.2235
	Y/L_p	0.2536	0.2729	0.1035	0.2151	0.4846
06	$\lvert\Delta\varepsilon_r^+\rvert$	0.0156	0.3016	0.0320	0.0320	0.4982
	X/L_p	0.6354	0.5546	0.7470	0.5546	0.4391
	Y/L_p	0.2459	0.4769	0.4961	0.4384	0.3806
	$\lvert\Delta\varepsilon_r^-\rvert$	0.0156	0.3015	0.0307	0.0305	0.5009
	X/L_p	0.7355	0.5122	0.6354	0.6469	0.5122
	Y/L_p	0.2267	0.2767	0.3845	0.3460	0.4037
07	$\lvert\Delta\varepsilon_r^+\rvert$	0.0207	0.3688	0.0309	0.0317	0.6681
	X/L_p	0.3313	0.8009	0.0965	1.0357	0.9780
	Y/L_p	0.2575	0.0727	0.3729	0.0689	0.5115
	$\lvert\Delta\varepsilon_r^-\rvert$	0.0208	0.3661	0.0295	0.0302	0.6674
	X/L_p	0.9934	0.4314	0.9664	0.9780	0.1774
	Y/L_p	0.2459	0.0073	0.4461	0.0535	0.3229
08	$\lvert\Delta\varepsilon_r^+\rvert$	0.0157	0.2471	0.0323	0.0324	0.5436
	X/L_p	0.6316	0.8702	0.1196	0.5199	0.2813
	Y/L_p	0.2882	0.2267	0.3267	0.1304	0.4153
	$\lvert\Delta\varepsilon_r^-\rvert$	0.0159	0.2463	0.0309	0.0309	0.5447
	X/L_p	0.6393	1.0357	0.5777	0.8663	0.5238
	Y/L_p	0.2882	0.5115	0.3575	0.4268	0.4268
09	$\lvert\Delta\varepsilon_r^+\rvert$	0.0224	0.6060	0.0299	0.0311	0.4556
	X/L_p	0.3390	0.6123	1.1165	0.7894	0.6777
	Y/L_p	0.2498	0.4345	0.4769	0.0496	0.0304
	$\lvert\Delta\varepsilon_r^-\rvert$	0.0223	0.6068	0.0285	0.0295	0.4532
	X/L_p	0.5353	0.8548	0.3044	1.1473	0.8048
	Y/L_p	0.1920	0.2882	0.3729	0.4692	0.0419
10a	$\lvert\Delta\varepsilon_r^+\rvert$	0.0389	0.7007	0.1563	0.1570	3.6397
	X/L_p	0.9748	0.2204	0.7131	0.7978	0.8901
	Y/L_p	0.0147	0.4343	0.3573	0.0493	0.0609
	$\lvert\Delta\varepsilon_r^-\rvert$	0.0397	0.6984	0.1273	0.1279	3.6930
	X/L_p	0.9133	0.8132	0.7747	1.0826	0.8209

Table D.4 – continued from previous page

Test		$\overline{u}$	$\overline{w}$	$\overline{u'}$	$\overline{w}$	$\overline{u'w'}$
	Y/L_p	0.0917	0.1263	0.4920	0.2957	0.2187
10b	$\lvert\Delta\varepsilon_r^+\rvert$	0.0514	0.9469	0.1663	0.1709	3.4656
	X/L_p	0.5245	1.1365	0.6207	0.5245	0.6861
	Y/L_p	0.3419	0.2302	0.1687	0.2302	0.4227
	$\lvert\Delta\varepsilon_r^-\rvert$	0.0526	0.9537	0.1345	0.1378	3.5249
	X/L_p	0.3782	0.1010	0.8825	0.7785	0.2743
	Y/L_p	0.3419	0.2649	0.2687	0.2572	0.4304
10c	$\lvert\Delta\varepsilon_r^+\rvert$	0.0597	1.0466	0.2006	0.2054	4.3491
	X/L_p	0.6130	0.7246	0.9248	1.0711	0.4898
	Y/L_p	0.3342	0.3957	0.4804	0.1186	0.1802
	$\lvert\Delta\varepsilon_r^-\rvert$	0.0610	1.0425	0.1567	0.1595	4.3335
	X/L_p	0.5899	1.2173	0.5052	0.6284	0.5976
	Y/L_p	0.3457	0.1918	0.2379	0.0493	0.1725
10d	$\lvert\Delta\varepsilon_r^+\rvert$	0.0475	1.0761	0.1693	0.1744	4.1924
	X/L_p	0.9133	0.5630	0.3243	0.5707	1.0056
	Y/L_p	0.1802	0.0147	0.4535	0.4112	0.3380
	$\lvert\Delta\varepsilon_r^-\rvert$	0.0496	1.0728	0.1365	0.1407	4.1880
	X/L_p	0.7169	0.8209	0.7015	0.5630	1.1827
	Y/L_p	0.2803	0.0647	0.1687	0.4573	0.3688
10e	$\lvert\Delta\varepsilon_r^+\rvert$	0.1028	2.0644	0.3993	0.4080	7.3090
	X/L_p	0.9094	1.0595	0.7554	0.3666	0.6707
	Y/L_p	0.3342	0.1148	0.0108	0.1802	0.0686
	$\lvert\Delta\varepsilon_r^-\rvert$	0.1055	2.0765	0.2741	0.2787	7.4397
	X/L_p	1.0980	0.2396	0.7208	0.6130	0.4860
	Y/L_p	0.2071	0.0301	0.2726	0.4189	0.1648
10f	$\lvert\Delta\varepsilon_r^+\rvert$	0.0359	0.7163	0.1349	0.1368	4.1050
	X/L_p	0.4398	0.7747	0.5976	0.7439	0.6400
	Y/L_p	0.1494	0.0301	0.1687	0.4112	0.2495
	$\lvert\Delta\varepsilon_r^-\rvert$	0.0369	0.7140	0.1125	0.1139	4.1212
	X/L_p	0.5822	0.6707	0.4590	0.3859	0.6015
	Y/L_p	0.0917	0.4458	0.0493	0.2033	0.0378
10g	$\lvert\Delta\varepsilon_r^+\rvert$	0.0383	0.6951	0.1784	0.1817	4.3050

Table D.4 – continued from previous page

Test		$\overline{u}$	$\overline{w}$	$\overline{u'}$	$\overline{w}$	$\overline{u'w'}$
	X/L_p	1.1712	0.6438	0.0626	1.1827	0.8979
	Y/L_p	0.2918	0.3765	0.0609	0.3072	0.4265
	$\lvert\Delta\varepsilon_r^-\rvert$	0.0398	0.7008	0.1423	0.1437	4.4160
	X/L_p	1.2020	0.6669	0.8093	1.0942	0.8209
	Y/L_p	0.2726	0.4343	0.5112	0.3534	0.2610
10h	$\lvert\Delta\varepsilon_r^+\rvert$	0.0343	0.5167	0.1449	0.1468	3.8367
	X/L_p	0.7554	0.1472	1.1019	0.0626	0.7862
	Y/L_p	0.0378	0.4535	0.1994	0.2918	0.3303
	$\lvert\Delta\varepsilon_r^-\rvert$	0.0358	0.5217	0.1190	0.1201	3.8980
	X/L_p	0.7708	0.7439	0.2204	0.2743	1.0711
	Y/L_p	0.1109	0.4958	0.4843	0.1648	0.2148
11a	$\lvert\Delta\varepsilon_r^+\rvert$	0.0360	0.9048	0.1758	0.1762	4.5463
	X/L_p	0.8093	0.7246	0.9094	1.0634	0.8979
	Y/L_p	0.0840	0.3226	0.2033	0.3804	0.2764
	$\lvert\Delta\varepsilon_r^-\rvert$	0.0371	0.9113	0.1410	0.1401	4.6364
	X/L_p	0.4128	0.9556	0.6938	0.5476	0.7285
	Y/L_p	0.3419	0.0108	0.0532	0.2418	0.3226
11b	$\lvert\Delta\varepsilon_r^+\rvert$	0.0444	1.0748	0.1810	0.1811	3.5480
	X/L_p	0.9825	0.4667	0.0356	0.7785	0.9941
	Y/L_p	0.0185	0.1994	0.4458	0.1379	0.1148
	$\lvert\Delta\varepsilon_r^-\rvert$	0.0455	1.0659	0.1445	0.1434	3.5679
	X/L_p	1.0903	0.4205	0.5360	0.3898	0.4128
	Y/L_p	0.0416	0.0301	0.4381	0.1456	0.1841
11c	$\lvert\Delta\varepsilon_r^+\rvert$	0.0749	1.8363	0.3520	0.3558	6.6398
	X/L_p	1.1403	1.1558	1.0326	0.8825	1.2173
	Y/L_p	0.2071	0.0609	0.0378	0.5074	0.3188
	$\lvert\Delta\varepsilon_r^-\rvert$	0.0759	1.8454	0.2485	0.2452	6.5910
	X/L_p	1.0480	1.1827	0.8093	0.6477	0.2974
	Y/L_p	0.0262	0.0493	0.4958	0.4227	0.3496
11d	$\lvert\Delta\varepsilon_r^+\rvert$	0.0538	1.0895	0.2227	0.2250	5.0741
	X/L_p	0.6861	0.3821	0.1395	0.9055	0.4090
	Y/L_p	0.3111	0.0147	0.2918	0.1533	0.3226

Table D.4 – continued from previous page

Test		$\overline{u}$	$\overline{w}$	$\overline{u'}$	$\overline{w}$	$\overline{u'w'}$
	$\lvert\Delta\varepsilon_r^-\rvert$	0.0541	1.0857	0.1712	0.1717	5.1684
	X/L_p	0.5322	0.5322	0.8517	0.9633	0.2704
	Y/L_p	0.3611	0.4496	0.0917	0.3380	0.4766
11e	$\lvert\Delta\varepsilon_r^+\rvert$	0.0341	0.7548	0.1190	0.1198	3.0839
	X/L_p	0.9902	1.0826	0.2897	0.2858	0.8247
	Y/L_p	0.3419	0.3957	0.2726	0.0686	0.3842
	$\lvert\Delta\varepsilon_r^-\rvert$	0.0341	0.7524	0.1012	0.1018	3.1210
	X/L_p	1.1558	0.5630	0.8670	0.9094	0.7747
	Y/L_p	0.2495	0.4496	0.4227	0.5074	0.1609
11f	$\lvert\Delta\varepsilon_r^+\rvert$	0.0514	1.0574	0.2157	0.2197	5.9750
	X/L_p	1.1173	1.0903	0.6938	0.9440	0.4629
	Y/L_p	0.3265	0.3226	0.3804	0.1186	0.1725
	$\lvert\Delta\varepsilon_r^-\rvert$	0.0530	1.0561	0.1667	0.1683	5.9855
	X/L_p	0.5091	0.4898	0.0318	0.9133	0.6630
	Y/L_p	0.0724	0.0070	0.2456	0.5112	0.1725
11g	$\lvert\Delta\varepsilon_r^+\rvert$	0.0432	0.8174	0.2000	0.1997	5.2138
	X/L_p	1.1904	0.8132	0.4590	1.0942	0.5976
	Y/L_p	0.2610	0.1725	0.0955	0.2880	0.2187
	$\lvert\Delta\varepsilon_r^-\rvert$	0.0452	0.8259	0.1570	0.1554	5.2583
	X/L_p	1.1827	0.7593	0.5591	0.0510	0.0433
	Y/L_p	0.3419	0.0801	0.1186	0.3072	0.4689
11h	$\lvert\Delta\varepsilon_r^+\rvert$	0.0426	0.7581	0.2053	0.2065	5.1579
	X/L_p	1.2097	1.2135	0.4667	0.8901	0.3666
	Y/L_p	0.2841	0.1879	0.2880	0.4189	0.0570
	$\lvert\Delta\varepsilon_r^-\rvert$	0.0451	0.7601	0.1601	0.1592	5.2019
	X/L_p	0.6938	0.6053	1.1481	0.3821	0.6169
	Y/L_p	0.1263	0.1109	0.4189	0.0416	0.1879
12a	$\lvert\Delta\varepsilon_r^+\rvert$	0.0196	1.8220	0.2330	0.2422	4.6836
	X/L_p	0.6630	0.1203	0.0779	1.1750	0.5861
	Y/L_p	0.1494	0.4189	0.2264	0.0108	0.1841
	$\lvert\Delta\varepsilon_r^-\rvert$	0.0200	1.7990	0.1790	0.1834	4.7433
	X/L_p	1.0788	0.9902	0.4744	0.9364	0.5976

Table D.4 – continued from previous page

Test		$\overline{u}$	$\overline{w}$	$\overline{u'}$	$\overline{w}$	$\overline{u'w'}$
	Y/L_p	0.0262	0.3727	0.3072	0.3380	0.2110
12b	$\lvert\Delta\varepsilon_r^+\rvert$	0.0173	1.9077	0.1798	0.1911	3.7426
	X/L_p	0.4513	0.6361	0.5861	0.7285	0.4937
	Y/L_p	0.0108	0.0147	0.3688	0.4343	0.4920
	$\lvert\Delta\varepsilon_r^-\rvert$	0.0178	1.8988	0.1473	0.1522	3.7464
	X/L_p	1.0903	0.8786	0.6861	0.4590	0.4051
	Y/L_p	0.0763	0.4420	0.1533	0.1533	0.5112
12c	$\lvert\Delta\varepsilon_r^+\rvert$	0.0150	1.3746	0.1599	0.1670	3.5147
	X/L_p	1.1943	0.4205	0.7208	0.9364	0.3898
	Y/L_p	0.0878	0.0801	0.2649	0.4920	0.4073
	$\lvert\Delta\varepsilon_r^-\rvert$	0.0153	1.3799	0.1323	0.1360	3.5390
	X/L_p	0.4513	0.9210	0.9517	0.8594	1.1750
	Y/L_p	0.0532	0.0609	0.4804	0.2110	0.4958
12d	$\lvert\Delta\varepsilon_r^+\rvert$	0.0189	1.6719	0.2012	0.2124	3.7704
	X/L_p	0.7323	0.6400	0.0125	1.0865	1.1134
	Y/L_p	0.0147	0.0147	0.2995	0.1340	0.4073
	$\lvert\Delta\varepsilon_r^-\rvert$	0.0195	1.6473	0.1592	0.1657	3.8369
	X/L_p	0.5591	0.6015	0.6400	0.5437	0.3590
	Y/L_p	0.0147	0.0147	0.4727	0.0532	0.5035
12e	$\lvert\Delta\varepsilon_r^+\rvert$	0.0275	2.0150	0.3322	0.3479	5.6571
	X/L_p	1.0210	0.9094	0.3859	0.1780	0.8286
	Y/L_p	0.0378	0.0609	0.2610	0.0416	0.1648
	$\lvert\Delta\varepsilon_r^-\rvert$	0.0281	1.9831	0.2347	0.2447	5.8124
	X/L_p	0.5052	0.8901	0.5052	0.3666	1.1019
	Y/L_p	0.0686	0.0994	0.3380	0.4997	0.3573
12f	$\lvert\Delta\varepsilon_r^+\rvert$	0.0297	2.3799	0.3578	0.3742	6.6310
	X/L_p	0.9671	0.3282	0.3205	1.1943	0.2589
	Y/L_p	0.2995	0.5112	0.4689	0.1456	0.3072
	$\lvert\Delta\varepsilon_r^-\rvert$	0.0315	2.3467	0.2555	0.2561	6.5774
	X/L_p	0.8594	1.2058	0.3551	1.1596	0.8478
	Y/L_p	0.0224	0.4651	0.4304	0.2957	0.2418
12g	$\lvert\Delta\varepsilon_r^+\rvert$	0.0308	2.0944	0.3747	0.3847	6.1483

Table D.4 – continued from previous page

Test		$\overline{u}$	$\overline{w}$	$\overline{u'}$	$\overline{w}$	$\overline{u'w'}$
	X/L_p	0.2550	1.2135	0.9325	0.0164	0.7092
	Y/L_p	0.0378	0.2071	0.4804	0.0493	0.0724
	$\left\|\Delta\varepsilon_r^-\right\|$	0.0327	2.0402	0.2607	0.2636	6.2489
	X/L_p	0.4667	0.7747	0.3397	0.4513	0.3628
	Y/L_p	0.1841	0.0647	0.4997	0.4881	0.2764
12h	$\left\|\Delta\varepsilon_r^+\right\|$	0.0253	2.1796	0.3073	0.3170	5.9391
	X/L_p	0.3551	0.0202	0.1010	1.1211	0.4090
	Y/L_p	0.0147	0.2495	0.1687	0.0455	0.3149
	$\left\|\Delta\varepsilon_r^-\right\|$	0.0263	2.1534	0.2245	0.2257	6.0378
	X/L_p	0.9440	1.1096	0.7208	0.1819	0.8132
	Y/L_p	0.0455	0.0070	0.2495	0.4189	0.3457

APPENDIX E

RESULTS FOR MEAN TURBULENT TRANSPORT: TURBULENT CHARACTERISTICS OF THE DYNAMICALLY STABLE PLATE

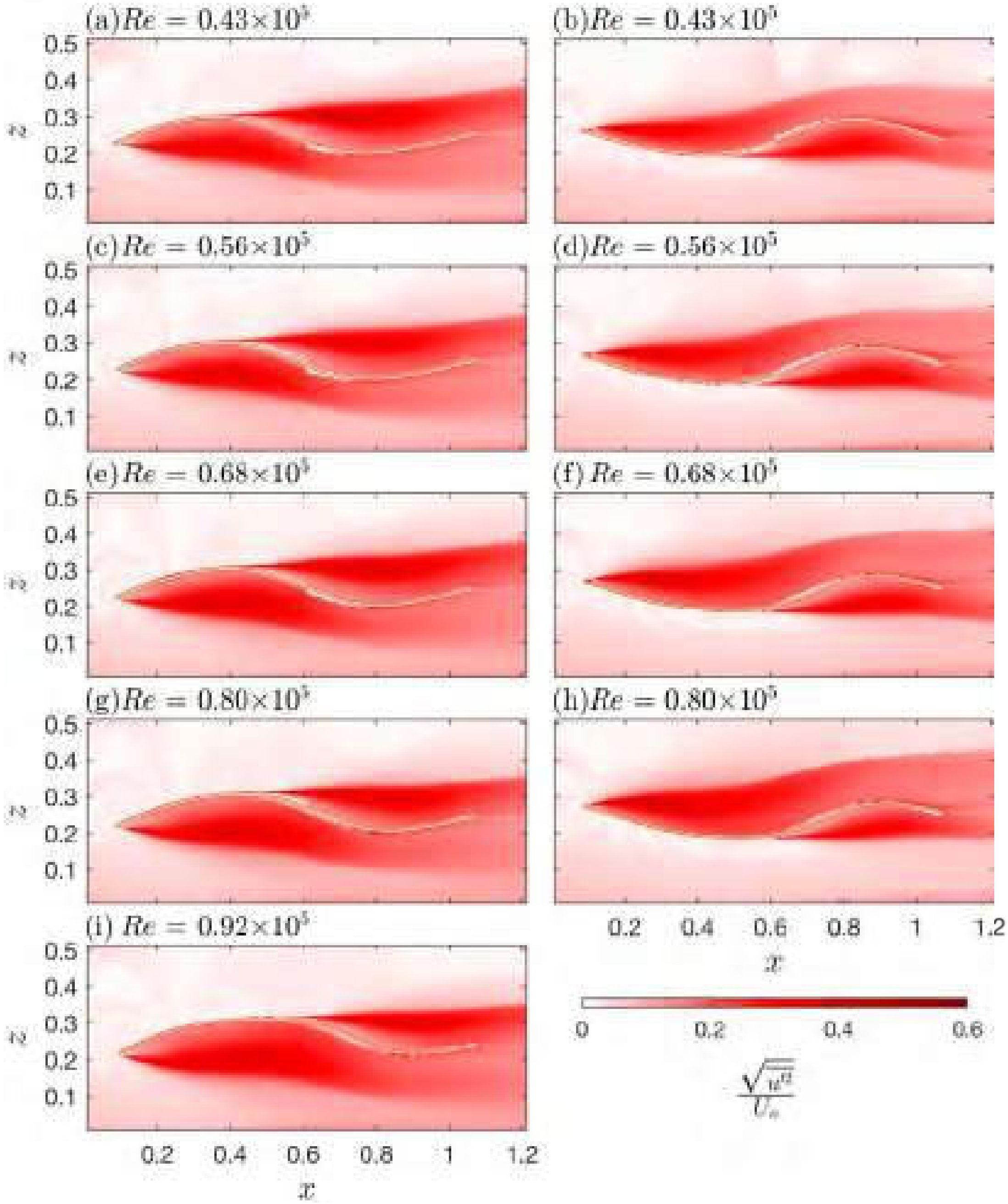

Figure E.1: Mean horizontal turbulent intensity.

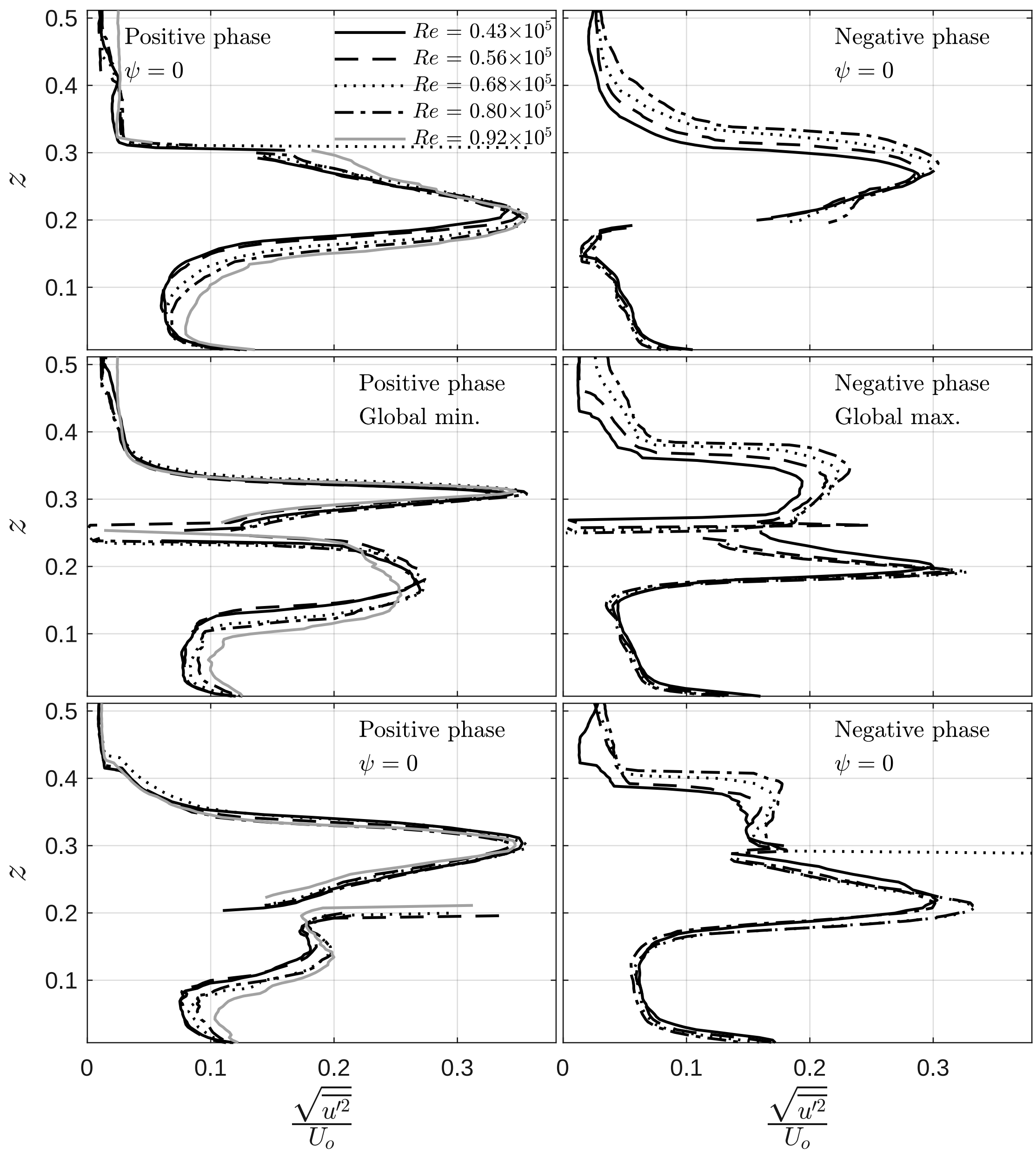

Figure E.2: Evolution of mean horizontal turbulent intensity on plate's curvature extrema.

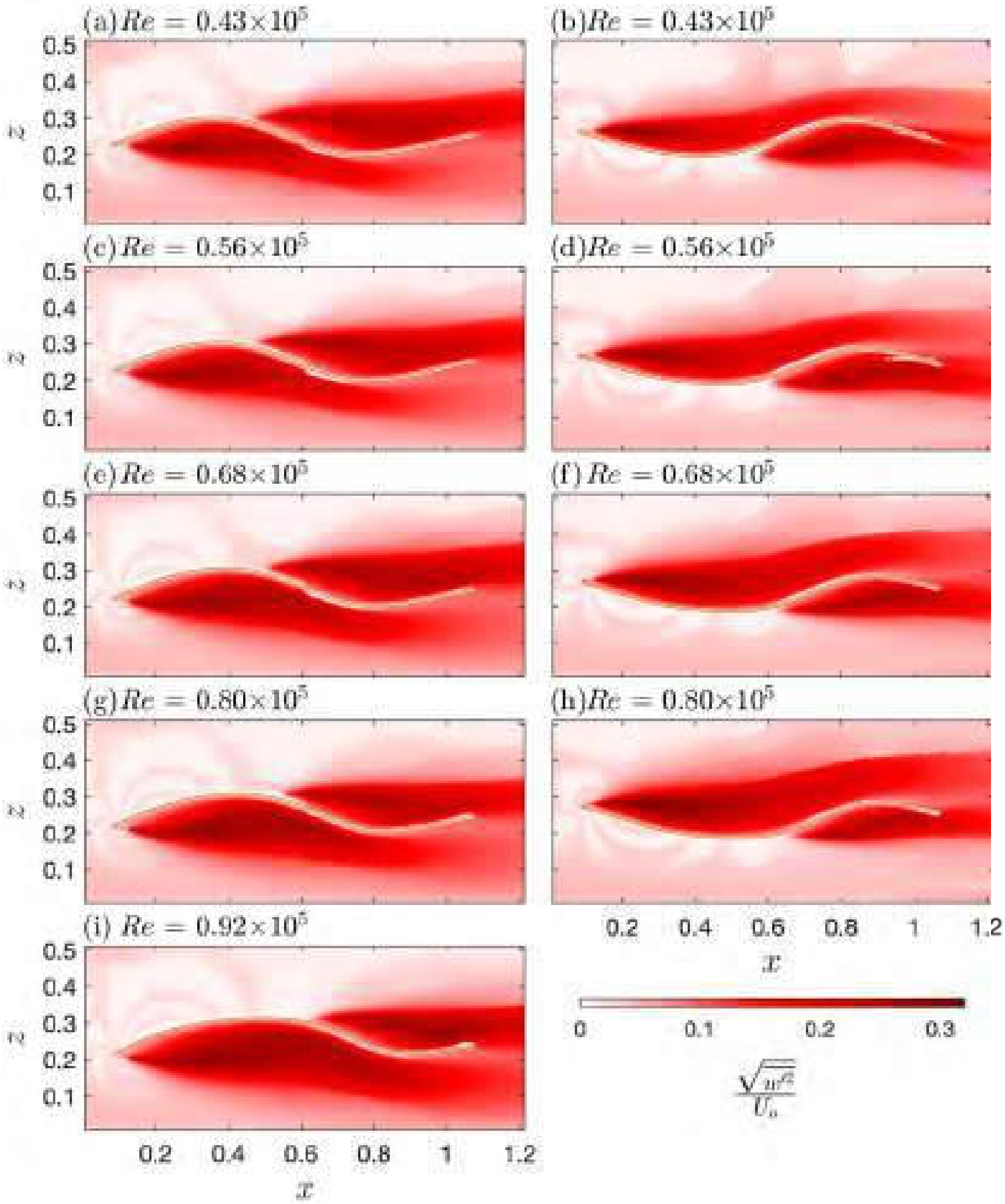

Figure E.3: Mean vertical turbulent intensity.

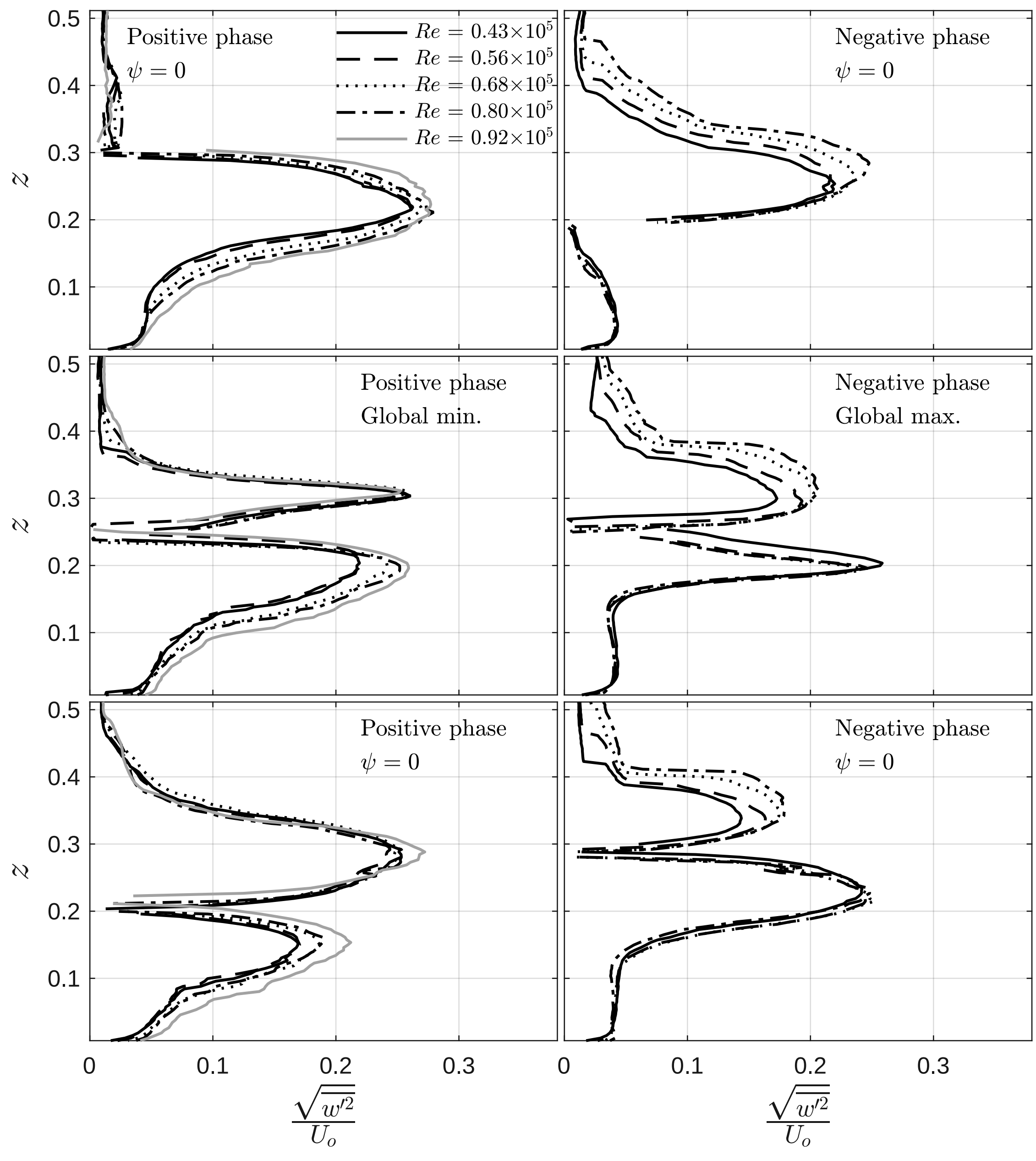

Figure E.4: Evolution of mean vertical turbulent intensity on plate's curvature extrema.

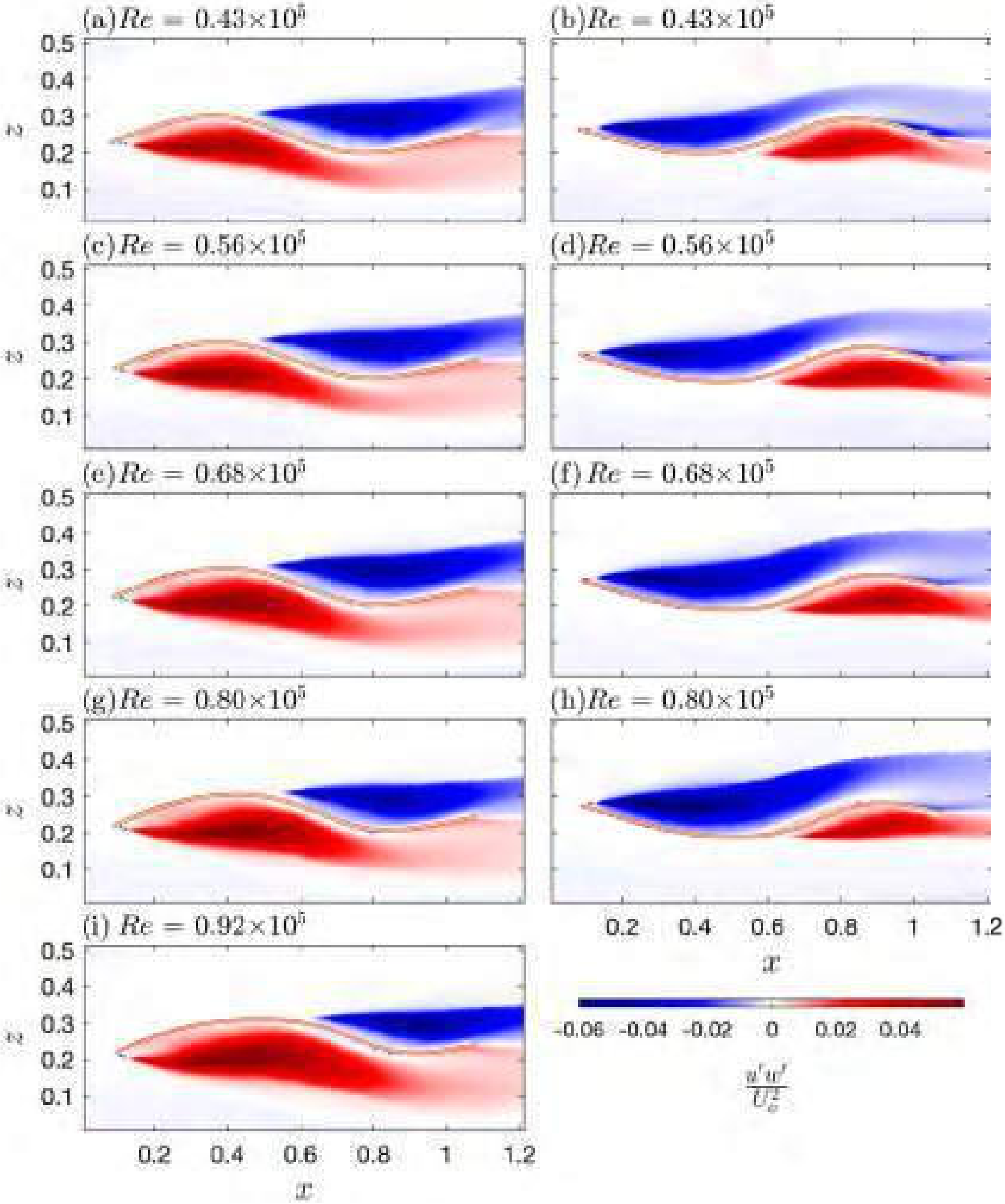

Figure E.5: Mean Reynolds stress.

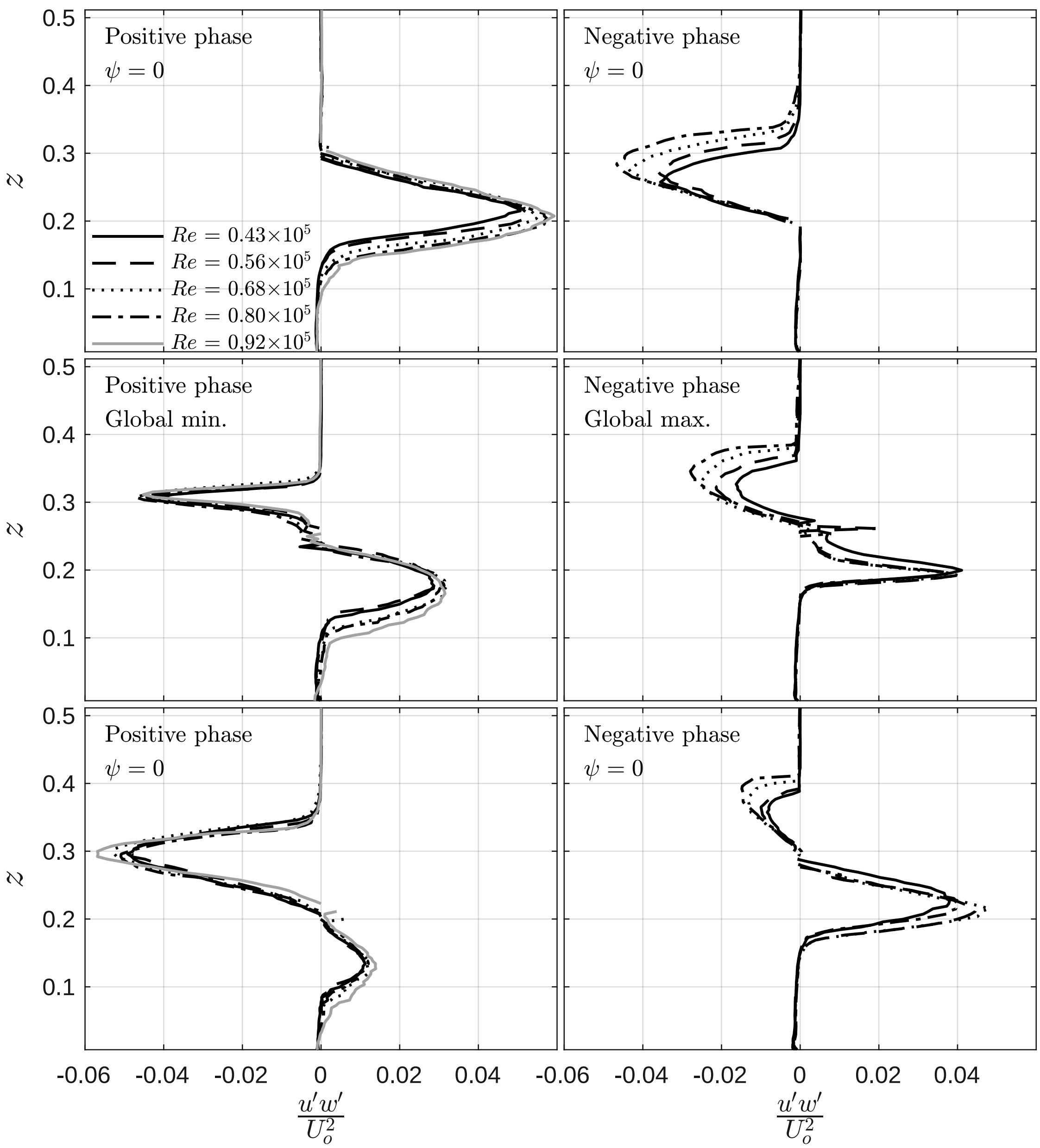

Figure E.6: Evolution of turbulent vertical transport of horizontal momentum on plate's curvature extrema.

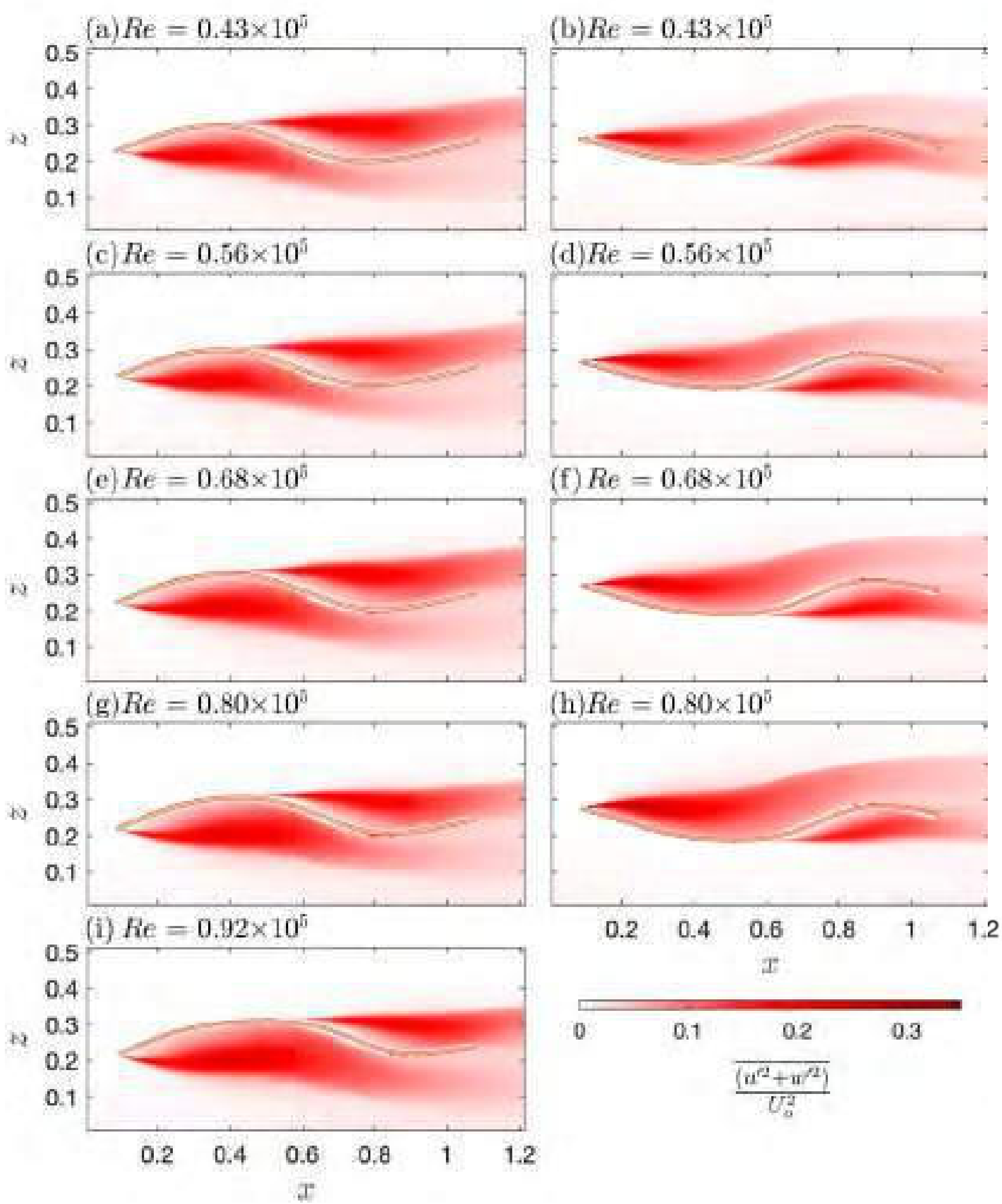

Figure E.7: Mean kinetic energy estimate.

APPENDIX F

EXAMPLE OF VORTICITY FIELD AT FLOW VELOCITIES WHERE PHASE-AVERAGE PROCEDURE BECOMES CHALLENGING

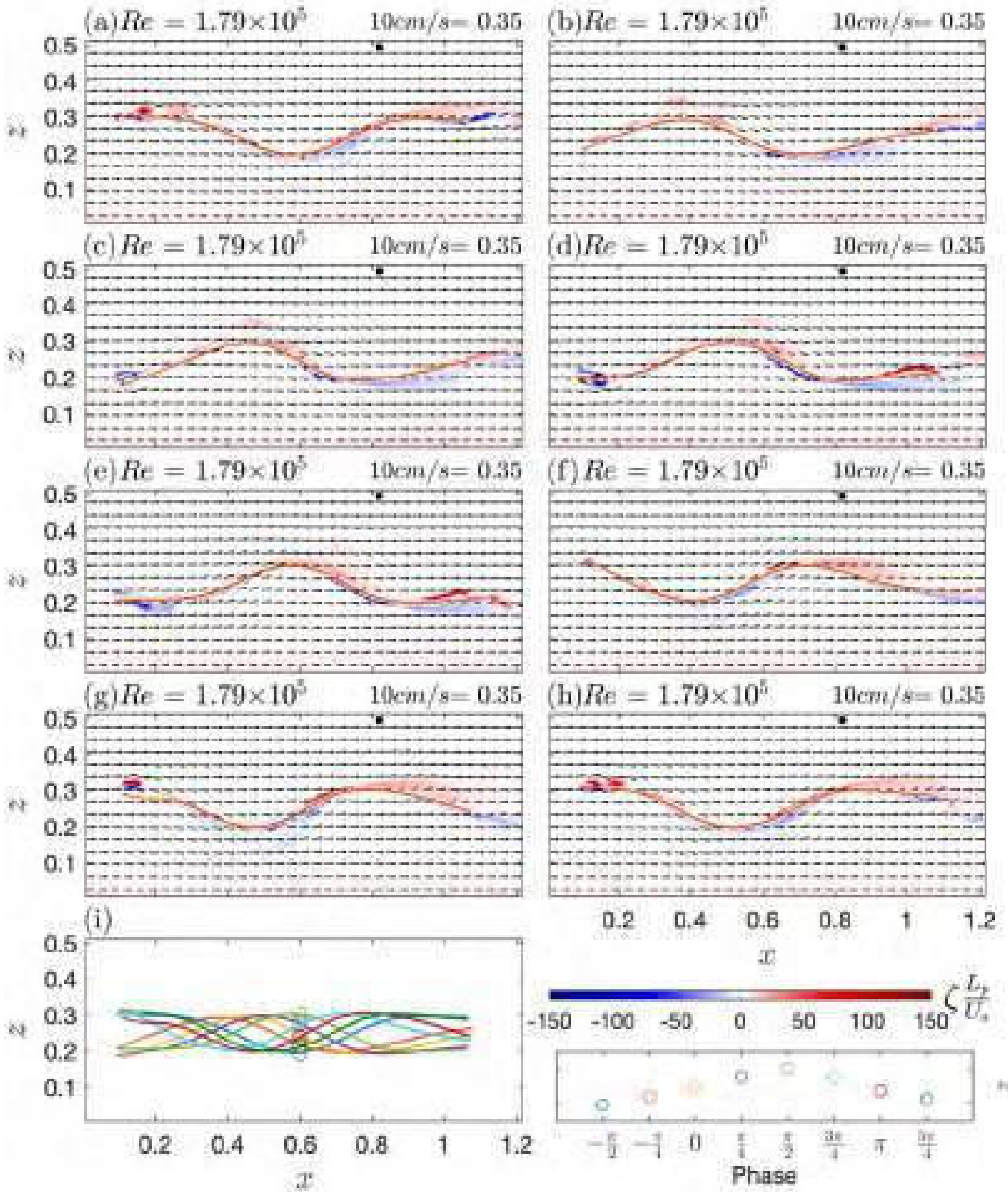

Figure F.1: Phase-averaged two dimensional vorticity fields for $Re = 1.79\times 10^5$.

APPENDIX G

RESULTS FOR PHASE-AVERAGED MEAN TURBULENT TRANSPORT: TURBULENT CHARACTERISTICS OF THE DYNAMICALLY UNSTABLE PLATE

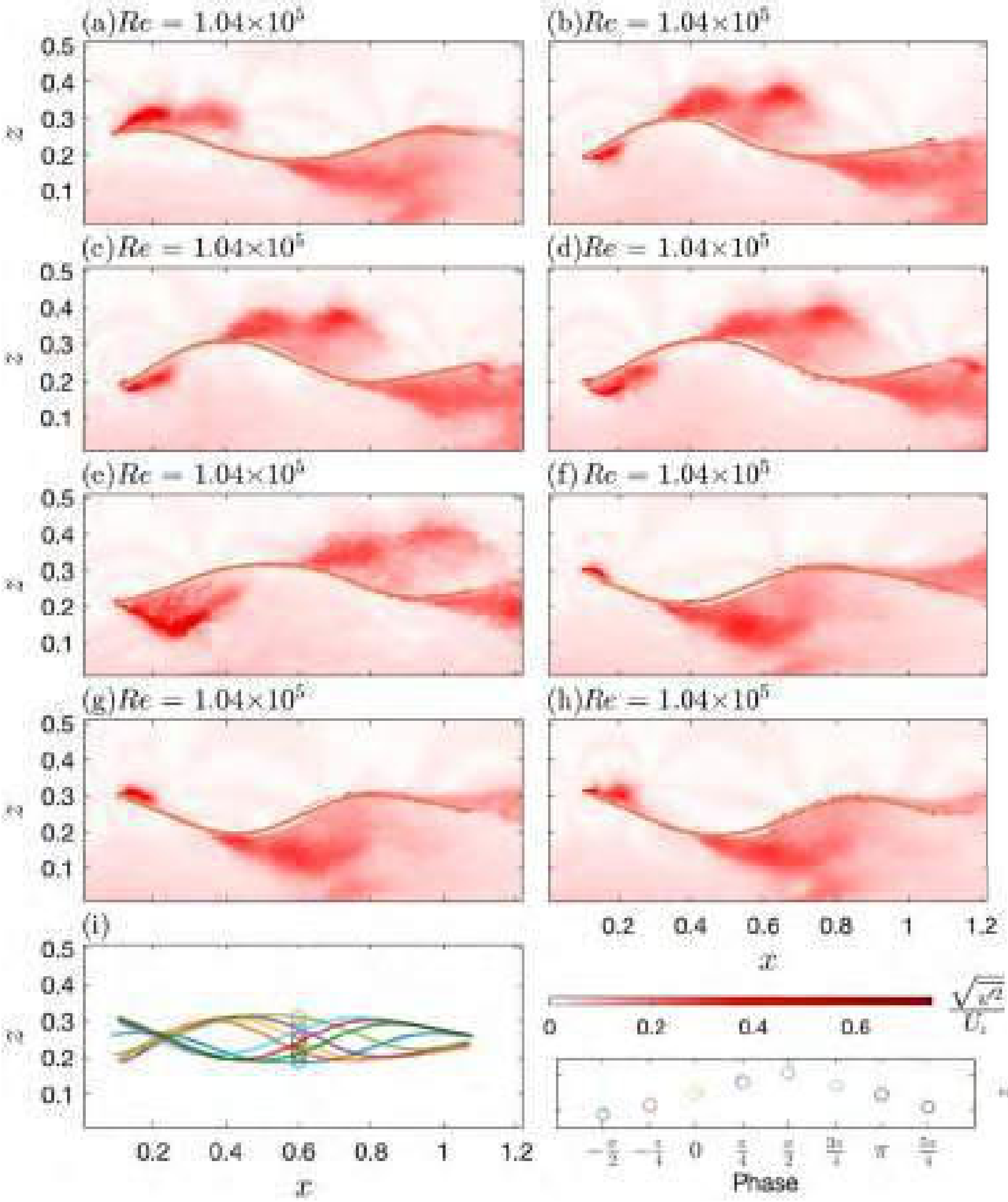

Figure G.1: Phase averaged horizontal turbulent intensity for $Re = 1.05 \times 10^5$.

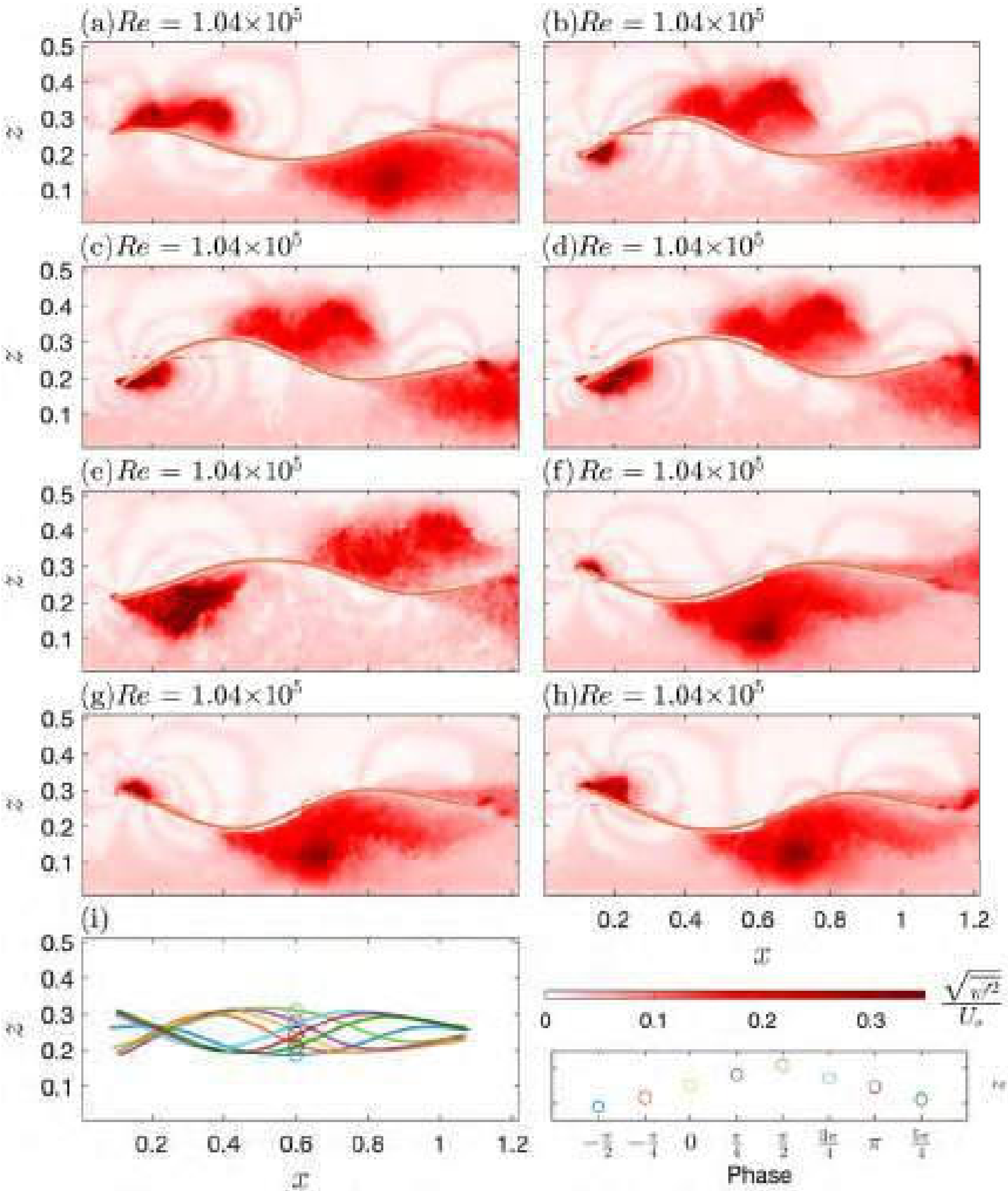

Figure G.2: Phase averaged vertical turbulent intensity for $Re = 1.05\times10^5$.

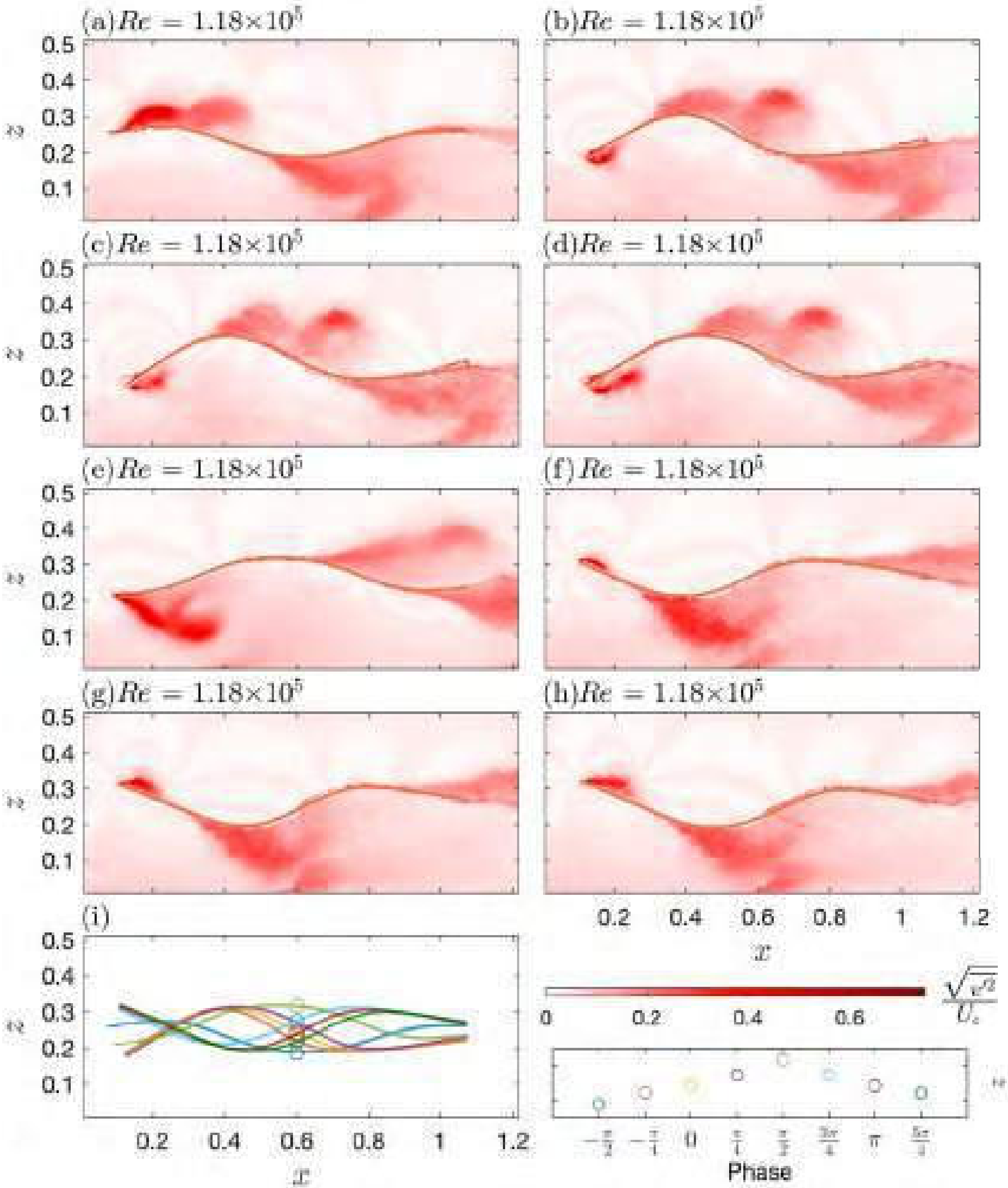

Figure G.3: Phase averaged horizontal turbulent intensity for $Re = 1.19 \times 10^5$.

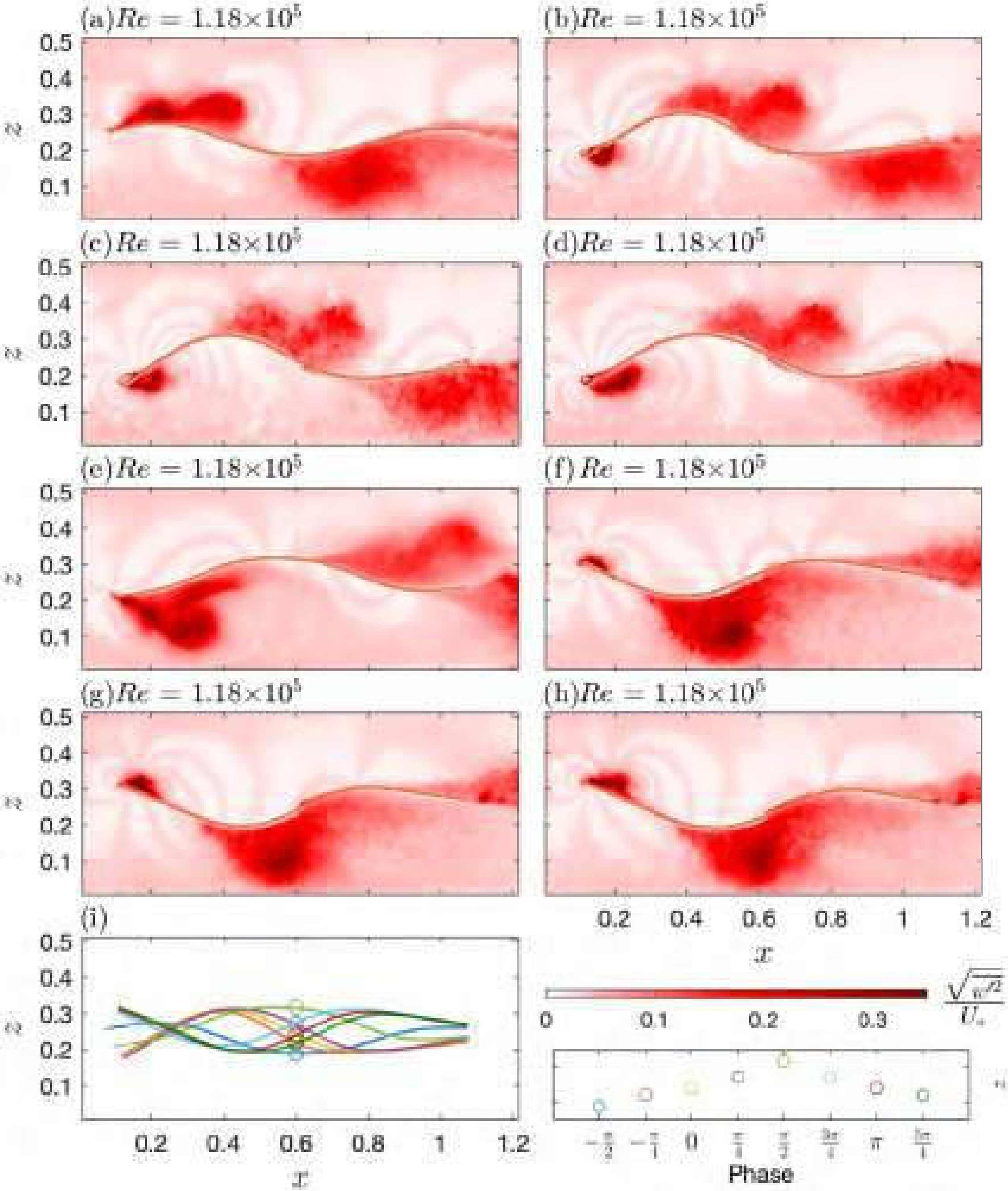

Figure G.4: Phase averaged vertical turbulent intensity for $Re = 1.19\times10^5$.

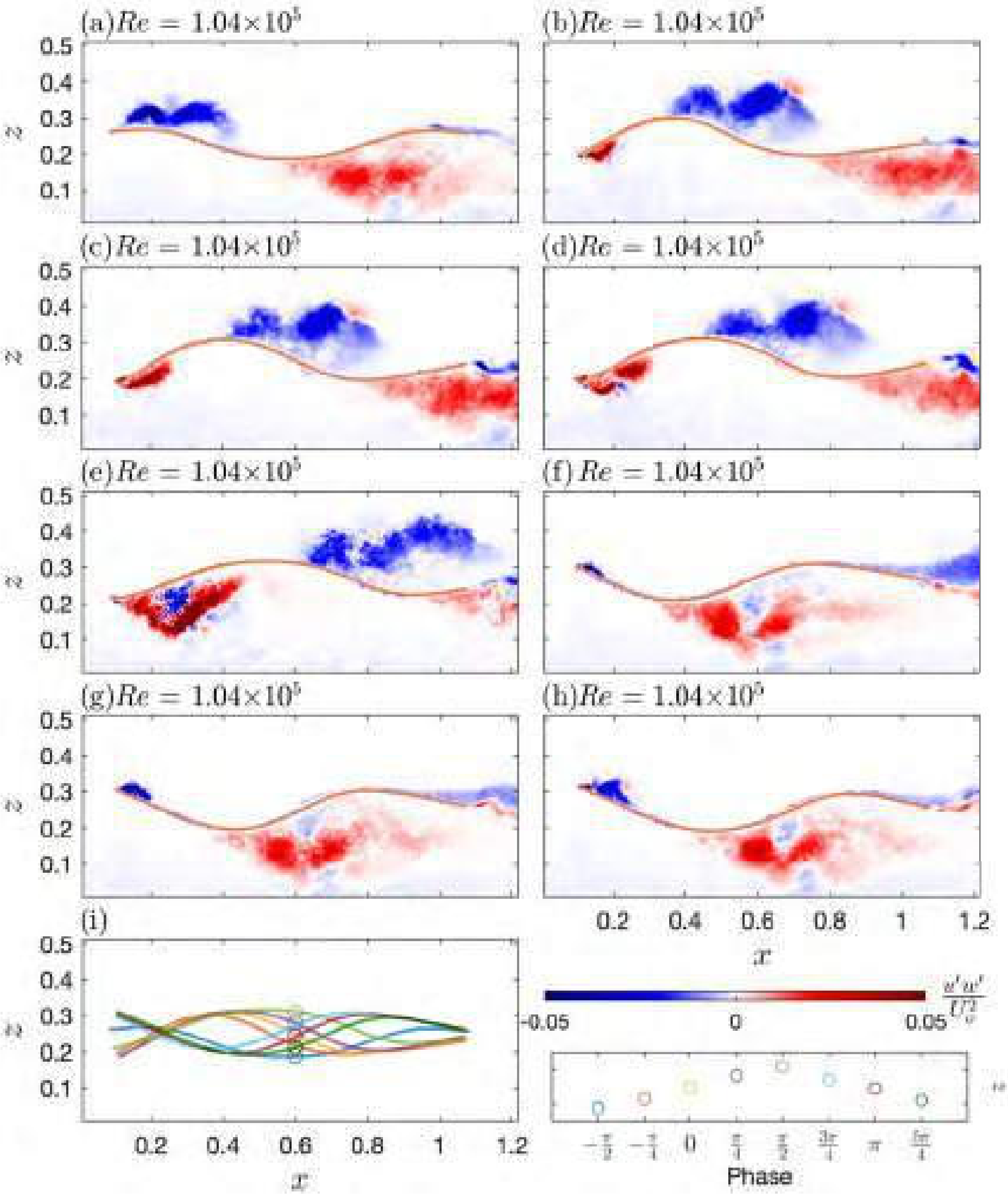

Figure G.5: Phase averaged Reynolds stress for $Re = 1.05 \times 10^5$.

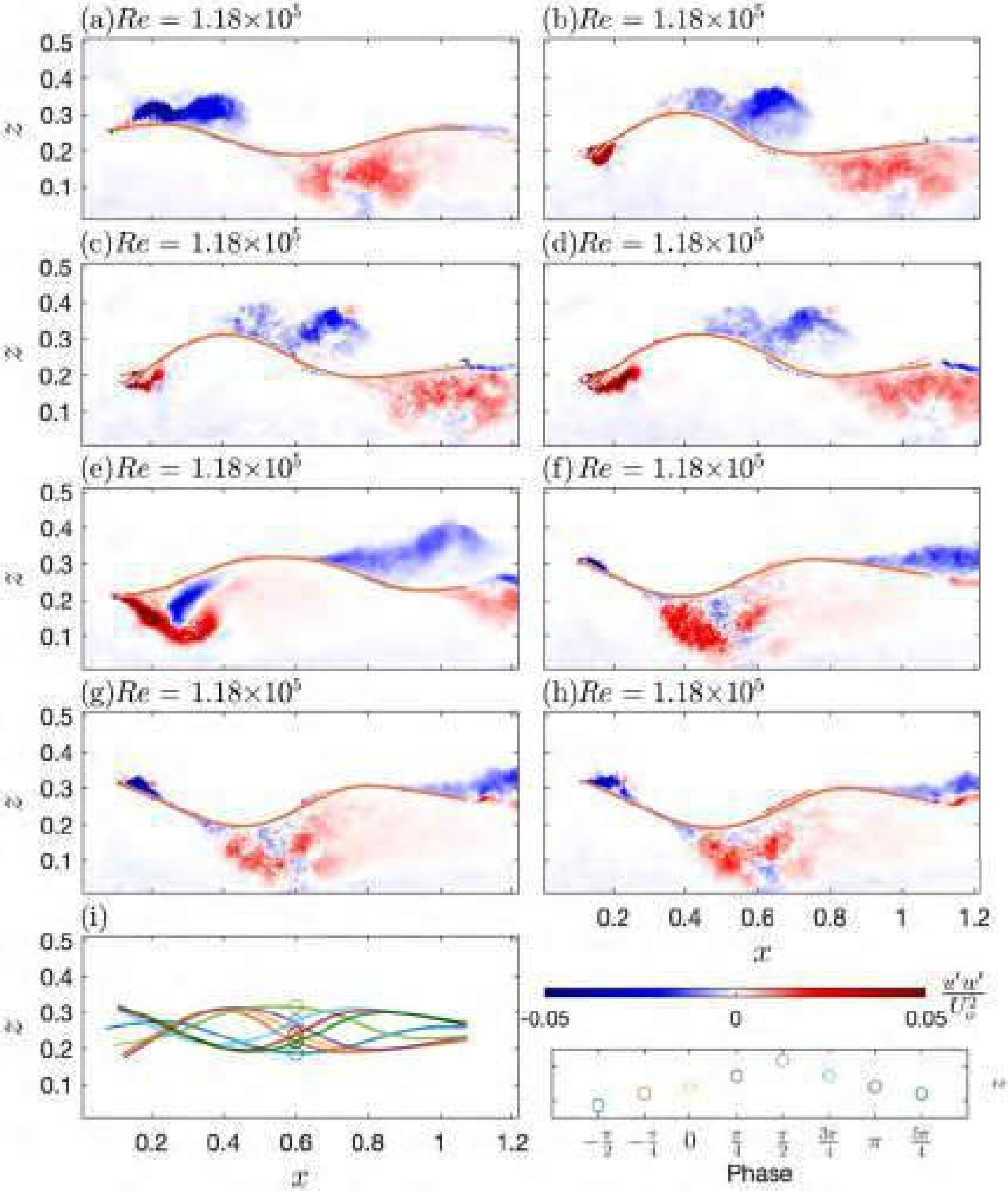

Figure G.6: Phase averaged Reynolds stress for $Re = 1.19 \times 10^5$.

APPENDIX H

ON THE LIMITATION OF TWO-DIMENSIONAL FOURIER TRANSFORM $2DFT$ AND COMPLEX ORTHOGONAL DECOMPOSITION COD TO DETERMINE WAVE NUMBERS, κ

The calculation of wave numbers, κ, is limited when implementing both $2DFT$ and COD because the induced deformation presents less than two wavelengths, λ (i.e., the truncated sinusoid does not have a finite bandwidth). To partially overcome this limitation, the data was padded with zeros to increase the sampling frequency of the sinusoid (i.e., decrease width of frequency bins) and reduce aliasing.

BIBLIOGRAPHY

(2012). ASTM D882-12(2012). Standard test method for tensile properties of thin plastic sheeting.

(2015). ASTM D2256/D2256M-10(2015). Standard test method for tensile properties of yarns by the single-strand method.

Akaydin, H. D., Elvin, N., and Andreopoulos, Y. (2010). Wake of a cylinder: a paradigm for energy harvesting with piezoelectric materials. *Exp. Fluids*, 49(1):291–304.

Akcabay, D. T. and Young, Y. L. (2012). Hydroelastic response and energy harvesting potential of flexible piezoelectric beams in viscous flow. *Phys. Fluids*, 24(5):054106.

Alben, S. and Shelley, M. J. (2008). Flapping states of a flag in an inviscid fluid: Bistability and the transition to chaos. *Phys. Rev. Lett.*, 100:074301.

Allen, J. J. and Smits, A. J. (2001). Energy harvesting eel. *J. Fluids Struct.*, 15(3-4):629–640.

Auman, L. and Wilks, B. (2005). Application of fabric ribbons for drag and stabilization. In *18th AIAA Aerodynamic Decelerator Systems Technology Conference and Seminar*, pages 1—9. American Institute of Aeronautics and Astronautics.

Balint, T. S. and Lucey, A. D. (2005). Instability of a cantilevered flexible plate in viscous channel flow. *J. Fluids Struct.*, 20(7):893 – 912.

Bickley, W. G. (1934). L. the heavy elastica. *Lond. Edinb. Dubl. Phil. Mag.*, 17(113):603–622.

Bigoni, D. (2012). *Nonlinear solid mechanics: bifurcation theory and material instability*. Cambridge University Press, New York.

Chang, Y. B. and Moretti, P. M. (2002). Flow-induced vibration of free edges of thin films. *J. Fluids Struct.*, 16(7):989–1008.

Charonko, J. J., King, C. V., Smith, B. L., and Vlachos, P. P. (2010). Assessment of pressure field calculations from particle image velocimetry measurements. *Meas. Sci. Technol.*, 21(10):105401.

Cheng, J.-Y., Zhuang, L.-X., and Tong, B.-G. (1991). Analysis of swimming three-dimensional waving plates. *J. Fluid Mech.*, 232:341355.

Coene, R. (1992). Flutter of slender bodies under axial stress. *Appl. Sci. Res.*, 49(2):175–187.

Connell, B. S. H. and Yue, D. K. P. (2007). Flapping dynamics of a flag in a uniform stream. *J. Fluid Mech.*, 581:33–68.

Cowen, E. A. and Monismith, S. G. (1997). A hybrid digital particle tracking velocimetry technique. *Exp. Fluids*, 22(3):199–211.

Crisfield, M. A. (1986). Snap-through and snap-back response in concrete structures and the dangers of under-integration. *Int. J. Numer. Meth. Eng.*, 22(3):751–767.

Dabiri, J. O., Bose, S., Gemmell, B. J., Colin, S. P., and Costello, J. H. (2014). An algorithm to estimate unsteady and quasi-steady pressure fields from velocity field measurements. *J. Exp. Biol.*, 217(3):331–336.

de Kat, R. and van Oudheusden, B. W. (2012). Instantaneous planar pressure determination from piv in turbulent flow. *Exp. Fluids*, 52(5):1089–1106.

Devore, J. L. (2016). *Probability and Statistics for Engineering and the Sciences*. Cengage Learning, 9th edition.

Doaré, O. and Michelin, S. (2011). Piezoelectric coupling in energy-harvesting fluttering flexible plates: linear stability analysis and conversion efficiency. *J. Fluids Struct.*, 27(8):1357–1375.

Doaré, O., Sauzade, M., and Eloy, C. (2011). Flutter of an elastic plate in a channel flow: Confinement and finite-size effects. *J. Fluids Struct.*, 27(1):76–88.

Dowell, E. H. (1966). Nonlinear oscillations of a fluttering plate. *AIAA J.*, 4(7):1267–1275.

Dowell, E. H. (1967). Nonlinear oscillations of a fluttering plate. ii. *AIAA J.*, 5(10):1856–1862.

Dowell, E. H. (1970). Flutter of buckled plates at zero dynamic pressure. *AIAA J.*, 8(3):583–584.

Dowell, E. H. (1975). *Aeroelasticity of plates and shells*. Number 1. Noordhoff International Publishing, Leyden, 1st edition.

Dowell, E. H. (1982). Flutter of a buckled plate as an example of chaotic motion of a deterministic autonomous system. *J. Sound Vib.*, 85(3):333–344.

Dowell, E. H. (2015). *A modern course in aeroelasticity*. Springer, Switzerland, 5th edition.

Dowell, E. H. and Ilgamov, M. (1988). *Studies in nonlinear aeroelasticity*. Springer-Verlag, New York.

Dunnmon, J. A., Stanton, S. C., Mann, B. P., and Dowell, E. H. (2011). Power extraction from aeroelastic limit cycle oscillations. *J. Fluids Struct.*, 27(8):1182–1198.

Efron, B. and Tibshirani, R. J. (1994). *An introduction to the bootstrap*. CRC press.

Eloy, C., Kofman, N., and Schouveiler, L. (2012). The origin of hysteresis in the flag instability. *J. Fluid Mech.*, 691:583–593.

Eloy, C., Lagrange, R., Souilliez, C., and Schouveiler, L. (2008). Aeroelastic instability of cantilevered flexible plates in uniform flow. *J. Fluid Mech.*, 611:97–106.

Eloy, C., Souilliez, C., and Schouveiler, L. (2007). Flutter of a rectangular plate. *J. Fluids Struct.*, 23(6):904–919.

Fancett, R. K. and Clayden, W. A. (1972). Subsonic wind tunnel tests on the use of streamers to stabilize the foil bomblet. Technical Report Memorandum 14/70, Royal Armament Research and Development Establishment.

Feeny, B. (2008). A complex orthogonal decomposition for wave motion analysis. *J. Sound Vib.*, 310(1):77–90.

Feldman, M. (2011). *Hilbert Transform Applications in Mechanical Vibration*. John Wiley & Sons, United Kingdom, 1st edition.

Fenlon, A. J. and David, T. (2001a). Numerical models for the simulation of flexible artificial heart valves: Part i-computational methods. *Comput. Meth. Biomech. Biomed. Eng.*, 4(4):323–339.

Fenlon, A. J. and David, T. (2001b). Numerical models for the simulation of flexible artificial heart valves: Part ii-valve studies. *Comput. Meth. Biomech. Biomed. Eng.*, 4(6):449–462.

Filardo, B. P. (2013). Pliant or compliant elements for harnessing the forces of moving fluid to transport fluid or generate electricity. US Patent 8,432,057.

Ghaemi, S., Ragni, D., and Scarano, F. (2012). Piv-based pressure fluctuations in the turbulent boundary layer. *Exp. Fluids*, 53(6):1823–1840.

Ghaemi, S. and Scarano, F. (2013). Turbulent structure of high-amplitude pressure peaks within the turbulent boundary layer. *J. Fluid Mech.*, 735:381426.

Giacomello, A. and Porfiri, M. (2011). Underwater energy harvesting from a heavy flag hosting ionic polymer metal composites. *J. Appl. Phys.*, 109(8):084903.

Golubović, L., Moldovan, D., and Peredera, A. (1998). Dynamics of the euler buckling instability. *Phys. Rev. Lett.*, 81:3387–3390.

Gui, L., Wereley, S. T., and Kim, Y. H. (2003). Advances and applications of the digital mask technique in particle image velocimetry experiments. *Meas. Sci. Technol.*, 14(10):1820.

Harne, R. L. and Wang, K. W. (2013). A review of the recent research on vibration energy harvesting via bistable systems. *Smart Mater. Struct.*, 22(2):023001.

Howell, R. M., Lucey, A. D., Carpenter, P. W., and Pitman, M. W. (2009). Interaction between a cantilevered-free flexible plate and ideal flow. *J. Fluids Struct.*, 25(3):544 – 566.

Huang, L. (1995). Flutter of cantilevered plates in axial-flow. *J. Fluids Struct.*, 9(2):127–147.

Huang, W. X., Shin, S. J., and Sung, H. J. (2007). Simulation of flexible filaments in a uniform flow by the immersed boundary method. *J. Comput. Phys.*, 226(2):2206–2228.

Huber, G. (2000). Swimming in flatsea. *Nature*, 408(6814):777–778.

Jaiman, R. K., Loth, E., and Dutton, J. C. (2004). Simulations of normal shock-wave/boundary-layer interaction control using mesoflaps. *J. Propul. Power*, 20(2):344—352.

Jia, L. B. and Yin, X. Z. (2008). Passive oscillations of two tandem flexible filaments in a flowing soap film. *Phys. Rev. Lett.*, 100:228104.

Jia, L. B. and Yin, X. Z. (2009). Response modes of a flexible filament in the wake of a cylinder in a flowing soap film. *Phys. Fluids*, 21(10):101704.

Kim, D., Cossé, J., Cerdeira, C. H., and Gharib, M. (2013). Flapping dynamics of an inverted flag. *J. Fluid Mech.*, 736:R1.

Kim, Y. and Peskin, S. C. (2007). Penalty immersed boundary method for an elastic boundary with mass. *Phys. Fluids*, 19(5):053103.

Kline, S. J. and McClintock, F. A. (1953). Describing uncertainties in single-sample experiments. *ASME Mech. Eng.*, 75(1):3–8.

Koschatzky, V., Moore, P. D., Westerweel, J., Scarano, F., and Boersma, B. J. (2011). High speed piv applied to aerodynamic noise investigation. *Exp. Fluids*, 50(4):863–876.

Kundu, P. K. and Cohen, I. M. (2008). *Fluid Mechanics*. Elsevier, 4th edition.

Levenberg, K. (1944). A method for the solution of certain problems in least-squares. *Quart. Appl. Math.*, 2:164–168.

Li, S., Yuan, J., and Lipson, H. (2011). Ambient wind energy harvesting using cross-flow fluttering. *J. Appl. Phys.*, 109(2):026104.

Liao, J. C., Beal, D. N., Lauder, G. V., and Triantafyllou, M. S. (2003). Fish exploiting vortices decrease muscle activity. *Science*, 302(5650):1566–1569.

Lighthill, M. J. (1960a). Mathematics and aeronautics. *J. Roy. Aero. Soc.*, 64(595):375–394.

Lighthill, M. J. (1960b). Note on the swimming of slender fish. *J. Fluid Mech.*, 9(2):305–317.

Lighthill, M. J. (1969). Hydromechanics of aquatic animal propulsion. *Annu. Rev. Fluid Mech.*, 1(1):413–446.

Lighthill, M. J. (1970). Aquatic animal propulsion of high hydromechanical efficiency. *J. Fluid Mech.*, 44(2):265301.

Lighthill, M. J. (1971). Large-Amplitude Elongated-Body Theory of Fish Locomotion. *P. Roy. Soc. Lond. B Bio.*, 179:125–138.

Liu, X. and Katz, J. (2006). Instantaneous pressure and material acceleration measurements using a four-exposure piv system. *Exp. Fluids*, 41(2):227.

Liu, X. and Katz, J. (2013). Vortex-corner interactions in a cavity shear layer elucidated by time-resolved measurements of the pressure field. *J. Fluid Mech.*, 728:417457.

Lloyd, D. W., Shanahan, W. J., and Konopasek, M. (1978). The folding of heavy fabric sheets. *Int. J. Mech. Sci.*, 20(8):521 – 527.

Love, A. E. H. (1927). *A Treatise on the Mathematical Theory of Elasticity*. Cambridge University Press.

Lucey, A. D. (1998). The excitation of waves on a flexible panel in a uniform flow. *Philos. Trans. A Math. Phys. Eng. Sci.*, 356(1749):2999–3039.

Marquardt, D. W. (1963). An algorithm for least-squares estimation of nonlinear parameters. *J. Soc. Inc. Appl. Math.*, 11(2):431–441.

Mathis, A., Mamidanna, P., Cury, K. M., Abe, T., Murthy, V. N., and M. Mathis, M. W. B. (2018). Deeplabcut: markerless pose estimation of user-defined body parts with deep learning. *Nature Neuroscience*, 21(9):1281–1289.

Michelin, S. and Doaré, O. (2013). Energy harvesting efficiency of piezoelectric flags in axial flows. *J. Fluid Mech.*, 714:489–504.

Michelin, S., Smith, S. G. L., and Glover, B. J. (2008). Vortex shedding model of a flapping flag. *J. Fluid Mech.*, 617:1–10.

Moon, F. C. (2004). *Chaotic and Fractal Dynamics: An Introduction for Applied Scientists and Engineers*. Wiley-VCH, Germany.

Moré, J. (1978). The levenberg-marquardt algorithm: Implementation and theory. In Watson, G. A., editor, *Numerical Analysis*, volume 630 of *Lecture Notes in Mathematics*, pages 105–116. Springer Berlin Heidelberg.

Müller, U. K. (2003). Fish 'n flag. *Science*, 302(5650):1511–1512.

Munk, M. M. (1924). The aerodynamic forces on airship hulls. Naca-tr-184, Nat. Adv. Com. Aero., Washington, NACA-TR-184.

Muriel, D. F. and Cowen, E. A. (2018). On the realization of a second buckling mode in a periodically-constrained heavy elastica. *Extreme Mechanics Letters*, 21:76 – 81.

Muriel, D. F., Tinoco, R. O., Filardo, B. P., and Cowen, E. A. (2016). Development of a novel, robust, sustainable and low cost self-powered water pump for use in free-flowing liquid streams. *Renew. Energ.*, 91:466–476.

Oertel, H. (2010). *Prandtl-Essentials of Fluid Mechanics*. Springer, New York.

Paidoussis, M. P. (1966). Dynamics of flexible slender cylinders in axial flow part 1. theory. *J. Fluid Mech.*, 26(4):717–736.

Paidoussis, M. P. (2016a). *Fluid-structure interactions: slender structures and axial flow*, volume 1. Academic Press, Oxford, 2nd edition.

Paidoussis, M. P. (2016b). *Fluid-structure interactions: slender structures and axial flow*, volume 2. Academic Press, Oxford, 2nd edition.

Pan, Z., Whitehead, J., Thomson, S., and Truscott, T. (2016). Error propagation dynamics of piv-based pressure field calculations: How well does the pressure poisson solver perform inherently? *Meas. Sci. Technol.*, 27(8):084012.

Powell, M. J. D. (1968). *A fortran subroutine for solving systems of non-linear algebraic equations*. AERE-R. H.M. Stationery Office.

Prandtl, L. (1952). *Essentials of Fluid Dynamics*. Hafner Publications, New York.

Rayleigh, L. (1879). On the instability of jets. *Proc. Lond. Math. Soc.*, X:4–13.

Reiss, E. L. (1969). Column buckling: an elementary example of bifurcation. In Keller, J. B. and Antman, S., editors, *Bifurcation theory and nonlinear eigenvalue problems*, pages 1–16. W. A. Benjamin, New York.

Ristroph, L. and Zhang, J. (2008). Anomalous hydrodynamic drafting of interacting flapping flags. *Phys. Rev. Lett.*, 101(19):194502.

Rojratsirikul, P., Genc, M., Wang, Z., and Gursul, I. (2011). Flow induced vibrations of low aspect ratio rectangular membrane wings. *J. Fluids Struct.*, 27(8):1296–1309.

Rojratsirikul, P., Wang, Z., and Gursul, I. (2010). Effect of prestrain and excess length on unsteady fluid structure interactions of membrane airfoils. *J. Fluids Struct.*, 26(3):359–376.

Roman, B. and Pocheau, A. (2002). Postbuckling of bilaterally constrained rectangular thin plates. *J. Mech. Phys. Solids*, 50(11):2379 – 2401.

Ryu, J., Park, S. G., Kim, B., and Sung, H. J. (2015). Flapping dynamics of an inverted flag in a uniform flow. *J. Fluids Struct.*, 57:159 – 169.

Sader, J. E., Cossé, J., Kim, D., Fan, B., and Gharib, M. (2016). Large-amplitude flapping of an inverted flag in a uniform steady flow ñ a vortex-induced vibration. *J. Fluid Mech.*, 793:524–555.

Santillan, S. T., Virgin, L. N., and Plaut, R. H. (2006). Postbuckling and vibration of heavy beam on horizontal or inclined rigid foundation. *J. Appl. Mech.*, 73(4):664–671.

Schouveiler, L. and Eloy, C. (2012). Flapping plate (s). In *Experimental and Theoretical Advances in Fluid Dynamics*, pages 3–14. Springer Berlin Heidelberg.

Shelley, M., Vandenberghe, N., and Zhang, J. (2005). Heavy flags undergo spontaneous oscillations in flowing water. *Phys. Rev. Lett.*, 94:094302.

Shelley, M. J. and Zhang, J. (2011). Flapping and bending bodies interacting with fluid flows. *Annu. Rev. Fluid Mech.*, 43:449–465.

Singh, K., Michelin, S., and Langre, E. D. (2012a). The effect of non-uniform damping on flutter in axial flow and energy-harvesting strategies. *Philos. Trans. A Math. Phys. Eng. Sci.*, 468(2147):3620–3635.

Singh, K., Michelin, S., and Langre, E. D. (2012b). Energy harvesting from axial fluid-elastic instabilities of a cylinder. *J. Fluids Struct.*, 30:159–172.

Smith, B. W., Chase, J. G., Nokes, R. I., Shaw, G. M., and Wake, G. (2004). Minimal haemodynamic system model including ventricular interaction and valve dynamics. *Med. Eng. Phys.*, 26(2):131–139.

Sodano, H. A., Park, G., and Inman, D. J. (2004). Estimation of electric charge output for piezoelectric energy harvesting. *Strain*, 40(2):49–58.

Souilliez, C., Eloy, C., and Schouveiler, L. (2006). An experimental study of flag flutter. In *ASME 2006 Pressure Vessels and Piping/ICPVT-11 Conference*, pages 465–472. American Society of Mechanical Engineers.

Taneda, S. (1968). Waving motions of flags. *J. Phys. Soc. Jpn.*, 24(2):392–401.

Taneda, S. and Tomonari, Y. (1974). Experiment on flow around a waving plate. *J. Phys. Soc. Jpn.*, 36(6):1683–1689.

Tang, L. and Paidoussis, M. P. (2007). On the instability and the post-critical behaviour of two-dimensional cantilevered flexible plates in axial flow. *J. Sound Vib.*, 305(1):97–115.

Tang, L., Paidoussis, M. P., and Jiang, J. (2009). Cantilevered flexible plates in axial flow: Energy transfer and the concept of flutter-mill. *J. Sound Vib.*, 326(1–2):263–276.

Taylor, G. W., Burns, J. R., Kammann, S. M., Powers, W. B., William, B., and Wel, T. R. (2001). The energy harvesting eel: a small subsurface ocean/river power generator. *IEEE J. Ocean. Eng.*, 26(4):539–547.

Techet, A. H., Allen, J. J., and Smits, A. J. (2002). Piezoelectric eels for energy harvesting in the ocean. In *The Twelfth International Offshore and Polar Engineering Conference*, pages 713–718. International Society of Offshore and Polar Engineers.

Timoshenko, S. and Woinowsky-Krieger, S. (1987). *Theory of plates and shells*. McGraw Hill, United States of America, 2nd edition.

Topea, C., L., Y. A., and Foss, J. F. (2007). *Handbook of Experimental Fluid Mechanics*. Springer-Verlag, Berlin.

Triantafyllou, M. S., Triantafyllou, G. S., and Yue, D. K. P. (2000). Hydrodynamics of fishlike swimming. *Annu. Rev. Fluid Mech.*, 32:33–53.

van Oudheusden, B. W. (2013). Piv-based pressure measurement. *Meas. Sci. Technol.*, 24(3):032001.

Vandiver, J. K. (1993). Dimensionless parameters important to the prediction of vortex-induced vibration of long, flexible cylinders in ocean currents. *J. Fluids Struct.*, 7(5):423–455.

Wang, C. Y. (1981). The ridging of heavy elastica. *ZAMM-Z. Angew. Math. Me.*, 61(2):125–126.

Wang, C. Y. (1983). Buckling of a heavy lamina by an edge displacement. *Int. J. Mech. Sci.*, 25(6):447–453.

Wang, C. Y. (1984a). Buckling and postbuckling of the lying sheet. *Int. J. Solids Struct.*, 20(4):351 – 358.

Wang, C. Y. (1984b). On symmetric buckling of a finite flat-lying heavy sheet. *J. Appl. Mech.*, 51(2):278–282.

Wang, C. Y. (1986). A critical review of the heavy elastica. *Int. J. Mech. Sci.*, 28(8):549–559.

Watanabe, Y., Isogai, K., Suzuki, S., and Sugihara, M. (2002a). A theoretical study of paper flutter. *J. Fluid Struct.*, 16(4):543–560.

Watanabe, Y., Suzuki, S., Sugihara, M., and Sueoka, Y. (2002b). An experimental study of paper flutter. *J. Fluid Struct.*, 16(4):529–542.

Watson, L. T. and Wang, C. Y. (1983). Periodically supported heavy elastic sheet. *J. Eng. Mech. ASCE*, 109(3):811–820.

Wereley, S. and Meinhart, C. (2001). Second-order accurate particle image velocimetry. *Exp. Fluids*, 31(3):258–268.

Williamson, C. H. K. (1996). Vortex dynamics in the cylinder wake. *Annu. Rev. of Fluid Mech.*, 28(1):477–539.

Xia, Y., Michelin, S., and Doaré, O. (2015). Fluid-solid-electric lock-in of energy-harvesting piezoelectric flags. *Phys. Rev. Applied*, 3:014009.

Zhang, C., Wang, J., Blake, W., and Katz, J. (2017). Deformation of a compliant wall in a turbulent channel flow. *J. Fluid Mech.*, 823:345390.

Zhang, J., Childress, S., Libchaber, A., and Shelley, M. (2000). Flexible filaments in a flowing soap film as a model for one-dimensional flags in a two-dimensional wind. *Nature*, 408(6814):835–9.

Zhu, L. D. and Peskin, C. S. (2002). Simulation of a flapping flexible filament in a flowing soap film by the immersed boundary method. *Journal of Computational Physics*, 179(2):452–468.